PERFORMANCE AND EMISSION OPTIMIZATION OF CIDI ENGINE THROUGH VARIOUS FUEL INJECTION STRATEGIES

Balaji Mohan

NATIONAL UNIVERSITY OF SINGAPORE

2015

PERFORMANCE AND EMISSION OPTIMIZATION OF CIDI ENGINE THROUGH VARIOUS FUEL INJECTION STRATEGIES

Balaji Mohan

(B.E., Anna University)

A THESIS SUBMITTED

FOR THE DEGREE OF DOCTOR OF PHILOSOPHY

DEPARTMENT OF MECHANICAL ENGINEERING

NATIONAL UNIVERSITY OF SINGAPORE

2015

DECLARATION

I hereby declare that the thesis is my original work and it has been written by me in its entirety.

I have duly acknowledged all the sources of information which have been used in the thesis.

This thesis has also not been submitted for any degree in any university previously.

Balaji Mohan

23 March 2015

Dedicated to

My Friends, Teachers and Family

Acknowledgments

First and Foremost, I would like to express my sincere gratitude to my supervisor Dr. Yang Wenming for his continuous support, patience, motivation, enthusiasm, and immense knowledge. He also helped me through all difficult times during my research in NUS by his clear guidance and suggestions. I would also wish to thank my co-supervisor Prof. Chou Siaw Kiang for giving me the opportunity to be part of this wonderful group of intellectuals. I am thankful to A/Prof. Lee Poh Seng who provided a high speed camera for this research which made the large part of the thesis. I also extend my gratitude to Dr. Chua Kian Jon, Ernest and A/Prof. Christopher Yap for their kind acceptance to be in the examination panel and for their inputs, suggestions and encouragement during my oral qualifying examination.

Without the help of a few people this thesis would have not been possible. I would like to take this opportunity to specially thank A/Prof. Valerie Golovitchev (Chalmers University of Technology) for his kind guidance and teaching the nuances of KIVA4 CFD code and my fellow research mates Dr. An Hui and Mr. Amin Magbhouli for travelling with me during initial struggle in understanding the KIVA4 CFD codes. I would also wish to thank my other research mates Dr. Yu Wenbin, who helped me with improving the experimental set-up, and Mr. Tay Kun Lin, Clement who extended his help during experimental works. I also thank other research mates Ms. Li Jing, Mr. Zhou Dezhi, Mr. Jiang Dongyue, and Mr.

Cui Xin. I also owe thanks to many laboratory staff members for the unconditional help that they provided during the experiments especially Mr. Tan Tiong Thiam (Energy Conversion lab), Mrs. Hung-Ang Yan Leng (Thermal Process Lab-I), Mrs. Roslina Bte Abdullah (Thermal Process Lab-II), Mr. Goh Tiong Lai, Alvin, Mr. Low Chee Wah, Joe (Impacts Lab), Mr. Tan Choon Huat (Advanced Manufacturing Lab), Mr. Sacadevan Raghavan (Air-Conditioning Lab), Mr. Lam Kim Song, Mr. Rajah s/o M Thangaveloo, Mr. Rajendran s/o Ponnusamy (Fabrication Support Centre). I also thank Dr. Karthik Balasubramanian, Mr. Mrinal Jagirdar and Mr. Matthew Law Lee Liong for teaching me how to use the high speed camera and sharing the camera during their busy schedule.

I would like to acknowledge National University of Singapore for providing me scholarship to pursue this research. I thank Ms. Sharen for her kind assistance in academic related administrative processes. I also thank Dr. Wang Junhong for his great support in solving technical issues related to HPC (High Performance Computing) services. I further extend my thanks to many anonymous reviewers of my manuscripts, whose constructive and invaluable comments and suggestions helped me to improve the quality of my research and encouraged me to further explore new ideas and thoughts.

A special thanks goes to Dr. Vallinayagam Raman, Dr. Vedharaj Sivasankaralingam who not only helped me through research but also made my stay in Singapore, a memorable one along with Dr. Meiyappan Lakshmanan, Dr. Sankaranarayanan Seetharaman, Mr. Anandhkumar Raju, Mr. Nivash Elango, Mr. Karthikraja Periasami, Dr. Karthikeyan Kumarasamy, Dr. Aravind Raghavendra, and Mr. Harikrishnan Sekar. I take this wonderful moment to thank my other friends who influenced my life particularly Mr. Mohanakrishnan Nagarajan, Mr. P.S. Senthilnathan, Mr. Sundar Ganesh, Mr. Ashwin Rajendran, Mr. Srikanth Raghavan, Mr. Bharath Sudarshan, Mr. Prakash Subburayan and Mr. Magesh Babu Dheenan.

Last but not the least; I would like to thank my mom Mrs. Lakshmi Mohan,

my dad Mr. Mohan Veerasamy, grandparents Mrs. Padmavathy Subramani and Mr. Subramani Achari, my brother Mr. Vignesh Mohan and other relatives for their unconditional shower of love towards me.

Balaji Mohan

Contents

Summary

Diesel engines are the most efficient energy conversion devices. However they have one serious drawback: the amount of exhaust emissions like NOx and particulate matter (PM) is comparatively larger than that of gasoline engines. The complete combustion of fuel leads to major reductions in the formation of exhaust emissions. The combustion process in diesel engine is significantly affected by the fuel-air mixing and accuracy in the injection processes. Therefore, by instituting a better fuel-air mixing, the particulate emissions can be reduced; however, nitrogen oxides tend to increase and vice-versa. Therefore the current goal of this thesis is to better understand the fuel-air mixing process and implement strategies to obtain NOx-soot trade-off. Therefore, this research is classified into three phases as follows:

In the first phase, a constant volume spray chamber was specially built to simulate the engine combustion chamber condition during injection process. The spray characteristics and fuel-air mixing of different fuels like diesel, pure biodiesel (B100) and blend fuel (B20) were investigated. The spray momentum was also measured to understand the cavitation phenomenon that takes place inside the injector nozzle holes. From this fundamental study, it was found that, in general, the momentum flux, spray tip penetration and fuel-air mixing increases with increasing pressure difference. It was also found that, B100 suffered from poor atomization which was ascertained from fuel volume and air entrainment analysis. From momentum flux data, it was found that cavitation inside the injector nozzle holes contributed significantly to the primary atomization of fuel.

In the second phase, a generalized hybrid spray model was developed and val-

idated with knowledge obtained from experiments. This new hybrid spray model was developed by coupling the cavitation induced spray sub model to classical KH-RT spray model and implemented in KIVA4 CFD code. In order to understand the cavitation phenomenon inside the injector nozzle holes, a detailed parametric study has been done using Fluent CFD package. From this study, the factors that affect cavitation are well understood and documented. Then the new hybrid spray model was extensively validated against experimental results from literature and in-house experiments. Then this new model was used to predict spray characteristics and fuel-air mixing of different fuels like diesel, pure biodiesel and blend fuels.

In the final phase, experiments were carried out by varying injection timing and injection pressure in a single cylinder diesel engine powered by biodiesel blend fuel. It was found that by either changing the fuel injection pressure or injection timing, the emission norms of genset can be achieved without compromising fuel consumption or engine modifications. Then 3D simulation was carried out using KIVA4 CFD code to investigate the effect of injection rate shaping by changing boot length and boot pressure on biodiesel fueled CI engine. It was found that NOx-soot trade-off could be obtained by either using long boot length or high boot pressure injection rate profiles.

List of Tables

List of Figures

Nomenclature

Roman Symbols

$\Re_B$	Bubble radius	[m]
$\vec{V}$	Mixture velocity	[m/s]
A/F	Air fuel ratio	
$C_\mu, C_{\epsilon_1}, C_{\epsilon_2}$	Empirical constants in $k-\epsilon$ turbulence models	
C_a	Area contraction coefficient	
C_D	Coefficient of discharge	
d, D	Diameter	[m]
E	Emissions	[ppm or g/h]
F	Force	[N]
F_s	Factor of safety	
k	Turbulent kinetic energy	
K_{factor}	K_{factor} of the nozzle hole	
L	Length	[m]
L_{bu}	Length of liquid core	[m]
M	Momentum	[N]
m	Mass	[kg]
n_B	Number of buubles	
P	Pressure	[MPa]
Q	Volume flow rate	[m^3/s]
R	Net mass source term	
S	Spray Penetration Length	[m]
Sc	Schmidt number	
T	Temperature	[K]

t	Time	[s]
u	Velocity	[m/s]
V	Spray volume	$[m^3]$
A	cross sectional area	$[m^2]$
B100	Pure biodiesel	
B20	Biodiesel 20% blend with Diesel	
H	Humidity	[g/kg]
k	Cavitation parameter	
Q	Heat release	[J]
T	Taylor number	
Z	Ohnesorge number	

Greek Symbols

$\sigma_k, \sigma_\epsilon$	Empirical constants in $k-\epsilon$ turbulence models	
$[\sigma]^t$	Allowable design stress	[MPa]
α	Spray cone angle	[radians]
α	Vapor volume fraction	
ΔP	Pressure drop	[Pa]
δ	Thickness of pressure chamber	[m]
δ_e	Effective thickness of the pressure chamber	[m]
ϵ	Turbulent dissipation	
η	Mechanical efficiency	[%]
γ	Ratio of specific heats	
Λ	Wavelength	[m]
μ	Viscosity	[Pas]
Ω	Growth rate	$[s^{-1}]$
ω_0	Initial droplet frequency	[Hz]
ϕ	Equivalence ratio	
ρ	Density	$[kg/m^3]$
σ	Maximum tensile strength	[MPa]

σ	Surface tension	[N/m]
θ	Spray angle	[radians]

Subscripts

a	Air
avg	Average
B	Bubbles
C	Critical
cav	Cavitation
$comp$	Compsite
e	Exhaust
f	Fuel
H	Hydraulic
i	Inner
i	mode
i, j, k	Direction vectors
in	Inlet
n	Nozzle
out	Outlet
SMD	Sauter mean diameter
t	Turbulence
v	Vapor
act	Actual
amb	Ambient
bu	Break-up
inj	Injection
KH	Kelvin-Helmholtz
l	Fuel/ liquid
max	Maximum
RT	Rayleigh-Taylor

th	Theoretical	

Abbreviations

BMEP	Brake Mean Effective Pressure	[bar]
BSEC	Brake Specific Energy Consumption	[kJ/kWh]
BSFC	Brake Specific Fuel Consumption	[g/kWh]
bTDC	before Top Dead Centre	[degree]
BTE	Brake Thermal Efficiency	[%]
CA	Crank Angle	[degree]
CAB	Cascade Atomization and drop Break-up model	
CFD	Computational FLuid Dynamics	
CI	Compression Ignition	
CO	Carbon mono oxide	
CO_2	Carbon di oxide	
CPCB	Central Pollution Control Board	
DI	Direct Injection	
DPF	Diesel Particulate Filter	
DT	Dwell Time	[degree]
EGR	Exhaust Gas Recirculation	
EGT	Exhaust Gas Temperature	[K]
ET	Energizing Time or Injection duration	[degree]
ETAB	Enhanced Taylor Analogy Break-up model	
FEA	Finite Element Analysis	
HC	Unburned Hydrocarbon	
HSU	Hartridge smoke unit	
IDI	Indirect Injection	
IRC	Injection Rate Control	
ISO	International Standard Organization	
KH	Kelvin-Helmholtz	
NDIR	Non-Dispersive Infrared analyser	

NO_x	Oxides of Nitrogen	
NOP	Nozzle Opening Pressure	
O_2	Oxygen	
PM	Particulate Matters	
ppm	Parts per million	
Re	Reynolds number	
ROI	Rate of Injection	
SCR	Selective Catalytic Reduction	
SMD	Sauter Mean Diameter	$[\mu m]$
SME	Soy methyl ester	
SO_2	Sulphur di oxide	
SOF	Soluble Organic Fraction	
SOI	Start of Injection	[degree]
TAB	Taylor Analogy Break-up model	
TDC	Top Dead Centre	
WCO	Waste Cooking Oil	
We	Weber number	
WF	Weighting Factor	

List of publications

Publications in peer reviewed journals related to thesis

1. **B Mohan**, WM Yang, KL Tay, W Yu, SK Chou. Numerical investigation on the effects of injection rate shaping on combustion and emission characteristics of biodiesel fueled CI engine. (Submitted for a special issue in Applied Energy) [SCI]

2. **B Mohan**, WM Yang, KL Tay, W Yu. Experimental study of spray characteristics of biodiesel derived from Waste cooking oil. Energy Conversion and Management. 88:622–632, 2014. DOI: 10.1016/j.enconman.2014.09.013. [SCIE]

3. **B Mohan**, WM Yang, KL Tay, W Yu. Macroscopic spray characterization under high ambient density conditions. Experimental Thermal and Fluid Science, 59:109–117, 2014. DOI: 10.1016/j.expthermflusci.2014.08.003. [SCIE]

4. **B Mohan**, WM Yang, V Raman, V Sivasankaralingam, SK Chou. Optimization of biodiesel fueled engine to meet emission standards through varying nozzle opening pressure and static injection timing. Applied Energy, 130:450–457, 2014. DOI: 10.1016/ j.apenergy.2014.02.033. [SCI] *(Special Issue: The 5th International Conference on Applied Energy (ICAE2013), Part I: Energy innovations for a sustainable world)*

5. **B Mohan**, WM Yang, W Yu. Effect of internal nozzle flow and thermophysical properties on spray characteristics of methyl esters. Applied Energy, 129:123–134, 2014. DOI: 10.1016/j.apenergy.2014.04.109. [SCI]

6. **B Mohan**, WM Yang, SK Chou. Cavitation in Injector Nozzle Holes– A Parametric Study. Engineering Applications of Computational Fluid Mechanics, 8(1):70–81, 2014. DOI: 10.1080/19942060.2014.11015498. [SCIE]

7. **B Mohan**, WM Yang, SK Chou. Development of an accurate cavitation coupled spray model for diesel engine simulation. Energy Conversion and Management, 77:269–277, 2014. DOI: 10.1016/j.enconman.2013.09.035. [SCIE]

8. **B Mohan**, WM Yang, SK Chou. Fuel injection strategies for performance improvement and emissions reduction in compression ignition engines-A review. Renewable and Sustainable Energy Reviews, 28:664–676, 2013. DOI: 10.1016/ j.rser.2013.08.051. [SCI]

Proceedings in peer reviewed conferences related to thesis

1. **B Mohan**, WM Yang, SK Chou. Effects of injection rate shaping on combustion and emission characteristics of biodiesel fueled CI engine - A CFD study. Sixth International Conference on Applied Energy ICAE 2014, Taipei, Taiwan. (Oral)

2. **B Mohan**, WM Yang, V Raman, V Sivasankaralingam, SK Chou. Optimization of biodiesel fuelled engine to meet emission standards through varying nozzle opening pressure and static injection timing. 5^{th} International Conference on Applied Energy ICAE 2013, Pretoria, South Africa. (Oral)

1

Introduction

1.1 Background and motivation

The diesel engine was first patented in 1892 by Rudolf Diesel and, since then it has revolutionized the entire road transportation system. Fig.1.1 shows the market share of diesel fuel in existing vehicles in European Union and among new vehicles produced all over the world in the year 2012. Diesel vehicles dominate the passenger car market in the European Union e.g., in 2012; 55% of all newly registered cars were powered by diesel engines [1]. Diesel engines are the preferred source of power not only among passenger cars but almost everything from generating electricity in industries to power trucks, boats and large ships.

The main disadvantage of compression ignited combustion compared to spark

Figure 1.1: Market share of diesel engines in existing passenger cars in EU (left pie chart) and new passenger cars produced across the world in 2012 [1]

ignited combustion is that the fuel-air mixture is not homogenous throughout the combustion chamber. The combustion in compression ignition engines is therefore predominantly governed by proper fuel-air mixing which is eventually defined by the spray characteristics of the fuel. Therefore, parts of combustion take place in environments short of oxygen, which are often called rich mixture or high equivalence ratio zones. This high equivalence ratio zones leads to soot formation. Fig.1.2 [2] shows the regions where emissions such as soot and thermal NO are formed. Most of the NO is formed in the flame front (green region) where the fuel-air mixture is approximately stoichiometric and the flame is the hottest. The gray region shows the initial soot formation area in the fuel spray and the orange/blue interface region shows the area where the soot oxidation takes place. This shows that spray characteristics and fuel-air mixing governs the emission formation and combustion efficiency in compression ignition engines.

NO_x (Nitrogen oxides) and particulate emissions are regulated in each country through various emission norms and regulations as these emissions are found to be detrimental for ecosystem. PM emissions are found to increase the respiratory symptoms, decrease lung functions, and induce asthma in human beings. NO_x emissions have shown to cause sensitivity to respiratory passage and also cause smog along with HC emissions under the influence of sunlight [3, 4, 5].

As explained earlier, combustion process in diesel engine is significantly affected by the fuel-air mixing process. Therefore, by instituting a better fuel-air mixing,

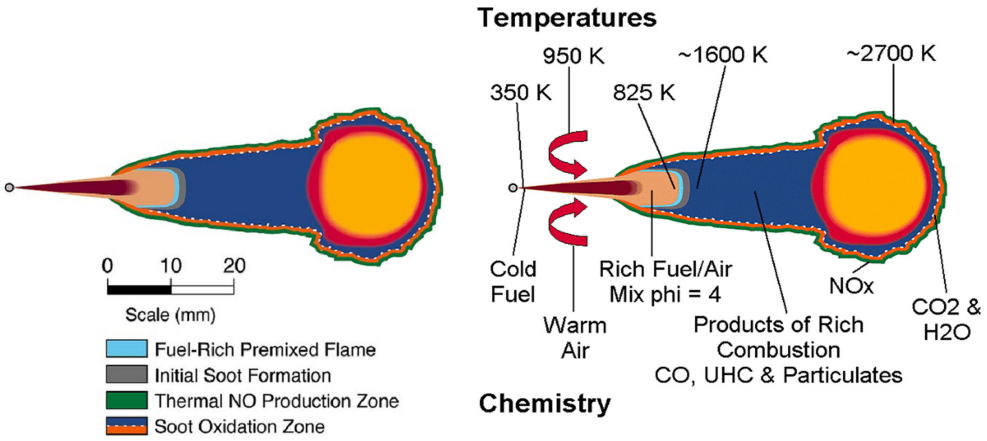

Figure 1.2: Summary of diesel combustion process [2]

the quantities of particulate emissions can be decreased; nonetheless, at the same time, nitrogen oxides tend to increase. Similarly, strategies to reduce NO_x tend to increase particulates as well as to reduce power output. The NO_x-soot trade-off can be explained from Fig.1.3. The NO_x and soot emissions are on either side of a seesaw which is pivoted on fuel consumption. Therefore, as shown in the figure, the engine manufacturers are posed with a great challenge of meeting both legislative emission norms imposed by various government bodies and fuel consumption rate expected by general public on buying their vehicles.

1.2 Scope of the thesis

1.2.1 Objectives

As mentioned earlier, the great concern in compression ignition engines is to reduce emissions without compromising the efficiency and fuel consumption. Therefore, the objective of this thesis is in line with the quote as follows

> *"Our ultimate goal is to create an engine that functions in harmony with nature while still meeting the demands of an ever-advancing civilization."*
>
> *- Takashi Suzuki, "The Romance of Engines"* [6]

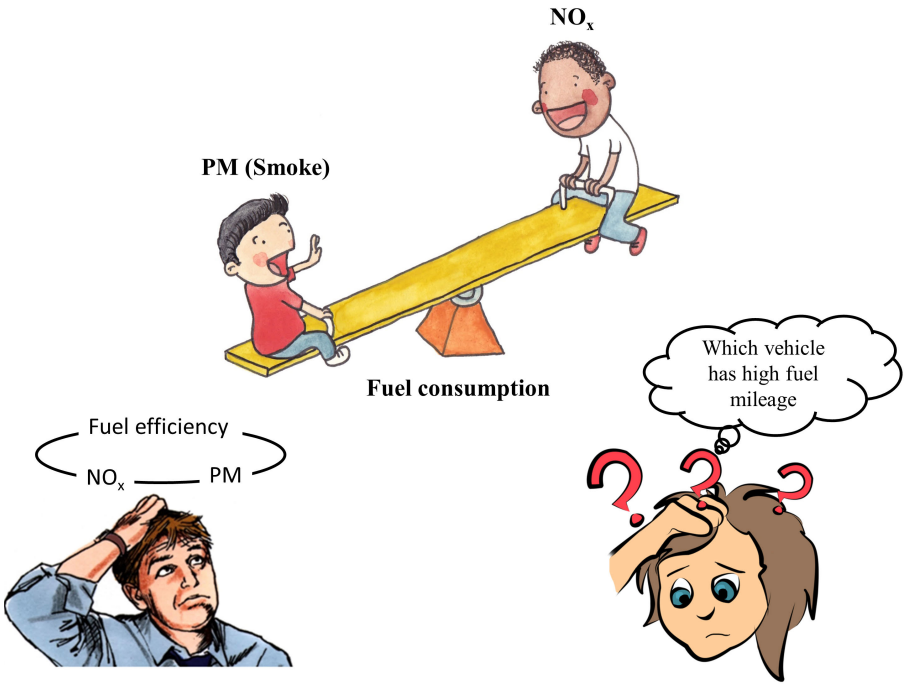

Figure 1.3: NO_x-soot trade-off

The primary focus of this thesis is to establish a better understanding on fundamental fuel-air mixing process and its impact on combustion process and emission formations and to achieve better NO_x-soot trade-off. Therefore, the objectives of this thesis is classified into fundamental experimental and simulation research on spray development and fuel-air mixing process followed by application on engine experiments and simulations. The main objectives of this thesis are summarized in the Fig.1.4:

- To discern the spray characteristics and its effect on combustion and emission formation, for which an experimental setup has to be designed and commissioned.

- To understand the detailed physics underlying the spray development process and establish the impact of cavitation on primary atomization.

- To develop a universal spray model to predict the spray characteristics of different fuels.

- To apply the knowledge obtained through this fundamental study to obtain

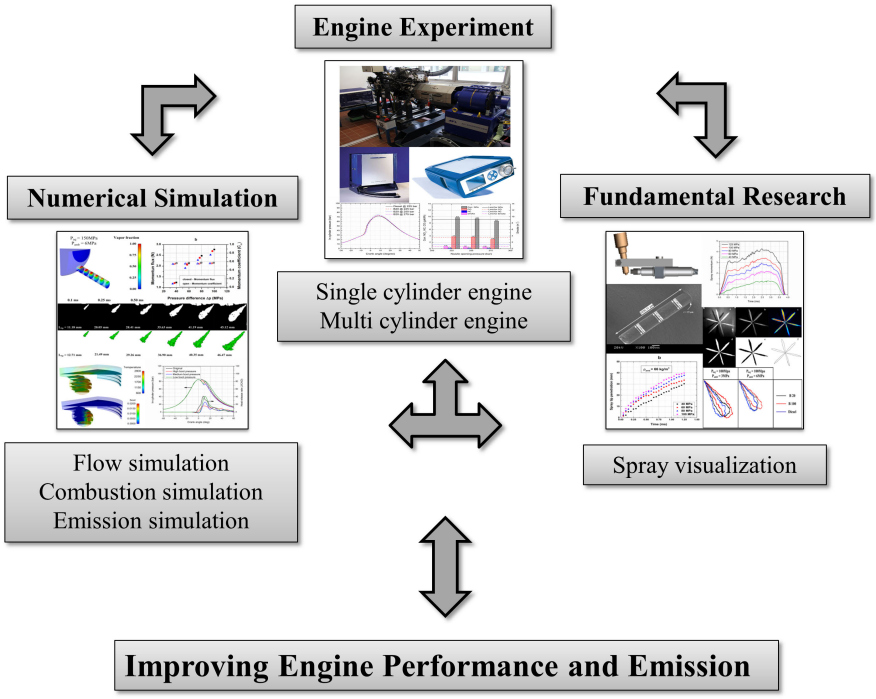

Figure 1.4: Objective of this thesis

better NO_x-soot trade-off.

1.2.2 Organization of the thesis

The thesis is organized into seven chapters. The organization is as follows

Chapter 1 This chapter introduces the motivation and objectives of this thesis.

Chapter 2 This chapter provides an extensive literature review on various injection strategies available to reduce emissions at source and its pros and cons. From the outcome of this literature review, it was found that fuel-air mixing defined by spray characteristics inside the combustion chamber is a significant factor which governs the combustion and emission formations. This paved the path for further investigations of spray and fuel air mixing process in subsequent chapters.

Chapter 3 This chapter elaborates design, fabrication and testing of high pressure constant volume spray chamber to simulate the environment inside the

combustion chamber during injection process. Then spray characteristics and fuel-air mixing process of different fuels were investigated using the set-up. The results were then used to develop a new hybrid spray model to predict the spray characteristics and atomization process.

Chapter 4 This chapter introduces fundamentals of cavitation phenomenon inside the diesel injector nozzle holes and its effect on primary atomization. A detailed parametric study has been provided in this chapter to better appreciate the factors that affect cavitation inception.

Chapter 5 This chapter details the development and validation of the new hybrid spray model to predict the spray characteristics and fuel-air mixing process in engine simulations. The new model was extensively validated against experimental results from literature and in-house experiments. This chapter also shows the capability of this new model in predicting spray characteristics of different fuels.

Chapter 6 This chapter presents both experimental and numerical investigation of different injection strategies on engine performance and emission formations. The effect of injection pressure and injection timing were experimentally studied in a single cylinder diesel engine and optimum pressure and timing were obtained. The effect of injection rate shaping was investigated using 3D CFD simulations. The results of both experimental and simulation findings were discussed in detail.

Chapter 7 This chapter summarizes the key findings and accomplishments of this thesis. Recommendations for future possible extension of this work have been discussed.

2

Fuel injection strategies - A review[1]

2.1 Introduction

Diesel engines are the most efficient energy conversion devices. However they have one serious drawback: the amount of exhaust emissions like NO_x and particulate matter (PM) is comparatively larger than that of gasoline engines. According to various reports [7, 8, 9, 10, 11, 12], the exhaust emissions from engines have undesirable effects on human health. The reduction of environmental pollutions from diesel engines is regulated by federal government regulations. In order to improve the air quality standards, regulations on emissions from mobile sources have

[1]Excerpts of this chapter, in part, is a reprint of previous publication titled "*Fuel injection strategies for performance improvement and emissions reduction in compression ignition engines—A review*", Renewable and Sustainable Energy Reviews 28, 664-676, 2013. DOI: 10.1016/j.rser.2013.08.051.

become stringent drastically in USA, Japan, Europe and other Asian countries over the decade. The European emission standards implement progressive and increasing stringent emission norms on passenger diesel cars [13] shown in Fig.2.1. These regulations have pressed the automobile industries to explore substitutes to conventional fuel injection systems and have enthused attention in development of various fuel injection strategies. The European Union emission standards [14] for passenger cars (Category M1) are summarized in the Table2.1.

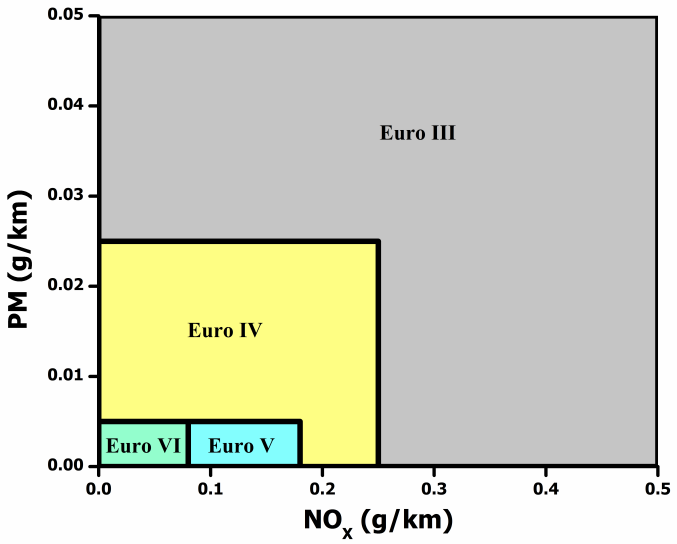

Figure 2.1: European emission standards for passenger diesel cars

The emissions formed are dependent upon the engine design, power output and working load. The complete combustion of fuel leads to major reductions in the formation of exhaust emissions. Complete combustion is a result of careful matching of air-fuel mixture and accuracy in the injection process. In order to reduce NO_x and PM formation it is necessary to understand the mechanisms of its formation.

2.1.1 NO_x and PM formation

Generally, the combustion process in a typical CI engine can be classified into four major phases [15] as shown in Fig.2.2, the heat release rate curve of a CI engine.

Table 2.1: European union emission standards for passenger cars

Tier	Date	CO	HC+NO_x	NO_x	PM	PN
			(g/km)			($\#/km$)
Euro 1*	Jul, 1992	2.72 (3.16)	0.97 (1.13)	-	0.14 (0.18)	-
Euro 2, IDI	Jan, 1996	1.0	0.7	-	0.08	-
Euro 2, DI	Jan, 1996 [a]	1.0	0.9	-	0.1	-
Euro 3	Jan, 2000	0.64	0.56	0.5	0.05	-
Euro 4	Jan, 2005	0.5	0.3	0.25	0.025	-
Euro 5a	Sep, 2009 [b]	0.5	0.23	0.18	0.005 [d]	-
Euro 5b	Sep, 2011 [c]	0.5	0.23	0.18	0.005 [d]	$6x10^{11}$
Euro 6	Sep, 2014	0.5	0.1	0.08	0.005 [d]	$6x10^{11}$

* All values outside bracket are for homologation limits and values within bracket are for conformity of production (COP) limits

[a] Until 3rd September, 1999, after that date DI must meet the IDI limits

[b] Jan, 2011for all models

[c] Jan, 2013 for all models

[d] 0.0045 g/km using the PMP measurement technique

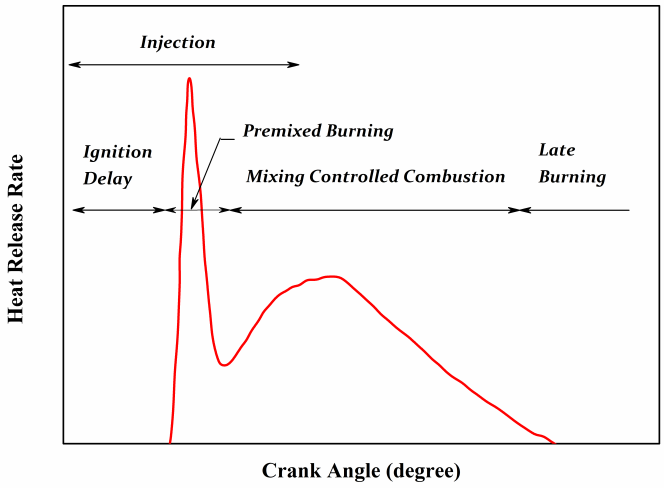

Figure 2.2: Typical heat release rate curve of a CI engine (redrawn from [15])

The four phases are ignition delay, premixed burning, mixing controlled combustion and late burning phase. The period from the start of fuel injection to the start of combustion is the ignition delay. During the premixed combustion phase, a rapid heat release from the combustion of fuel which premixes and ac-

cumulates during the ignition delay period takes place. A relatively slower and controlled mixing combustion takes place after the initial rapid premix burning, which is primarily governed by the fuel atomization, mixing of fuel vapor with air and chemical reactions. In the late combustion phase, the heat release rate slows down to a lower rate extending itself into the expansion stroke.

During the premixed combustion phase, poly aromatic hydrocarbons are formed which are the precursors of soot, due to the lack of air and fuel rich environment. The controlled mixing combustion phase takes place in two spatially separated stages. In the first stage, the fuel passes through a high fuel-rich premixed reaction zone and then in the second stage the fuel burns out in the turbulent diffusion flame at the jet periphery. Thus, for both combustion phases - initial premixed and controlled mixing; the fuel mixes with air, and gets vaporized and heated to ignition temperature. Then the fuel gets partially oxidized in a rich premixed reaction, and then completes combustion in a near-stoichiometric diffusion flame. The fuel rich premixed combustion produces partially burned products which lead to formation of soot. Though most of the soot burns out with the remaining fuel at the late combustion phase, a small part is not oxidized and converts to exhaust emission. Oxides of nitrogen (NO_x) are formed in the high-temperature regions in the hot product gases, and the rate of production increases exponentially with temperature. The NO_x and particulates are traded off against each other in several characteristics of engine design. High temperatures inside the combustion chamber help in reduction of particulates at the expense of high NO_x formation. At the same time low temperature inside the combustion chamber leads to less NO_x formation but increases the likelihood of high particulates formation. Thus a trade-off between NO_x and PM formation is more important to minimize both emissions[16].

2.1.2 Injection strategies

There are several ways to reduce NO_x and PM emissions. In some cases exhaust gas recirculation (EGR) is used to reduce NO_x emissions [17, 18, 19, 20], but it increases the PM emissions and also increases the soot deposits on engine components and decreases the durability of the engines. In EGR, the exhaust gas displaces the fresh air entering the combustion chamber; as a consequence lower amount of oxygen in the intake mixture is available for combustion. Reduced oxygen available for combustion lowers the effective air-fuel ratio. The specific heat of intake mixture also increases by addition of exhaust gas, which results in reduction of flame temperature. Thus the combination of lower oxygen content and reduced flame temperature reduces the rate of NO_x formation while increases the PM emissions accompanied by power loss [21]. The other ways to reduce emissions are by implementing various exhaust gas after treatment devices such as diesel particulate filter (DPF) and selective catalytic reduction (SCR). DPF is able to capture and remove diesel particulate matters and soot, while SCR can convert NO_x emissions to nitrogen and water by catalytic reactions. Though after treatment devices promise to reduce NO_x and PM emissions to a greater extent [22, 23, 24, 25, 26, 27, 28, 29], they result in high capital and maintenance cost. Though there are many emission reduction techniques available, reducing the pollutants at source is the most beneficial method. The modern electronic fuel injection system is known to keep the emission levels within limits without compromising the performance of the engine and will continue to play a vital role in the development of improved diesel engines for the foreseeable future. The following principles and strategies improves fuel-air mixing and diffusion combustion process that leads to reduction of both NO_x and particulates formation [30, 31].

- Injection pressure level controlling spray penetration and improving atomization.

- Fuel should be distributed mainly within the air inside the combustion cham-

ber with minimum possible wall wetting.

- Nozzle configuration, such as, number of spray holes, diameter, orientation, nozzle tip protrusion inside the combustion chamber, all affecting fuel distribution and atomization within the combustion chamber.

- Use of variable injection timing and variable injection rate technology.

In the past, mechanical fuel injection systems with an average injection pressure of 200–300 bar were used, and only one injection per cycle was allowed. Due to poor mixing with air, the resulting cloud of fuel had wide range of temperature in the combustion chamber. The combustion in the fuel rich region of the flame produced soot, and the leaner regions produced NO_x. To overcome this, electronic fuel injection systems today operate at high pressure and have more number of holes per injector. For multiple injection holes, the fuel clouds are smaller than those from a single injector hole. The temperature difference across the spray clouds is far narrower; this offers better air utilization within the combustion chamber and leads to reduction in emissions. The electronic fuel injection systems are replacing the conventional mechanical systems in the high speed DI diesel engines. The benefits of electronic fuel injection systems [32] are

- Very high fuel injection pressures up to 2000 bar to atomize fuel into very fine droplets for fast vaporization.

- High velocity of fuel spray that penetrates the combustion chamber within a short time to fully utilize the air charge.

- Precisely controlled injection.

- High accuracy of fuel metering to control power output and limit smoke.

- Variations in the quantity of fuel injected among different cylinders are drastically minimized.

- Controlled initial rate of injection to reduce noise and emissions.

- Sharp end of injection to eliminate nozzle dribble, prevent nozzle fouling and reduce smoke and hydrocarbon emissions.
- Injection rate shaping for controlling heat release rates during premixed and diffusion combustion phases for reducing noise and formation of smoke and NO_x.
- Split injection to avoid rapid heat release rate at the start of combustion and prevent NO_x formation.

Most of these injection strategies employed, directly or indirectly influence the fuel spray formation inside the combustion chamber. Thus the fuel spray plays a vital role in the combustion phenomena inside the compression ignition engines. Though many researchers adopt various injection strategies as a tool to reduce emissions and improve engine performance, but there is no comprehensive review on this topic found in literature. From this point of view, the purpose of this chapter is to review the various fuel injection strategies viz injection pressure, injection timing, injection rate shaping and split/ multiple injections in CI engines to simultaneously improve performance and reduce the exhaust emissions.

2.2 Injection pressure

The search for better combustion in the field of diesel engines, regardless the engine size and use has a strong link to the capability of the fuel injection equipment to generate high injection pressures. Spray properties are improved by higher injection pressures. Usually the spray penetration length increases with higher injection pressures and low ambient density, while the spray angle increases with increase in ambient density. Fig.2.3 shows the trend in diesel fuel injection pressure over the last three decades [33]. Fuel injection pressures range from 200 - 2500 bar based on the fuel injection systems used. Research has shown that by further increasing the injection pressure more benefits in terms of performance and reduction in emissions are to be realized [34, 35].

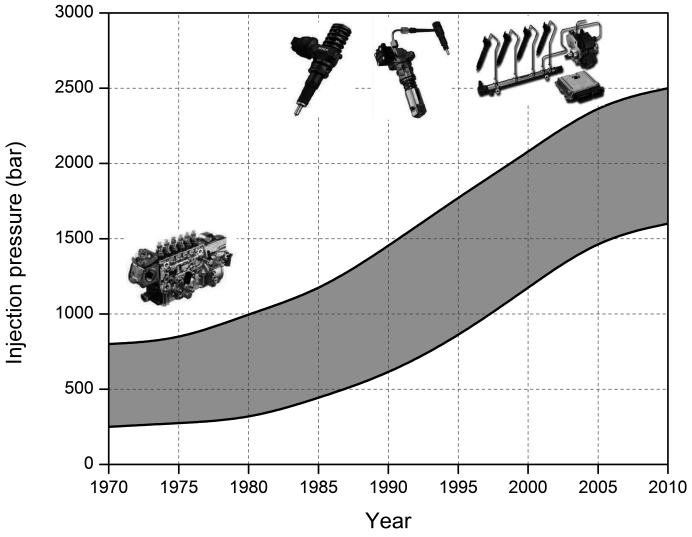

Figure 2.3: Trends in diesel injection pressure[33]

Spray penetration is improved at higher injection pressures [36, 37, 38]. The speed and extent to which fuel penetration occurs inside the combustion chamber decides the air utilization and the fuel-air mixing rates. In some combustion chamber design, where high swirl ratio and hot walls are achieved requires high penetration for proper combustion of fuel however in case of multi hole injection, the probability of spray hitting the cold regions may produce more unburned or partially burned emissions. Less spray penetration may lead to improper mixing rate and poor air utilization, which lead to high emissions. Thus the spray penetration is an important factor in deciding the engine emissions, which requires careful optimization of injection pressure for varying speed and load conditions. Thus the spray penetration length prediction becomes more important and interesting for more researchers. Dent [39] predicted the spray penetration length S, based on a gas jet mixing model for the spray as shown in Eq.2.1

$$S = 3.07(\frac{\triangle P}{\rho_{amb}})^{\frac{1}{4}}(tD_n)^{\frac{1}{2}}(\frac{294}{T_{amb}})^{\frac{1}{4}} \tag{2.1}$$

where,ΔP is the pressure drop across the nozzle, t is the time after of start

of injection, and D_n is the diameter of the nozzle hole, ρ_g is the ambient density, T_{amb} is the ambient temperature. This model predicts the spray penetration length at best for nozzles where $2 \leq \frac{L_n}{D_n} \leq 4$ and for $t > 0.5$ ms but at high ambient densities i.e. $p > 100$ atm, the model over predicts the penetration. Hiroyasu et al. [40] based on diesel injection in high pressure chambers, predicted the penetration length as a function of time, ambient conditions and injection pressure. According to their model the penetration increases as a function of time t until jet break up, immediately after break up, the penetration increases as function of $\sqrt{t}$. The Hiroyasu model is given by the Eqns.2.2 and 2.3

$$t < t_{break} \ : \ S = 0.39(\frac{2\triangle P}{\rho_l})^{\frac{1}{2}}t \tag{2.2}$$

$$t > t_{break} \ : \ S = 2.95(\frac{\triangle P}{\rho_{amb}})^{\frac{1}{4}}(tD_n)^{\frac{1}{2}} \tag{2.3}$$

where,$t_{break} = \frac{29\rho_l D_n}{(\rho_{amb}\triangle P)^{\frac{1}{2}}}$, ΔP is the pressure drop across the nozzle, t is the time after of start of injection, and D_n is the diameter of the nozzle hole, ρ_l, ρ_{amb} are the liquid fuel and ambient density.

2.2.1 Effect of injection pressure on different fuel

The injection pressure has a significant effect on performance and emissions formations. In general, increasing the injection pressure causes an earlier start of combustion relative to the TDC because of improved atomization which results in better air fuel mixing. As a result of this, the cylinder charge gets compressed as the piston moves towards TDC resulting in relatively higher temperatures during combustion which facilitates increased NO_x formation due to high premixed heat release rate and lowers the HC formation. Similarly due to lower ignition delay period at high injection pressure, engine power output gets improved, resulting in better BSFC and on contrary lower injection pressure results in poor BSFC due to longer ignition delay due to improper atomization and mixing process. Much

literature are found in support of the above theory. İçıngür and Altiparmak [41] studied the effects of fuel injection pressures on diesel engine performance and emissions. They studied the effect of lower injection pressures of 100, 150, 200, 250 bar. They found that at the higher pressure of 250 bar, NO_x was increased and smoke was decreased. Also there was considerable increase in the engine torque and power output from the engine. Çelıkten [42] investigated the effect of injection pressure on engine performance and exhaust emissions in indirect injection (IDI) engine. He also varied the injection pressure from 100 to 250 bar in steps of 50 bar. Interestingly, he found that 150 bar injection pressure resulted in maximum performance, after which the performance deteriorated. This may due to the fact that for IDI engine, a too high fuel injection pressure may lead to more fuel burnt in the swirl chamber/prechamber, resulting in a slightly reduced output power. They also found that higher injection pressure reduced SO_2, CO_2 and O_2 while lower injection pressure resulted in decreased NO_x and smoke emissions.

Recently, bio-diesel fuels promise to be a clean, alternative and renewable source of energy. Bio-diesels have a number of properties that make it an excellent alternative fuel for diesel engines [43, 44, 45, 46, 47]. Fuel injection pressure also has a significant role in improving the performance and emission characteristics of other alternate fuels like biodiesel and its blends with diesel. Gumus et al. [48] reported the effect of fuel injection pressure on diesel engine fueled with biodiesel-diesel fuel blends. They examined the effect of four different injection pressures 180, 200, 220, 240 bar on performance and exhaust emissions. The BSFC of higher percentage biodiesel-diesel blends decreased with increased injection pressure while increased injection pressure caused decreased smoke, HC and CO but increased CO_2, O_2 and NO_x. However increased or decreased injection pressure increased BSFC values compared to original injection pressure of 200 bar for both diesel and lower percentage of biodiesel-diesel blends. Sayin and Gumus [49] investigated the impact of injection pressure on performance and emission of biodiesel-diesel blends. The increased injection pressure gave better results for BSFC, BTE and BSEC

compared to original and reduced injection pressures because of finer breakup of fuel droplets which provided surface area and better mixing with air leading to better combustion. Smoke, HC and CO decreased while NO_x emissions increased with increase in injection for all fuel blends. Canacki et al. [50] examined the effect of injection pressure on the performance and emission characteristics of diesel engine fueled with methanol blended diesel fuel. They used three different injection pressures 180, 200, 220 bar to study its effect on four different loads 5, 10, 15 and 20 Nm at constant engine speed of 2200 rpm. The results showed that with increase in injection pressure NO_x and CO_2 increased while smoke, CO and HC were decreased. In contrast, performance parameters like BSFC, BSEC and BTE were best at original injection pressure of 200 bar and gets poor on either increasing or decreasing the injection pressure. It was also notable that peak in-cylinder pressure and heat release rates increased on increasing injection pressure due to decrease in ignition delay. Purushothaman and Nagarajan [51, 52] examined the effect of injection pressure on heat release rate and emissions on diesel engine fueled with orange skin powder diesel solution. They used three different injection pressures 215, 235 and 255 bar. For injection pressure of 235 bar, they obtained increased peak cylinder pressure, BTE and peak heat release rate, also NO_x increased by 26%, whereas CO, HC and smoke decreased by 39, 66 and 27% respectively for 30% orange skin powder solution compared with the diesel fuel. Puhan et al [53] investigated the effect injection pressure on high linolenic linseed oil methyl ester fueled diesel engine. At higher injection pressure of 240 bar, thermal efficiency and BSFC improved with decreased CO, smoke, HC and slight increase in NO_x. The effect of injection pressure on jatropha methyl ester fueled engine was investigated by Jindal et al. [54]. They chose three injection pressures 150, 200, 250 bar for their study. It was found that at injection pressure of 250 bar, the BSFC increased by 10% and BTE improved by 8.9% with reduction of HC, NO_x, and smoke at lower level while CO increased from base injection pressure. However the performance and emissions were still lower than those of

diesel. Pandian et al. [55] studied the effect of injection pressure on pongamia biodiesel blends. The injection pressure was varied from 150-250 bar in steps of 25 bar. The significant result was that when injection pressure was increased from 150 to 225 bar, the BTE improved with lower BSEC. CO, HC and smoke emissions were also reduced with increase in NO_x. However with further increase in injection pressure, the results were negated. Belagur and Chitimini [56] evaluated the effect of injection pressure on the performance, emission and combustion characteristics of diesel engine fueled with hone oil and its blends. They also reported that by increasing the injection pressure, the BTE and NO_x emissions were increased and CO, HC and smoke emissions were reduced. It was also found that upon increasing injection pressure, the ignition delay gets reduced. A recent study by Kannan and Anand [57] on the effect of injection pressure on engine performance and emission with biodiesel derived from waste cooking oil revealed that increasing injection pressure at 25.5° bTDC resulted in significant improvement of BTE, in-cylinder pressure and heat release rate with reduction in NO_x and smoke emissions.

2.2.2 Effect of ultra-high injection pressure

Since the introduction of electronic fuel injection equipment, higher injection pressure has become practical solution to improve performance and reduce emissions. Up to mid-eighties, 1000 bar injection pressure with an inline or a rotary pump system was an achievement. Since then, this figure has been raised up to 1600-1800 and even beyond 2000 bar. The high pressure makes the spray droplets near the nozzle susceptible to breakup processes, however with rapid declines in droplet diameters, droplets further away from nozzle becomes less susceptible to aerodynamic breakup even though they still possessed velocities of up to 200m/s [58]. Pierpont and Reitz [59] studied the effect of high injection pressures on the engine performance and emissions. When injection pressure was increased from 720 to 960 bar, there was decrease in particulates when further increased from 960 to 1220 bar, there was a substantial improvement, however when further increased

from 1220 to 1600 bar, there was only a small gain because the driving torque required by the fuel pressure to decrease particulate was not worth compensating the deterioration in BSFC. Also higher injection pressure leads to higher premix burn fraction which contributed to an increase in NO_x. It was also noted that when injection pressure was increased from 720 to 1600 bar, there was an increase of 3% in BSFC to maintain NO_x level constant. So this study concludes that on higher injection pressure, increase in NO_x emission is substantially high which overrules the reduction in particulates and BSFC. Su et al. [60] examined increased injection pressure up to 1600 bar in diesel engine as well as some spray tests were also carried out. The results showed that increased injection pressure led to lower PM and higher NO_x and the lower PM was attributed to smaller average drop sizes, as measured by the sauter mean diameter (SMD). Dodge et al. [61] reported that the use of high injection pressures significantly reduced soot formation and PM emissions with slight increase in NO_x emissions. However, a significant penalty of using very high injection pressure was increased BSFC, which is expected due to higher friction on the injector cam and to irreversible energy losses in compressing the fuel in the plunger barrel. Also another potential penalty in using high injection pressures was increased injection cam wear in the fuel injection pump. Pickett and Siebers [62] studied the effect of injection pressure on soot in diesel fuel jets injected into high temperature high pressure constant volume combustion vessel. An increase in injection pressure caused a decrease in soot levels due to coupled effects of decrease in the amount of air entrainment and fuel air premixing that occurred upstream of the lift off length and a decrease in the residence time in the fuel jet sooting regions due to higher injection velocities. The peak soot in the fuel jet decreased linearly with the increasing injection velocity. Wang et al. [63] studied the effect of ultra-high injection pressure on flame structure and soot formation in constant volume combustion vessel. Fig.2.4 shows the effect of injection pressure on soot luminosity and flame size. It was reported that soot luminosities and flame size at injection pressure of 1000 bar were appreciably stronger and

smaller respectively than those of 2000 and 3000 bar. However, when integrated soot luminosity is calculated by summing up the gray scale intensities of all the pixels, interestingly, reduction in soot luminosities was achieved when injection pressure increased from 1000 to 2000 bar when further increased to 3000 bar there was no significant change (Fig.2.5). The soot reduction with increase in injection pressure was mainly attributed to the better spray atomization and improved air entrainment.

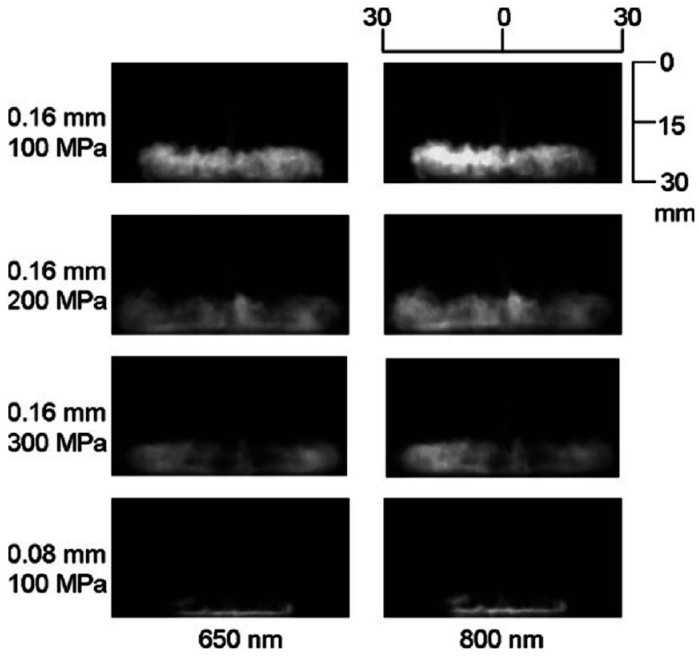

Figure 2.4: Effect of ultra-high injection pressure on soot luminosity and flame size at end of injection [63]

The regulation of diesel engine exhaust particle emission is focused on soot particles. The diesel soot particles are mainly composed of highly agglomerated solid carbonaceous material, ash, volatile organic and sulfur compounds. Fig.2.6 [64] shows the typical particle size distribution of diesel soot. The nucleation mode is generally smaller in modal diameter than the soot mode. The formation of nucleation particles is considered to take place in the cooling dilution, outside the tailpipe, but in some cases they contain non-volatile fractions called core. The other mode is accumulation mode which is mainly associated with carbonaceous agglomerates and the volatile matter adsorbed on their surface. The third mode

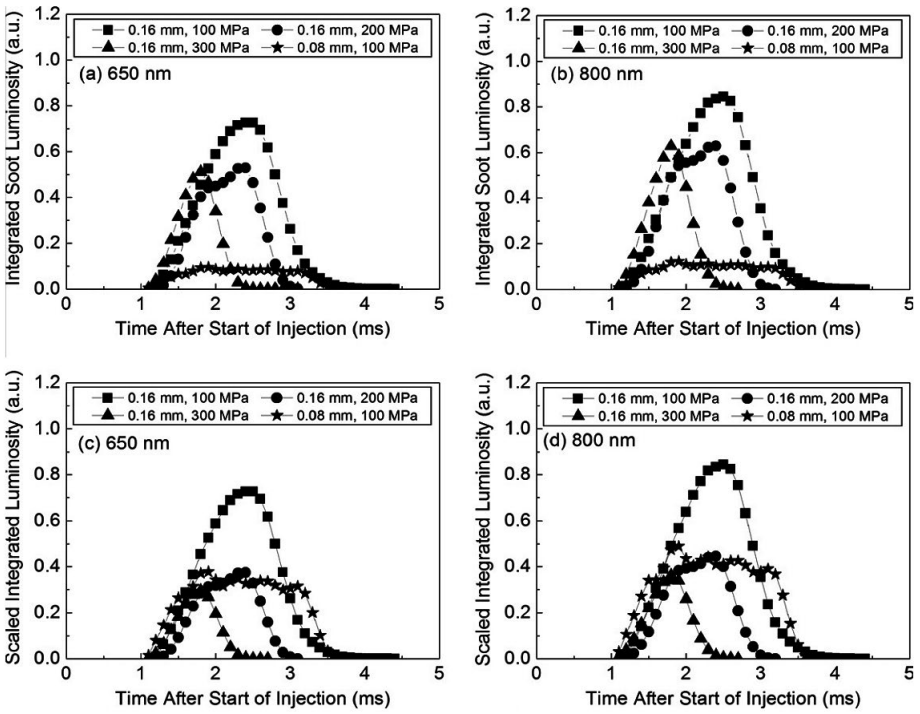

Figure 2.5: Effect of ultra-high injection pressure on temporal integrated soot luminosity [63]

consists of particles deposited on the engine cylinder and exhaust system walls and later re-entrained [65].

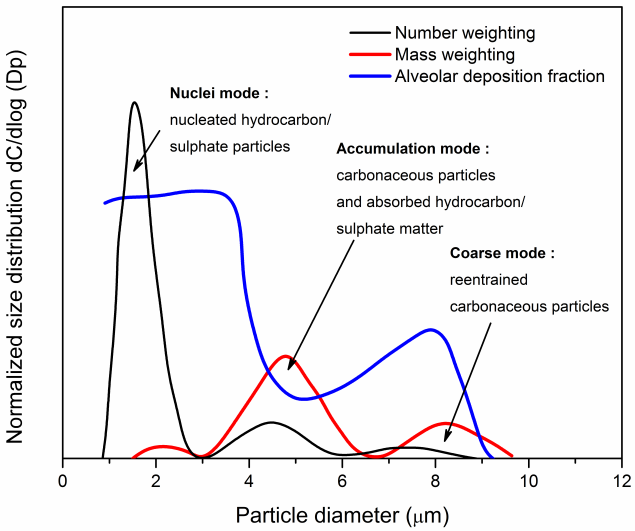

Figure 2.6: Typical diesel soot particle size distribution

Pagan [66] studied the effect of fuel injection pressure on particle size distri-

butions emitted by diesel engines. The number size distribution shifted towards more nuclei mode particles as the injection pressure was increased. The general conclusion obtained from their study is that decrease in the total number concentration at higher injection pressure and in some cases, an increase in the number of nuclei mode particles was observed. Desantes et al. [64] investigated the influence of injection pressure on the aerosol exhaust particle size distribution. Increasing injection pressure was generally found to reduce the accumulation mode particle number and a sharp increase in the nucleation mode particle number was resulted when the injection pressure was highest for some engine conditions. Lähde et al. [67] investigated the fuel injection pressure on non-volatile particle emission. Their study revealed that increase in fuel injection pressure changed the dry particle size in all loads and number emissions of the core particles was dependent on injection pressure, i.e. the number of the core particles increased with increase in injection pressure however at low load, the mode was unstable or not detected. The size of core particles was around 5nm at high loads for all injection pressure whereas it was below 5nm and dependent on injection pressure at medium loads.

From the literature, it is clear that significant reduction of soot emissions is obtained by increasing injection pressures, with injection pressures ranging from 1000 bar to 2000 bar and above in some cases. However increasing injection pressure generally leads to increased NO_x emissions, but this can be offset by using rate shaping and more retarded injection timing with the help of same advancement in fuel injection equipment.

2.3 Injection rate shaping

Fuel injection rate shaping is a phenomenon to vary the injection rate over the course of a single fuel injection. As NO_x is produced at high temperature zones, which are highly dependent on the initial heat release rate, less quantity of fuel should be injected at the beginning of the injection phase, in order to limit initial

heat release and NO_x formation. Fig.2.7 [68] shows the optimum injection rate with various engine speed and load. From figure, it is evident that within the ignition delay period, the injection rate has to be small, with increasing load, the injection rate or the main injection should be increased and to control the injection rate, the parameters like injection pressure, spray hole diameter, number of spray holes and injection duration must be optimized.

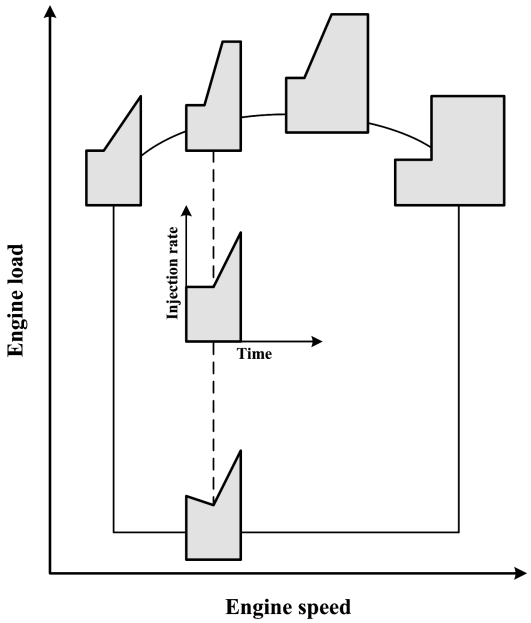

Figure 2.7: Optimum injection rate with various engine speed and load [68]

In mechanical fuel injection systems, this was achieved by changing the cam profile [69], but it suffered a big disadvantage that it cannot be modified for different speed and loading conditions of the engine. With advance in fuel injection technology and improvement in common rail electronic fuel injection systems, the fuel injection rate shaping has become true when Jose of Chrysler corporation filed their first patent on method of fuel injection rate control in 1993 [70]. In 1998, Ganser [71] published his results on design and testing of injection rate control (IRC) in a common rail injector. Some of the vital findings of his research are that the IRC works in the operating pressure range of 500-1500bar, the amount of fuel injected with IRC during ignition delay period can be reduced by a maximum factor 4 and IRC is also possible with pilot injections which can be followed by main injection without IRC and the separation time between them is selectable.

Though it was a pioneering effort in injection rate control, but it fails to account for the change in engine performances with and without IRC. In the same year, Nishimura et al. [72] studied the effects of fuel injection rate on combustion and emission in a DI diesel engine. They studied the effect of pilot injection, gradual shaped injection profile using needle lift control and boot shaped injection profile using pressure control. They evaluated the effect of different fuel injection rates in terms of combustion, emission and combustion noise. They found that pilot injection helped in simultaneous reduction in NO_x and noise with minimum deterioration in smoke, with slow needle lift, they found both NO_x and smoke reduced but no substantial improvement in noise, with boot shaped injection control, it was found that smoke and combustion noise is greatly reduced with compensation of deterioration in fuel economy. These results were very promising to use injection rate control as a significant strategy in reducing emissions. As in electronic fuel injection system, the design of fuel injectors governs the fuel injection rate, which made many fuel injection equipment manufacturers to come up with an improved design of fuel injector nozzle assembly for effective rate shaping [73, 74, 75, 76, 77, 78, 79, 80, 81, 82, 83, 84]. As injection rate shape also depends on the injection pressure, which is maintained constant using a common rail, results nearly in rectangular rate shapes. In order to overcome this difficulty, researchers [85, 86] came up with a solution of using two common rails one with low pressure and other with high pressure. With this type of next generation common rail system, they have achieved boot shaped fuel injection rate and when tested with single cylinder research engine, the results were very promising in improvement of NO_x–fuel consumption and NO_x–PM trade-offs.

Hwang et al. [87] studied the effect of fuel injection rate on pollutant for different engine speeds, loading conditions and swirl ratios. They optimized injection rate patterns for various engine conditions based on exhaust emissions. However, they failed to address the effect of rate shaping on engine performance such as fuel consumption and thermal efficiency. The comparison between square, ramp

and boot injection rate profiles were done by Benajes et al [88]. Fig.2.8 shows the ideal and actual square, ramp and boot type injection rates. The comparison revealed that square pattern leads to higher spray tip penetration due to the higher pressure at the start of injection, even if the injection duration are adjusted to match the same fuel quantity to be injected, while ramp always has medium penetration and boot has the lowest penetration. Interestingly the spray cone angles showed no change with different injection patterns. Beck and Chen [89] done a high speed combustion analysis on injection rate shaping and concluded that fuel quantity should be less than 10% of total fuel injected during pre-injection. In general with injection rate shaping NO_x was reduced with slight increase in the smoke and BSFC. Desantes et al. [90] studied the effects of fuel rate shaping on engine performance and emissions. The boot type injection profile was generated using modified pump line nozzle systems. They varied different characteristic parameters of the boot type of injection like boot pressure, length and durations (see Fig.2.8). Their interesting findings were, in general boot type injections reduce NO_x emission in expense of increased soot and fuel consumption, which even results ineffective at medium engine loads, since the increase in soot was higher than the relative decrease in NO_x emissions. However some specific boot shapes proved better emissions and performance trade-offs.

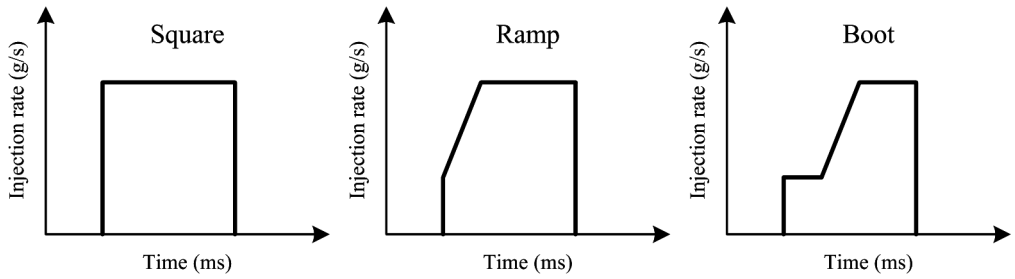

Figure 2.8: Ideal square, ramp, and boot type injections [88]

Desantes et al. [91] also studied the effect of fuel rate shaping on engine combustion phenomenon. They found that, in general, any changes to the boot type injections produced evident changes in the diffusion combustion phase and boot type injections are useful in reducing NO_x only at high speed, high load

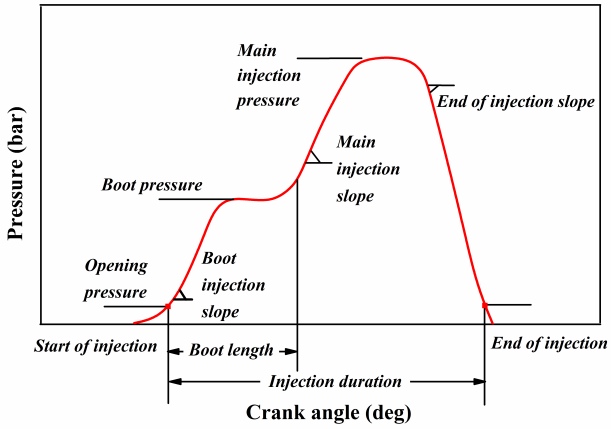

Figure 2.9: Characteristics of fuel injection rate shape (redrawn from [90])

conditions than in medium speed, low load conditions. Ghaffarpour et al. [92, 93] also reported very similar results through numerical analysis using KIVA II CFD package. Their results also showed that injection rate shaping was effective in reducing NO_x emissions at high speeds and medium loads but ineffective for medium speeds and low loads.

Literature shows that injection rate shaping is a very effective strategy for reducing NO_x emissions at certain loading conditions. However, the reduction of NO_x accompanies increase in fuel consumption and soot formation in most cases.

2.4 Injection timing

Injection timing plays a vital role in combustion phenomena and pollutant formation. The injection timing affects the ignition delay because the air temperature and pressure change significantly close to TDC. As advancing the injection timing, the initial air temperature and pressure are lower so ignition delay will increase while retarding the injection timing i.e closer to TDC, when air temperature and pressure are slightly higher results in shorter ignition delay. However, retarding or advancing injection timing beyond certain limits which varies from engine to engine may result in poor combustion. Injection timing variations also have strong effect on NO_x formation. Retarded injection timing, may help to control NO_x emissions with substantial penalty in fuel consumption, and also increases

unburned hydrocarbons, smoke and particulate emissions [15]. Therefore, finding an optimum injection timing for best performance and lower emissions is required.

2.4.1 Effect of injection timing on different fuels

In general, biodiesel results in more NO_x emissions when used in a diesel engine than with same engine conditions due to various factors. One of the factors for higher NO_x emissions from biodiesel was because of its distinct properties like higher viscosity, isentropic bulk modulus and lower compressibility factor [94, 95, 96, 97, 98]. By varying injection timing from its default has proved to improve performance and emissions. Suryawanshi and Deshpande [99] studied the effects of fuel injection timing on pongamia methyl ester fuelled diesel engine. With reduced injection timing, it was possible to achieve reduced NO_x, HC and CO emissions with negligible effect on fuel consumption rate. Similar trends were observed with BTE and exhaust gas temperature with retarded injection timing; however in-cylinder gas pressure and ignition delay was reduced. Nwafor et al. [100] reported that longer ignition delays by using rapeseed oil in diesel engine can be compensated by advanced injection timing with a penalty of increase in fuel consumption. Reddy and Ramesh [101] studied the effect of injection timing on jatropha oil and concluded that by advancing the injection timing by 3° from original injection timing of diesel, increased the BTE and also reduction in HC and smoke were observed. Ganapathy et al. [102] studied the influence injection timing on jatropha methyl ester. It has been observed that advance in injection timing from default value caused considerable reduction in BSFC, CO, HC and smoke levels and increase in BTE, maximum in-cylinder pressure, maximum heat release rate and NO_x emission. However retarded injection timing caused effects in the other way, hence an optimum injection timing was found for optimum balance between the performance an emission of jatropha methyl ester compared to diesel. Sayin and Gumus [49] studied the impact of injection timing on biodiesel-blended diesel fuel. Three different injection timings were selected for the study

15°, 20° and 25° bTDC. The original injection timing of 20° bTDC gave best results of BSFC, BSEC and BTE compared to advancing or retarding injection timing. Since advance injection timing gives more time for carbon oxidation, led to lesser smoke, HC and CO whereas NO_x emissions were reduced by retarding the injection timing because of lower combustion temperature in the cylinder. Pandian et al. [55] investigated the influence of injection timing on performance and emission of pongamia biodiesel-diesel blends. When injection timing was advanced from 18° to 30° bTDC, CO, HC, and smoke emissions were reduced with increase in NO_x emissions and the best performance parameters were obtained at 21° bTDC. Advanced injection timing gives increased in-cylinder peak pressure and increase in the oxides of nitrogen were within acceptable limits for methyl tallow ester and methyl soy oil ester [103]. The engine also showed low carbon monoxide and unburned hydrocarbon emissions and also there were no perceptible changes in BSFC and smoke levels at advanced engine timing. The impact of injection timing on the performance of mahua methyl ester was studied by Raheman and Ghadge [104]. The results showed that there was significant decrease in BSFC and EGT and increase in BTE to meet the performance in par with the diesel fuel when injection timing was advanced. Monyem et al. [105] studied the influence of injection timing on biodiesel and found that there was significant decrease in CO and HC emissions in a range of injection timing and NO_x emissions were increased by 3° advance and reduced considerably by 3° retardation from the default injection timing. Gumus et al. [106] reported that original timing gave the best results for BSFC, BSEC and BTE compared to advanced and retarded injection timing for canola oil methyl ester. Though they have not reported any effect of injection timing on emissions, but shows that varying injection timing may not help obtaining best results, but optimum results may be achieved with this strategy when compared with balance between performance and emissions. Retarded injection timing was also beneficial in reducing the NO_x, CO, and HC, while increasing BTE, CO_2 and smoke under all loading conditions when fueled with waste plastic oil [107]. Hari-

ram and Kumar [108] investigated the effect of injection timing on combustion, performance and emission parameters of diesel engine fueled with algal oil methyl ester (AOME). They found that advancing injection timing, improved BSFC and reduced HC, CO and smoke with increase in heat release rate, BMEP and NO_x, while retardation results in marginal improvement in heat release rate, BMEP and NO_x emissions with increase in BSFC, HC, CO and smoke. Finally they found optimum injection timing to be 340 CAD which evident better combustion and performance with minimal emissions.

Varying fuel injection timing also benefits the dual fuel engines in terms of improving thermal efficiency and reducing emissions. Abd Alla et al. [109] studied the effect of injection timing on dual fuel in order to reduce the emissions and improve the thermal efficiency at lower loads. Interestingly, when the injection timing of the pilot fuel was advanced thermal efficiency was improved with some compensational increase in the NO_x emissions and reduction in CO and HC were observed. However at medium and high loads advancing injection timing led to early knocking. Therefore the advance timing of pilot fuel in dual fueled engines was not beneficial for medium and high loads. Noguchi et al. [110] also reported that retardation of injection timing of pilot fuel in diesel-alcohol dual fuel helps in reducing the knocking in engines. Sayin et al. [111, 112] investigated the impact of injection timing on diesel alcohol dual fuel. It was observed that on retarding injection timing from original timing resulted in increase in CO and HC and decrease in NO_x and CO_2 while results were reversed when the injection timing was advanced from original default value. Kegl [113] found the optimal injection timing for biodiesel fueled engine for reduced harmful emissions and better performance. The optimized injection timing was found to be 19° bTDC, for 25% reduction of CO and NO_x and 30% for HC reduction and smoke reduced by 50% also with 5% reduction in engine power output and 10% increase in BSFC. Injection timing was also proved to find optimum between performance and emissions of engine powered by natural gas [114, 115]. Mohammed et al. [116] conducted experiments

to investigate the effects of injection timing on engine characteristics and emissions of a DI engine fueled with NG – hydrogen blends (0; 3; 5; 8%). Three injection timings (120°; 180°; 300° bTDC) were chosen for their study. It was found that the performance and NO_x emission were higher for 180° bTDC followed by 300° bTDC and 120° bTDC injection timing. The total HC and CO were found to decrease while CO_2 was found to increase with advancing the injection timing.

2.4.2 Effect of injection timing on low heat rejection (LHR) engines

The engines with thermal barrier coating to reduce heat transfer between in-cylinder gas and coolant is low heat rejection engines (LHR). Some important advantages of LHR engines are improved fuel economy, reduced engine noise; higher energy in exhaust gases and multi-fuel capability of operating low cetane fuels, but the main disadvantage is high level of NO_x emissions. Injection timing also proved to reduce NO_x emissions from low heat rejection engines [117]. Kamo et al. [118] suggested retarded injection timing results in fuel economy improvement apparently at all speeds due to higher premix combustion, lower diffused combustion and reduced heat transfer losses. Parlak et al. [119] studied the effect of injection timing on low heat rejection indirect injection engines in the aim of reducing NO_x. When NO_x-BSFC trade off was considered then by retarding the fuel injection timing by 4° CA results in optimum reduction in NO_x, by neglecting NO_x-BSFC trade-off maximum 40% reduction in NO_x was achieved by retarding injection timing. Buyukkaya and Cerit [120, 121] also studied the effect of injection timing on LHR engine. By retarding 2° from the original timing of 18° bTDC, there was a reduction of 2% and 11% in BSFC and NO_x respectively.

In general, advancing the injection timing will benefit in better performance with increase in NO_x and smoke whereas retarded fuel injection timing results in better NO_x and smoke emissions with no or little deterioration to the engine performance in terms of fuel consumption and thermal efficiency.

2.5 Split/ multiple injections

Nowadays, high pressure common rail fuel injection systems allow a very high degree of flexibility in the timing and quantity control of multiple injections, which can be used to obtain significant reductions in engine noise and emissions without compromising its performance and fuel consumption. Fig.2.10 shows typical multiple injections and its benefits on engine performance and emission reductions. One or two pilot injections at low pressure help in reducing engine noise as well as NO_x emissions. Either rectangular shape i.e. fully opened needle or boot type rate shaped main injection will aid in NO_x reduction in support to close pilot injections. Coupled post injection with high pressure will help in reducing soot emissions while late post injection at moderate pressure helps to manage exhaust gas temperature for regeneration of diesel particulate filter and to provide hydrocarbons for NO_x adsorber catalyst [33].

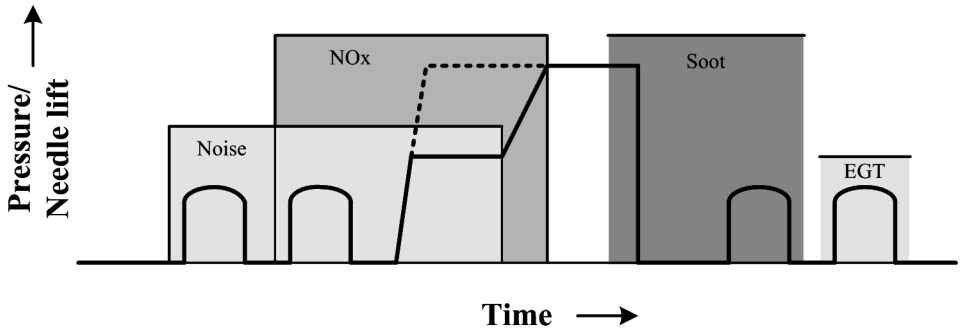

Figure 2.10: Typical multiple injection used [33]

The nomenclature of injection profile can be interpreted from the Fig.2.11 which consists of two pilot injections and one after/ post injection. The main parameters of the injection profile are start of injection (SOI), energizing time of an injection or injection duration (ET) and dwell time, time interval between the end of an injection and the start of the following one (DT) [122].

Multiple injection or split injections have been proposed as a means to decrease particulate emissions significantly without a significant penalty in NO_x emissions [123]. However considerable retardation of injection timing is possible by using

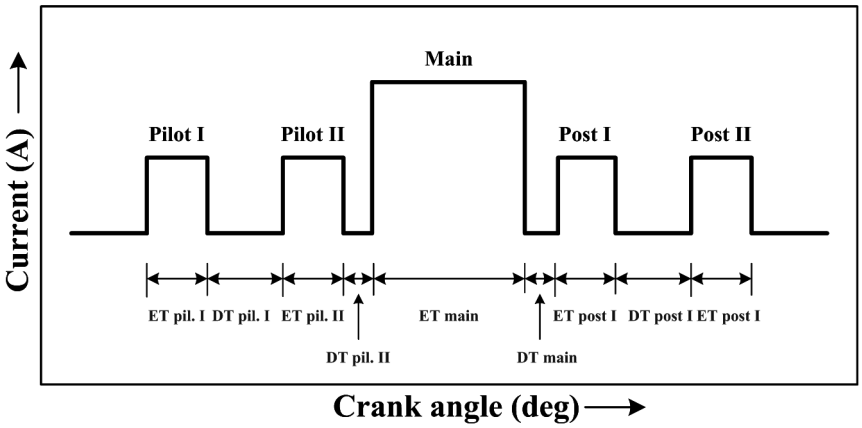

Figure 2.11: Injection profile nomenclature [122]

pilot injection and combination of pilot injection and higher injection pressure controls simultaneous reduction in NO_x by 35% and smoke by 60-80% without worsening the fuel economy compared with single injection [124]. In spite of injection timing, dwell time between two consecutive injections also plays a major role in performance and emissions. When dwell time is reduced, the fuel of the second injection was burned closer to TDC, resulting in lower fuel consumption, however combustion noise will increase with shorter dwell time and smoke emission gets increased, which is related to the characteristics of low temperature combustion, where an increase in local burning temperature leads to higher soot formation [125]. Durnholz et al. [126] studied the effect of pilot injection on combustion noise, performance and emissions and they found on using a pilot injection, noise level decreased by 10dBA when it is used at optimum condition and NO_x emissions was reduced by 30% and HC can be cut down to half while black smoke levels can be kept constant. Later Pierpont et al. [127] used multiple injection strategy to reduce both NO_x and particulate emissions. Interestingly they found optimized multiple injection by varying fuel distribution in each pulse and the dwell between pulses for each operating condition reduces particulates at all NO_x levels, however it comes with penalty of increase in BSFC by 3-4%. Tow et al. [128] reported that by implementing triple injections gave better results compared to single and double injections, however double injection with long delay between successive injections reduced particulates by a factor of three with no increase in NO_x. An

increasing separation between pilot and main injection also reduces NO_x but long delay may lead to high smoke, similarly closer post injection may lead to reduce particulate emissions while increasing delay beyond certain point may result in steep increase in BSFC and HC emission [129]. Dividing the pilot injection into a series of smaller injections serves to further decrease the noise while suppressing the increase of HC emission and fuel consumption. These effects result from the enhanced heat release rate of pilot injection fuel, which is due to the reduced amount of adhered fuel on the cylinder wall. However at light loads, fuel quantity of pilot injection should be decreased and the injection must be prior to the main injection for suppressing the possible increase in smoke and HC. Post/ after injection should be immediately injected after main injection in order to reduce smoke, HC and fuel consumption. Fig.2.12 [130] shows the cylinder pressure and heat release rate for typical pilot injection. Combustion of early pilot injection generates mild heat release in two stages consisting of cool flame and hot flame combustion. The premixed combustion due to early pilot injection causes mild increase in cylinder pressure and shortens the main ignition delay leading to decrease in combustion noise and also reduces smoke by enhanced mixing of air in the cylinder.

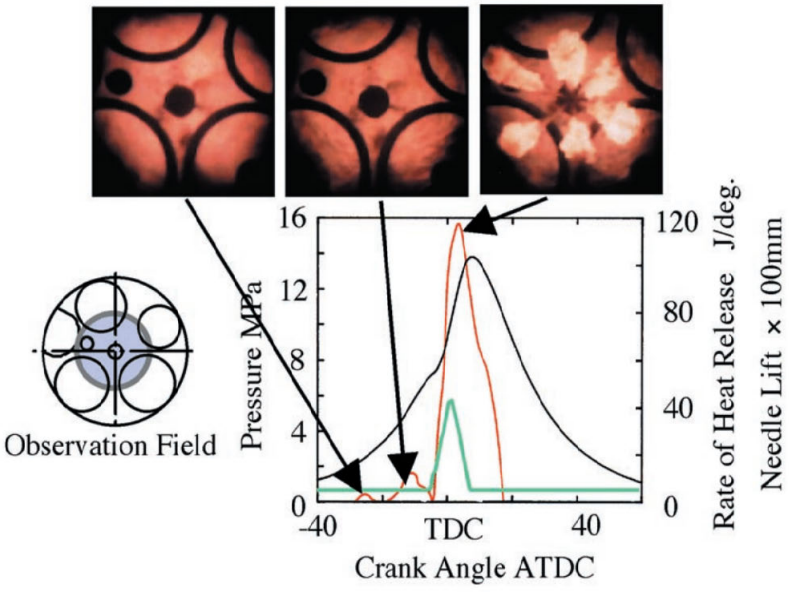

Figure 2.12: Combustion process of early pilot injection [130]

Choi and Reitz [131] studied the effect of split injection on oxygenated fuel blends at low and high low load conditions. At high loads, split injection had a favourable effect on soot emissions compared to single injection results, similarly at low loads, split injection helped in reducing particulate emissions compared to single injections. Later, Fang and Lee [132] showed that split injection are beneficial in reducing NO_x in biodiesel fuel. They also visualized the combustion phenomena of split injection inside the combustion chamber (Fig. 2.13). From the combustion chamber luminosity images, it is clear that NO_x formation in biodiesel is lesser than diesel by changing pilot injection timing and retarding the main injection.

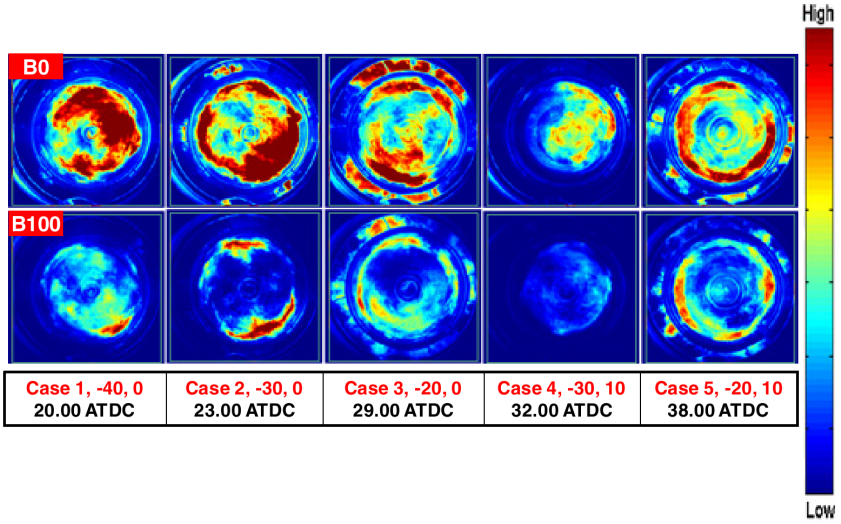

Figure 2.13: Combustion images of biodiesel and diesel with pilot injections [131]

Split injections helps in reducing diesel engine exhaust emissions and when optimized will result in better NO_x-PM trade off with comparatively better performance when compared with single injection and using other injection strategies.

Table 2.2: Summary of injection strategies in literature

Author	Strategy used	Fuel	BSFC	NO_x	HC	CO	Smoke
İçıngür and Altiparmak [41]	Injection pressure	Diesel	↓	↑	na	na	↓
Çelıkten et al. [42]	Injection pressure	Diesel	↓	↓	na	na	↓
Gumus et al. [48]	Injection pressure	Biodiesel blends	↓	↑	↓	↓	↓
Sayin and Gumus [49]	Injection pressure	Biodiesel blends	↓	↑	↓	↓	↓
Canacki et al. [50]	Injection pressure	Methanol blends	↑↓	↑	↓	↓	↓
Purushothaman et al. [51, 52]	Injection pressure	Orange skin powder solution in diesel	↓	↑	↓	↓	↓
Puhan et al. [53]	Injection pressure	Linolenic methyl ester	↓	↑	↓	↓	↓
Jindal et al. [54]	Injection pressure	Jatropha methyl ester	↓	↓	↓	↑	↓
Pandian et al. [55]	Injection pressure	Pongamia methyl ester	↓	↑	↓	↓	↓
Belagur and Chitimini [56]	Injection pressure	Hone oil and blends	↓	↑	↓	↓	↓
Kannan and Anand [57]	Injection pressure	Waste plastic oil	↓	↓	na	na	↓
Pierpont and Reitz [59]	High Injection pressure	Diesel	↑↓	↑	na	na	↓
Su et al. [60]	High Injection pressure	Diesel	na	↑	na	na	↓

Dodge et al. [61]	High Injection pressure	Diesel	↑	↑	na	na	↓
Pickett and Siebers [62]	High Injection pressure	Diesel	na	na	na	na	↓
Nishimura et al. [72]	Injection rate shaping	Diesel	↑	↓	na	na	↓
Beck and Chen [89]	Injection rate shaping	Diesel	↑	↓	na	na	↑
Benajes et al. [88]	Injection rate shaping	Diesel	↑	↓	na	na	↑
Desnates et al. [90, 91]	Injection rate shaping	Diesel	↑	↓	na	na	↑
Suryavanshi and Deshpande [99]	Injection timing	Pongamia methyl ester	↑↓	↓	↓	↓	na
Nwafor et al. [100]	Injection timing	Rapeseed oil	↑	na	na	na	na
Reddy and Ramesh [101]	Injection timing	Jatropha Oil	↓	na	↓	na	↓
Ganapathy et al. [102]	Injection timing	Jatropha methyl ester	↓	↑	↓	↓	↓
Sayin and Gumus [49]	Injection timing	BIodiesel blends	↑↓	↑	↓	↓	↓
Pandian et al. [55]	Injection timing	Pongamia methyl ester	↓	↑	↓	↓	↓
Yahya and Marley [103]	Injection timing	Methyl tallow ester and methyl soy oil ester	↑↓	↑	↓	↓	↑↓
Raheman and Ghadje [104]	Injection timing	Mahua methyl ester	↓	na	na	na	na
Monyem et al. [105]	Injection timing	Biodiesel	na	↑	↓	↓	na

Gumus et al. [106]	Injection timing	Canola methyl ester	↓	na	na	na	na
Mani and Nagarajan [107]	Injection timing	Waste plastic oil	↓	↓	↓	↓	na
Hariram and Kumar [108]	Injection timing	Algal oil methyl ester	↓	↑	↓	↓	↓
Abd Alla et al. [109]	Injection timing	Dual fuel	↓	↑	↓	↓	na
Sayin et al. [111, 112]	Injection timing	Diesel Alcohol dual fuel	na	↑	↓	↓	na
Kegl [113]	Injection timing	Biodiesel	↑	↓	↓	↓	↓
Mohanmmed et al. [116]	Injection timing	Natural gas and hydrogen	na	↑	↓	↓	na
Shundoh et al. [124]	Split/ multiple injections	Diesel	↑↓	↓	na	na	↓
Durnholz et al. [126]	Split/ multiple injections	Diesel	na	↓	na	na	↓
Pierpont et al. [127]	Split/ multiple injections	Diesel	↑	↓	na	na	↓
Chen [129]	Split/ multiple injections	Diesel	↑	↓	↑	na	↓
Choi and Reitz [131]	Split/ multiple injections	Oxygenated fuel	na	na	na	na	↓
Fang and Lee [132]	Split/ multiple injections	Biodiesel	na	↓	na	na	na

↑ - Increase, ↓ - Descrease, ↑↓ - no significant effect, na - Data not available

2.6 Summary

A review was conducted of the literature concerning emission control in diesel engine by different fuel injection strategies. The strategies covered in this review are varying injection pressure, injection timing, injection rate shape and split/ multiple injections. Researchers have carried out many experimental works to study the effect of injection strategies on engine performance and emission formation. Table 2.2 shows the summary of the extensive review done on the injection strategies. The table gives an insight on the effect of various strategies on performance and emissions achieved experimentally. Some of the prominent points showing the effect of above listed strategies on engine performance and emissions for diesel and other biofuels are listed below

- Increasing injection pressure, in general results in an increase of thermal efficiency and better fuel consumption and less CO, HC and smoke emissions. However, it results in higher NO_x emissions.

- Ultra high injection pressures results in reduction of soot emissions mainly attributed by better spray atomization and air entrainment, however leads to increased NO_x and BSFC. Very high injection pressures also have a significant effect on soot particle size distribution.

- Injection rate shaping is a good strategy in reducing NO_x at certain loading conditions, but using ramp or boot shaped injection rates always accompanies increased soot formation and fuel consumption.

- Advanced injection timing results in increased NO_x while reduces fuel consumption, and emissions like CO, HC and smoke, although advancing beyond certain limit may result in high smoke and poor performance.

- Similarly retarding injection timing results in reduced NO_x, while increasing other emissions such as CO, HC and smoke and also deteriorates fuel consumption.

- In general, an optimized timing has to be found for any engine and fuel to strike a balance between performance and emissions.

- Pilot injection help in reducing combustion noise and NO_x emissions and immediate post injection may help in soot oxidation and late post injection helps in regeneration of diesel particulate filter.

- Multiple injections are known for reducing both NO_x and PM emissions simultaneously, but immense trials have to be carried out in prior to fix various parameters to balance emissions and performance of the engine.

Many studies have shown comprehensively that there is a very large, still unexploited potential for improvements in fuel injection parameters. Overall, based on engine operating and design parameters, the type of fuel injection strategy or combination has to be chosen accordingly to govern the fuel-air mixing process. In overall, based on engine operating and design parameters, the type of fuel injection strategy or combination has to be chosen accordingly. Generally combination of one or more strategies may help to strike a balance between reducing emissions and improve the performance of the engine. These also provide major reductions in pollutions particularly with respect to NO_x and PM reduction and hence provide the flexibility in controlling the PM-NO_x trade-off for future vehicles to meet more and more stringent emission norms. As the injection strategies govern the spray characteristics and fuel-air mixing process, it is necessary to understand it in detail. Thus, the following chapters deal with understanding the physical process involved in spray development and fuel-air mixing process through fundamental experiments and simulation of spray atomization and its application on combustion and emission formation using various injection strategies.

3

Experimental analysis of spray development[1]

3.1 Introduction

A key motivating force in the development of modern diesel technology is the increasingly stringent emission norms. The range of techniques being probed include increased injection pressure, injection rate shaping, multiple injections and fine tuning the nozzle geometry. As diesel engine combustion and emissions mainly

[1]Excerpts of this chapter, in part, is a reprint of previous publications titled "*Macroscopic spray characterization under high ambient density conditions*", Experimental Thermal and Fluid Science 59, 109-117, 2014. DOI: 10.1016/j.expthermflusci.2014.08.003. and "*Experimental study of spray characteristics of biodiesel derived from Waste cooking oil*", Energy Conversion and Management 88, 622-632, 2014. DOI: 10.1016/j.enconman.2014.09.013.

rely on spray characteristics, the study of spray dynamics gains significance in meeting stringent emission regulations. The fuel spray in the diesel engine helps in preparation of fuel-air mixture for efficient combustion with less pollutants formation [15]. The spray break up process is highly complex involving multiphase flow and various physical phenomena like cavitation and turbulence inside injector nozzle holes, primary and secondary break-up, evaporation and coalescence. Nevertheless, Spray characteristics like spray tip penetration, spray angle, spray momentum and spray volume are essential factors to understand the process of spray atomization and air-fuel mixing. Thus quantifying these macroscopic spray characteristics will benefit in improved modeling of the spray development process and hence the combustion process accurately.

In order to study the spray development process in detail, optical accessible test rigs such as the optical research engine [133, 134, 135, 136], rapid compression machines [137, 138] and constant volume chambers [37, 139, 140, 141, 142] were used in literature. The main requirement of any optical test rig is that it should simulate the ambient gas conditions that are representative of those in engines during the injection process. Rapid compression machines are being used to study diesel combustion, however they are difficult to build, operate and control. Apart from these drawbacks, they also suffer from producing high noise and strong vibrations due to compression strokes which make it difficult to implement visualization systems. As an alternative, constant volume chambers are used extensively by researchers to study spray characteristics. Also there are several designs of constant volume chambers available [143]. These possess certain advantages such as ease to build and control due to the lack of moving parts but they also strive from disadvantages such as the inability to simulate very high temperatures due to the limitation of material thermal properties. However, the results are really useful in simulating non-evaporating sprays under different ambient gas densities [140, 141, 144, 145]. The macroscopic spray characteristics can be very well captured by using direct photographic imaging techniques [144, 146].

The combustion characteristics are greatly influenced by the fuel-air mixing process and the local distribution of the fuel in the combustion chamber, which is eventually controlled by the fluid dynamics. Hence, information on the spray characteristics is necessary to model the spray breakup process accurately. The combustion process may then be modelled in detail with a high level of confidence. Therefore in this study, a constant volume spray chamber was equipped with optical visualization system to measure the in-cylinder pressure conditions prevailing during injection process. Also spray momentum measurement facility was incorporated to study spray momentum flux under various injection pressure. With the developed experimental setup, non-evaporative spray characterization of different fuels was done at higher injection pressure and ambient density.

3.2 Experimental setup

The experimental set up is shown in Fig.3.1. The macroscopic spray characterization has been performed in constant volume high pressure chamber to reproduce the high gas density inside the diesel combustion chamber during the compression stroke. This high pressure chamber, image acquisition system, injection system, and image processing technique used for the investigation are described briefly in the following paragraphs.

3.2.1 Constant volume spray chamber

The constant volume spray chamber is shown in Fig.3.2. The spray chamber has been developed to allow optical access to the whole length of long, free sprays of fuel oil, at ambient pressures up to 6 MPa, for measurement of spray dynamics using various instrumentation. The design pressure was chosen to represent typical diesel engine compression pressures. The internal volume is about 6 liters. A high degree of optical access is required for measurements of the spray and its surroundings. Optically polished quartz glass windows are fitted to allow capturing

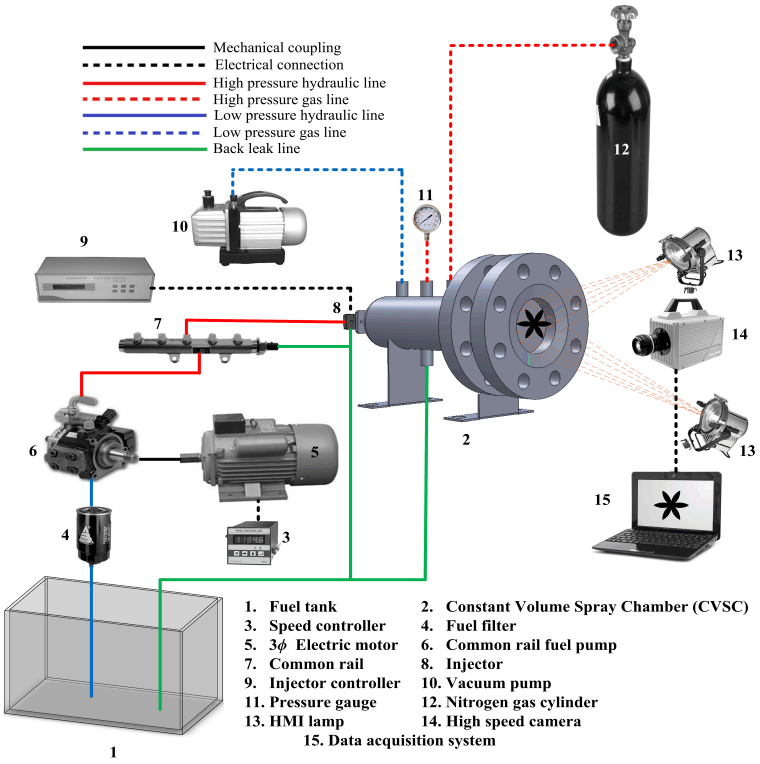

Figure 3.1: Experimental setup

spray images. The viewing area of window is $\phi 150mm$. The inner faces of the window were recessed in the inner chamber surface to avoid contamination by the spray liquid. To seal the windows, an O-ring is employed around the window periphery. This allows a pressure tight seal without the need to apply clamping forces, reducing the risk of window cracking.

3.2.1.1 Design of high pressure chamber

The chamber body, end lids and window retaining flanges are made of S30408 (0Cr18Ni9) stainless steel with a design tensile strength of 130MPa at 50°C. The design of high pressure chamber was done in accordance to GB150.3-2011 [147]. The thickness of the pressure chamber (δ) is calculated by the formula

$$\delta = \frac{P_c D_i}{2\left[\sigma\right]^t \phi - P_c} \tag{3.1}$$

where, P_c is the design pressure (taken as 7.2 MPa, 120% of the maximum operating pressure, 6MPa), D_i is the inner diameter of the chamber (taken as 121

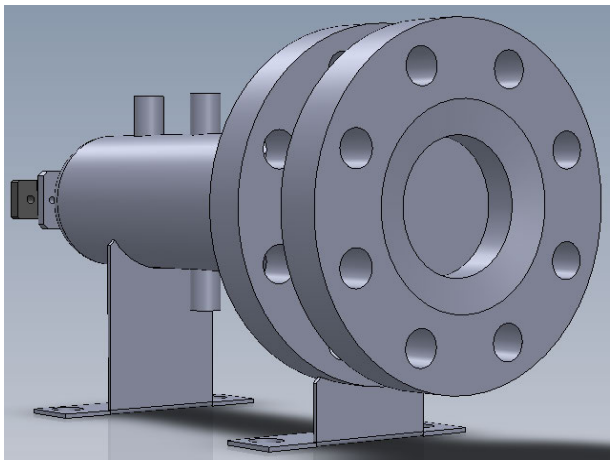

Figure 3.2: Constant volume spray chamber

mm), $[\sigma]^t$ is the allowable design stress (obtained from material design data as 137 MPa [147]), ϕ is the welding head coupling coefficient (taken as 1.0).

The calculated thickness of the chamber is 3.27 mm. Hence the effective thickness δ_e is assumed to be 5.25 mm. The nominal thickness Is calculated from the effective thickness from the relation given as

$$\delta_n = \delta_e + C_1 + C_2 \tag{3.2}$$

Thus the nominal thickness of the chamber is calculated as 6mm. For the calculations to be correct, the following condition should be satisfied

$$[\sigma]^t \phi \geq \sigma^t \tag{3.3}$$

where,

$$\sigma^t = \frac{P_c (D_i + \delta_e)}{2\delta_e} \tag{3.4}$$

The calculated σ^t is 86.57 MPa which is less than $[\sigma^t]\,\phi = 137$ MPa. Hence the calculated nominal thickness is sufficient to withstand the design pressure of the chamber. For detailed drawing of high pressure chamber refer Appendix A.

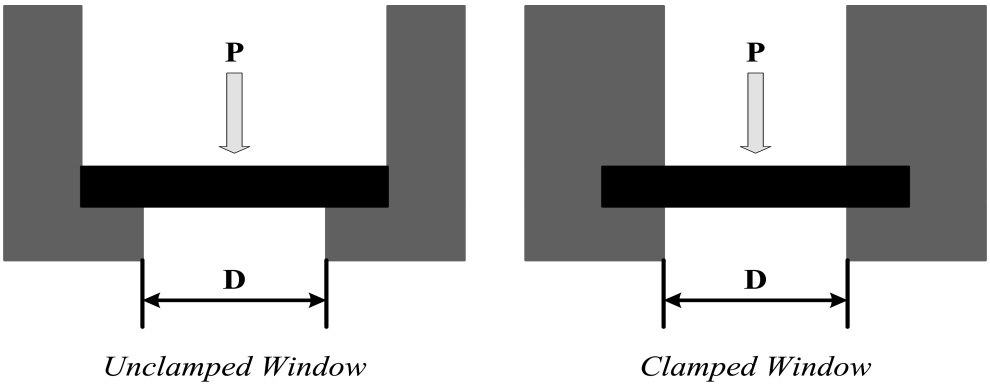

Figure 3.3: Unclamped and clamped pressure window

3.2.1.2 Design of optical pressure window

The windows are made of high quality fused quartz glass. The windows have highly polished surfaces for good optical properties such that surface flaws are minimized. Initially, the minimum thickness for pressure window glass was found by using stress analysis.

The maximum stress σ_{max} on a uniformly loaded window is given by

$$\sigma_{max} = \frac{KD^2P}{4T^2} \tag{3.5}$$

and,

$$\sigma_{max} = \frac{\sigma}{F_s} \tag{3.6}$$

where, K is a constant whose value depends on the method of support, upon the force introduced in clamping and upon the brittle / ductile character of the window material involved. Empirically, a K value of 0.75 is suitable for most optical crystals when the perimeter is clamped, and a value 50% greater when unclamped, i.e. $K_c = 0.75$ and $K_u = 1.125$ (Fig.3.3 shows difference between clamped and unclamped windows), D is the unsupported diameter of the window glass, P is the differential pressure the window is subjected to, T is the minimum thickness of the window glass, σ is the maximum tensile strength of the material used for pressure window, and F_s is the safety factor and it was taken as 7 for this calculation.

From Eqns.2.1 and 2.2, the minimum thickness of the pressure window glass is given by

$$T = D.\sqrt{\frac{F_s K P}{4\sigma}} \tag{3.7}$$

The pressure window glass is clamped in our application to provide additional strength. The design tensile strength for quartz with good surface quality is 48 MPa. However, a recommended maximum tensile strength, which takes into account surface flaws and fatigue, is 6.8 MPa [148] (which also incorporates a safety factor of 7). The design differential pressure was considered to be 7.2 MPa. For this condition, the minimum thickness of the quartz glass to be used was calculated to be $56.5mm$ and we chose $60mm$ thick glass for the optical pressure window.

Then the calculated glass thickness was subjected to finite element analysis (FEA) to ensure the deflection was within limits. ANSYS release 13.0 commercial FEA software was used for this purpose. The mesh used for the simulation is shown in Fig.3.4.The mesh size used was around 250000 cells with element size of 3mm. The ANSYS linear element SOLID95 was used for the analysis of the glass window. SOLID95 is a linear element and is well suited to model curved boundaries. These elements can also be tetrahedral and can automatically transit between hexahedral and tetrahedral using pyramids. It can tolerate irregular shapes without much loss of accuracy [149].

The quartz windows were analyzed using the maximum principal stress criterion as well as a cracking analysis for brittle materials incorporated in ANSYS. This analysis uses supplied values of material tensile and compressive strength to check for possible onset of cracking. For these analyses, tensile strength of 6.8MPa and compressive strength of 1100MPa were used. The simulations were performed for different chamber pressure from 10-60 bar. It was found that no crack was observed even at maximum pressure of 60 bar (see Fig.3.5). Fig.3.6 shows the total deflection observed for various chamber pressure obtained from the simulation.

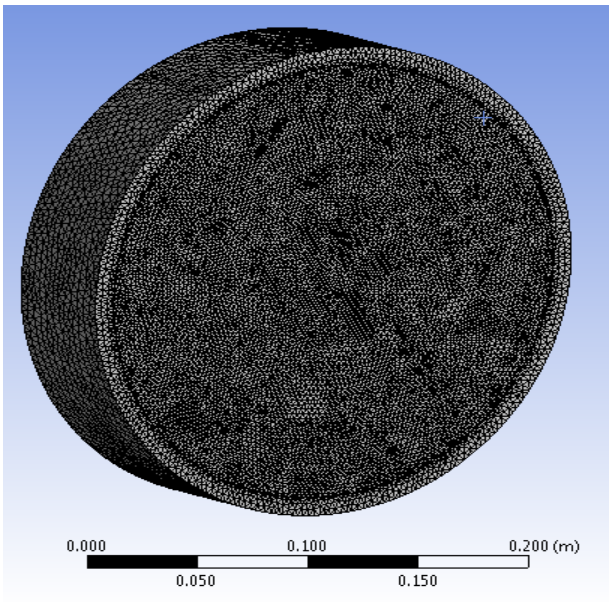

Figure 3.4: Mesh used for FEA analysis of quartz glass

The maximum deflection of $5.3 * 10^{-5}m$ was observed at chamber pressure of 60 bar. The maximum deflection was well within the minimum deflection required for crack initiation in the quartz glass. Hence the thickness of 60mm and quartz glass as material was fixed for the optical pressure window.

3.2.1.3 Hydrostatic test

A standard hydrostatic test to 90 bar, 125% of the design pressure, was conducted. The pressure for the hydrostatic test was calculated as follows

$$P_t = 1.25 P_c \frac{\sigma}{[\sigma]^t} \tag{3.8}$$

where, the test pressure for hydrostatic test is calculated as 9 MPa.

The hydrostatic test was done based on the cycle as shown in Fig.3.7. The chamber passed the hydrostatic test without any deformation or problem and the same was certified by the profession engineer (PE). The PE certificate is attached in the Appendix A.

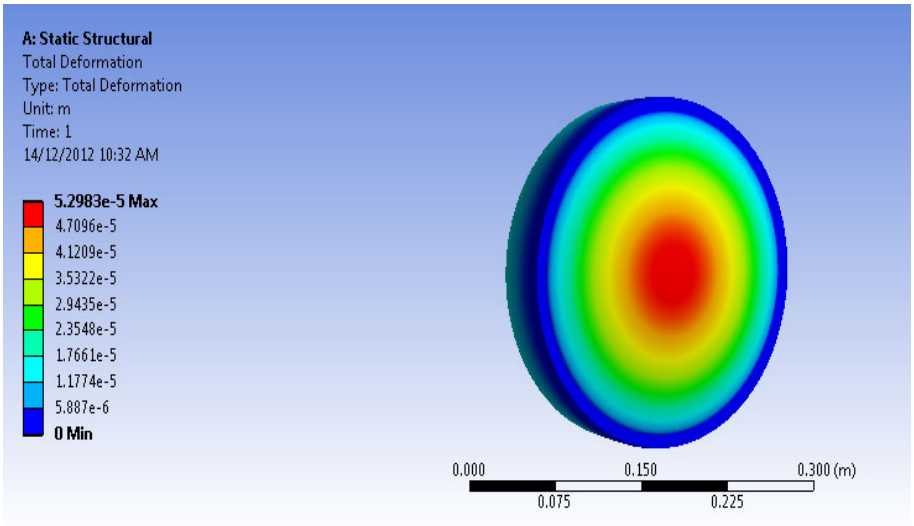

Figure 3.5: Total deflection at chamber pressure of 60 bar

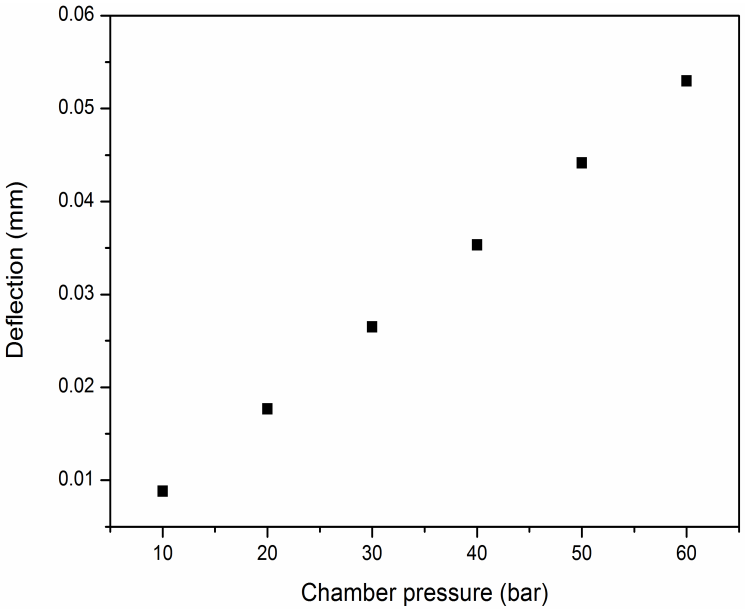

Figure 3.6: Total deflection vs chamber pressure calculated from FEA simulation

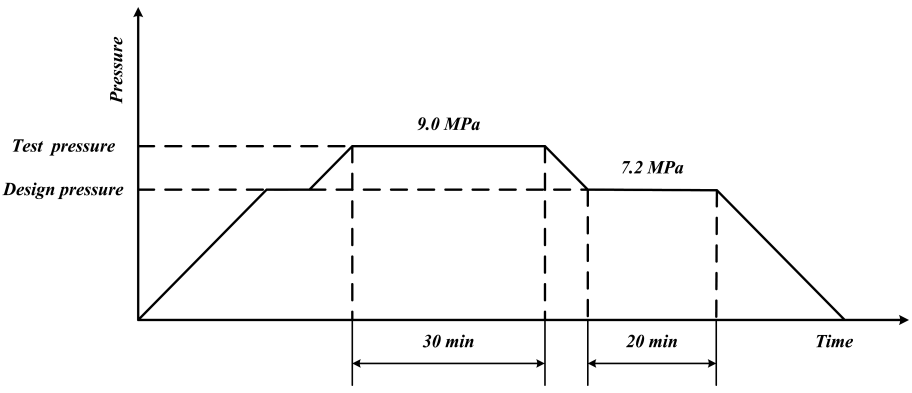

Figure 3.7: Cycle followed for hydrostatic test

3.2.2 Fuel injection system

The fuel injection system consists of common rail fuel injectors, common rail, Denso common rail pump, electronic control unit, electric motor to run the high pressure CR pump and high pressure fuel lines connecting pump, common rail and fuel injectors.

The motor for running common rail pump to obtain the required injection pressure is a critical component of the system.The motor was carefully chosen to obtain injection pressure of maximum $1600bar$. The calculation used in selecting the motor is as follows

$$Power = \frac{\triangle P * Q}{\eta} \quad kW \tag{3.9}$$

where, $\triangle P$ is the pressure difference in bar, Q is the volume flow rate in $^{m^3}/_s$ and η is the mechanical efficient chosen to be 85% based on available data. The volume flow rate of the pump is calculated by the formula as shown below

$$Q = \frac{n * \pi d^2 h * N}{4 * 60} \tag{3.10}$$

where, n is the number of plungers in the fuel pump, d is the diameter of the plunger in m, h is the stroke of the plunger in m and N is the maximum speed at which the pump operates in rpm, in this case the maximum operating speed was restricted to $1000rpm$ for safety considerations and keep the power requirement minimum. Thus from the calculation, the power requirement for the motor was $2.08kW$. Thus we chose a $2.23kW$ motor with maximum drive torque of $21.3Nm$ at $1000rpm$ for this application.

The common rail injector (Fig.3.8) used to investigate the spray characteristics of diesel fuel is a 7-hole injector. The dimensions of the nozzle hole were determined by using a silicone mold of Polydimethylsiloxane (PDMS) material by approach similar to Macian et al [150]. The scanning electron microscope (SEM) image and dimensions of the nozzle hole is shown in Fig.3.9. The measured dimensions shows

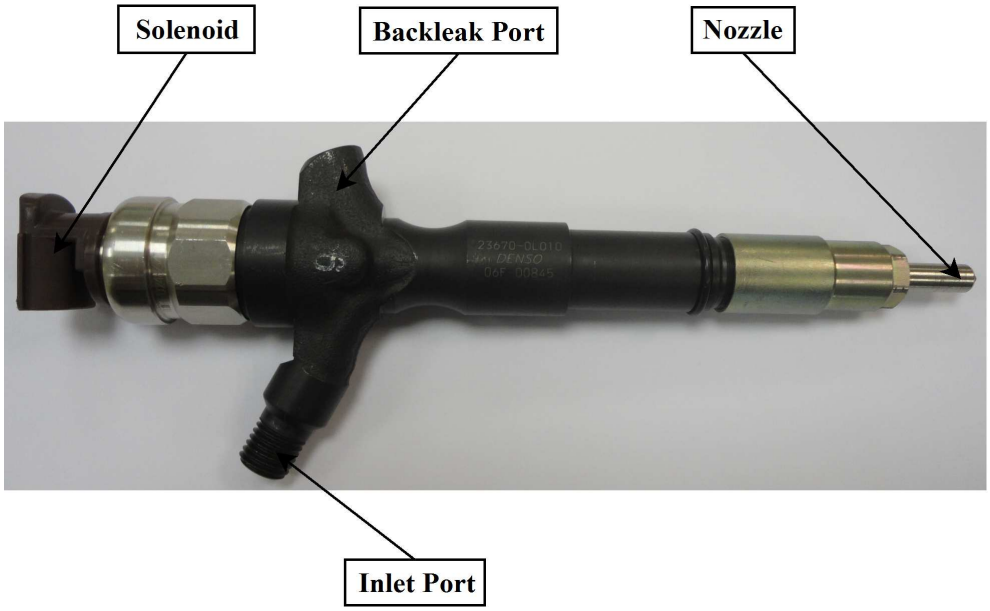

Figure 3.8: Commercial Denso common rail injector

that the orifice diameter is 175±3µm and length of orifice is 1000±50µm, radius of curvature at the inlet is 15µm and the angle of the spray is 150±2°. The exit diameter of the nozzle hole was also measured in terms of pixels using an optical microscope. The scale used for the measurement is 1 : 1, so one pixel measured is equal to 1 µm. The exit diameter measured using this method was also around 175 ± 3 µm. The injector nozzle hole under optical microscope is shown in Fig.3.10.

3.2.3 Image acquisition and image processing

The spray visualization was carried out with Photron Fastcam SA5 high speed camera. The camera sensor is 12 bit monochrome with a spatial resolution of 20µm pixel with a minimum exposure time of 1µs. The images were captured at 20000 frames per second with a maximum spatial resolution of 832x448 pixels and temporal resolution of 50µs. The high speed camera was equipped with a Nikon lens (Nikkor AF 28-85mm $f/1 : 3.5 \sim 4.5$) with C-mount adapter. Illumination was provided by 400W Hydrargyrum medium-arc iodide (HMI) lamp with high speed electronic ballast to limit current and voltage.

The image processing was done in two stages, (i) processing of spray images using custom code written in Matlab and (ii) quantifying spray characteristics

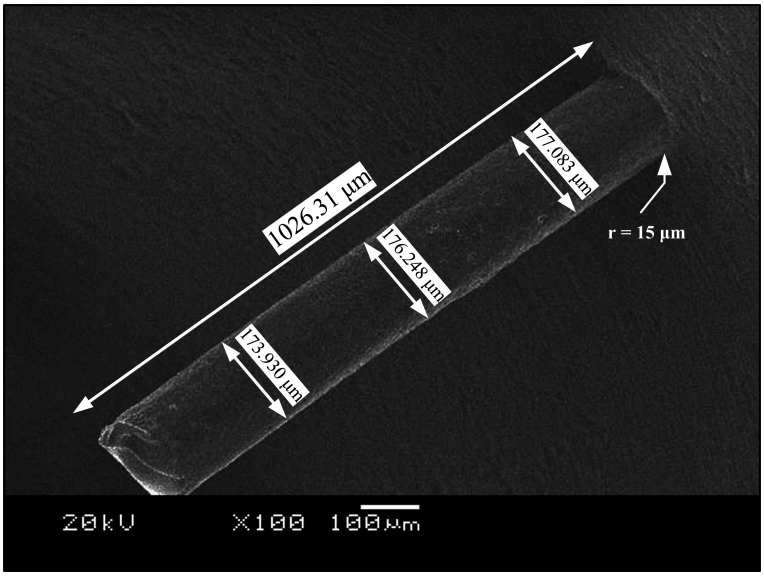

Figure 3.9: SEM image of nozzle hole dimensions of the injector used

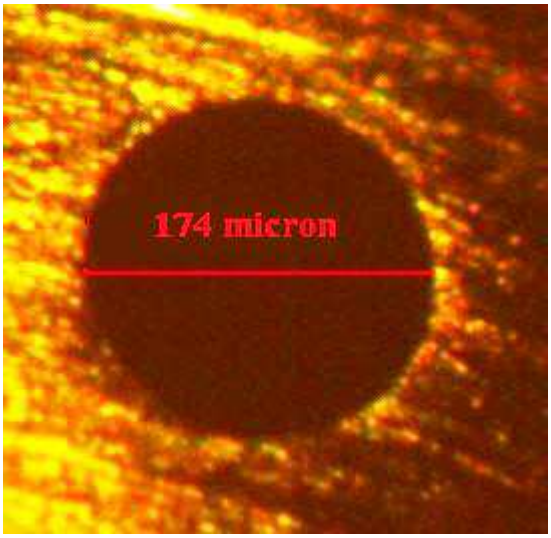

Figure 3.10: Nozzle hole measurement under optical microscope

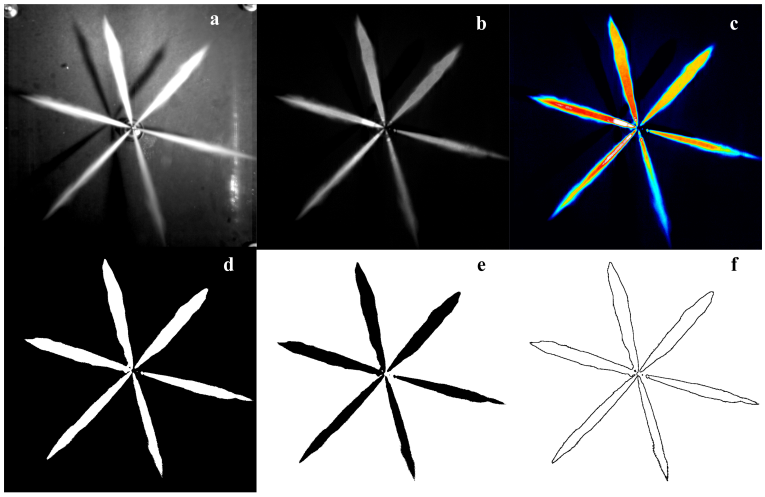

Figure 3.11: Image processing a) original image b) background separated c) colored based on light intensity d) binary converted e) complement of d f) edge detected of spray at 800 bar injection pressure

using ImageJ code. The sequence of steps involved in image processing is shown in Fig.3.11 and 3.12. The raw spray image is background subtracted to eliminate non-uniform illumination and isolate the spray. Then the isolated spray images are subjected to threshold using Otsu method [151]. Then the edge detection is performed using the Canny edge detection method [152]. Finally the spray tip penetration and the spray angle are quantified from the processed image using ImageJ code.

3.2.4 Spray momentum measurement

The spray momentum measurement was done similar to Payri et al [153] at atmospheric condition. The schematic of spray momentum measurement is shown in Fig.3.13. By principle of conservation of momentum, the force (F) measured by the force sensor gives the momentum flux $\left(\dot{M}\right)$ from the fuel injector nozzle. The spray momentum is measured using calibrated Kistler force sensor (type 9207). The Kistler force sensor is piezo-electric type capable of measuring force between $\pm$50N with transverse force sensitivity of $\leq\pm$0.05N. A circular target was directly screwed to the sensor head to prevent the sensor from direct impact from spray and also provide sufficient target area for spray impingement. The force sensor

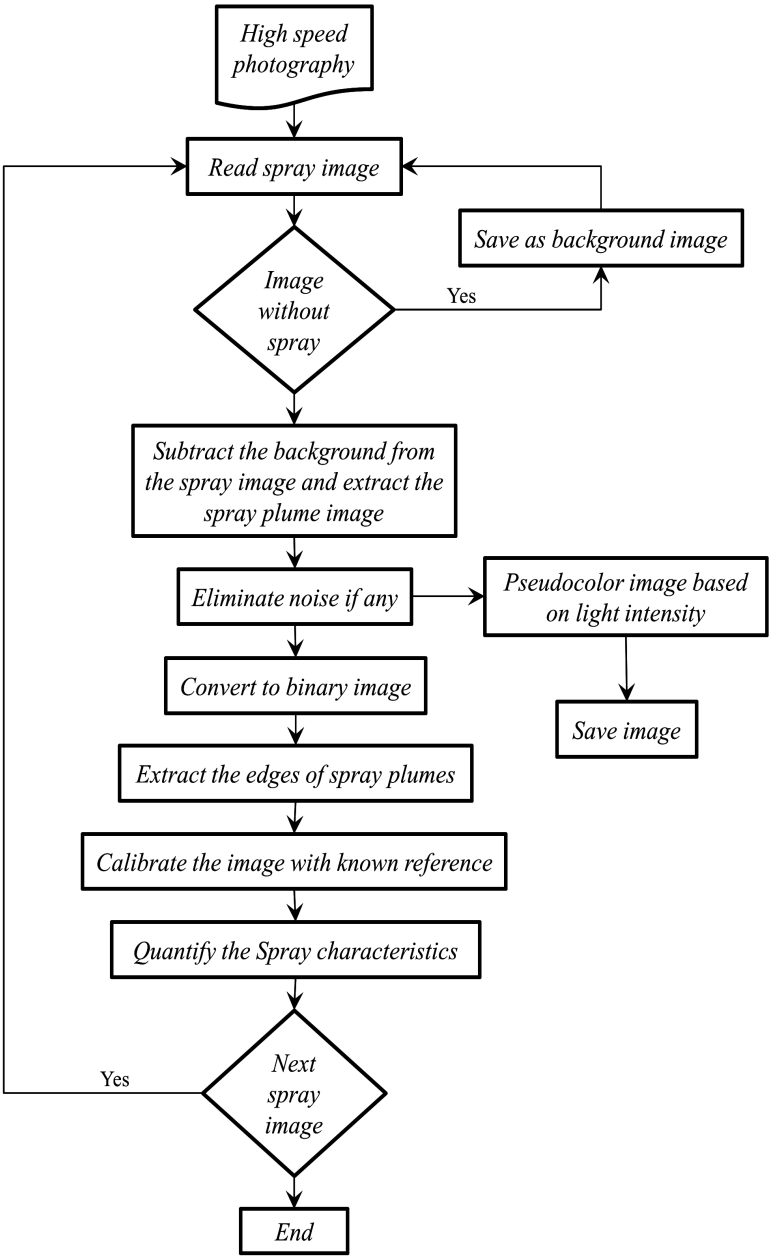

Figure 3.12: Flowchart showing steps involved in image processing

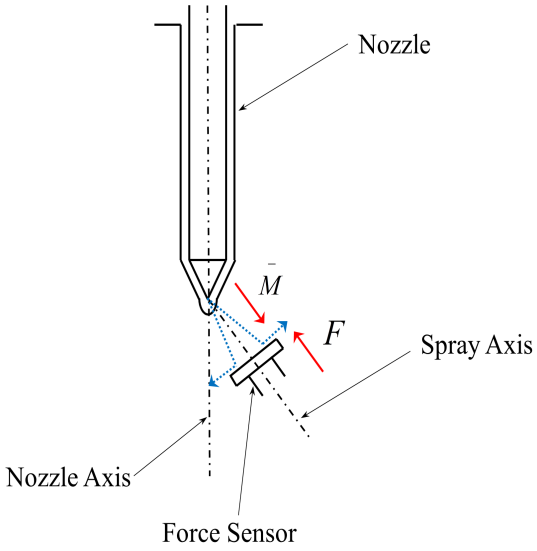

Figure 3.13: Schematic of spray momentum measurement

was fixed to a nozzle using a custom designed fixture (See Appendix B for detailed drawings) which can also be used to position the sensor axially. The travel of the sensor can range from 0 mm to 12 mm along the spray axial direction from the nozzle exit. The output of the sensor is connected to a charge amplifier which is then connected to monitoring computer through a data acquisition system (NI-6210) capable of acquiring data at 250kS/s.

3.3 Definition of spray characteristics

The actual spray tip penetration was calculated similar to the method used by Delacourt et al. [140] as shown in Eq. 3.11

$$S = S^{'} \csc\left(\frac{\alpha}{2}\right) \tag{3.11}$$

where, S is the actual spray tip penetration in mm, $S^{'}$ is the spray tip penetration measured from spray images from tip of the nozzle to the farthest axial location of the spray boundary in mm as shown in Fig.3.14 and α is the cone angle of the spray in *radians*.

The spray angle is calculated as shown in Eq.3.12 [140]

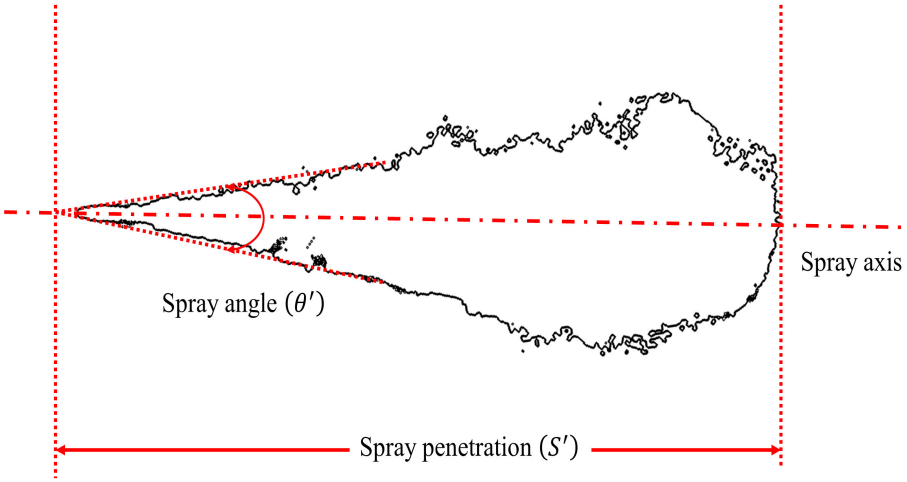

Figure 3.14: Definition of spray characteristics

$$\theta = 2 \arcsin\left(\sin\left(\frac{\theta'}{2}\right)\sin\left(\frac{\alpha}{2}\right)\right) \tag{3.12}$$

where, θ is the actual spray angle in *radians* and θ' is the spray angle in *radians* measured from the spray images between the tangent lines fitted through the upstream half of the spray contour as shown in Fig.3.14.

The spray velocity is the spray tip velocity calculated from the spray tip penetration and time difference between two consecutive spray images.

The fuel spray volume is calculated by assuming it to be a cone with hemisphere as given in Eq.2.3 [140]

$$V(t) = \frac{1}{3}\pi S(t)^3 \tan^2\left(\frac{\theta}{2}\right)\frac{\left(1+2\tan\left(\frac{\theta}{2}\right)\right)}{\left(1+\tan\left(\frac{\theta}{2}\right)\right)^3} \tag{3.13}$$

where, $V(t)$ is the spray volume at time in mm^3 and $S(t)$ is the spray tip penetration at time in mm.

The mass of air entrained within the fuel spray was calculated using the model proposed by Rakapoulos et al. [154] as given in Eq.3.14

$$m_a(t) = \left(\frac{\pi}{3}\right)\left(\tan\left(\frac{\theta}{2}\right)\right)^2 S(t)^3 \rho_{amb} \tag{3.14}$$

where, $m_a(t)$ is the mass of air entrained within the fuel spray at time in kg

and ρ_{amb} is the ambient air density in $^{kg}/_{m^3}$.

The equivalence ratio along the axial direction of the spray can be calculated based on the correlation suggested by Naber et al. [37] by assuming that the fuel sprays behave similar to that of gaseous turbulent jets. The equation for equivalence ratio at any axial location in the spray is given in Eq.3.15

$$\phi(x) = \frac{2\left(\frac{A}{F}\right)_{st}}{\sqrt{1+16\left(\frac{x}{x^*}\right)^2}-1} \tag{3.15}$$

where, $\phi(x)$ is the equivalence ratio at any axial location x, $\left(\frac{A}{F}\right)_{st}$ is the stoichiometric air-fuel ratio, x is the axial location in the spray in mm and x^* is the characteristic length scale in mm given as follows in Eq.3.16

$$x^* = \sqrt{\frac{\rho_f}{\rho_{amb}}}\frac{\sqrt{C_a}D_n}{a\tan\left(\frac{\theta}{2}\right)} \tag{3.16}$$

where, ρ_f is the fuel density in $^{kg}/_{m^3}$, C_a is the area contraction coefficient calculated from the numerical simulation of cavitating injector nozzle holes, D_n is the injector nozzle hole diameter in mm and a is an arbitrary constant whose value can be between 0.84 to 0.7 and in this study it is assumed to be 0.73 as suggested by Naber et al. [37].

3.4 Results and discussion

3.4.1 Diesel fuel

3.4.1.1 Spray momentum flux

The instantaneous spray momentum flux has been measured at two different axial distances from the nozzle exit i.e. at 5 and 10 mm for different injection pressures at atmospheric conditions. Fig.3.15 shows the momentum flux for injection pressure of 125 MPa measured at 5 and 10mm from the nozzle exit. By the principle of conservation of momentum, the axial momentum flux along the axial direction

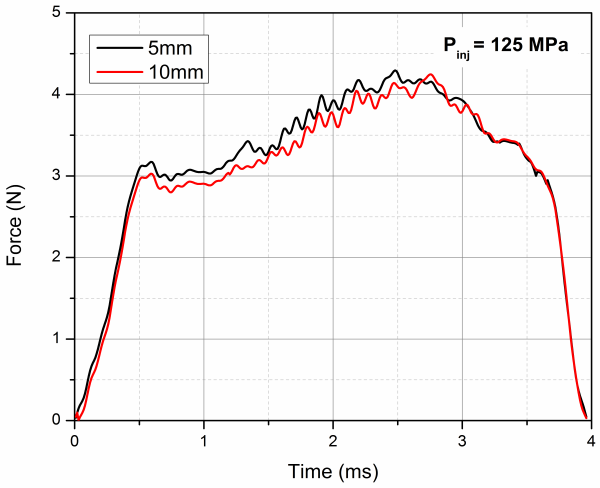

Figure 3.15: Spray momentum flux measured at 5 and 10mm axially from nozzle exit

should be constant and equal to the momentum flux at the nozzle exit. This means, the reduction in axial velocity farther from the nozzle exit is compensated by the bigger spray cross sectional area due to air entrainment. Interestingly, it was found that measurement made at 10mm from the nozzle exit is slightly lower than that measured at 5mm. This may be due to the air entrainment into the spray which increases the spray cross sectional area and hence exceeds the frontal area of the force sensor. Therefore, the sensor measures partial momentum flux at 10mm from the nozzle exit. This phenomena was also observed by Payri et al. [155]. Thus for further measurements, the sensor front area where the spray impinges is made sure that it is bigger than the spray cross sectional area and therefore the position of sensor is fixed at 5mm axially from the nozzle exit.

Fig.3.16 shows injection rate and spray momentum flux from one of the holes for different injection pressures. As can be seen from the figure, the momentum flux increases when the injection pressure increases. This shows that as injection pressure increases the spray is more penetrative with higher injection velocity. Fig.3.17 shows the average momentum flux calculated over the time at which the needle is fully opened and momentum coefficient calculated as follows

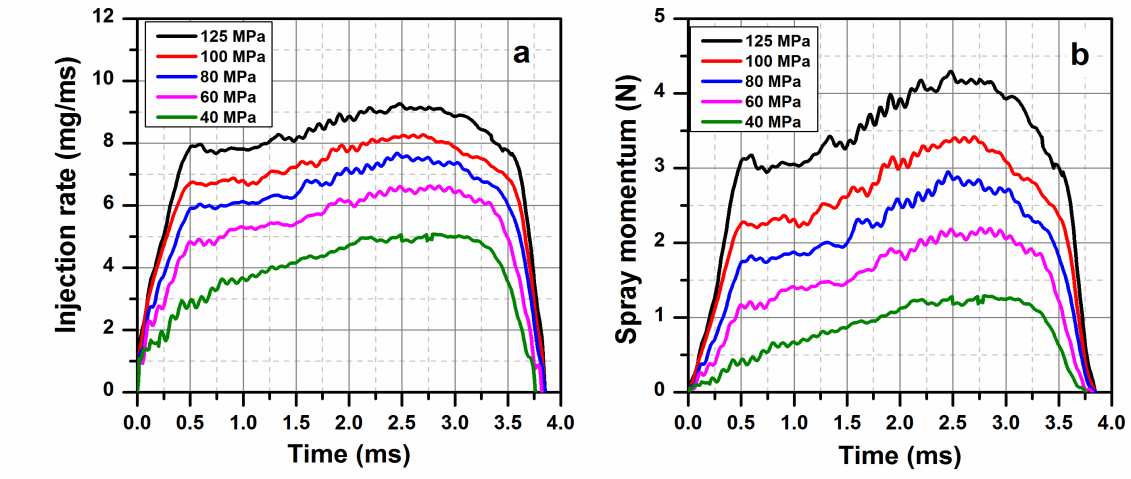

Figure 3.16: Injection rate and spray momentum flux at different injection pressures

$$C_m = \frac{M_{act}}{M_{th}} \tag{3.17}$$

$$C_m = \frac{F}{m\sqrt{\frac{2(P_{inj}-P_{amb})}{\rho_l}}} \tag{3.18}$$

where, M_{act} is the actual momentum flux in N, M_{th} is the theoretical momentum flux in N, F is the force measured from force sensor in N, $\dot{m}$ is the mass flow rate of fuel from one hole in $\frac{kg}{s}$, P_{inj} is the injection pressure in Pa, P_{amb} is the ambient pressure in Pa and ρ_l is the fuel density in $\frac{kg}{m^3}$.

Fig.3.17 shows the average momentum flux and momentum coefficient for different injection pressures measured under atmospheric conditions. From figure, it is clear that the average momentum flux is directly proportional to the injection pressure. However, the momentum coefficient remains constant from 40MPa to 125 MPa. This interesting behavior may be due to effect of cavitation inside the injector nozzle hole. Similar results were obtained by Payri et al. [153] and they have confirmed that the increase in momentum coefficient is interrupted as the cavitation starts inside the nozzle hole and also they have reported that the momentum coefficient is independent of cavitation number under cavitating conditions. This means the momentum coefficient remains constant for particu-

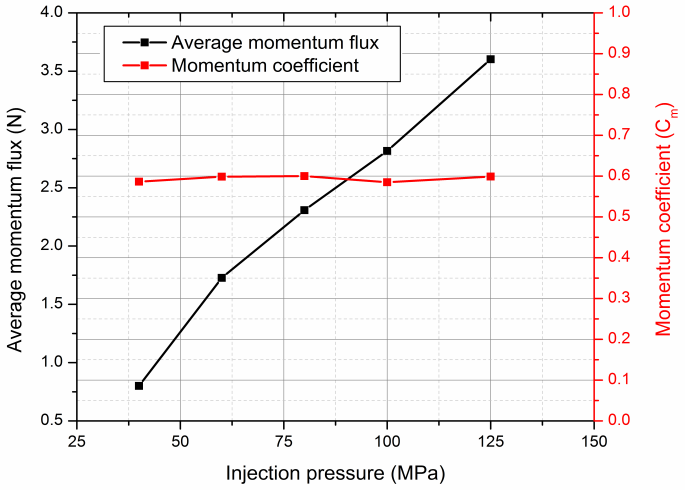

Figure 3.17: Average momentum flux and momentum coefficient

lar geometry under different injection and ambient pressure conditions as far as cavitation takes place inside the nozzle hole.

3.4.1.2 Spray characteristics

Fig.3.18 shows the spray tip penetration for different injection pressures and ambient densities. The results obtained shows that the spray tip penetration increases with increasing injection pressure. This is mainly due to increased spray momentum possessed by the fuel at higher injection pressures which is evident from the spray momentum results obtained. As the ambient density increases, the spray tip penetration decreases, which is mainly due to fact that the spray loses momentum under higher ambient density conditions. The results obtained are very well in line with those of other researchers [37, 139, 140]. The spray evolution with time is shown in Fig.3.19. The reduction in spray momentum can also be supported by the spray velocity as shown in Fig.3.20. The spray velocity increases with increasing injection pressure which is due to increase in spray momentum and as the ambient density increases, the spray velocity is reduced showing that the momentum decreases quickly with the increase in ambient density.

As the spray angle is quite stable with time, Fig.3.21 shows the average value

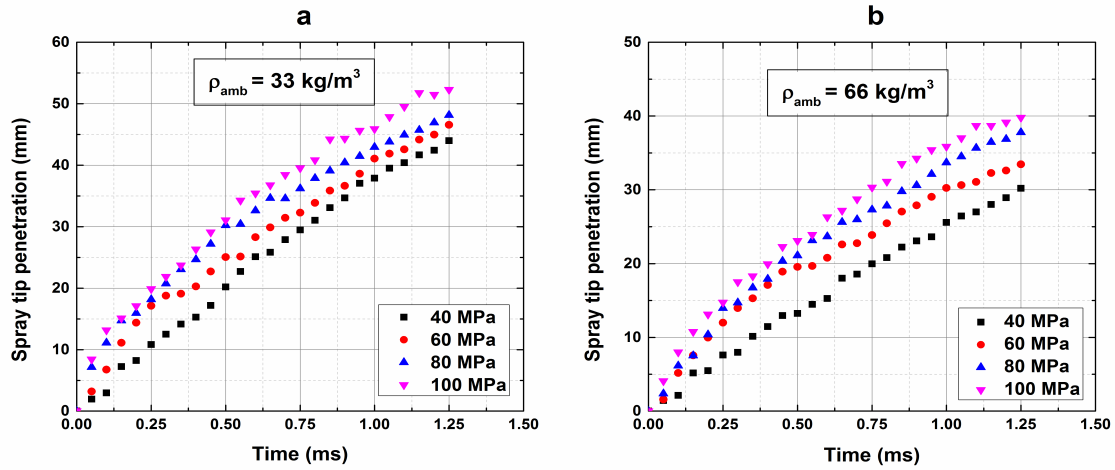

Figure 3.18: Spray tip penetration at different injection pressure and ambient density

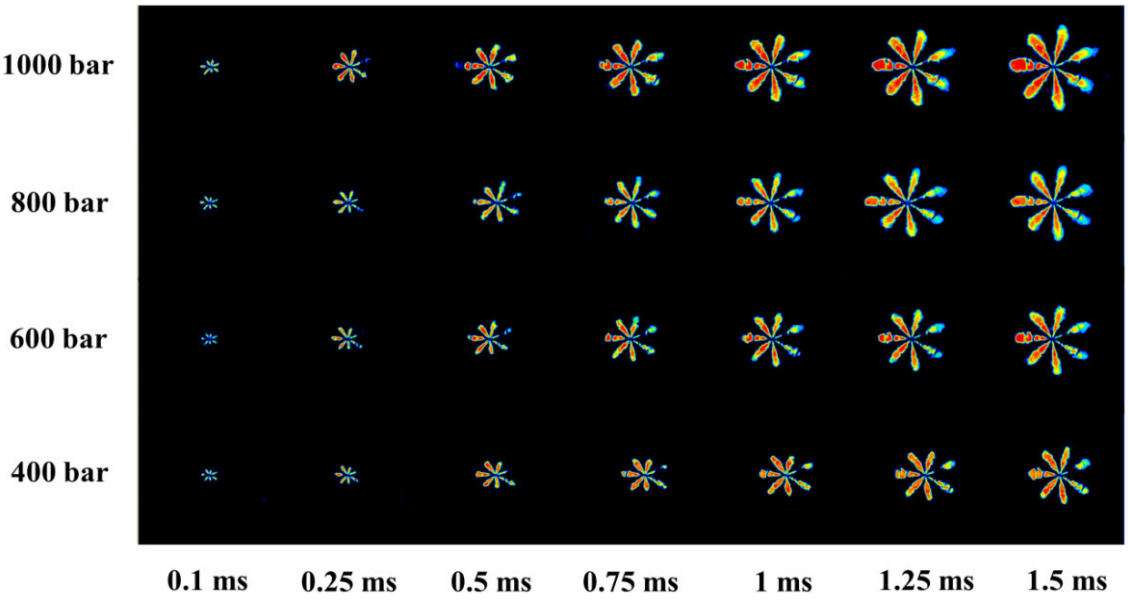

Figure 3.19: Spray evolution at different injection pressure under ambient density of 66 $^{kg}/_{m^3}$

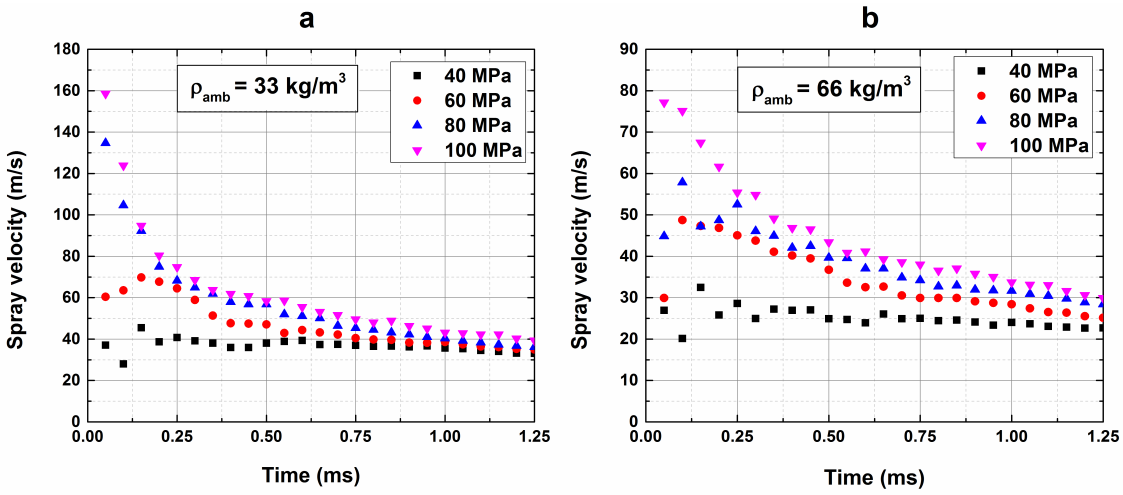

Figure 3.20: Spray velocity at different injection pressure and ambient density

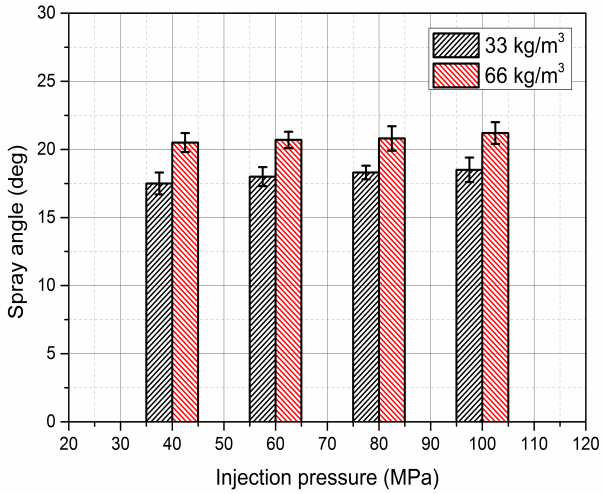

Figure 3.21: Averaged spray angle at different injection pressure and ambient density

of spray angle observed during the quasi-steady stage. It is very clear from the figure that as the ambient density increases the spray angle increases. This is because; as the ambient density increases the resistance to spray development in axial direction is restricted resulting in wider spray angles. It is also interesting to note that there is no significant effect of injection pressure on spray angle, which conveys that spray angle is more affected by ambient density than injection pressure.

Fig.3.22 shows the spray volume at different injection pressure and ambient

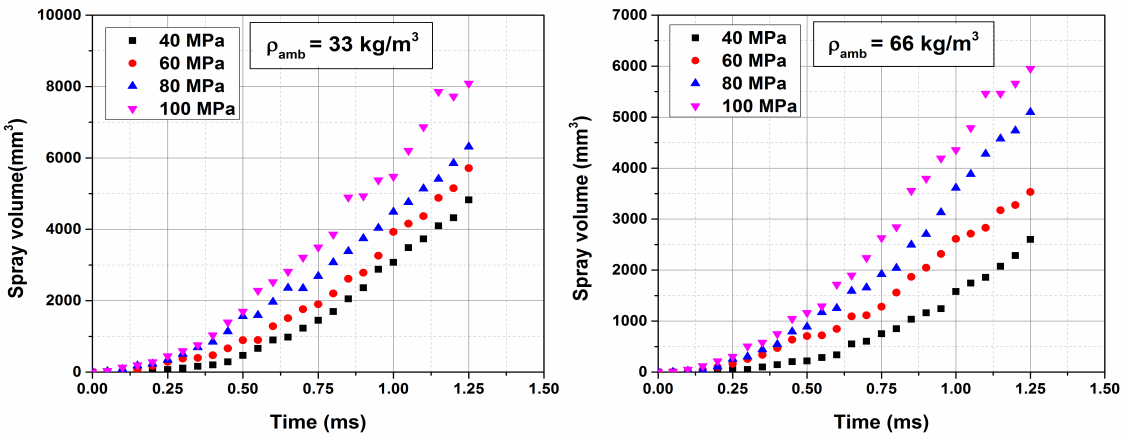

Figure 3.22: Spray volume at different injection pressure and ambient density

density. Spray volume gives an insightful detail on the air fuel mixing based on air entrainment. Higher spray volume results in greater air entrainment and air fuel mixing is better. Conversely, reduced spray volume results in lower air entrainment and the air fuel mixing is poor. From the same figure, it can be noted that, the spray volume increases with injection pressure which obviously shows that as the injection pressure increases the droplet size decreases and the probability of air entrainment between the droplets increases. As the injection pressure is lower, the droplet sizes would be large for any air entrainment which makes the spray volume smaller. At higher ambient density, the spray volume with time seems to be lower than at lower density; however when we take spray penetration distance into account, the spray volume at higher density is found to be higher for same penetration distance. This may be due to higher spray angle at higher density. This shows that the air fuel mixing is better at higher ambient density than at lower density for same penetration.

3.4.2 Biodiesel fuel and its blend

The experiments were carried out with biodiesel produced from waste cooking oil (B100) and its blend (B20) with diesel. B20 was prepared by mixing 20% by volume of biodiesel with diesel. B20 blend was chosen in this study as B20 exhibited comparable performance and emission characteristics to that of diesel

Table 3.1: Fuel properties

Properties	Measurement method	ULSD	B100
Density at 20°C ($^{kg}/_{m^3}$)	EN 12185	840	883.5
Viscosity at 20°C ($^{mm^2}/_{s}$)	EN ISO 3104	2.8	4.36
Cetane number	EN 1ISO 5165	52	58
Flash point ($°C$)	prEN 3679	42	170
Calorific value ($^{MJ}/_{kg}$)	ASTM D240	45	38.6
Copper corrosion strip test (50°C/3 hrs)	EN ISO 2160	Class 1	Class 1
Sulphur content (mg/kg)	prEN 20846	<15	3.1

fuel as reported earlier by our group [45]. The composition of biodiesel mainly depends on its feedstock, however in the case of waste cooking oil biodiesel, it is challenging to identify the feedstock as there are wide variety of cooking oils available. The only way to get some insights about its composition is to perform gas-chromatography analysis. Therefore in order to identify the composition of biodiesel used in this study, GC-MS (Gas Chromatography-Mass Spectrometer) analysis was done. The HP5-ms column (25 m x 0.32 mm ID x 0.45 mm OD) was used in this study. 1µL of analyte was injected at 260 ° C in splitless mode. The oven temperature was programmed from 150 ° C with a hold time of 5 min and then first ramp was initiated at temperature gradient of 12 ° C/min up to 200 ° C with a hold time of 17 min and then second ramp was programmed at temperature gradient of 3 ° C/min up to 252 ° C with a hold time of 6.5 min. Helium with 99.99% of purity was used as a carrier gas. Constant flow of carrier gas was set as 0.6 mL/min on the column. Based on the retention time, the constituents at 9.998 min, 12.661 min, 12.842 min and 13.321 min were identified as Hexadecanoic acid, methyl ester (Methyl Palmitate), 9,12-Octadecadienoic acid(Z,Z)-, methyl ester (Methyl Linoleate), 9-Octadecenoic acid, methyl ester (Methyl Oleate), and Octadecanoic acid, methyl ester (Methyl Stearate) respectively from the standard database. The GC-MS spectrum for biodiesel used in this study along with its composition in mass percentage is shown in Fig.3.23. The typical fuel properties were summarized in the Table 3.1.

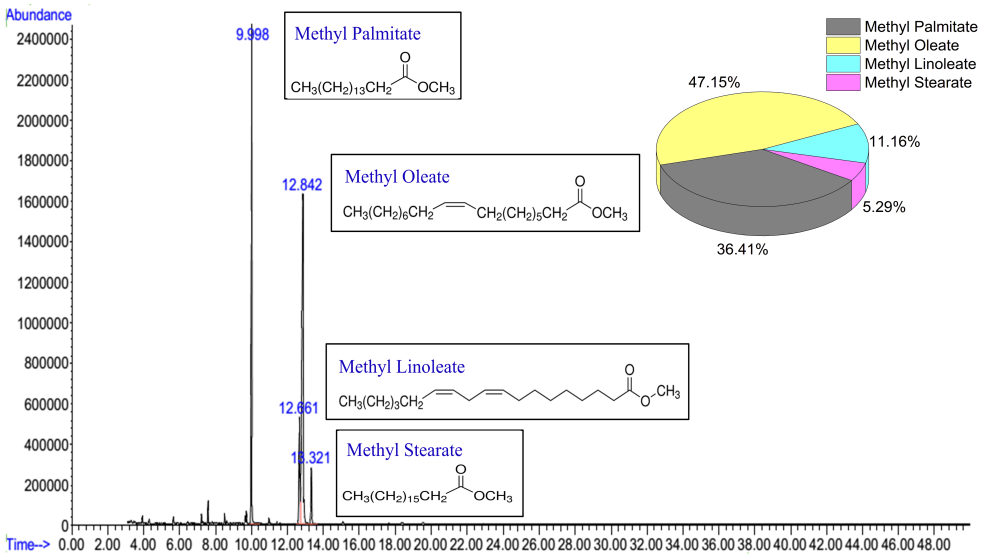

Figure 3.23: GC-MS result of waste cooking oil biodiesel

3.4.2.1 Spray morphology

The spray evolution of different fuels under fuel injection pressure of 100MPa and different ambient pressures are shown in Fig.3.24. B100 shows narrower and longer spray compared to diesel and B20 sprays. Also B100 sprays shows darker images compared to B20 and diesel spray images due to weak light scattering from B100 spray. This is due to poor atomization of B100 sprays due to high viscosity and surface tension. The bright spray images of diesel suggest that the diesel undergoes better atomization leading to smaller droplets which highly scatter the light back to the camera [142]. From these images, it can be noted that the atomization of diesel is superior followed by B20 and B100 sprays. Also the spray images of diesel and B20 has some small vortex like structures on its spray boundary which indicates that ambient gas entrainment is better in those sprays compared to B100 which has no such structures on its surface.

Fig.3.25 shows a comparison of the spray boundaries of different fuels superimposed on one another at ambient pressures of 3 and 6MPa. It could be seen from the figure that the spray shape is tilted axially for different fuels. This may be due to two factors (i) high resistance offered by the ambient gas density or (ii) by the effect of cavitation inside the nozzle holes. The level of cavitation inception inside

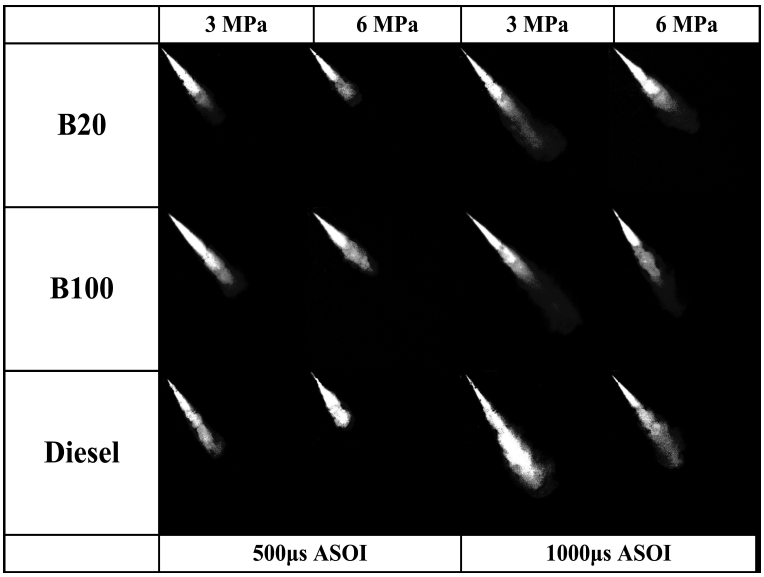

Figure 3.24: Spray evolution for injection pressure of 100MPa under different ambient pressures

the nozzle holes creates an asymmetry in the spray [156] and also leads to much greater spray angles [156, 157]. Thus considering the asymmetry spray shape, the diesel fuel should have undergone stronger cavitation than B20 and B100 fuels. In order to support this claim, a numerical simulation on cavitation inside nozzle holes was done using Fluent 12.0. The numerical model is explained in detail in Chapter 4. The cavitation contours for different fuels is shown in Fig.3.26. The red color in the contours denotes complete fuel vapor and blue color denotes complete liquid fuel. Thus, from the figure it is clear that cavitation is greater with diesel fuel due to its lower viscosity [158] then with B20 and then B100 fuels. It should also be noted that for the same injection pressure, as the ambient pressure increases, the cavitation is inhibited. The discharge coefficient also decreased with increasing cavitation which means that the discharge coefficient is higher for B100 followed by those for B20 and diesel fuels. Thus from this simulation results, it can be suggested that the change in orientation of spray shapes may be due to effect of higher cavitation inside nozzle holes for diesel and B20 fuels compared to B100.

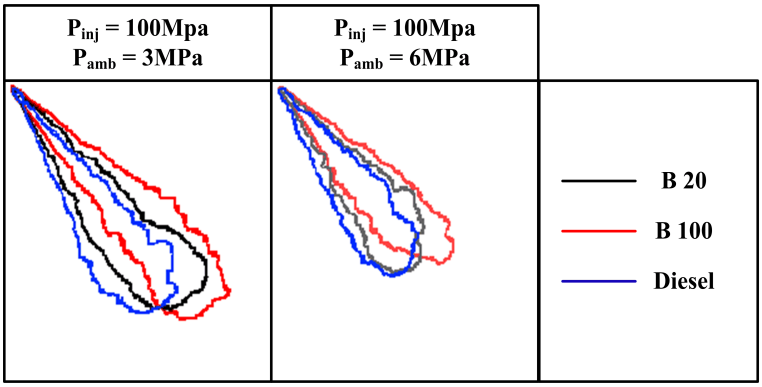

Figure 3.25: Spray boundary comparison for different fuels

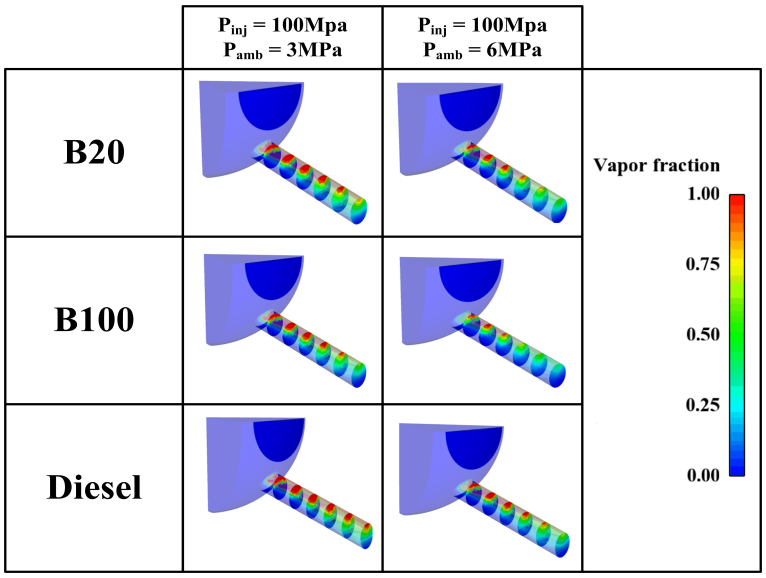

Figure 3.26: Cavitation contours for different fuels

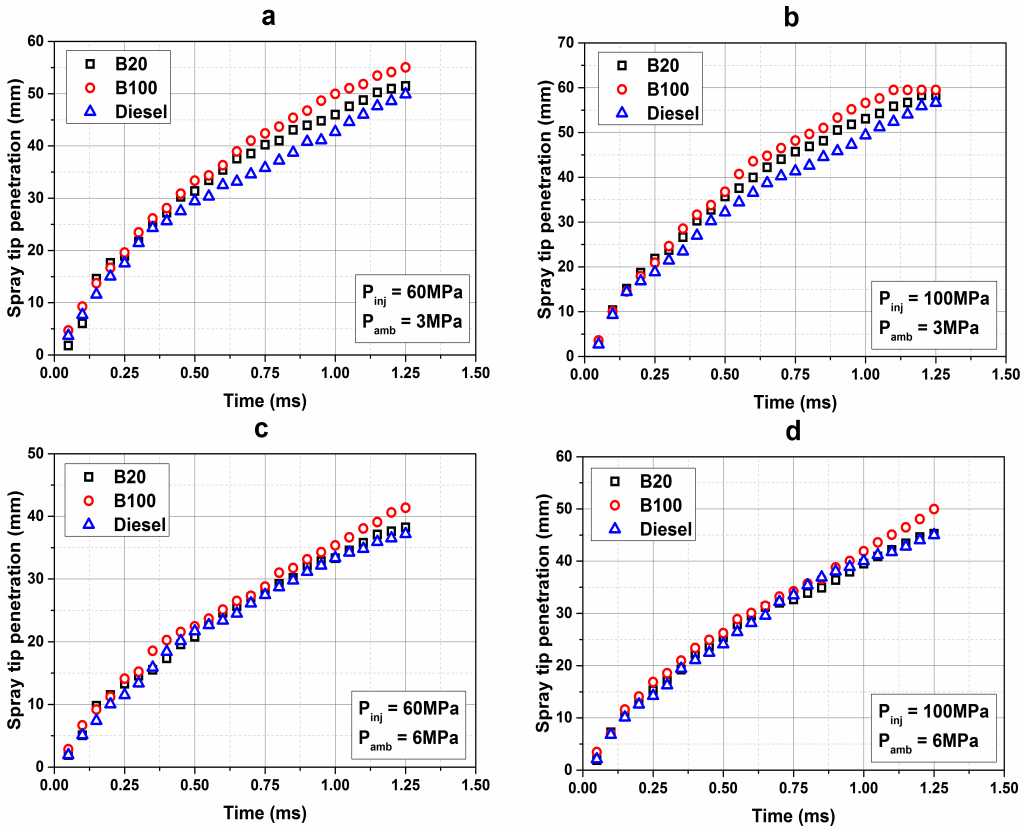

Figure 3.27: Spray tip penetration for different fuels

3.4.2.2 Macroscopic spray characteristics

Spray tip penetrations for diesel and biodiesel fuels are shown in Fig.3.27. Under ambient pressure of 3MPa, there is a significant difference in the spray tip penetrations between diesel, B20 and B100 fuels, and as the injection pressure increases the difference gets reduced slightly. The difference in spray tip penetration also decreases with increasing ambient pressure. At ambient pressure of 6MPa, the difference between diesel and B20 spray penetrations is small for both 60 and 100MPa injection pressures. However with B100 there is a slightly higher spray tip penetration. The longer spray penetration of B100 at all conditions can be because of higher momentum possessed due to two reasons (a) high discharge coefficient from the nozzle exit [159] as discussed earlier (b) poor atomization leading to larger droplets due to its high viscosity. However, the spray tip penetration of diesel and B20 are comparable under all conditions of injection and ambient pressures.

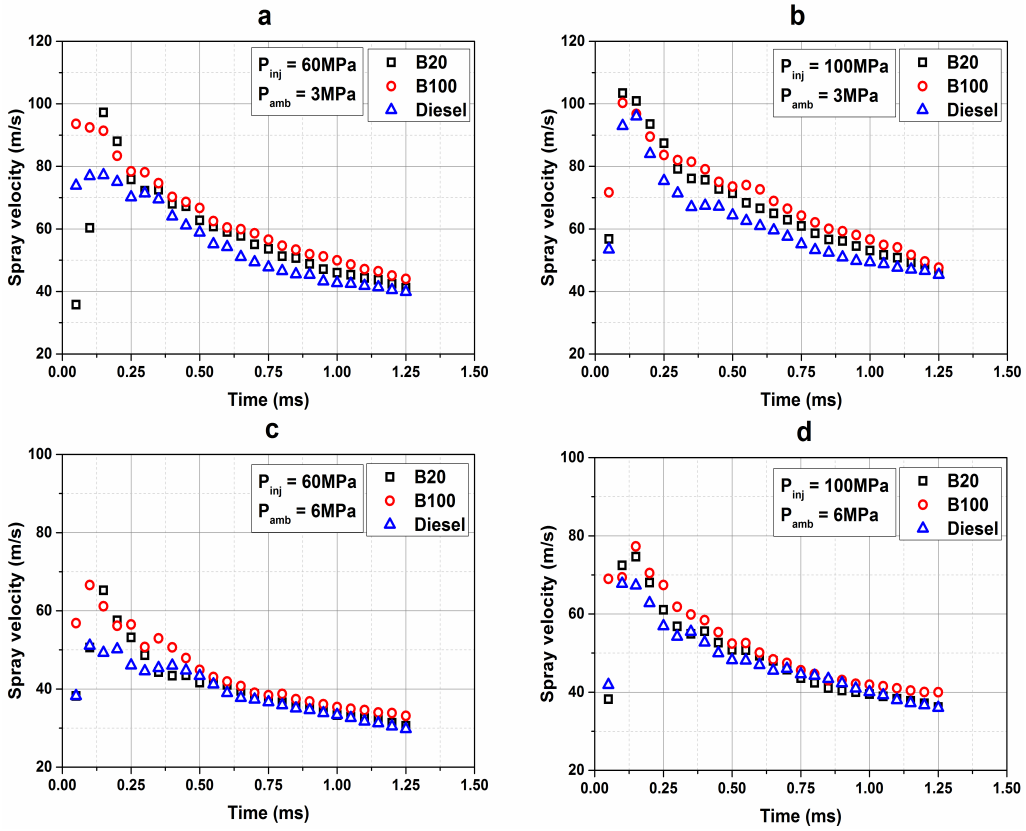

Figure 3.28: Spray velocity for different fuels

The spray velocity for different fuels is shown in Fig.3.28. The spray velocity was calculated as the rate of spray tip penetration between two successive spray images. It can be observed that the spray velocity decreases quickly over time for all the injection pressures. The peak spray velocity is higher with 100MPa injection pressure than that at 60MPa due to the high kinetic energy involved. It should also be noted that the spray velocity is comparatively lower under high ambient conditions regardless of injection pressure. This is because of the high resistance to the spray evolution from the high gas density environment. Also it was observed that the spray velocity of B100 is higher compared to those of B20 and diesel fuels, which indicates that B100 is a more penetrative fuel.

The spray angle comparison between diesel, B20 and B100 fuels are shown in Fig.3.29. It can be noted that the spray angle of B20 and diesel are almost the same and B100 has smaller spray angle at all conditions. The smaller spray angle of B100 may be due to its viscosity and higher momentum as explained earlier. It

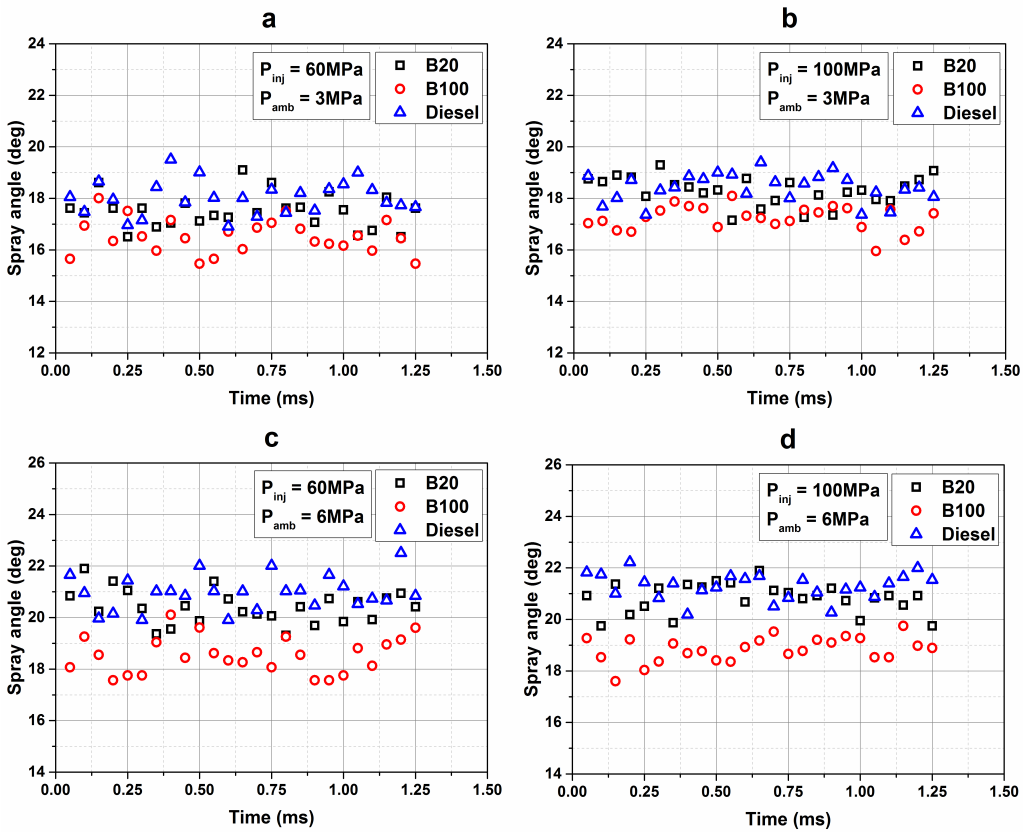

Figure 3.29: Spray angle for different fuels

is also interesting to note that the spray angle is almost insensitive to the injection pressure, while the ambient pressure has a substantial effect on the spray angle. At high ambient pressure, the fuel spray is subjected to high resistance which impedes its axial development leading to wide spray angle.

3.4.2.3 Air entrainment analysis

Fig.3.30 shows the spray volume comparison between diesel, B20 and B100 fuels. The spray volume gives some insight into the quality of fuel air mixing. The spray volume was plotted against spray tip penetration to avoid the influence of injection timing on volume. The spray volumes of diesel and B20 are almost the same under all conditions of injection pressure and ambient pressures. However, with B100 spray volume is smaller, which may be because of the smaller spray angle with the B100 fuel as a result of its higher viscosity. This shows that the fuel air mixing of B20 is in par with that of diesel fuel and it is poor for B100 fuel.

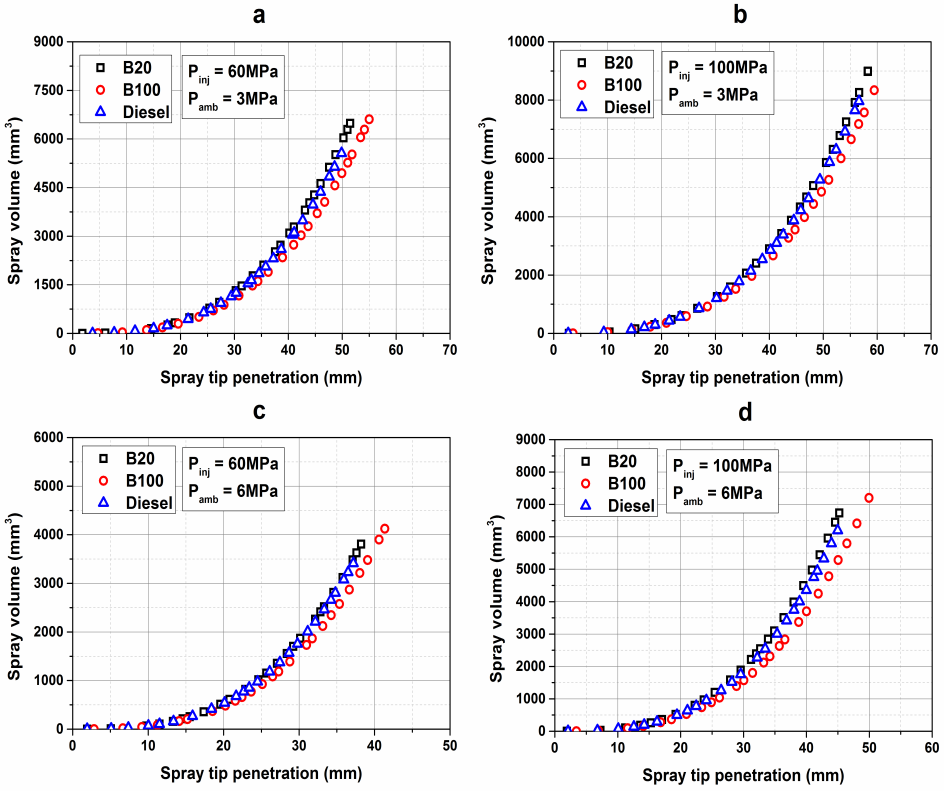

Figure 3.30: Spray volume for different fuels

The mass of air entrained for different fuel sprays is shown in Fig.3.31. The mass of air entrained within the fuel spray also shows the same trend as that of the spray volume. The mass of air entrained within B100 fuel spray is low compared to those for diesel and B20 sprays. This is also because of the narrow spray angle produced by the B100 sprays. It is also interesting to find that this correlation also shows that both diesel and B20 fuel sprays have almost same mass of air entrained within their sprays under all injection pressure and ambient conditions. This can be interpreted that the B20 and diesel shows same level of air entrainment within their sprays.

The equivalence ratio at the leading edge of the spray is shown in Fig.3.32. The equivalence ratio irrespective of injection and ambient pressure shows a decreasing trend with spray tip penetration. This means downstream of the spray, the air-fuel mixture becomes lean indicating an oxidizer-rich environment. It is also very interesting to note that unlike fuel volume and amount of air entrain-

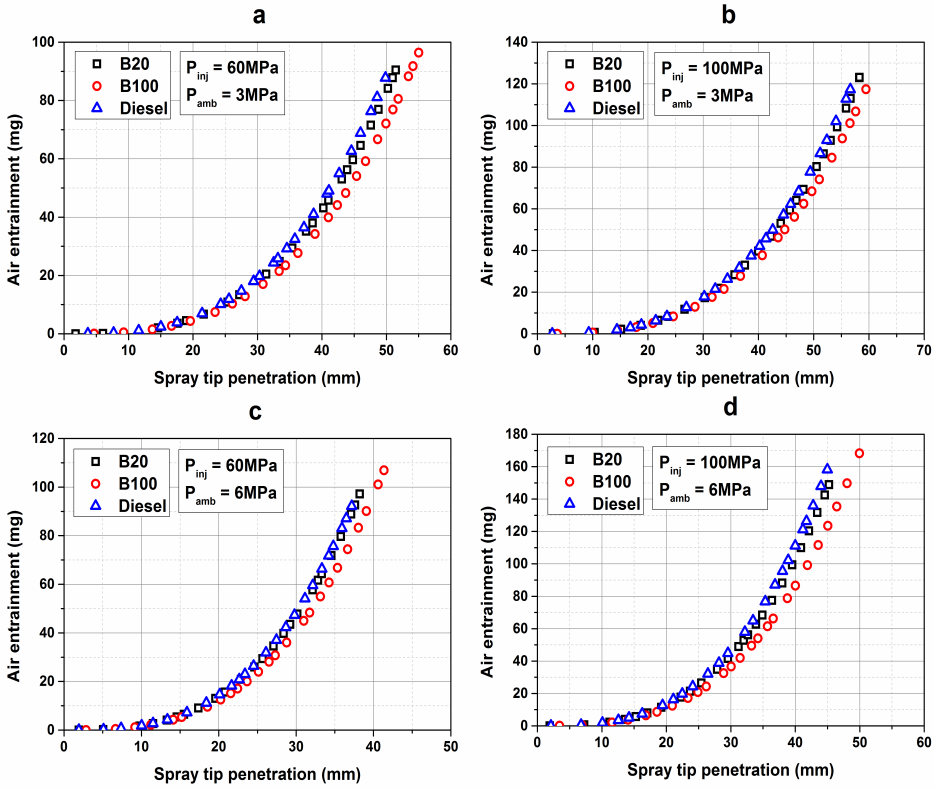

Figure 3.31: Mass of air entrained within different fuel sprays

ment results, equivalence ratio shows that B100 and B20 have almost the same equivalence ratio that is slightly lower than that of diesel fuel. This is because of that fact that biodiesel fuels have oxygen inherent in its chemical structure which has lower stoichiometric air-fuel ratio compared to diesel fuel. Because equivalence ratio as shown in its equation depends on the stoichiometric air-fuel ratio, B100 has low equivalence ratio. In case of B20 though compared to B100, has lesser oxygen content within it, also shows equivalence ratio on par with B100. This may be because of wider spray angle due to enhanced air-fuel mixing. However, diesel fuel with wider spray angle under all conditions compared to B20 and B100 shows high equivalence ratio due to its high stoichiometric air-fuel ratio. It should also be noted that the equivalence ratio is reduced with an increase in ambient pressure, which may be also due to wider spray angle observed on increasing ambient pressures.

The air entrainment analysis gives some insightful explanation on the combus-

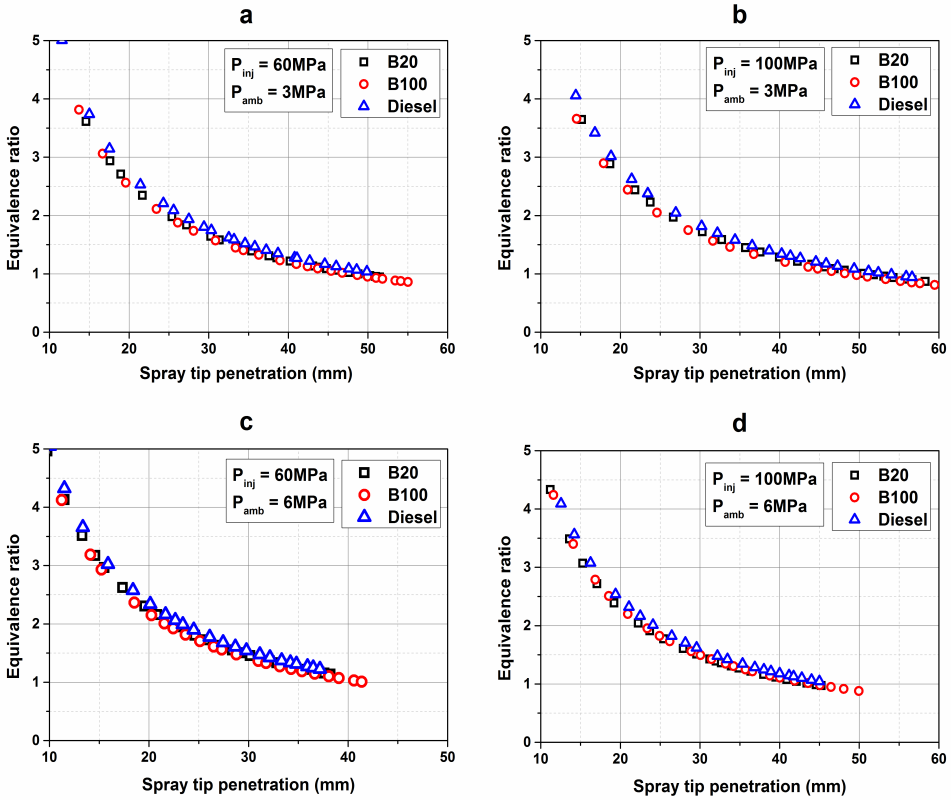

Figure 3.32: Equivalence ratio along axial direction

tion of biodiesel and its blend fuels. Though, from the results, diesel and B20 sprays show almost same level of air-fuel mixing under different injection pressure and ambient pressure conditions, but due to the slightly lower calorific value of B20 compared to diesel fuel gives marginally lower performance as reported by many researchers [45, 87, 160]. B100 fuel shows comparatively poor atomization compared to B20 and diesel fuels. However the presence of inherent oxygen in its chemical structure improves its equivalence ratio downstream the fuel spray at par with B20 and diesel. This may result in lower PM emissions as reported by researchers through quantifying its performance and emission characteristics on engines [161, 87, 160, 162].

3.5 Summary

This chapter focused at development of constant volume spray chamber to visualize the spray development process and study macroscopic characteristics of diesel, biodiesel and blend fuels at higher ambient density and injection pressure. The following observations can be drawn from the results obtained

- Spray momentum flux increases as injection pressure increases and decreases as ambient density increases. However, the momentum coefficient remains almost constant irrespective of injection pressure and ambient density variations as far as cavitation occurs inside the nozzle holes. The results shows that cavitation is also a significant factor in spray atomization which should be eventually taken into account during modeling the atomization process.

- Spray tip penetration and spray velocity of diesel fuel increases with increase in injection pressure and decreases with ambient density, but spray cone angle is constant with injection pressure and increases with increasing ambient density.

- In general, fuel air mixing is better at higher injection pressure. For same spray tip penetration, fuel air mixing is better at higher ambient density due to bigger spray angle.

- Spray shapes of different fuels show change in orientation. This phenomenon is due to the different levels of cavitation inside the injector nozzle holes for B20, B100 and diesel fuels and resistance offered to the spray development by high ambient pressures.

- B100 gives longer spray tip penetration and higher spray velocity compared to B20 and diesel fuels. B20 and diesel fuel showed smaller difference in penetration and velocity under high ambient pressure.

- B100 showed narrow spray angles than B20 and diesel. The spray angles are

unaffected by injection pressure, but increasing ambient pressure showed significant increase in spray angles of all fuels.

- Spray volume and mass of air entrained within the spray showed that B100 has poor air-fuel mixing compared to B20 and diesel fuels. This was due to narrow spray angles and high penetration possessed by B100 fuel.

- The equivalence ratio of B100 was comparatively lower indicating a leaner mixture followed by those of B20 and diesel fuel. This indicates the reason for lower PM and smoke emissions when using B100 and B20 fuels, viz the inherent oxygen content present in biodiesel structure. Diesel fuel showed a higher equivalence ratio due to its high stoichiometric air-fuel ratio.

In this chapter, the spray characteristics of different fuels have been studied in detail and it was found that cavitation inception inside the injector nozzle holes plays a significant role in the primary atomization of fuel spray. Therefore, the phenomenon of cavitation and its effect on primary atomization should be well understood to better perceive the underlying physics of the spray development process and use the undertanding in developing a better spray model for compression engine applications.

4

Cavitation Modeling[1]

4.1 Introduction

One of the important methods in reducing the exhaust emissions from compression ignition engines at source is by improving the spray break up and introducing smaller droplets inside the combustion chamber. According to Arcoumanis et al. [163] , the primary break up of liquid jets at the nozzle exit can be caused by a combination of three mechanisms : turbulence within the liquid phase, implosion of cavitation bubbles and aerodynamic forces acting on the liquid jet. The flow inside

[1]Excerpts of this chapter, in part, is a reprint of previous publication titled "*Cavitation in Injector Nozzle Holes - A Parametric Study*", Engineering Applications of Computational Fluid Mechanics 8 (1), 70-81, 2014. DOI: 10.1080/19942060.2014.11015498. and "*Macroscopic spray characterization under high ambient density conditions*", Experimental Thermal and Fluid Science 59, 109-117, 2014. DOI: 10.1016/j.expthermflusci.2014.08.003.

the fuel injector nozzle has significant effects on the spray formation. Cavitation occurs if the local pressure drops below the vapor pressure of the liquid at local temperature. With the high pressure drop across the injection nozzle, the liquid tends to accelerate within the small nozzle holes. This acceleration of liquid inside the nozzle generates a high level of turbulence, which has an instability effect on the jet leaving the nozzle exit. At the sharp edges inside the nozzle holes, for example at the inlet of the nozzle hole, the streamlines converge with the effective cross section of the flow, leading to accelerated velocity of the liquid. According to the Bernoulli principle, this causes a reduction in the local static pressure, which it can reach a value as low as the vapor pressure of the liquid. This phenomenon is schematically shown in Fig.4.1 (redrawn from [164]), where the theoretical (linear) pressure distribution inside the nozzle hole is compared to a more realistic distribution along a streamline. Cavitation bubbles are formed inside the nozzle hole because of the cavitation phenomena. These cavitation bubbles are swept out of the nozzle into the combustion chamber. As the bubbles are introduced into combustion chamber pressure, they implode and contribute to further break up of the spray [164]. This leads to finer droplets of fuel which aids in faster evaporation of fuel. Thus, understanding the phenomenon of cavitation inside the nozzle holes is very important for the study of spray behavior and its break up theory.

Takenaka et al. [165] studied experimentally the nucleation process of the cavitation using neutron radiography and reported the formation of vapor bubbles in the nozzle hole. Inamura et al. [166] reported that as the back pressure increases, the cavitation is not observed for the same injection pressure. Many previous research works have also shown that cavitation inside the nozzle hole affects the spray characteristics [167, 168, 169, 170]. The very first experimental attempt to understand the effect of cavitation in fuel injector nozzles on spray breakup was done by Bergwerk [171]. He found that cavitation inside the real sized nozzles influence the fuel jet. Then these findings were further supported by an extensive

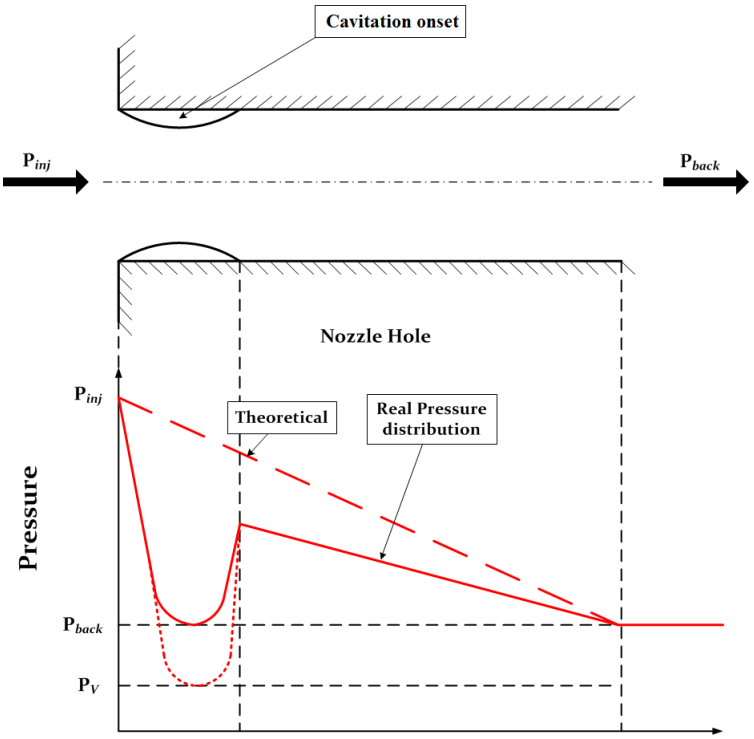

Figure 4.1: Schematic illustration of cavitation formation inside the nozzle hole (Redrawn from [164])

study of nozzle flows done by Reitz and Bracco (1982). One of the pioneering works on the effect of cavitation on spray evolution was done by Chaves et al. [172], and they reported that the spray angle increases with cavitation inception. Arcoumanis et al. [173, 174] studied the cavitation and observed that it did not scale up, and therefore real size experiments were needed to study actual cavitating flow behavior. Subsequent studies employed real size nozzle orifices. Badock et al. [175] showed experimentally that increasing the conicity and radius of curvature at the nozzle inlet could reduce cavitation. Desantes et al. [176] also reported that the cone angle of the fuel spray was found to be increased due to the formation of vapor inside the nozzle. Payri et al. [177, 153] also reported that the spray cone angle and outlet speed increases with the cavitation, and then investigated the spray momentum measurements in order to explain the effects of nozzle geometry. Suh et al. [178] also studied experimentally and reported that cavitation enhanced the fuel spray characteristics and the primary fuel breakup due to the turbulence created inside the nozzle. Many experimental studies have been conducted to

show that the occurrence of cavitation inside the nozzle makes substantial contribution to the break-up of the exiting liquid jet [179, 180, 181, 182, 183, 178, 184]. Thus, understanding the phenomenon of cavitation inside the nozzle holes is very important for the study of spray behavior and its break up theory.

Recently, bio-diesel fuels promise clean, alternative and renewable source of energy. Bio-diesels have a number of properties that make it an excellent alternative fuel for diesel engines, particularly because of its low emissions compared with the diesel fuel [44, 43]. Moreover, the distinct properties of biodiesel may influence the cavitation phenomenon in the nozzle hole. Thus analysis of flow cavitation for bio-diesel is of great interest.

In this chapter, the numerical simulation results of cavitation phenomena in nozzle spray holes are reported. The computations involve the use of the Schnerr and Sauer two phase and k-ϵ turbulence models. The commercial computational fluid dynamics (CFD) software Fluent 12.1 is used for the computations. The numerical results were validated against the experimental results of Winklhofer et al. [185] for U throttle geometry and a good qualitative and quantitative agreement was observed. Then parametric study which includes the effect of injection pressure (15-125 MPa) under constant back pressure of 10 MPa, transient behavior under high injection pressure of 100 MPa, and different geometries on cavitation phenomenon was carried out for diesel and SME bio-diesel. Finally, conclusions were drawn based on the results presented.

4.2 Numerical Method

The finite volume based CFD software Fluent 12.1 was used to perform the numerical simulation of the flow inside the nozzle hole. The nozzle flow is considered to be isothermal. Cavitation model proposed by Schnerr and Sauer was used in this simulation. This two-phase model considers a mixture comprising liquid fuel and vapor. The mixture is modeled as incompressible. In addition, a no-slip condition

between the liquid and vapor phase is assumed. Then the mixture properties are computed using the Reynolds-averaged continuity and momentum equations

$$\frac{\partial u_j}{\partial x_j} = 0 \tag{4.1}$$

$$\rho \frac{\partial u_i u_j}{\partial x_j} = -\frac{\partial P}{\partial x_i} + \frac{\partial \tau_{ij}}{\partial x_i} \tag{4.2}$$

where

$$\tau_{ij} = (\mu + \mu_t) \left\{ \frac{\partial u_i}{\partial x_j} + \frac{\partial u_j}{\partial x_i} \right\} \tag{4.3}$$

and

$$\mu_t = C_\mu \rho \left(\frac{k^2}{\epsilon} \right) \tag{4.4}$$

where μ is viscosity and μ_t is the turbulent viscosity.

According to Margot et al. [186] and Andriotis et al. [187], there is no maximum difference with different turbulence models in predicting cavitation inception and Andriotis et al. [187] suggested the use of the standard turbulence model. Hence in order to account for the large pressure gradients, the standard turbulence model is incorporated along with the non equilibrium wall functions given by

$$\rho \frac{\partial u_j k}{\partial x_j} = -\tau_{ij} \frac{\partial u_i}{\partial x_j} - \rho\epsilon + \frac{\partial}{\partial x_j} \left[\left(\mu + \frac{\mu_t}{\sigma_k} \right) \frac{\partial k}{\partial x_j} \right] \tag{4.5}$$

$$\rho \frac{\partial u_j \epsilon}{\partial x_j} = -C_{\epsilon 1} \tau_{ij} \frac{\partial u_i}{\partial x_j} \frac{\epsilon}{k} - C_{\epsilon 2} \rho \frac{\epsilon^2}{k} + \frac{\partial}{\partial x_j} \left[\left(\mu + \frac{\mu_t}{\sigma_\epsilon} \right) \frac{\partial \epsilon}{\partial x_j} \right] \tag{4.6}$$

The following values were used for $k - \epsilon$ turbulence model

$$C_\mu = 0.09 \qquad C_{\epsilon 1} = 1.44 \qquad C_{\epsilon 2} = 1.92 \qquad \sigma_k = 1.0 \qquad \sigma_\epsilon = 1.30$$

where C_μ, $C_{\epsilon 1}$, $C_{\epsilon 2}$, σ_k, σ_ϵ are constants of turbulence model

The turbulent viscosity is modeled for the whole mixture.

According to Schnerr and Sauer [188, 189, 190], the equation for the vapor volume fraction is given by the general form

$$\frac{\partial(\alpha\rho_v)}{\partial t} + \frac{\partial u_j \alpha}{\partial x_j} = \frac{\rho_v \rho_l}{\rho}\frac{D\alpha}{Dt} \tag{4.7}$$

where α is the vapor volume fraction, ρ_v is the vapor density, ρ_l is the liquid density, ρ is the mixture density, and $\vec{V}$ is the mixture velocity. The net mass source term R is given by

$$R = \frac{\rho_v \rho_l}{\rho}\frac{d\alpha}{dt} \tag{4.8}$$

Schnerr and Sauer used the following expression to connect the vapor volume fraction (α) to the number of bubbles per volume of liquid

$$\alpha = \frac{n_B \frac{4}{3}\pi \Re_B^3}{1 + n_B \frac{4}{3}\pi \Re_B^3} \tag{4.9}$$

where n_B is the number of bubbles and $\Re_B$ is the bubble radius.

According to the Rayleigh-Plesset equation, the bubble dynamics equation can be simplified as

$$\frac{D\Re_B}{Dt} = \sqrt{\frac{2}{3}\frac{P_v - P}{\rho_l}} \tag{4.10}$$

where P_v is the vapor pressure and P is the ambient cell pressure.

The expression of the net mass transfer combining Eqns.4.8, 4.9 and 4.10

$$R = \frac{\rho_v \rho_l}{\rho}\alpha(1-\alpha)\frac{3}{\Re_B}\sqrt{\frac{2}{3}\frac{(P_v - P)}{\rho_l}} \tag{4.11}$$

where the bubble radius $\Re_B$ from Eq.2.2 is given by

$$\Re_B = \left(\frac{\alpha}{1-\alpha} \frac{3}{4\pi} \frac{1}{n_B} \right)^{\frac{1}{3}} \tag{4.12}$$

The mass transfer rate R in the Schnerr and Sauer model is proportional to $\alpha(1-\alpha)$. The function $f(\alpha_v, \rho_v, \rho_l) = \frac{\rho_v \rho_l}{\rho} \alpha(1-\alpha)$ approaches zero when $\alpha = 0$ and $\alpha = 1$, and reaches the maximum in between. If no bubbles are created or destroyed, the bubble number density would be constant. The final form of the model is given as

$$R_e = \frac{\rho_v \rho_l}{\rho} \alpha(1-\alpha) \frac{3}{\Re_B} \sqrt{\frac{2}{3} \frac{|P_v - P|}{\rho_l}} \tag{4.13}$$

4.2.1 Constitutive relations

Numerical simulations were carried out to study the effect of the cavitation on mass flow rate $\dot{m}$. The mass flow rate $\dot{m}$ is given by

$$\dot{m} = A_{th} C_a \sqrt{2\rho(P_{inj} - P_v)} \tag{4.14}$$

where C_a is the coefficient of contraction given by

$$C_a = C_D \sqrt{\frac{P_{inj} - P_v}{\triangle P}} \tag{4.15}$$

where C_D is the coefficient of discharge defined as

$$C_D = \sqrt{\frac{\frac{1}{2}\rho \bar{V}^2}{\triangle P}} \tag{4.16}$$

A non - dimensional number, cavitation parameter K is defined as

$$K = \frac{P_{inj} - P_v}{\triangle P} \tag{4.17}$$

and the pressure difference $\triangle P$ is given by

$$\triangle P = P_{inj} - P_{amb} \tag{4.18}$$

The other non-dimensional numbers used in the discussion are Reynolds number (Re) and Weber number (We) given as

$$Re = \frac{\rho \bar{V} D_H}{\mu} \tag{4.19}$$

$$We = \frac{\rho \bar{V}^2 D_H}{\sigma} \tag{4.20}$$

where $\bar{V}$ is the average mixture outlet velocity, A_{th} is the theoretical cross sectional area, ρ is the mixture density, P_{inj} is the injection pressure, P_{amb} is the ambient pressure or the ambient pressure and P_v is the vapor pressure of the fluid, μ is the dynamic viscosity, σ is the surface tension of the fuel bubbles and D_H is the hydraulic diameter of the nozzle hole.

The level of turbulence at the nozzle exit is calculated by an initial amplitude parameter as defined by Li et al. [191] and Som et al. [192] . It is defined as

$$A_0 = \frac{2}{5 D_H \omega_0} \sqrt{\frac{2}{3} K_{avg}} \tag{4.21}$$

where, K_{avg} is the average kinetic energy calculated from the simulations and ω_0 is the initial droplet oscillation frequency [193] given by

$$\omega_0 = \sqrt{\frac{64\sigma}{\rho D_H^3} - \left(\frac{10\mu}{\rho D_H^2}\right)^2} \tag{4.22}$$

4.2.2 Physical model

The physical model used in the simulation was a thin slice model of the U-throttle geometry used by Winklhofer et al. [185]. As the geometry was axi-symmetric, only one half of the geometry was considered for the simulations. The dimensions of the U-throttle nozzle were $300 * 301 \mu m$ at the throat, $300 * 284 \mu m$ at the outlet

and the length of the nozzle was $1000\mu m$. Because of the computational time limitations, the current study dealt with a thin slice of $20\mu m$ in z axis as shown in Fig.4.2.

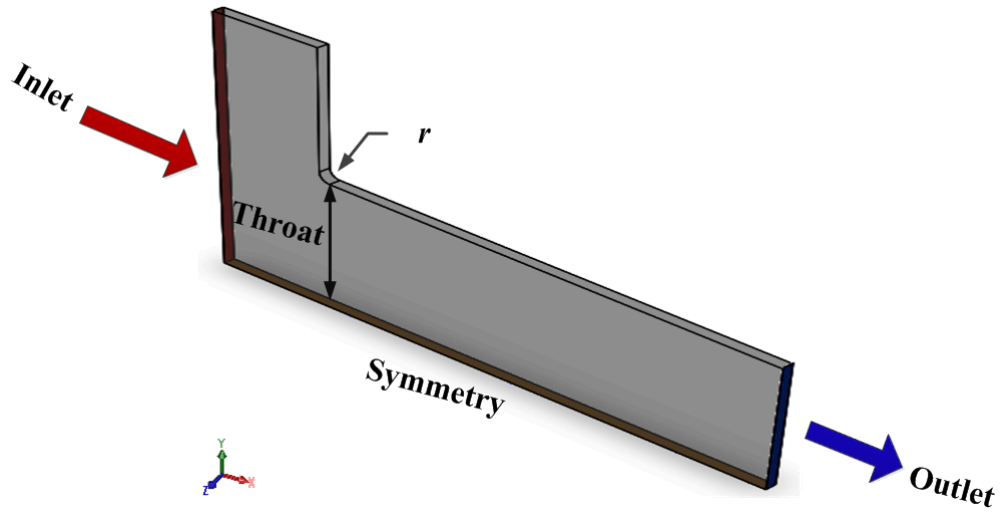

Figure 4.2: Schematic representation of the problem

4.2.3 Boundary conditions

The boundary conditions for the flow inside the injector nozzle were defined as follows

Inlet The fuel was introduced into the inlet. The boundary condition for the inlet was set as pressure inlet.

$$P = P_{inj}$$

For fluctuating injection pressure a user defined function was written in C program.

Outlet The outlet boundary condition was also set as pressure outlet.

$$P = P_{amb}$$

Axis The axis of the nozzle was defined as axis boundary condition.

Wall The no-slip boundary condition was set at the walls of the nozzles.

$$\bar{V} = 0$$

The same boundary conditions were considered for the transient simulation at time $t = 0s$.

4.2.4 Numerical approach

The model geometry was meshed using the pre-processor of Fluent, GAMBIT 2.3.16. The Semi Implicit Pressure Linked Equation-Consistent (SIMPLE-C) algorithm was used for pressure-velocity coupling, and second order upwind differencing scheme was used for the discretization. The under-relaxation factors were carefully adjusted to ensure convergence of the solution. The residues for convergence criteria were kept below 10^{-5}. The mesh independence study was done for 2D case of the same geometry. The three different mesh sizes of 6285, 15170 and 34085 cells were used in the simulation and the mass flow rate was compared to ensure grid independent solution. It was found that mesh sizes of 15170 cells and 34085 cells gave results of 3.75% deviation whereas the results from the mesh size of 6285 cells gave about 6.25% deviation as compared to the experimental result for a pressure difference of 6 MPa. The comparison of the results is shown in Table 4.1. Therefore, for thin slice of the same geometry, the mesh size of 112380 cells with an average cell size of $0.03 - 0.04\mu m$ was used. A fine structured mesh was used throughout the domain to capture the large pressure and velocity gradients related to the inception of cavitation (Fig.4.3).

Table 4.1: Grid independence check

No. of cells	Mass flow rate (g/s) at $\triangle P = 6MPa$	
	Numerical	Experimental [185]
6285	7.66	
15170	7.48	7.41
34085	7.48	

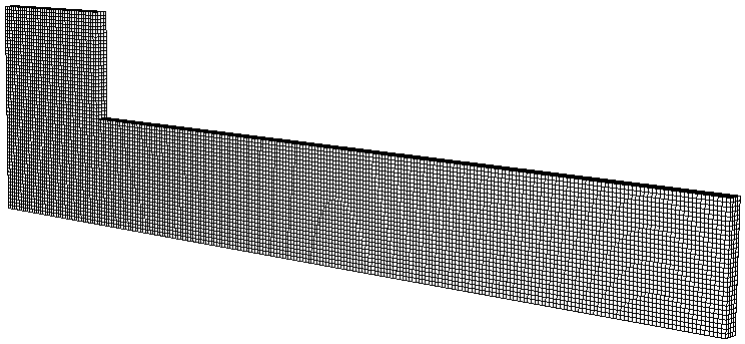

Figure 4.3: Mesh used for simulation

4.3 Results and Discussion

4.3.1 Validation

The simulation results were compared with the Winklhofer et al experimental results [185] for model validation. As in the experiments, the injection pressure P_{inj} was kept constant at 10 MPa and the back pressure P_{amb} was varied from 1.5 to 8MPa for the simulations and corresponding mass flow rates $\dot{m}$ were calculated for diesel as the working fluid. The properties of diesel fuel [194, 195] used in the simulation are shown in Table 4.2.

Table 4.2: Fuel properties used

Properties	Diesel		SME - Bio-diesel	
	Liquid	Vapor	Liquid	Vapor
Density ($^{kg}/_{m^3}$)	832	0.1361	870	8.5
Dynamic viscosity ($^{kg}/_{ms}$)	$2.1 * 10^{-3}$	$5.953 * 10^{-6}$	$3.9 * 10^{-3}$	10^{-5}
Vapor pressure @ 30^0 C (Pa)	2000		1	

Fig.4.4 shows the comparison of the numerical results with the experimental results. The mass flow rate was calculated using Eq.4.14 from the results obtained through the numerical simulations. The difference between the predicted and experimental values is less than 5%. The simulation predicts the start of cavitation at par with the experiment. The start of cavitation occurs at the pressure difference of 6 MPa.

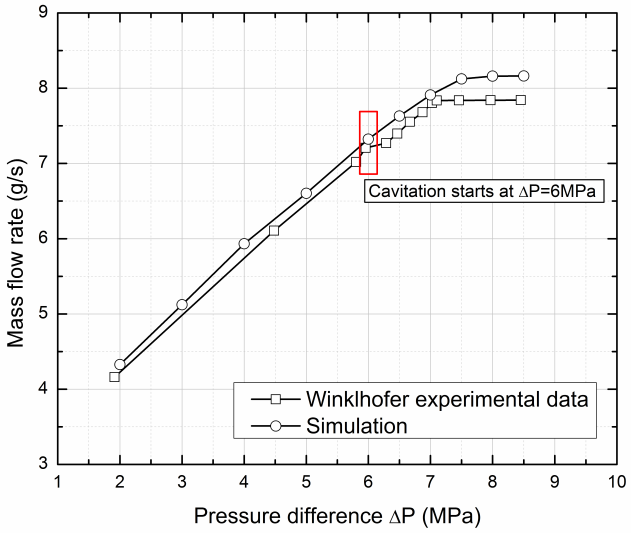

Figure 4.4: Experiment vs Simulation results

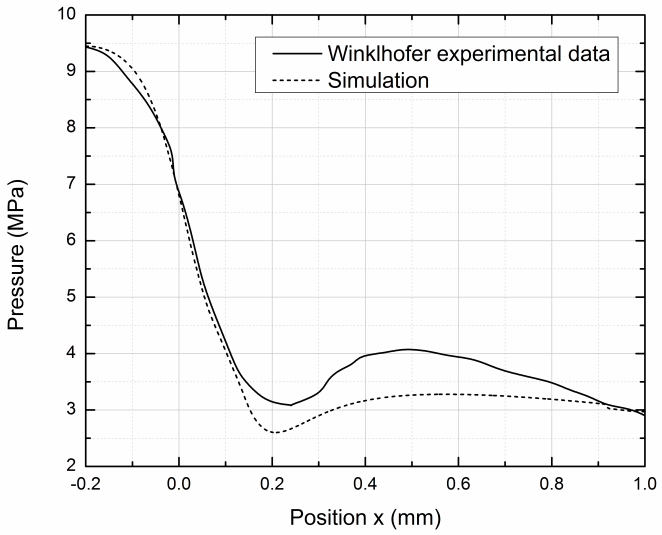

Figure 4.5: Pressure distribution along axial direction

Fig.4.5 illustrates the pressure distribution along the symmetry line compared with the experiment for pressure difference of 7 MPa. The pressure distribution is in good agreement with that expected from the theory as explained earlier when discussing Fig.4.1 and we observed a good qualitative agreement between the simulation and the experimental results. The validation was also done with the velocity profile in the throttle entrance regime which should obviously be affected by the

flow separation and the presence of gas between the fluid and the channel wall. The experimental and simulation results were compared for condition without cavitation ($\Delta P = 5.5MPa$) and with cavitation ($\Delta P = 6.7MPa$) at a position $53\mu m$ inside the throttle hole in x-direction (see Fig.4.6). The simulation show a good agreement with the experimental data.

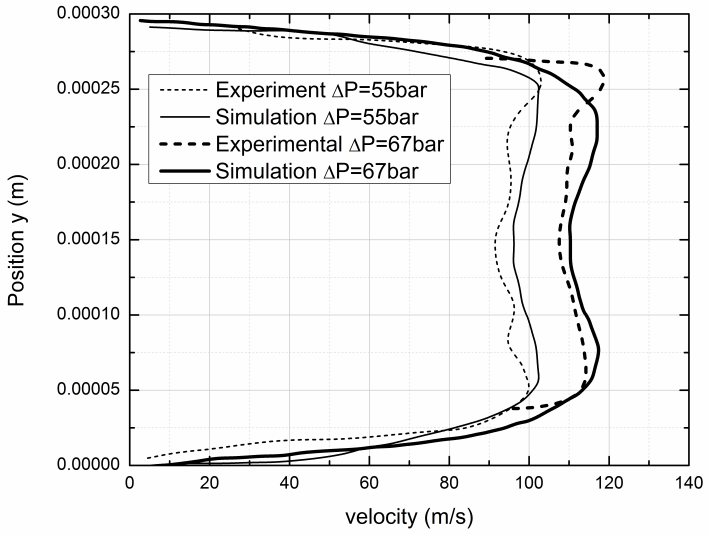

Figure 4.6: Velocity Profiles at distance 53μm inside throttle hole in x direction

Fig.4.7 shows the liquid fraction and pressure contours at ΔP = 7MPa. This pressure difference is chosen because it is the experimental critical pressure difference above which the mass flow becomes choked. From Fig.4.7, it is clear that the cavitation appears in the nozzle hole entrance due to abrupt change of the flow direction associated with large pressure drop (evident from pressure contours) and very high fuel velocity. With decreasing back pressure or increasing pressure difference, the cavitation expands up to the exit with major volume fraction of vapor at the upper and lower part of the nozzle. This observation was also made by other researchers [186, 188, 192, 189].

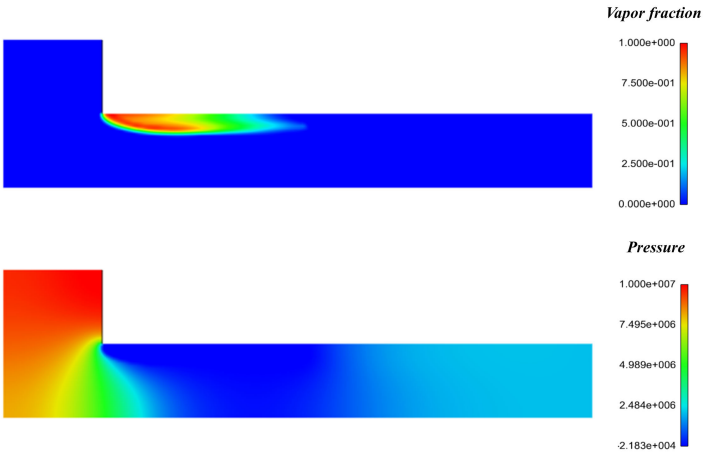

Figure 4.7: Liquid fraction and pressure contours at $\Delta P = 7MPa$

4.3.2 Effect of injection pressure on cavitation

To study the effect of injection pressure on the cavitation, the back pressure was kept constant at 10 MPa, a typical compression pressure inside the turbocharged engines. The injection pressure was varied from $15 - 125$ MPa, typical injection pressure range for common rail fuel injection system. The effect of injection pressure was studied for both diesel and SME bio-diesel. The properties for SME - bio-diesel [195, 196, 197, 198, 199] used for the simulation are shown in Table 4.2.

The effect of injection pressure on cavitation was measured in terms of cavitation parameter k and coefficient of discharge. The coefficient of discharge increases with cavitation parameter and then becomes constant as shown in Fig.4.8. The region up to which the coefficient of discharge increases with the cavitation parameter is termed as cavitating region and the region where the coefficient of discharge reaches steady state is termed as non-cavitating region. In the cavitating region, the cavitation gets enhanced whereas in the non-cavitating region, the cavitation phenomenon does not occur. The cavitation occurs inside the nozzle below the cavitation parameter of 1.7 for this geometry. From Fig.4.8, it is also evident that the coefficient of discharge for bio-diesel is higher compared with the diesel. Also from the simulation it was noted that the vapor volume fraction for bio-diesel was lesser compared to diesel. These two factors shows that the cavitation is less

pronounced in bio-diesel.

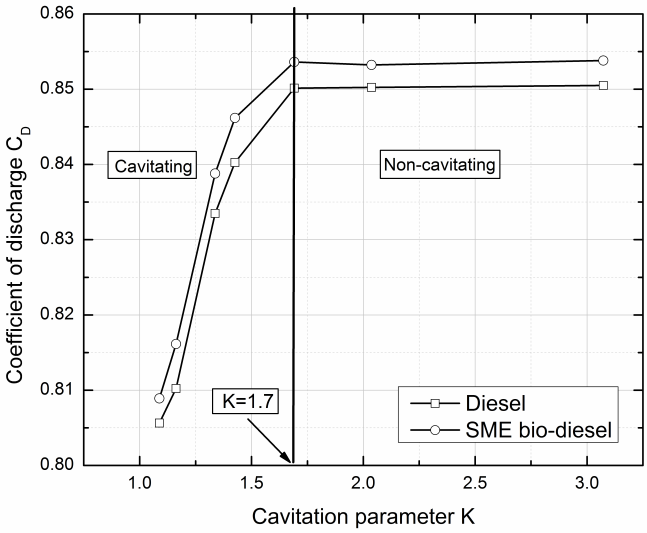

Figure 4.8: Effect of coefficient of discharge with cavitation parameter for constant $P_{back} = 10MPa$

The mass flow rate for varying injection pressure for both diesel and SME bio-diesel is shown in Fig.4.9. The mass flow rates of both the diesel and bio-diesel fuel are almost the same from 15 to 25 MPa as there is no cavitation taking place with both the fuels under this pressure range. From 25 MPa, the mass flow rate of bio-diesel is slightly higher than that of the diesel. This is because of the higher viscosity and lower saturation pressure. The less viscous diesel fuel has higher Reynolds number which results in stronger cavitation in the nozzle. This shows that reduction in viscosity causes higher cavitation in the nozzle. These results confirm that Reynolds number is an important parameter for cavitating flow. The results obtained are consistent with those of Shi and Arafin [158]. However, the start of cavitation phenomenon occurs at the same injection pressure for both diesel and bio-diesel fuels. This is because of the sharp pressure gradient at the entry of the nozzle for both the fuels which leads to start of cavitation at injection pressure of 25 MPa or at cavitation parameter of 1.7 for this geometry. This shows that the bio-diesel inhibits the cavitation phenomenon compared to diesel. According to Payri et al. [157] the cavitation increases spray cone angle, hence a

small cone angle is expected for bio-diesel which may result in less effective air – fuel mixing and a poor combustion process is also expected.

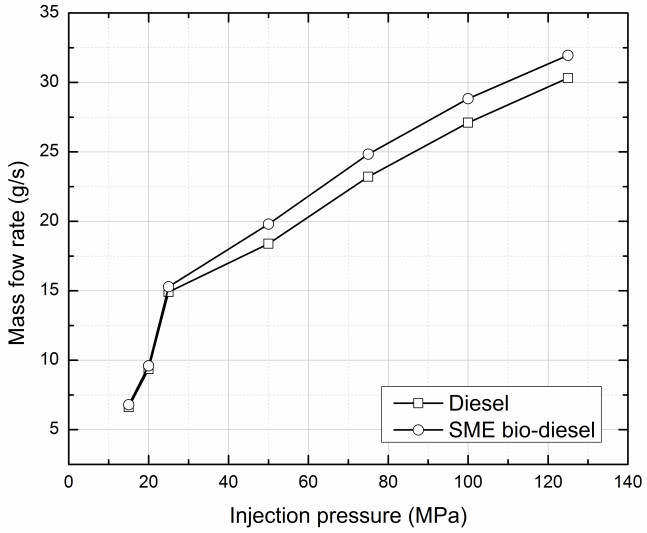

Figure 4.9: Effect of injection pressure on mass flow rate

Fig.4.10 shows the significance of Reynolds number on cavitation phenomenon. Under constant back pressure, the cavitation parameter decreases gradually with increase in the Reynolds number. The cavitation starts at Re=19823.9 for diesel fuel, and at Re=10945.2 for bio-diesel. As the Reynolds number is higher for diesel fuel compared to bio-diesel for the same pressure difference, the diesel fuel suffers stronger cavitation than bio-diesel. From Fig.4.11, for an injection pressure of 25 MPa, the dynamic pressure is higher and absolute pressure is lower than that of the bio-diesel, which clearly infers that the lower viscosity promotes the cavitation. Fig.4.12 shows the effect of Weber number on cavitation. The Weber number shows similar trend as Reynolds number with cavitation parameter. The difference in Weber number for both diesel and bio-diesel is lower for the same cavitation parameter, but its numerical value is very high. As Weber number is a function of surface tension, as shown in Eq.4.20, it can be inferred that surface tension has little or no effect on the cavitation phenomenon.

Fig.4.13 shows that the initial amplitude parameter increases linearly with the

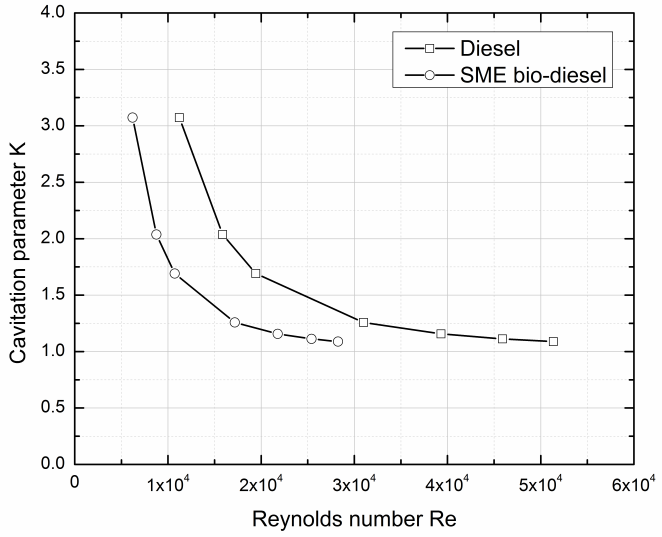

Figure 4.10: Reynolds number vs cavitation parameter

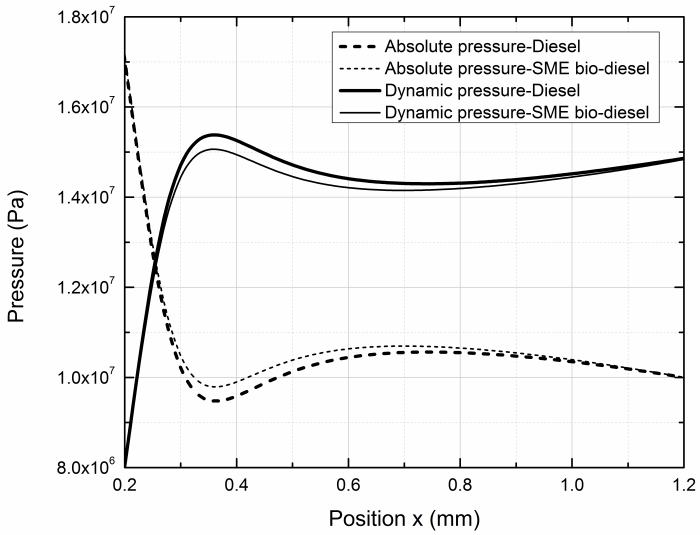

Figure 4.11: Absolute and dynamic pressure comparison for both diesel and biodiesel at injection pressure 25 MPa

injection pressure for both diesel and SME bio-diesel. This interesting result indicates higher turbulence levels at the nozzle exit as the injection pressure increases. These results also suggest that the primary breakup model should account for the effects of cavitation and turbulence in addition to the aerodynamic effect. Although the initial amplitude parameter for SME bio-diesel is lower compared to

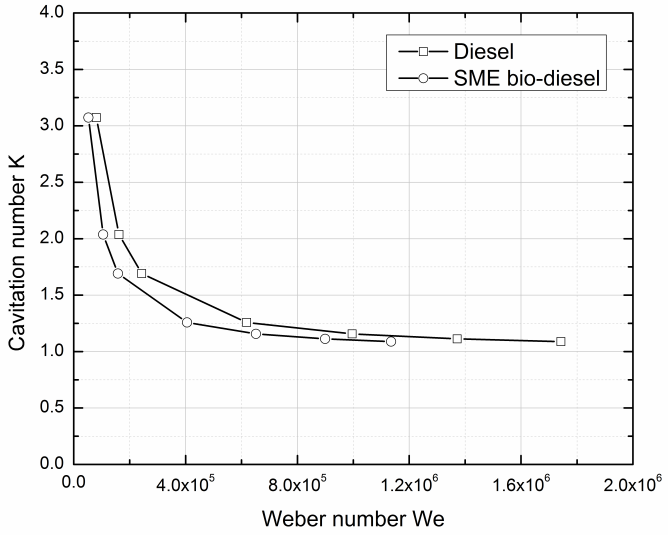

Figure 4.12: Weber number vs cavitation parameter

that for diesel, since cavitation is inhibited in bio-diesel due to higher viscosity and density which implies significantly lower level of turbulence at the nozzle exit compared to diesel. However the effect of cavitation cannot be neglected for both fuels.

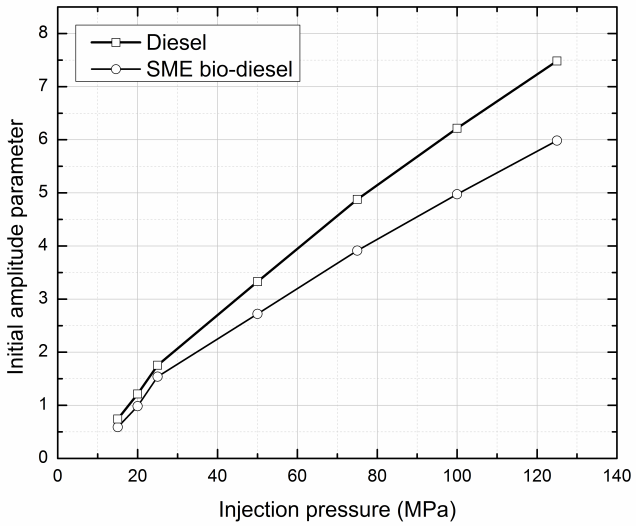

Figure 4.13: Effect of injection on initial amplitude parameter

4.3.3 Transient analysis

The simulation was done for transient conditions to find the progress of cavitation with time. For this simulation, injection pressure of 100 MPa and back pressure of 10 MPa was maintained. The development of cavitation with time for both diesel and bio-diesel is shown in Fig.4.14. The cavitation starts at 4 µs for diesel and 5 µs for bio-diesel, after the flow starts inside the nozzle hole and the cavitation attains steady state at 16 µs for diesel and for bio-diesel after about 17 µs. From Fig.4.14, it is clear that the cavitation in diesel fluid is more pronounced than that in the bio-diesel because of lower density and viscosity for both liquid and vapor state and higher vapor pressure for diesel fuel. Fig.4.15, shows the vapor volume fraction with time, which also confirms that the cavitation in diesel fuel is more pronounced than that in bio-diesel.

Fig.4.16 shows the variation of mass flow rate $\dot{m}$ with time. The mass flow rate of both diesel and bio-diesel follows the same trend. The mass flow rate increases initially, then decreases and attains steady state. The reason for this trend can be explained from the variation of coefficient of contraction, C_a with time. It is evident that the mass flow rate follows the same trend as that of C_a , as the mass flow rate is directly proportional to the C_a for the same injection pressure as per Eq.4.14. The coefficient of contraction increases at start because it is the time taken for the fuel to fill the nozzle hole. Then it decreases up to 16 µs and 17 µs for diesel and bio-diesel respectively as the phenomenon of cavitation reaches the outlet of the nozzle and then it becomes steady and hence the mass flow rate also decreases and becomes steady.

4.3.4 Effect of different geometries on cavitation

The effect of different geometries was studied based on the four geometries chosen as shown in Table 4.3. The geometries were classified based on the inlet diameter D_{in} and K_{factor}. The K_{factor} is the measure of taper and is defined as

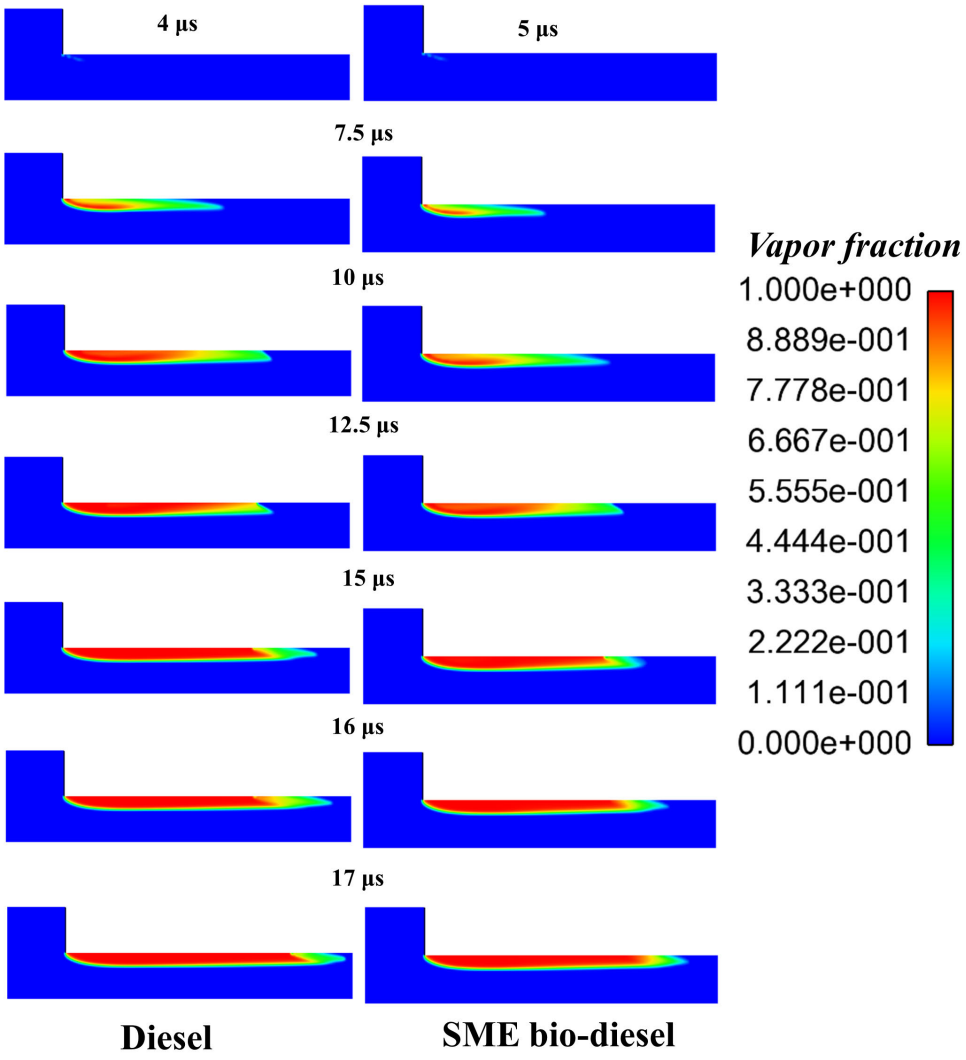

Figure 4.14: Formation of cavitation with time for both diesel and biodiesel

$$K_{factor} = \frac{D_{in} - D_{out}}{10} \tag{4.23}$$

where D_{in} is inlet diameter and D_{out} is outlet diameter in μm. Generally, there are three types of nozzle holes based on K_{factor} - as shown in Fig.4.17 viz. zero K_{factor}, positive K_{factor} and negative K_{factor}. Zero K_{factor} is one with same inlet and exit diameter, positive K_{factor} nozzles has a larger inlet diameter compared to that of exit diameter, a form of convergent nozzle and negative K_{factor} has a smaller inlet diameter than that of exit diameter, a form of divergent nozzle. Usually the former two types are commonly used in commercial diesel injectors, whereas negative K_{factor} nozzles are not used as they are diffusive nozzles, which

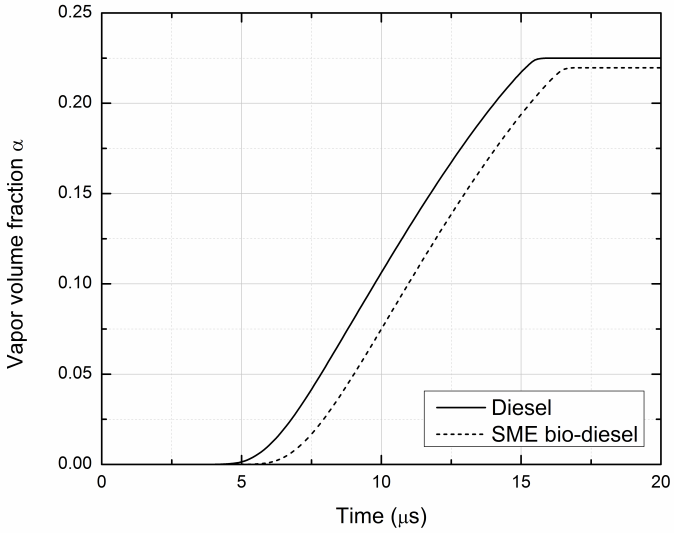

Figure 4.15: Vapor volume fraction

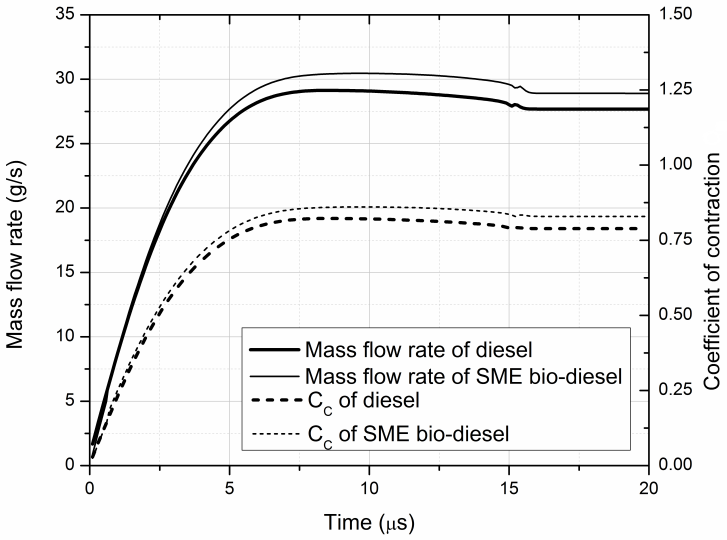

Figure 4.16: Mass flow rate and coefficient of contraction with time

are characterized by lower velocity at the exit, and possibly poor atomization of fuel.

Table 4.3: Different geometries used in simulation

Geometry	D_{in} (μm)	D_{out} (μm)	k_{factor}	r (μm)
1	301	284	1.7	20
2	299	299	0	20
3	316	299	1.7	20
4	175	175	0	20
5	192	175	1.7	20

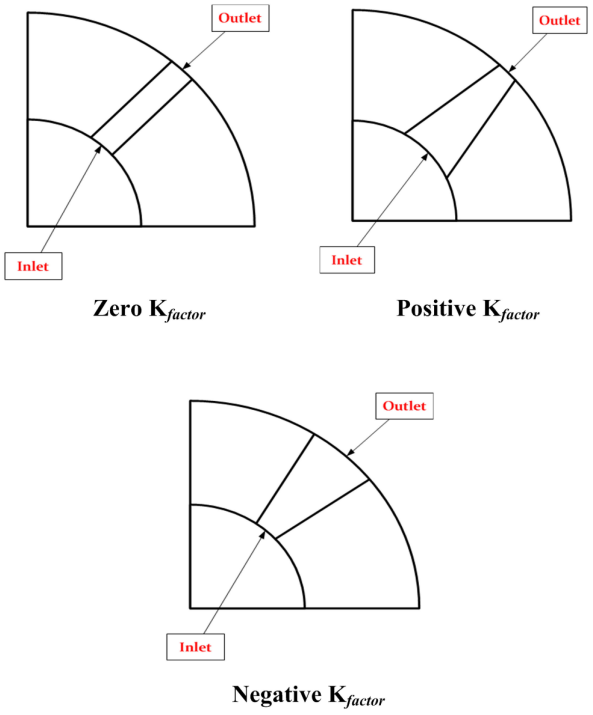

Figure 4.17: Types of K_{factor}

Geometries 1 and 2 were the same as the U and J throttle geometries of Winklhofer et al. [185] respectively. The exit diameters of Geometries 4 and 5 were obtained from 6 holes commercial Denso common rail injector used in Toyota 2KD−FTV engine of capacity 2.5 liters. The exit diameter of the nozzle hole was measured using optical microscope and was found to be around 175±3 μm. Geometries 1 and 2 have the same inlet diameter but different K_{factor}, whereas Geometries 2 and 3 are of same exit diameter but with different K_{factor} values and Geometries 4 and 5 are similar to Geometries 2 and 3 but with overall smaller dimensions.

The numerical simulation was conducted with diesel as working fluid for injection pressure between 15 - 125 MPa and maintaining the back pressure constant at 10 MPa. The effect of K_{factor} , inlet diameter and exit diameter on mass flow rate considering the cavitation phenomenon is shown in Fig.4.18. When the K_{factor} increases while keeping the exit diameter the same, the mass flow rate increases at the exit of the nozzle hole as evident from the results obtained for Geometries 2 and 3. From simulation it was found that vapor volume produced for Geometry 3 is lower than that with Geometry 2. This shows that lower K_{factor} tends to enhance cavitation and hence leads to lesser mass flow rate. However the start of cavitation is unaffected by the K_{factor}. For both Geometries 2 and 3, the cavitation starts at the injection pressure of 25 MPa. For same K_{factor} but with different exit diameter (geometries 1 and 3), the mass flow rate of geometry 3 with higher exit diameter has higher mass flow rate because of higher exit cross sectional area. When both the inlet and exit diameters decrease with the same K_{factor}, the mass flow rate decreases as the nozzle hole diameter decreases. Also the start of cavitation occurs at lesser pressure difference for smaller nozzle diameter. The Geometry 4, in which both inlet and exit diameters are smaller than those of Geometry 2 but with the same K_{factor} , has lower mass flow rate. The cavitation starts early at the pressure difference of 20 MPa for Geometry 4. From the results obtained, it is clear that the mass flow rate increases as K_{factor} increases or as the nozzle contracts. As the diameter decreases, the effective flow area decreases which also decreases the net mass flow rate through the nozzle hole. From Geometries 4 and 5, it is obvious, that the effect of K_{factor} on the mass flow rate is small or negligible for smaller nozzle diameter.

Fig.4.19 shows the exit velocity for different K_{factor}. For higher K_{factor}, the exit velocity is higher because of its convergent nature, which converts the pressure energy into kinetic energy. The higher velocity of fuel spray will lead to break up in the atomization regime, and results in droplets whose average diameter is much smaller than the nozzle diameter [15]. This will have a significant effect on

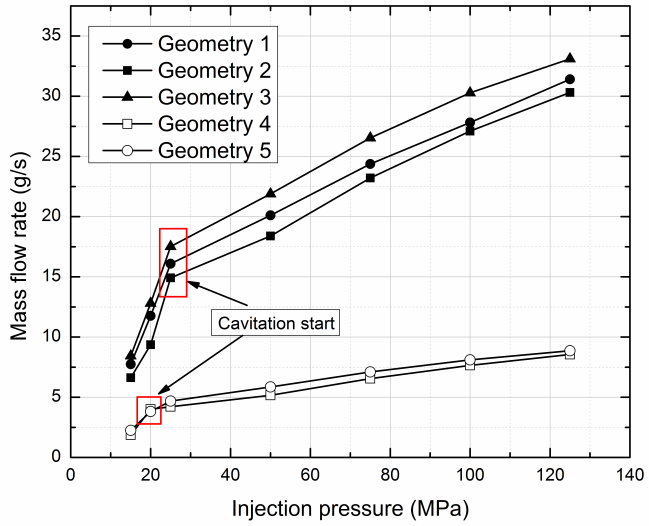

Figure 4.18: Effect of different geometries on cavitation

combustion and emission.

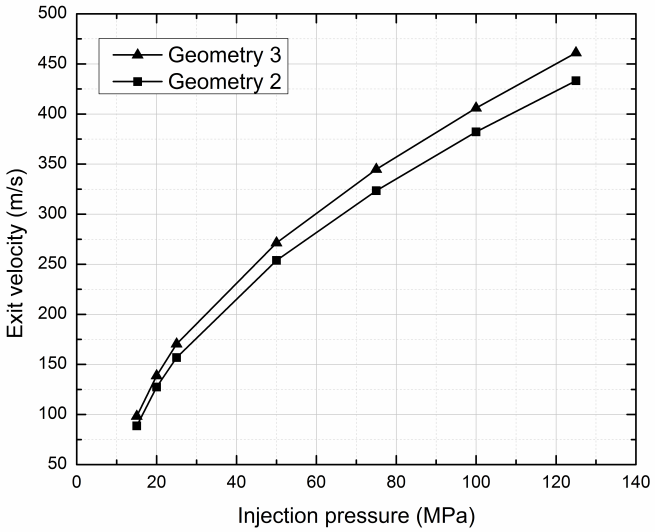

Figure 4.19: Exit velocity for different K_{factor}

4.3.5 Validation of model with in-house experiment

The cavitation model was then validated with the in-house experimental data obtained from the momentum flux measurements reported in the Chapter 3. For

validation, the momentum flux was also obtained from the internal nozzle flow simulations. Fig.4.20a shows the comparison of momentum coefficient between experiment and simulation and it is found that the model predicts the experimental results with a maximum deviation of 6.8%. The momentum flux and momentum coefficient at different injection pressures and ambient densities are shown in Fig.4.20b. It should be noted that the momentum flux decreases with increase in ambient density but the momentum coefficient remains constant irrespective of injection pressure and ambient density supporting the result obtained by Payri et al. [153] . It was also observed that cavitation inception occurs at all chosen injection pressures and ambient densities, which also supports the reason for constant momentum coefficient. Fig.4.21 shows the cavitation contours inside the injector nozzle holes for different injection pressures under an ambient pressure of 6 MPa. From the same Fig., it can be observed that as the pressure difference was increased, the amount of vapor volume fraction was also increased due to cavitation. This is due to high turbulence generated as a result of the conversion of pressure energy to kinetic energy.

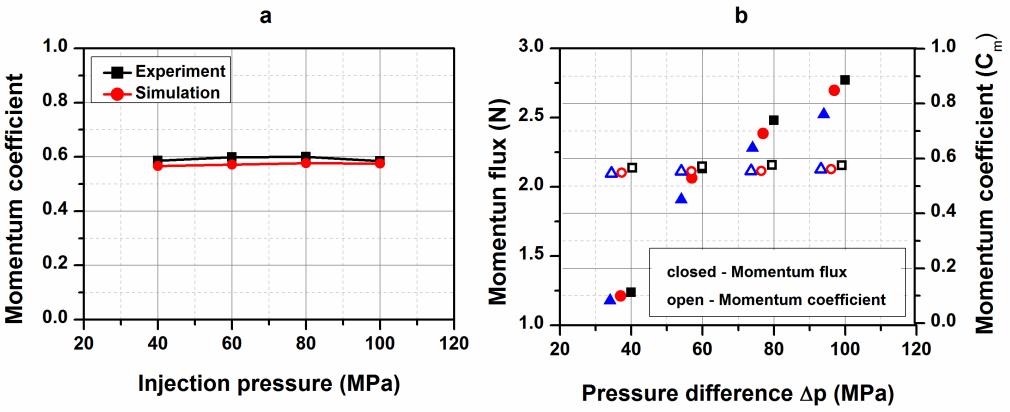

Figure 4.20: (a) Comparison between experimental and simulation momentum coefficient (b) spray momentum flux and momentum coefficient at different injection pressure and ambient density from simulation.

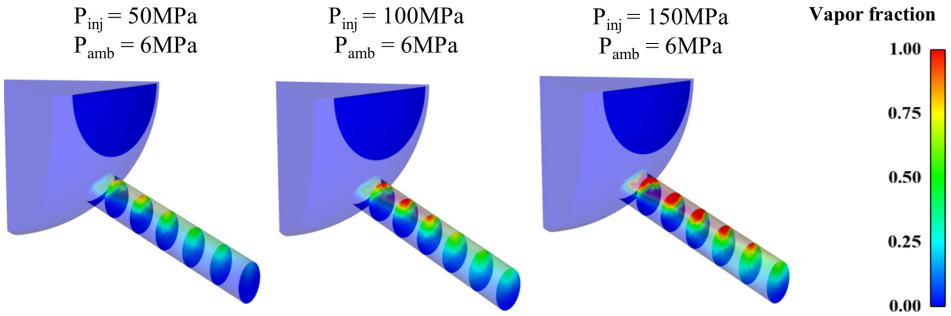

Figure 4.21: Cavitation contours at different injection pressure under ambient pressure of 6 MPa

4.4 Summary

A numerical study was performed to investigate the effect of different fuels, injection pressure, time and different geometries on the cavitation phenomenon inside the injector nozzle hole. The following observations were made based on the results from the numerical simulations performed.

- The cavitation phenomenon is found pronounced with diesel fuel than with SME bio-diesel because of its fluid properties. Cavitation in diesel occurs at high Re number compared to bio-diesel because of higher dynamic pressure due to lower viscosity. Also very high numerical value of Weber number shows that surface tension has no significant effect on cavitation.

- The cavitation of both the fuels with time were compared with the formation of vapor phase, which also shows that bio-diesel inhibits the cavitation phenomenon because of higher viscosity.

- The mass flow rate increases with the increasing K_{factor} for bigger inlet and exit diameter but no significant effect is observed with smaller diameter nozzles. A significant decrease in mass flow rate is observed for smaller diameter from bigger diameter with the same K_{factor}. The exit velocity for higher K_{factor} is higher, which may help in finer atomization of fuel.

- The model also predicts the cavitation in good agreement with the in house experimental results.

The study presented here confirms that the model is good in predicting the cavitation in diesel fuel injectors. In subsequent chapters, the model will be used to introduce the effect of cavitation and turbulence inside the injector nozzle holes in to the spray break up process.

5

Development and Validation of new hybrid fuel spray model[1]

Spray processes play an important role in many technical systems and industrial applications. Examples are spray cooling, spray painting, crop spraying, humidification and spray combustion in furnaces, gas turbines, rockets as well as diesel and gasoline engines. The role of fuel spray in combustion process is to break up the liquid fuel into smaller droplets thus increasing the surface area for evaporation

[1]Excerpts of this chapter, in part, is a reprint of previous publications titled "*Development of an accurate cavitation coupled spray model for diesel engine simulation*", Energy Conversion and Management 77, 269-277, 2014. DOI: 10.1016/j.enconman.2013.09.035. "*Effect of internal nozzle flow and thermo-physical properties on spray characteristics of methyl esters*", Applied Energy 129, 123-134, 2014. DOI: 10.1016/j.apenergy.2014.04.109. and "*Experimental study of spray characteristics of biodiesel derived from Waste cooking oil*", Energy Conversion and Management 88, 622-632, 2014. DOI: 10.1016/j.enconman.2014.09.013.

to provide gaseous fuel for combustion. The physical development of fuel spray occurs in three stages as described

- First stage, the liquid jet breaks up to form a cluster of fuel droplets.
- Second stage, the cluster of droplets forms coalescence leading to further droplet break up.
- Third stage, diffusion of fuel droplet takes place and starts evaporating, forming a dilute droplet region, where droplet to droplet interactions get minimized and the motion of droplet is governed predominantly by the local gas-field.

The general spray properties are shown in Fig.5.1. The important properties of spray are

- Break up length L_{bu}, the length of the liquid core.
- Spray tip penetration length S, the total length of the spray tip penetrated into the combustion chamber.
- Spray angle θ, the angle formed by the spray cloud.
- Droplet diameter D_{SMD}, sauter mean diameter of the droplet.

The factors that affect the fuel spray formation and its properties are

- Injection pressure
- Ambient density
- Cavitation

5.1 Spray regimes

The secondary break-up of liquid fuel droplets into even smaller droplets is primarily driven by aerodynamic forces employed on the drops by the surrounding

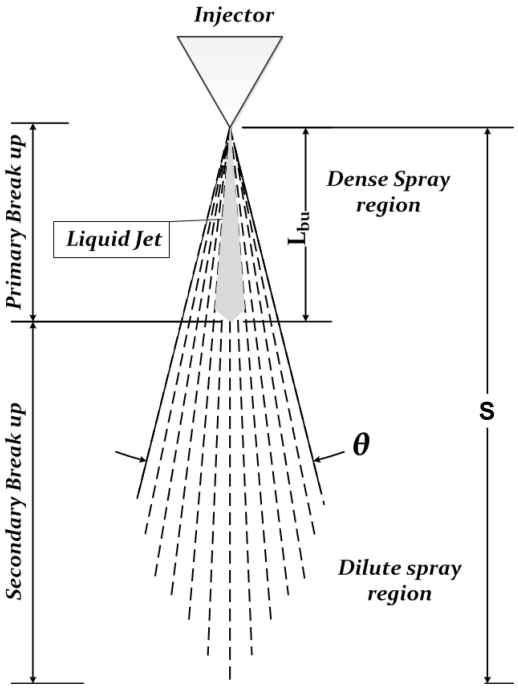

Figure 5.1: Spray Properties

gas phase. These forces cause a distortion of the initially spherical droplet that will eventually lead to break-up if the surface tension that counteracts the deformation is exceeded. There are generally five different break-up regimes shown in Fig.5.2 [200].

According to Wierzba [200], for very low Weber numbers near the critical value of about $We_c = 6$, the droplet executes an oscillation and may break-up into two new droplets of approximately equal size. If the Weber number is slightly increased the original drop will be deformed into a bag shape. After break-up a bimodal droplet size distribution will result with larger droplets originating from the rim and smaller ones originating from the trailing edge. For Weber numbers between approximately 10 and 25 an additional streamer-shaped interior may develop within the bag, leading to a class of droplets with a similar size to the ones resulting from the rim of the bag. Stripping break-up occurs for Weber numbers between 25 and 50. It is characterized by very small secondary droplets that are stripped or sheared off the surface of the bigger parent droplet. Finally, for large Weber numbers above about 50 the so-called catastrophic break-up takes place. It is dominated by surface instabilities that develop on a liquid-gas interface. In

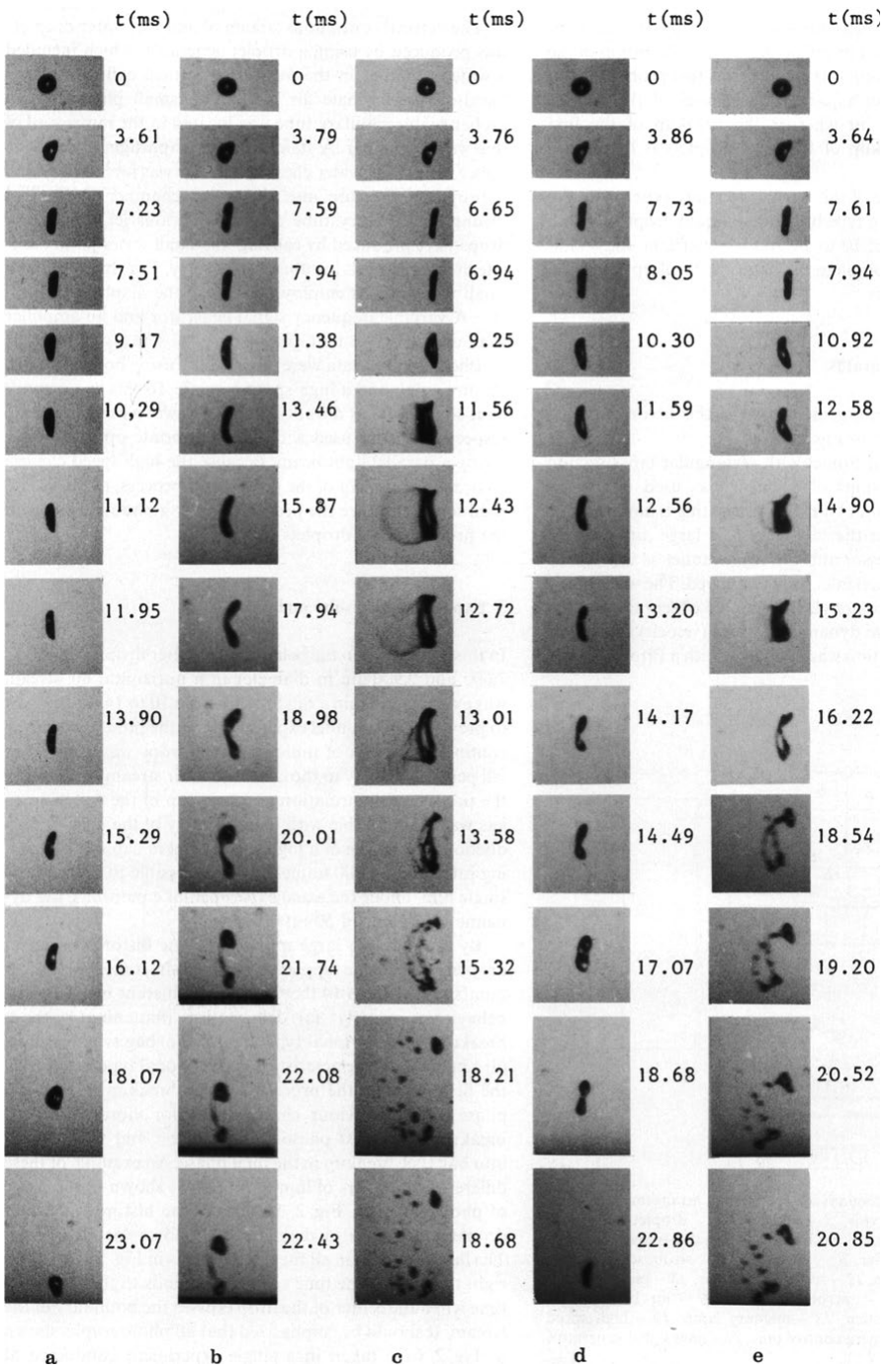

Figure 5.2: Drop break-up regimes a) vibrational break-up, b) bag break-up, c) bag/streamer break-up, d) stripping break-up, and e) catastrophic break-up [200]

high pressure diesel sprays all of the above mechanisms may be present.

5.2 Atomization models

Atomization represents an example of a complex gas-liquid flow: Near the nozzle, the liquid, initially introduced as a continuous jet, disintegrates into filaments and drops by interacting with the gas. Atomization is also important in a wide variety of other applications such as liquid metals, environmental spraying, printing, food processing as a significant parameter of the subsequent droplet formation and dispersion. This has led researchers to focus on theoretical and experimental analysis of this phenomenon. Spray modeling for diesel engine dates from the late 1970s as the development of CFD methodology for diesel engine calculations started. Spray modeling is considered key component in diesel combustion simulations, because of the controlling role the fuel injection process plays in the combustion and emissions of the engine. Since then many spray models have been developed to simulate the actual injection and spray development process inside the combustion chamber. Some note worthy spray models being used in diesel engine simulations in various commercial and open source engine CFD codes are explained in detail in the upcoming sections.

5.2.1 Taylor analogy break-up (TAB) model

The Taylor analogy break-up (TAB) model was first proposed by O'Rourke and Amsden [193] for simulating the spray process in KIVA CFD code. TAB model is based on the analogy between an oscillating and distorting drop and a spring mass system suggested by Taylor [201]. The external force acting on the mass, the restoring force of the spring, and the damping force are considered analogous to the gas aerodynamic force, the liquid surface tension force, and the liquid viscosity force respectively. The parameters and constants in the TAB model Equations have been determined from the theoretical and experimental results,

and the model has been applied successfully to sprays.

The Equation of a damped, forced harmonic oscillator is given by

$$m\ddot{y} = F - ky - d\dot{y} \tag{5.1}$$

In accordance to Taylor analogy, the physical dependencies of the coefficient in Eq.5.1 are

$$\frac{F}{m} = C_F \frac{\rho_g u^2}{\rho_l r}, \quad \frac{k}{m} = C_k \frac{\sigma}{\rho_l r^3}, \quad \frac{d}{m} = C_d \frac{\mu_l}{\rho_l r^2} \tag{5.2}$$

where ρ_g and ρ_l are the gas and liquid densities, u is the relative velocity between gas and droplet, r is the droplet radius, σ is the gas liquid surface tension coefficient and μ_l is the liquid viscosity and C_F, C_k and C_d are dimensionless constants. It was assumed that break-up occurs if and only if $y > C_b r$, where $C_b$is another dimensionless number. On substituting Eq.5.2 in Eq.5.1 and solving we get

$$y\left(t\right) = \frac{C_F}{C_k C_b} We + e^{-\frac{t}{t_d}} \left| \left(y_0 - \frac{C_F}{C_k C_b} We \right) cos\omega t + \frac{1}{\omega} \left(\dot{y}_0 + \frac{y_0 - \frac{C_F}{C_k C_b} We}{t_d} \right) sin\omega t \right| \tag{5.3}$$

where

$$We = \frac{\rho_g u^2 r}{\sigma}, \tag{5.4}$$

$$y_0 = y\left(0\right), \tag{5.5}$$

$$\dot{y}_0 = \frac{dy}{dt}\left(0\right), \tag{5.6}$$

$$\frac{1}{t_d} = \frac{C_d}{2} \frac{\mu_l}{\rho_l r^2}, \tag{5.7}$$

and

$$\omega^2 = C_k \frac{\sigma}{\rho_l r^3} - \frac{1}{t_d^2} \tag{5.8}$$

In TAB model, in addition to arrays specifying the particle position, velocity, size and temperature, to implement the model, two additional arrays specifying the values of y and $\dot{y}$ of each particle were used. For each particle, first We, t_d, and ω^2 were calculated. A value of $\omega^2 \leq 0$ occurs only for very small drops for which distortions and oscillations are negligible. Thus if $\omega^2 \leq 0$, then $y^{n+1} = \dot{y}^{n+1} = 0$, where the superscript n+1 denotes advanced time value. If $\omega^2 > 0$, then the amplitude A of the undamped oscillation is calculated

$$A^2 = \left(y^n - \frac{We}{12}\right)^2 + \left(\frac{\dot{y}^n}{\omega}\right)^2 \tag{5.9}$$

If $\frac{We}{12} + A \leq 1.0$, then according to Eq.5.3, the value of y will never exceed unity and break up will not occur and for these condition y and $\dot{y}$ are simply updated as given below

$$y^{n+1} = \frac{We}{12} + e^{-\frac{\triangle t}{t_d}} \left\{ \left(y^n - \frac{We}{12}\right) cos\omega\triangle t + \frac{1}{\omega}\left(\dot{y}^n + \frac{y^n - \frac{We}{12}}{t_d}\right) sin\omega\triangle t \right\} \tag{5.10}$$

and

$$\dot{y}^{n+1} = \frac{\left(\frac{We}{12} - y^{n+1}\right)}{t_d} + \omega e^{-\frac{\triangle t}{t_d}} \left\{ \frac{1}{\omega}\left(y^n + \frac{\dot{y}^n - \frac{We}{12}}{t_d}\right) cos\omega\triangle t - \left(y^n - \frac{We}{12}\right) sin\omega\triangle t \right\} \tag{5.11}$$

If $\frac{We}{12} + A \geq 1.0$, the break-up is possible, then breakup time t_{bu} is calculated assuming that the drop oscillation is undamped for its first period. Again this is true for all except very small drops. The time t_{bu} is the smallest root greater than t^n of the equation

$$\frac{We}{12} + Acos\left|\omega\left(t - t^n\right) + \phi\right| = 1 \tag{5.12}$$

where

$$cos\phi = \frac{y^n - \frac{We}{12}}{A} \tag{5.13}$$

and

$$sin\phi = -\frac{\dot{y}^n}{(A\omega)} \tag{5.14}$$

Break-up is calculated only when when $t^n \leq t_{bu} \leq t^{n+1}$. To conserve mass, the number of drops N associated with the computational particle is adjusted according to

$$N^{n+1} = N^n \left(\frac{r^n}{r^{n+1}}\right)^3 \tag{5.15}$$

The TAB model is best for low Weber number sprays. However, for extremely high Weber number sprays which result in shattering of droplets, cannot be described by the spring mass analogy.

5.2.2 Enhanced Taylor analogy break-up model (ETAB) model

The Enhanced Taylor analogy break-up model (ETAB) model was proposed by Tanner [202] in 1997. This model uses the droplet deformation dynamics from the standard TAB model, but it provides a new strategy for the description of the droplet break-up process. The droplet disintegration is modeled via an exponential law which relates the mean product droplet size size to the break-up time of the parent drop. The main assumption for this model is that the rate of product droplet generation is proportional to the number of product droplets given as

$$\frac{dn\,(t)}{dt} = 3K_{br}n\,(t) \tag{5.16}$$

By the mass conservation principle between the parent and the product droplets

$$n\left(t\right) = \frac{m_o}{\overline{m}\left(t\right)} \tag{5.17}$$

where m_o is the mass of the parent drop and $\overline{m}$ is the mean mass of the product droplets. Using Eq.5.17 in Eq.5.16, leads to the break-up law which relates the product droplet size to the break-up time. The break-up time is calculated from the TAB model.

$$\frac{d\overline{m}}{dt} = -3K_{br}\overline{m} \tag{5.18}$$

The break-up constant K_{br} depends on the break-up regime and is given by parent drop properties and is given as

$$K_{br} = \begin{cases} k_1 & if \quad We \leq We_t \\ k_2\omega\sqrt{We} & if \quad We > We_t \end{cases} \tag{5.19}$$

Bag break-up happens if $We \leq We_t$ and stripping break-up happens if $We > We_t$, where We_t is the regime-diving Weber number. The values of k_1 and k_2 have been adjusted as $k_1 = k_2 = \frac{2}{9}$ in order to match experimentally determined drop sizes.

From Eq.5.18, the ratio of child to parent droplet radii is given as

$$\frac{r}{a} = e^{-K_{br}t} \tag{5.20}$$

where a and r are the radii of the parent and product drops, respectively. The global effect of the ETAB model is that it generally predicts greater child droplet diameters than the original TAB model. As a result, a more realistic droplet size distribution, especially in the thick spray regime close to the injection nozzle is obtained.

5.2.3 Cascade atomization and drop break-up (CAB) model

The CAB model [203] is an extended approach of ETAB model. In the CAB model the break-up condition is determined by means of the drop deformation dynamics of the standard TAB model [193]. It was observed that the drops near the nozzle exit exceed the transition Weber number of the stripping/ catastrophic break-up regime which prompted the development of the CAB model. Similar to ETAB model, in conjunction with the mass conservation principle between parent and product droplets, leads to the basic cascade break-up law

$$\frac{d\overline{m}\,(t)}{dt} = -3K_{br}\overline{m}\,(t) \tag{5.21}$$

where $\overline{m}\,(t)$ denotes the mean mass of the product drop distribution and the break-up frequency K_{bu} depend on the drop break-up regimes. The break-up frequency can be expressed as

$$K_{bu} = \begin{cases} k_1\omega & if \quad We_c < We \leq We_{b,s} \\ k_2\omega\sqrt{We} & if \quad We_{b,s} < We \leq We_{s,c} \\ k_3\omega We^{\frac{3}{4}} & if \quad We_{s,c} < We \end{cases} \tag{5.22}$$

where the drop oscillation frequency ω is given by

$$\omega^2 = \frac{8\sigma}{\rho_l a^3} - \frac{25\mu_l^2}{4\rho_l^2 a^4} \tag{5.23}$$

For the model implementation in this study , a uniform product drop size distribution has been assumed, by which Eq.5.21 becomes

$$\frac{r}{a} = e^{-K_{bu}t_{bu}} \tag{5.24}$$

where a and r are the radii of the parent and product drops, respectively, and t_{bu} is the breakup time.

In the CAB model, the determination of the spray angle has been considerably

simplified. The main reason for this is that the ETAB model constant C_α, which determines the initial spray angle, is dependent on the model constant for the jet break-up length C_λ. This dependence does not allow for an independent choice of the two parameters, but it has the advantage that the initial spray angle adjusts automatically to changes in the gas pressure, once the constants have been turned to a particular nozzle as shown below

$$tan\left(\frac{\theta}{2}\right) \approx \sqrt{\frac{\rho_l}{\rho_g}} \tag{5.25}$$

The product droplet radii for the CAB model decrease with increasing Weber number, and the ratio is larger than for the ETAB model throughout the entire range, a fact which results in an improved prediction of the drop size distributions for the CAB model.

As expected, the product droplet radii for the CAB model decrease with increasing Weber number, and the ratio is larger than for the ETAB model throughout the entire range, a fact which results in an improved prediction of the drop size distributions for the CAB model.

5.2.4 Blob injection model

A blob injection model injects liquid drops with a diameter equal to an effective nozzle diameter, and an injection velocity that is calculated from the rate of injection (ROI) profile. In the traditional approach, the primary of the jet is considered aerodynamic break-up mechanism using Kelvin-Helmholtz instability [204, 205][206]. The schematic showing surface waves and break-up on a liquid jet or blob and schematic illustration of the blob injection model are shown in Fig.5.3 and 5.4 respectively.

The KH model considers break-up resulting from waves growing at the liquid surface. Due to the relative velocity between the gas and liquid phases, the growth of KH instabilities induces the shearing of the droplets from the liquid surface. The break-up of droplet parcels is calculated by assuming that the radius of newly

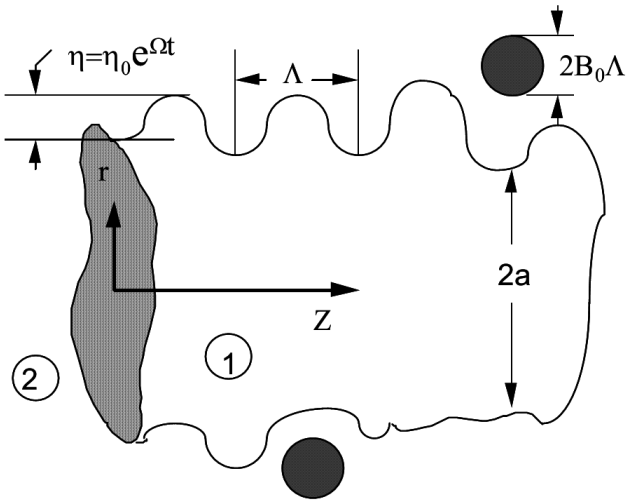

Figure 5.3: Schematic showing surface waves and break-up on a liquid jet or blob [207]

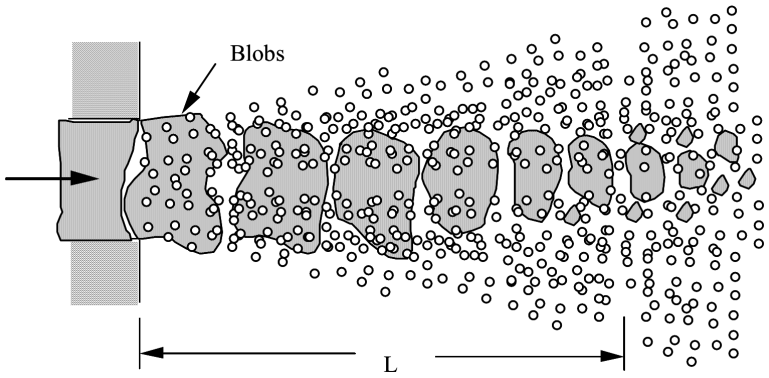

Figure 5.4: Schematic illustration of the blob injection model [204]

formed droplets (r_{KH}) is proportional to the wavelength of the fastest growing surface wave on the parent droplet i.e.,

$$r_{KH} = B_0 \Lambda_{KH} \tag{5.26}$$

where Λ_{KH} is the wavelength corresponding to the KH wave with the maximum growth rate, Ω_{KH}, and B_0 is a constant. During break-up, the radius of the parent droplet parcel (r) decreases continuously according to the following Equation until it reaches the droplet radius:

$$\frac{dr}{dt} = \frac{r - r_{KH}}{\tau_{KH}}, \quad r_{KH} \leq r \tag{5.27}$$

$$\tau_{KH} = 3.276 \frac{B_1 r}{\Omega_{KH} \Lambda_{KH}} \tag{5.28}$$

where τ_{KH} is the break-up time, Ω_{KH} and Λ_{KH} are given as

$$\Omega_{KH} = \frac{0.34 + 0.38 We_g^{1.5}}{(1+Z)(1+1.4T^{0.6})} \sqrt{\frac{\sigma}{\rho_l r^3}} \tag{5.29}$$

$$\Lambda_{KH} = \frac{9.02 r \left(1 + 0.45\sqrt{Z}\right)(1 + 0.4T^{0.7})}{\left(1 + 0.865 We_g^{1.67}\right)^{0.6}} \tag{5.30}$$

where

$$\begin{aligned} Z\ (Ohnesorge\ number) &= \frac{\sqrt{We_l}}{Re_l} \\ We_l\ (Weber\ number) &= \frac{\rho_l U_r^2 r}{\sigma} \\ Re_l\ (Reynolds\ number) &= \frac{U_r r}{v_l} \\ T\ (Taylor\ number) &= Z\sqrt{We_g} \\ We_g\ (Weber\ number) &= \frac{\rho_g U_r^2 r}{\sigma} \end{aligned} \tag{5.31}$$

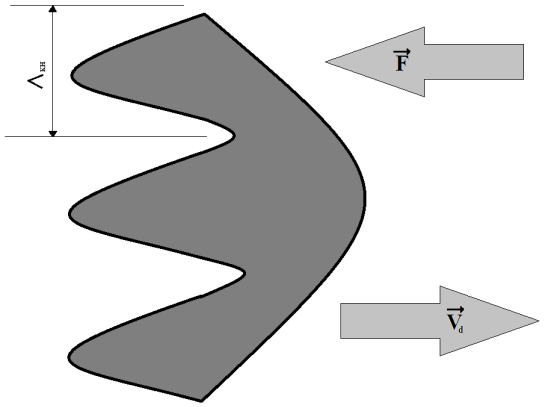

Figure 5.5: Schematic illustration of Rayleigh-Taylor instabilities on a liquid droplet [164]

where, σ, ρ_g U_r, ρ_l, *and* v_l are surface tension, gas density, relative velocity between the liquid and gas phases, liquid density and liquid viscosity respectively. The instantaneous length scale for every parcel is calculated as follows:

$$L_{KH} = r - r_{KH} \tag{5.32}$$

It should be noted that in many recent applications of the blob injection method KH break-up model has been combined with the so called Rayleigh-Taylor break-up model in order to estimate the disintegration of the blobs into secondary droplets. In fact, the model is not only used to estimate the disintegration of primary blobs but also to model the subsequent break-up of secondary droplets into even smaller droplets.

5.2.5 Rayleigh-Taylor model

In diesel sprays injected liquid droplets have very high initial velocities and they decelerate rapidly due to drag forces. Fig.5.5 shows the schematic illustration of Rayleigh-Taylor instabilities on a liquid droplet. Hence Rayleigh-Taylor instability can be important in the droplet mechanism, in addition to the KH instability [208, 209, 210].

Neglecting liquid viscosity and considering surface tension only, the analytical

fastest-growing frequency, Ω_{RT}, and the corresponding wave number, K_{RT}, are represented as

$$\Omega_{RT} = \sqrt{\frac{2}{3\sqrt{3\sigma}} \frac{\left[-g_t\left(\rho_l - \rho_g\right)\right]^{3/2}}{\rho_l + \rho_g}} \tag{5.33}$$

$$K_{RT} = \sqrt{\frac{-g_t\left(\rho_l - \rho_g\right)}{3\sigma}} \tag{5.34}$$

where g_t is the acceleration in the direction of travel and defined as $g_t = \overrightarrow{g}.\overrightarrow{j} + \overrightarrow{a}.\overrightarrow{j}$, where $\overrightarrow{g}$ is the gravity, $\overrightarrow{a}$ represents the droplet acceleration, and $\overrightarrow{j}$ is the unit vector tangent to the droplet trajectory. The wavelength , $2\pi C_{RT}/K_{RT}$, is compared to the distorted droplet's diameter, and if the wavelength is smaller than the droplet diameter, RT waves are assumed to be growing on the surface of the droplet.The amount of time that the waves grow is tracked and compared to a break-up time which is assumed to be

$$\tau_{RT} = \frac{C_\tau}{\Omega_{RT}} \tag{5.35}$$

where C_{RT} is an adjustable constant, nominally assumed equal to 1. After the break-up time has elapsed the parent droplet is broken up into a collection of smaller drops which have radii

$$r_{RT} = \frac{\pi C_{RT}}{K_{RT}} \tag{5.36}$$

where C_{RT} is assumed equal to 0.3. Droplet break-up process in this model is essentially similar to that in the wave model, i.e., the radius of the parent droplet parcel decreases continuously according to the following Equation until it reaches the droplet radius:

$$\frac{dr}{dt} = \frac{r - r_{RT}}{\tau_{RT}} \tag{5.37}$$

The instantaneous length scale is calculated as

$$L_{RT} = r - r_{RT} \tag{5.38}$$

The original RT model does not account for viscous effects. Senecal et al. [211] extended the standard RT model to include viscosity effects which can have large effects for high deceleration typically experienced by spray droplets [212].

5.2.6 Cavitation induced breakup model

The cavitation patterns decrease the radius of the injected parcels from the orifice radius. The assumption in this model is that the cavitation bubbles formed inside the nozzle holes are swept out by turbulence and either they burst out on the surface or collapse before reaching it. For both these cases a characteristic time scale can be calculated, the smaller of which causes the further breakup. According to Bianchi and Pelloni [213] and Arcoumanis and Gavaises [214], the characteristic time scale of the cavitation is assumed to be the smaller of the collapse time and the burst time

$$\tau_{cav} = min\left(\tau_{coll}; \tau_{burst}\right) \tag{5.39}$$

where, the collapse time $\tau_{collapse}$ of a bubble with radius R_{cav} is evaluated from the Rayleigh theory [215]

$$\tau_{collapse} = 09145 R_{cav} \sqrt{\frac{\rho_l}{\rho_v}} \tag{5.40}$$

The burst time, calculated taking into account the time required for the cavities to reach the jet surface, is defined as

$$\tau_{burst} = \frac{r_{hole} - R_{cav}}{u_L^{'}} \tag{5.41}$$

where, $u_L^{'}$ is the velocity of jet fluctuation $\left(u_L^{'} = \sqrt{\frac{2K_{avg}}{3}}\right)$ and it is obtained

from the cavitation simulation presented in Chapter 4, K_{avg} is the average kinetic energy at the orifice exit obtained from the , R_{cav} is the radius of an equivalent bubble having the same area as all the cavitating bubbles, defined as

$$R_{cav} = \sqrt{r_{hole}^2 - r_{eff}^2} \tag{5.42}$$

where, r_{hole} is the geometrical nozzle and radius r_{eff} is the radius of the effective flow area at the nozzle exit, defined as

$$r_{eff}^2 = C_C r_{hole}^2 \tag{5.43}$$

where, C_c is the area coefficient or coefficient of contraction obtained from the cavitation simulation presented in earlier chapter. Combining Eqns.5.42 and 5.43, we get

$$R_{cav} = r_{hole}\sqrt{1 - C_C} \tag{5.44}$$

The length scale of the cavitation induced atomization L_{cav} is estimated according to Arcoumanis and Gavaises [214] as

$$L_{cav} = 2\pi \left(r_{hole} - R_{cav}\right) \tag{5.45}$$

The radius of the parent droplet decreases continuously according to the following Equation until it becomes

$$\frac{dr}{dt} = -C_{cav}\frac{L_{cav}}{\tau_{cav}} \tag{5.46}$$

where, C_{cav} is the model constant which takes the value 0.025 for vaporizing spray and 0.05 for non-vaporizing spray [216].

5.3 New hybrid fuel spray model

There are many atomization models used to predict the spray process in the diesel combustion chamber [217, 218, 219, 193, 202, 220, 221, 222] as explained in previous sections. However the most widely used atomization model is the KHRT model for diesel engine simulations [208, 206, 223, 210, 224]. In the KHRT model, the KH model is used for primary break-up whereas the combined KHRT model is used for secondary break-up. The KH model was developed based on Kelvin-Helmholtz instabilities which account for aerodynamic instability due to shear of liquid surface and the RT model was developed based on the Rayleigh-Taylor instabilities which accounts for the acceleration instability on the droplet surface. However, this model doesn't account for the cavitation behavior and its impact on the spray break-up process. Though some researchers have studied the effects of cavitation on spray [214, 225, 226], either they have used a one dimensional model or phenomenological model to predict the cavitation phenomena inside the nozzle orifice. Except for the work of Berg et al. [156] and Som and Aggarwal [216], the effects of cavitation on spray break-up were not captured very well with the modeling of spray development. Berg et al. used two different approaches to model the spray by considering the internal nozzle flow in 'AVL FIRE' CFD code. The approaches were 1) Two stage approach in which separate internal flow simulations were done and the results were used in the spray model, 2) Coupled approach in which both internal flow and spray regions are treated with same fluid model but different inter-facial exchange terms were used in the spray and cavitation regions. However in their work only qualitative comparison were done with the experimental investigation and no quantitative results were presented. In Som and Aggarwal's work, they adopted the approach very similar to the two stage approach of Berg et al. using 'CONVERGE' CFD code, however they differed from the latter in the method of coupling the internal flow simulations and spray break-up models. They have done some extensive evaluations and reported both

qualitative and quantitative results. However in the earlier work, the cavitation coupled spray model was not validated against the engine combustion characteristic data. The combination of very few literature and absence of validation against engine experimental data provided motivation for this present work.

In this work, the simulation procedure is undertaken in two steps. The first step is simulation of the cavitating nozzle with the two-fluid model and the second step is the simulation of spray propagation using the new hybrid spray break-up model combining KHRT spray model and the cavitation sub model. Local distributions of flow field variables in the nozzle orifice obtained from the simulation of cavitating nozzle flow are used in spray breakup model. These results introduce the effects of turbulence and vapor volume formation into the breakup model. The models used in both steps of the simulation procedure are explained in detail in the sections below. The hybrid spray model was then extensively validated against the experimental data of both non-vaporizing and vaporizing sprays obtained from constant volume combustion vessel available in literature in relation to liquid length, spray penetration and fuel vapor penetration. Also the new model was validated against engine combustion characteristics like in-cylinder pressure and heat release rate using the results obtained in-house.

In the present work, the computations were carried out by using the KIVA4 CFD code [227, 228] coupled with CHEMKIN II. KIVA4 code uses finite volume scheme and solves the conservation of mass, momentum and energy Equation. The new hybrid spray model explained in subsequent sections was incorporated into the KIVA4 CFD code.

The hybrid model was implemented in a similar way as that implemented by Som and Aggarwal [216]. The length to time scale ratio was calculated for each process as given in Eqns.5.27, 5.37 and 5.46. The rate of decrease in droplet radius was calculated based on the ratio of length to time scale. Thus the dominant breakup process is determined by the maximum ratio as follows

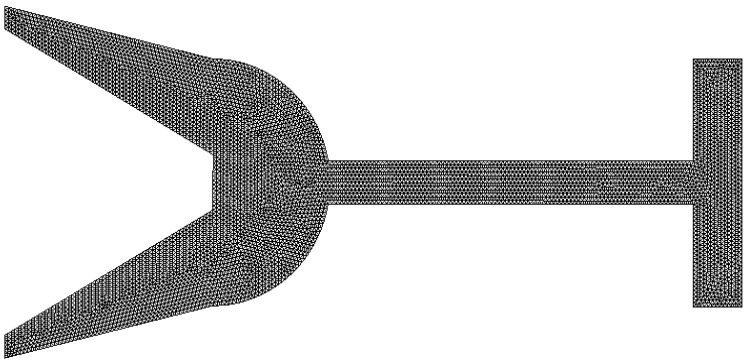

Figure 5.6: Grid used for internal flow simulations

$$\frac{L_{bu}}{\tau_{bu}} = max\left\{\frac{L_{KH}}{\tau_{KH}}, \frac{L_{RT}}{\tau_{RT}}, \frac{L_{cav}}{\tau_{cav}}\right\} \tag{5.47}$$

In this model, the parent parcels are subjected to breakup by competition between the three sub models. This model was implemented into KIVA4 using a program coded in FORTRAN language. The results from internal flow simulations were used as the input for this hybrid model to correctly capture the turbulence and cavitation parameters. The principal models of KIVA4 code accounts for the turbulence, collision and coalescence, and multicomponent fuel evaporation models.

5.4 Grid generation

For internal flow simulations the grid was generated using Gambit 2.4 as shown in Fig.5.6. The mesh size used for internal flow simulation using fluent was 366324 cells. The grid was generated for fully opened needle position.

For spray simulation three different grids – Grids 1, 2 and 3 were generated with 53671, 184671, 458731 cells respectively as shown in Fig.5.7. The grids were generated using Ansys ICEM CFD mesh generating software. The cylindrical geometry of the mesh used for spray simulation was $\phi 75 * 150mm$. The grid sizes 184671 and 458731 are much finer than those usually considered for complete internal combustion engine simulations.

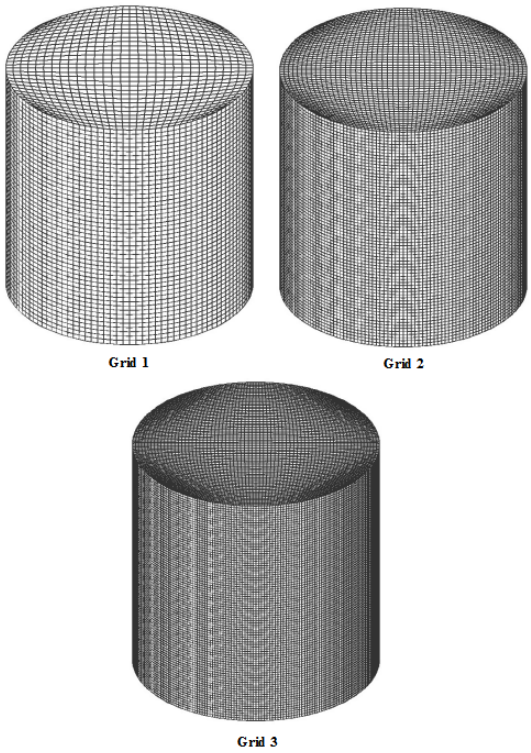

Figure 5.7: Grids used for spray simulations

5.5 Results and discussion

5.5.1 Validation with Sandia National Laboratory experimental results

5.5.1.1 Internal flow simulation

In compression ignition engines, the injection pressure can vary from 200 to 2000 bar or more, and hence under such high pressure conditions, it is significant to study the internal nozzle flow characteristics. The internal flow simulations were done for all cases of injection pressure and ambient conditions described in Tables 5.1 and 5.2 and the subsequent results were used for further spray simulations. For engine validation, the injector nozzle used for internal flow simulations consists of 6 holes with 175μm in diameter. However for computations, a single hole was used in assuming the flow to be symmetric across all the holes and the peak combustion pressure inside the combustion chamber is used as the ambient conditions. For

explanation of the phenomena, an example case test conditions [139] and fuel properties [195, 229] as shown in Table 5.1 were used.

Fig.4.8 shows the effect of coefficient of discharge with respect to the cavitation parameter. The coefficient of discharge and cavitation parameter are calculated from the simulation as given in Eqns.5.48 and 5.49

$$Coefficient\,of\,discharge\,C_d = \frac{m_a}{m_{th}} = \frac{m_a}{A_{th}\sqrt{2 * \rho_l * \triangle P}} \tag{5.48}$$

$$Cavitation\,parameter\,K = \frac{P_{inj} - P_v}{\triangle P} \tag{5.49}$$

where $\triangle P = P_{inj} - P_{amb}$. With an increasing amount of cavitation (decreasing K), C_d will start to decrease at some critical point. The critical value of K is shown by a line drawn in Fig.4.8. The critical point is also called the point where mass flow collapse occurs, which is related to the onset of choked flow. Choked flow is a term used for a flow state through a restriction where the downstream pressure no longer influences the flow velocity. From Fig.4.8, the region up to which C_d increases is said to be cavitating region (lower ambient pressure) and the region where C_d reaches steady state is non-cavitating region (higher ambient pressure). For lower ambient pressure the cavitation is more pronounced to occur whereas for higher ambient pressures the occurrence of cavitation is less.

Fig.5.9 shows cavitation inception for injection pressure of 137MPa and ambient pressure of 6MPa. From Fig.5.9, it is interesting to note that the cavitation inception is first observed at the orifice inlet and it proceeds all the way long to the outlet of the orifice, and also it can be noted that the vapor phase is also swept outside the exit to some extent. This clearly shows that the effects of cavitation inside nozzles and its turbulence should be incorporated into the primary break up model along with the aerodynamic effect.

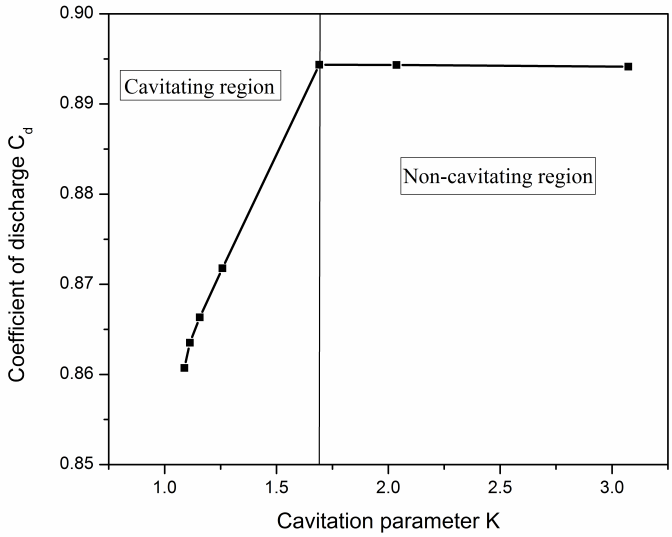

Figure 5.8: Effect of cavitation parameter on coefficient of discharge

Table 5.1: Test conditions used for internal flow simulations [139]

Injection system	Common rail
Nozzle geometry	Cylindrical, non hydroground
Number of orifices	1
Orifice diameter, d	246 µm
Injection pressure P_{inj}	137 MPa
Ambient pressure P_a	0.9-9 Mpa
Fuel	Diesel
Fuel liquid density ρ_l	$832^{kg}/_{m^3}$
Fuel liquid Viscosity μ_l	$2.1 * 10^{-3 kg}/_{ms}$
Fuel vapor density ρ_v	$0.1361^{kg}/_{m^3}$
Fuel vapor viscosity μ_v	$5.953 * 10^{-6 kg}/_{ms}$
Vapor pressure P_v @ 30 ° C	20 mbar

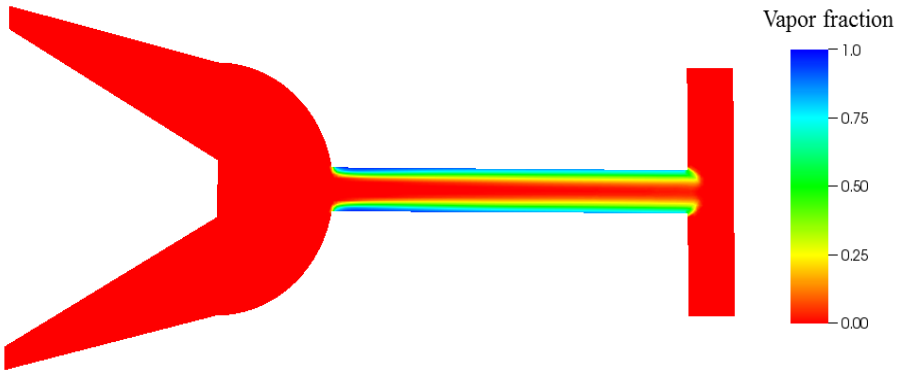

Figure 5.9: Vapor volume fraction

5.5.1.2 Spray simulation

In order to validate the new hybrid spray model, the simulation results were compared with experimental results available in the literature. Extensive validation of new hybrid model was done with vaporizing and non-vaporizing spray results obtained from the constant volume combustion chamber.

The effect of the new spray breakup model was examined for vaporizing and non-vaporizing conditions with the experimental measurements by Naber et al. [37] and Siebers and Dennis [139] in constant volume combustion chamber. The experimental conditions chosen for the simulations are shown in Table 5.2. The spray parameters like liquid length and vapor penetration length were used for the validation. The liquid length is the important spray characteristic as over penetration may result in wall impingement on combustion chamber and piston and under penetration may result in poor utilization of air. Vapor penetration is also important characteristic representing the vaporizing spray which defines the fuel vapor penetration extent and indirectly the amount of fuel air mixing. In this simulation the vapor penetration was calculated as the distance between the nozzle tip and location of 5% vapor content in the spray. The spray tip penetration for non-vaporizing spray was calculated as the distance between the nozzle tip and the location of 95% of the total liquid mass at any given instant. A separate FORTRAN code was written to calculate the values of liquid length, vapor penetration, and total spray penetration at every time step and the same was made to output as a text file.

It is not possible to apply the new hybrid spray model without considering the effect of grid resolution. Grid resolution is more critical as in high pressure and high dense spray simulations, the volume occupied by liquid is considered small compared to the volume occupied by the gas phase. Fig.5.10 shows the effect of three different grid resolutions on spray penetration compared with the experimental data. The conditions used for grid independency test are 246μm orifice diameter, 1000K ambient temperature, 135 MPa injection pressure and 438K fuel

Table 5.2: Test cases used for spray simulations [139, 37]

Injection system	Common rail
Nozzle geometry	Cylindrical, non hydroground
Number of orifices	1
Orifice diameter, d	246 μm, 257 μm
Injection pressure P_{inj}	135, 137 MPa
Chamber density ρ_a	$6.8 - 30.2 {}^{kg}/_{m^3}$
Chamber temperature T_a	451-1300 K
Ambient gas composition	$N_2 = 0.693, O_2 = 0.21, CO_2 = 0.061, H_2O = 0.036$

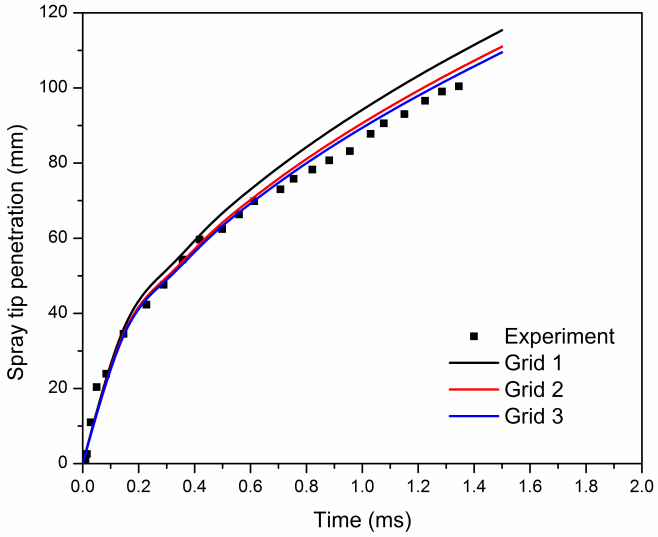

Figure 5.10: Effect of grid resolution on spray penetration

temperature and at 7.3 ${}^{kg}/_{m^3}$ ambient density. The maximum error in predictions of spray penetration using Grids 1, 2 and 3 were 9.1, 3.8 and 3.4%, respectively. Though the prediction improves with higher grid resolution, it comes with the costs of very high computational storage and running time. Thus considering computational cost and not compensating accuracy, the Grid 2 with 184671 cells was used for all further simulations and results presented.

The new hybrid spray model was compared with the classical Taylor–Analogy Break-up (TAB) model [193] and KHRT model. Fig.5.11 shows the spray tip penetration predicted by the different models. The conditions used are same as the one used in the grid independency test. From the predictions, the TAB model and

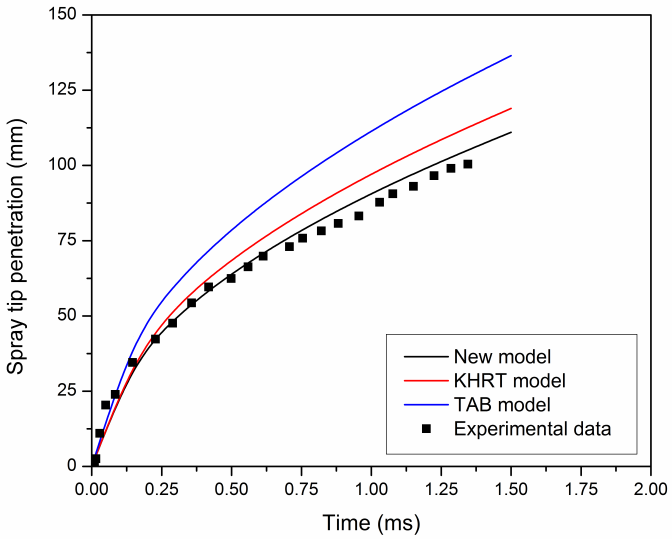

Figure 5.11: Comparison of different spray models against spray tip penetration

KHRT models over-predict the spray tip penetration by maximum of 26.5 and 10.2% respectively from the experimental data. However as explained earlier the new model deviates only 3.4% maximum from the experimental data. Fig.5.12 shows the Sauter Mean Diameter (SMD) predicted by three spray models. It is clear that the TAB model and KHRT model predicts larger SMD compared to the new model. It is very likely that this is the cause for longer tip penetration lengths predicted by the TAB and KHRT models. As larger droplets face smaller aerodynamic drag per unit volume and is also difficult to evaporate, thereby resulting in longer penetration lengths predicted by TAB and KHRT models compared to the new model developed. It should be noted that there is one significant difference in numerical implementation of classical KHRT and new spray model, the classical KHRT model considers the characteristic time scales in determining the dominant break-up mechanism, however in the new model, it uses the ratios of length to time scale to select the dominant mechanism as explained earlier.

Fig.5.13 shows the comparison of experimental results and simulation results for liquid length at various ambient densities. The conditions used for this simulations are 246μm orifice diameter, 1000K ambient temperature, 135 MPa injection

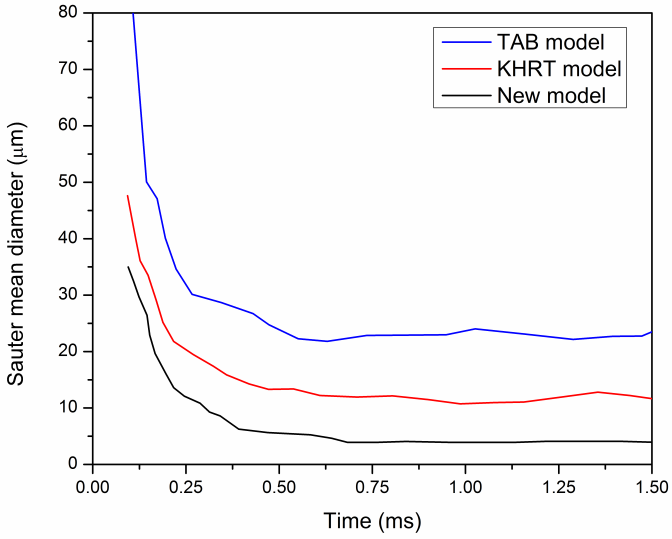

Figure 5.12: Comparison of different spray models against Sauter Mean Diameter (SMD)

pressure and 438K fuel temperature at three different ambient densities (7.3, 14.8, and 30.2 $^{kg}/_{m^3}$). The liquid length decreases with the ambient temperature for a given ambient density due to increased evaporation rate and liquid length also decreases with ambient density for a given ambient temperature as the spray loses more energy due to high ambient pressures. This overall behavior of spray is fairly well captured by the new hybrid spray model. The comparison of experimental images of the spray with the simulation indicating the liquid length is also shown in Fig.5.14. The spray images obtained through simulations is very close to the experimental images.

Figs.5.15 and 5.16 show the comparison of experimental and simulation results of spray tip penetration for both non-vaporizing and vaporizing spray. The conditions used for these simulations are 257μm orifice diameter, 137 MPa injection pressure and 451K and 1000K ambient temperature for non-vaporizing and vaporizing spray cases respectively at three different ambient densities (7.3, 14.8, and 30.2 $^{kg}/_{m^3}$ for non-vaporizing and 6.8, 13.9, and 28.6 $^{kg}/_{m^3}$ for vaporizing sprays). The most interesting trend shown by the penetration data is the decrease in penetration with an increase in ambient density and also it is noticeable trend that

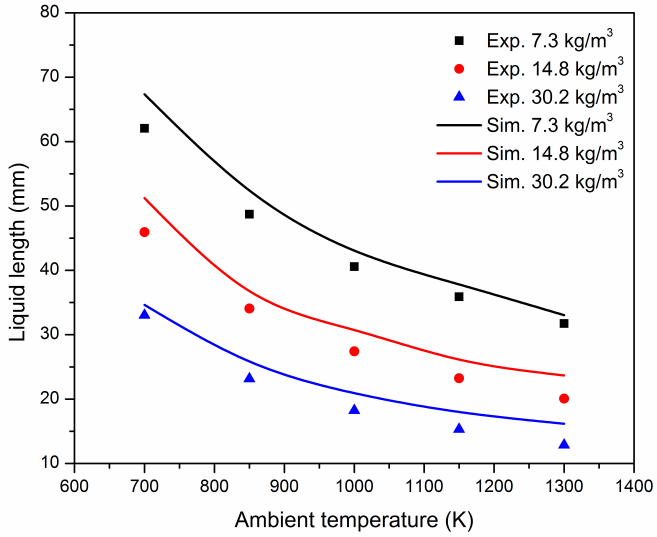

Figure 5.13: Comparison of simulation with experimental liquid length data

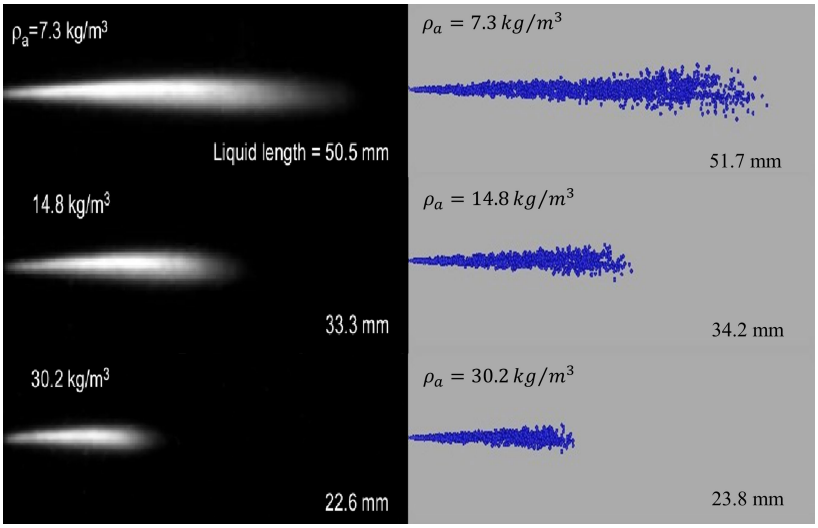

Figure 5.14: Comparison of simulation and experimental spray images

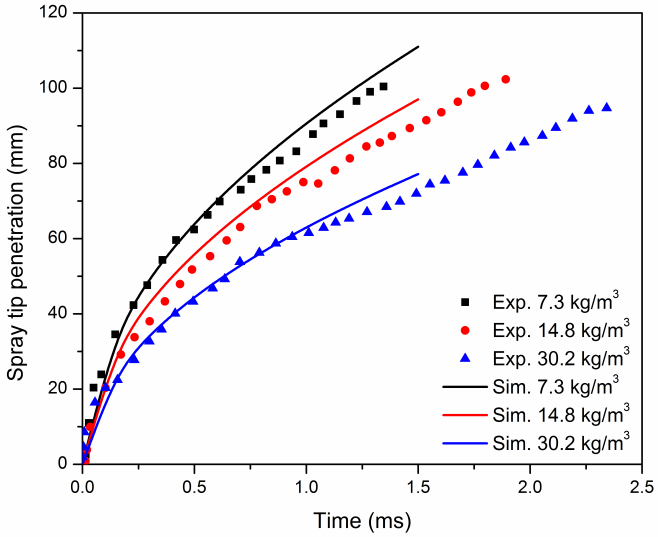

Figure 5.15: Comparison of simulation with experimental spray tip penetration of non-vaporizing sprays

rate of penetration decreases with time for experimental data. These experimental trends have been observed by many researchers. These trends were very well captured in the simulation using the new hybrid spray model.

5.5.2 Validation with in house experimental results

Fig.5.17 shows the comparison of spray tip penetration predicted by KHRT model and new hybrid model with experimental results. The symbols and lines represent experimental and simulation results, respectively. The experimental spray tip penetration is the result of average spray tip penetration of all seven holes obtained from image processing at each time sequence. The minimum and maximum spray tip penetrations measured at each time sequence out of all seven holes were plotted as bars along with averaged values. From the figure, it can be noted that the difference between the minimum and maximum values is small and hence the average spray tip penetration values are taken for discussion. The spray tip penetration from experimental results is calculated as the distance of spray from the tip to the nozzle hole and for simulation; it is calculated as the distance between the tip of the nozzle to the location where 95% of liquid mass is present at

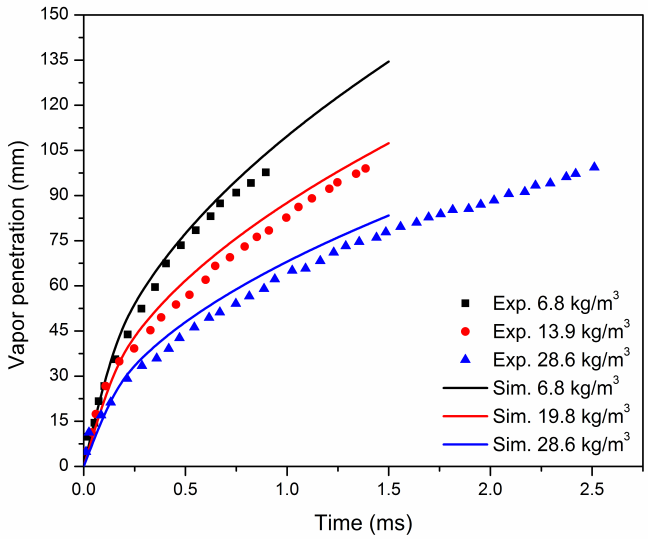

Figure 5.16: Comparison of simulation with experimental vapor penetration length of vaporizing sprays

any instant. From the figure, it is clear that the new hybrid model predicts better compared to the KHRT model. The KHRT model predicts longer penetration compared to experimental results. This may be due to prediction of the large Sauter Mean Diameter (SMD) because the fundamentals of primary atomization are not well captured by this model. On the other hand, the new model which takes into account the cavitation and turbulence inside the nozzle hole predicts the spray tip penetration at par with experimental results. This indicates that the new hybrid model has successfully incorporated essential fundamental physics of the primary atomization.

Fig.5.18 shows the comparison between experimental and simulation results of spray tip penetration and it can be noted that the model predicts the spray tip penetration in par with experimental results. The comparison of spray development between experimental and simulation results is shown in Fig.5.19 for injection pressure of 100 MPa and ambient density of 66 kg/m 3 . For computational time and cost, only one of the sprays is modeled. The hybrid spray model also predicts the shape of the spray at par with experimental results. This shows that the cavitation and turbulence generated inside the nozzle holes have substan-

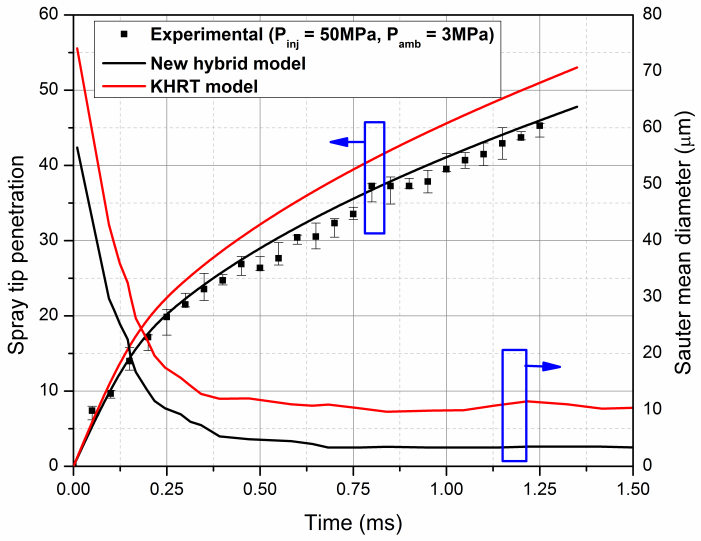

Figure 5.17: Comparison between KHRT and new hybrid model

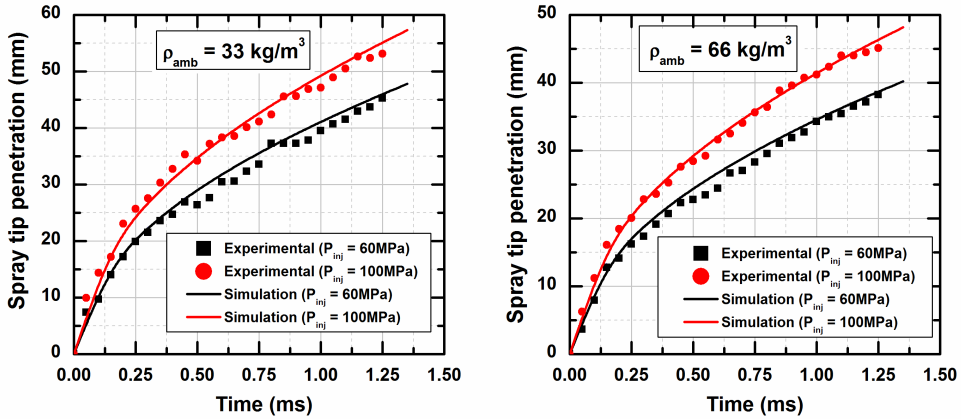

Figure 5.18: Comparison of in house experimental and simulation spray tip penetration

tial effect on the spray development process which should be given significance during modeling of spray combustion phenomena.

Fig.5.20 shows the overall sauter mean diameter (SMD) and liquid length of fuel spray injected at different injection pressure under 6 MPa ambient pressure and 1000 K ambient temperature. The simulations were performed under inert atmosphere of nitrogen to avoid combustion. The liquid length is referred to the length of the liquid core in vaporizing fuel spray. The liquid length of the fuel spray increases with increase in the injection pressure due to high spray momentum with increasing injection pressure. However, the rate of increase declines towards higher

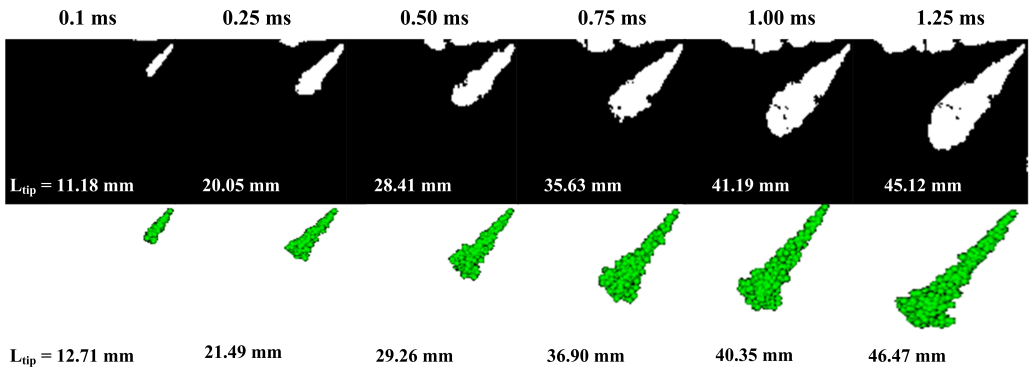

Figure 5.19: Comparison of spray evolution between in house experiment and simulation

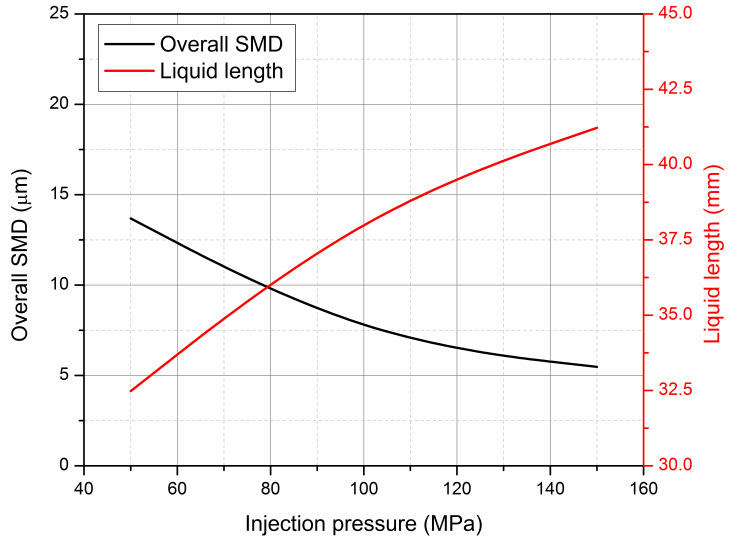

Figure 5.20: Overall SMD and liquid length under 6 MPa ambient pressure and 1000 K ambient temperature

injection pressure, this may be due to the effect of increased vaporization of smaller fuel droplets produced at higher injection pressure. The overall SMD shows a decreasing trend with increased injection pressure due to better atomization and hence better vaporization at higher injection pressure.

5.5.3 Spray characteristics of biodiesel

Researchers are coming up with new biodiesel fuels from different feedstock based on the local availability and cost [230, 231]. The combustion process of different fuels is significantly affected by the fuel spray atomization process and cetane number

etc. The computational fluid dynamic (CFD) tools become valuable in reducing the number of experiments in optimizing the engine performances. However, the predicted levels of pollutant concentration and power output are comprehensively dependent on the description of the spray breakup process. The difference in thermo-physical properties of biodiesel derived from different feedstock have significant effect on the fuel spray atomization, combustion and emission formation. In order to improve the performance of different biodiesel in terms of emissions and power output, various injection strategies have been implemented, after all, the combustion process is governed by the spray breakup process [232]. The spray break-up process controls the fuel-air mixing by better atomization followed by evaporation of fuel which eventually allows the combustion process to reach high efficiencies. In addition, the fuel injected at high pressures creates turbulence in interaction with the swirl flow inside the combustion chamber and affects the combustion speed.

Usually biodiesel have methyl esters with as many as 17-19 carbon atoms. Different biodiesels have different compositions of methyl esters. However, the major constituent governs the chemical and physical properties of the biodiesel fuel. Generally, for modeling purpose, the properties of major composition of the methyl esters are used to depict the properties of biodiesel fuel [233] or properties of mixture composition are considered [234, 235]. According to literature [236, 237], biodiesel generally have higher composition of methyl stearate (C18:0), methyl oleate (C18:1) and methyl linoleate (C18:2) (refer Table 3 in [236] and Table 6 in [237]). Though there are many experimental studies related to biodiesel spray development [141, 238, 239, 142], discovery of new feedstock makes it difficult to generalize the phenomenon. Nevertheless, there are some simulations on spray behavior found in literature related to specific biodiesel like soy bean [240, 241] and rape seed based biodiesel [233], but their results cannot be further extended in interpreting the behavior of other biodiesel.

The study on spray characteristics of biodiesel taking into account of cavitation

in the nozzle holes is very limited and it should be noted that the simulations were only done for soy bean based methyl esters [242, 195]. The differences in thermo-physical properties are also expected to significantly affect the nozzle flow characterization and eventually the spray breakup of biodiesel fuels. Thus the spray breakup process of biodiesel should include the cavitation phenomenon that influences the atomization process. Availability of very few studies on modeling spray atomization of biodiesel taking into account the nozzle flow characterization and absence of extension of work to different biodiesel provided motivation for the present work.

In this study, the spray atomization of three major methyl esters present in biodiesel: methyl oleate, methyl stearate and methyl linoleate were studied in order to generalize the spray behavior of different biodiesel. A new hybrid spray model which includes cavitation induced breakup model coupled with KHRT model was used in this study. In order to account for the cavitation into the spray model, internal flow simulations were done in prior for all three methyl esters and compared with diesel. The spray behavior of different methyl esters were compared with diesel in terms of spray tip penetration, Sauter mean diameter (SMD), liquid length at different injection pressure and ambient conditions.

5.5.3.1 Thermo-physical properties

The spray behavior depends on the thermo-physical properties of the fuel; hence it is necessary to understand them in detail. The properties were calculated for three main methyl esters found in majority of bio-diesel fuels and its blends, viz, methyl oleate, methyl stearate and methyl linoleate and for diesel, the standard thermo-physical properties available in KIVA4 fuel library was used. The properties of the fuels were calculated based on the prediction models suggested by An et al. [243]. According to An et al. the predictions of properties shows very good agreement with the data compilation results (experimental data) available in literature. The properties such as latent heat of vaporization, vapor pressure, viscosity, surface

Table 5.3: Predicted critical properties

Fuels	Critical Temperature	Critical Pressure	Critical Volume
	$T_c(K)$	P_c (bar)	V_c $(\mathrm{cm}^3/\mathrm{mol})$
Methyl Palmitate	782	12.5	1014
Methyl Stearate	774	11.46	1126
Methyl Oleate	772	11.68	1106
Methyl Linoleate	795	11.91	1086
Methyl Lenolenate	801	12.14	1066
Soy Methyl Ester (SME)	785.7	12.08	1082.1

tension, thermal conductivity, and density as a function of temperature were found for different methyl esters and compared with diesel as presented in Fig.5.21a-f. The properties of methyl esters were calculated based on group contribution methods from critical temperature, critical pressure and accentric factors for different fuels. The thermo-physical properties of Soy methyl ester (SME) bio-diesel were calculated based on mixture composition method [235, 244]. The critical properties predicted for methyl esters and SME bio-diesel are given in Table 5.3. The methods and empirical relations used to find the properties are presented in Table 5.4.

From Fig.5.21a, it is clear that the latent heat of vaporization for diesel is lower than those of esters in general. Also methyl ester has a slower evaporation rate than that of diesel. Fig.5.21b represents the vapor pressure comparison of diesel and methyl esters, in general methyl esters has low vapor pressure confirming slower evaporation rates and less tendency to cavitate than diesel fuel. The viscosity comparison is shown in Fig.5.21c, the viscosity of methyl esters are higher than diesel. The surface tension of different fuels shown in Fig.5.21d, shows no significant difference between them. However the slope of different fuels is different. Form Fig.5.21e, the thermal conductivity of diesel is much higher compared with that of methyl esters, which shows that diesel droplets conduct more heat than other methyl esters. Fig.5.21f compares liquid density; it is clear from the figure that methyl esters have higher density than diesel because of their longer carbon

chain and high molecular weight. The properties SME biodiesel mainly falls between methyl linoleate and methyl oleate which are its two major compositions by mass. These thermo-physical properties of three methyl esters and SME biodiesel were updated to the fuel library of KIVA4 for calculating the spray behavior.

5.5.3.2 Nozzle flow simulation

Cavitating flow inside the fuel injector nozzles is known to be an important factor affecting the fuel atomization and consequently the combustion process in diesel engines and hence it is significant to understand the nozzle flow of different fuels. For computation purposes, only one nozzle orifice was used taking advantage of the assumption of symmetric flow across the nozzles. The simulations were carried out for three different injection pressures (50, 100, and 150Mpa) under two ambient pressure conditions (3 and 6MPa).

Fig.5.22 shows the comparison of vapor volume fraction formed with different fuels viz diesel, methyl oleate, methyl stearate, and methyl linoleate under different injection pressures and at constant ambient pressure of 6MPa. It is observed that the amount of vapor volume formed depends on the pressure difference across the nozzle. Diesel undergoes higher cavitation than the methyl esters; this is because of the lower viscosity of diesel compared to other methyl esters as shown in Fig.5.21c. The cavitation inception also varies with different methyl esters based on their viscosity. As seen from Fig.5.21c, the viscosity of methyl linoleate is least followed by methyl oleate and stearate among different methyl esters. The same trend is observed with the vapor contours in Fig.5.22, methyl linoleate cavitates more followed by methyl oleate and methyl stearate. The reason for fuel with lesser viscosity to cavitate more may be due to the fact that reduction in viscosity increases the Reynolds number of the flow, which in turn creates more turbulence in the nozzle flow and eventually leads to greater cavitation [158]. Similar trends were also observed in experimental investigation of cavitation phenomenon of biodiesel in injector nozzles by Suh et al [178] and Zhong et al [245].

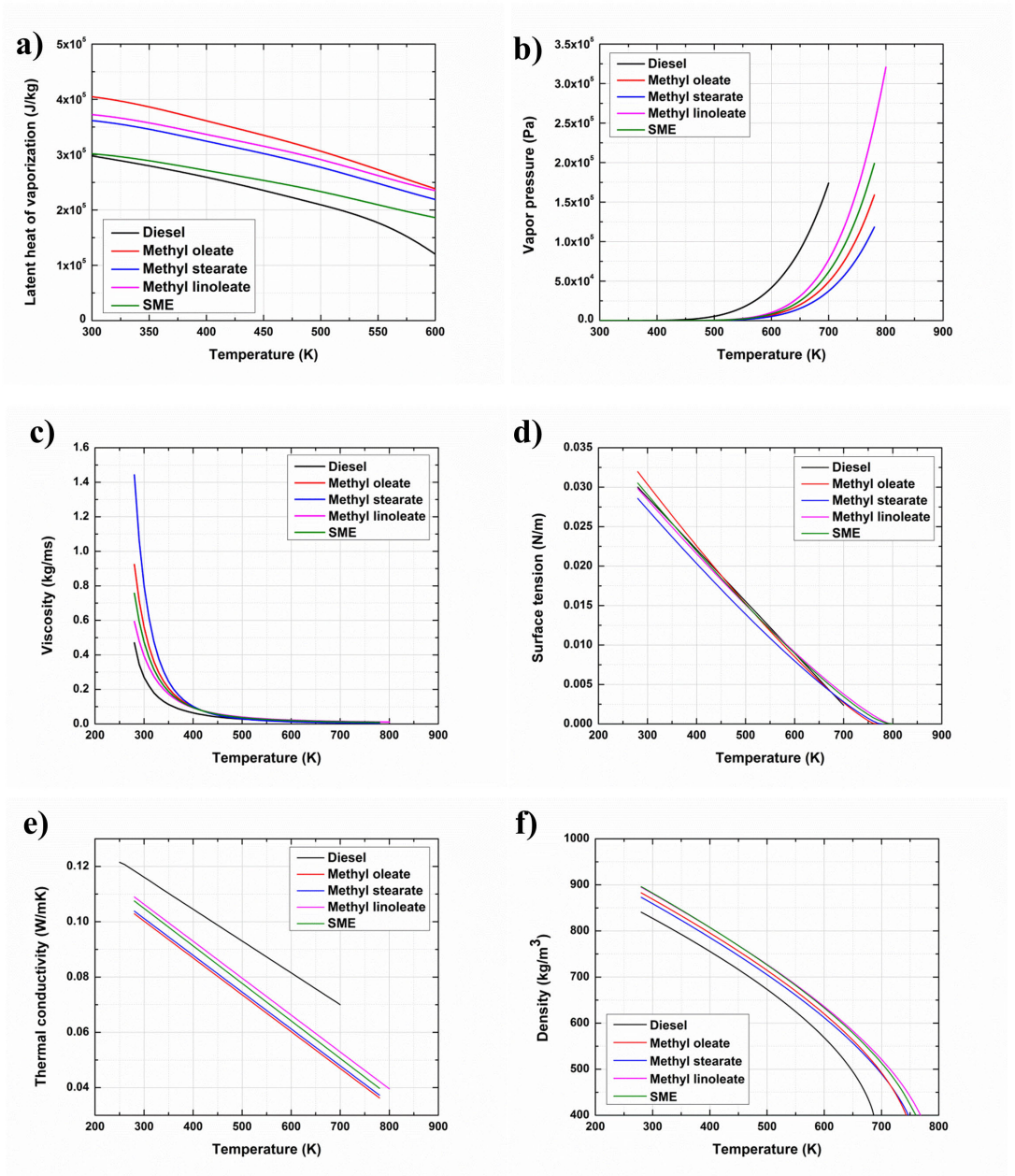

Figure 5.21: Thermo-physical properties of pure methyl esters, diesel and Soy methyl ester (SME)

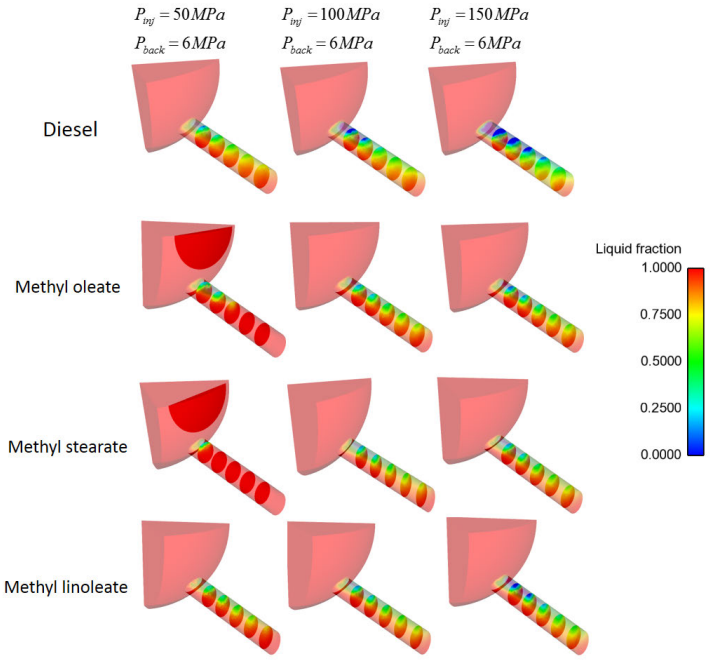

Figure 5.22: Cavitation inception for different fuels under different injection pressure at constant ambient pressure of 6MPa

Fig.5.23a illustrates the mass flow rate and coefficient of discharge for different fuel under different injection pressures and at constant ambient pressure of 6MPa. The results indicate that the mass flow rate of diesel is lesser compared to that of methyl esters, this is because of higher cavitation than methyl esters. This can be explained from the discharge coefficient, as it is least for diesel fuel, as discharge coefficient directly depends on the effective cross sectional area. As the effective cross sectional area decreases with increasing cavitation inception, the mass flow rate decreases. The mass flow rate of methyl linoleate is least among the methyl esters, as it undergoes higher cavitation due to its low viscosity as explained earlier. However, interestingly the mass flow rate of methyl stearate and methyl oleate shows no significant difference irrespective of their differences in viscosity, this may be due to the higher density of methyl oleate than other methyl stearate which compensates its low viscosity (see Fig.5.21f). Fig.5.23b represents the injection velocity of various fuels under different injection pressure and ambient pressure of 6MPa. The injection velocity shows increasing trend with the decrease of viscosity, this is because of the fact that less viscous flow is subjected to less viscous loss,

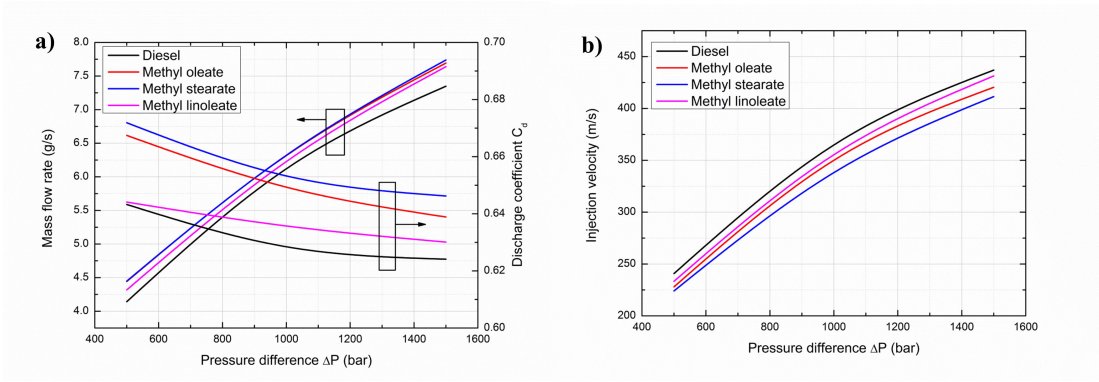

Figure 5.23: a) Mass flow rate and discharge coefficient b) injection velocity of different fuels at different injection pressure and at ambient pressure of 6MPa

and hence high exit velocity. From these results of nozzle flow simulation, it can be concluded that less viscous fuels are subjected to high cavitation and injection velocity which will aid in better atomization than high viscous fuels. In general, this result agrees well with the fact that the diesel fuel undergoes better atomization compared to biodiesel fuels. As previously discussed, it is also observed that the biodiesel with maximum percentage composition of methyl linoleate is subjected to high cavitation and injection velocity followed by biodiesel with high composition of methyl oleate and methyl stearate.

5.5.3.3 Spray characteristics of pure methyl esters

Fig.5.24 shows the comparison of spray tip penetration between diesel and methyl esters under non evaporating conditions for injection pressure of 100MPa, ambient pressure of 6MPa and ambient temperature of 300K. The simulation was carried out under inert atmosphere of nitrogen. The injection duration was maintained constant for all fuels throughout the spray simulation. It should be noted that the penetration of methyl esters is longer than that of diesel. This result confirms with many experimental measurements which shows biodiesel has longer penetration than that of diesel [142, 246, 159]. A similar trend is observed for injection pressures of 50 and 150MPa under same ambient conditions. Among the methyl esters, methyl linoleate shows the shortest penetration and stearate has the longest penetration. In general, the longer penetration of the methyl stearate compared

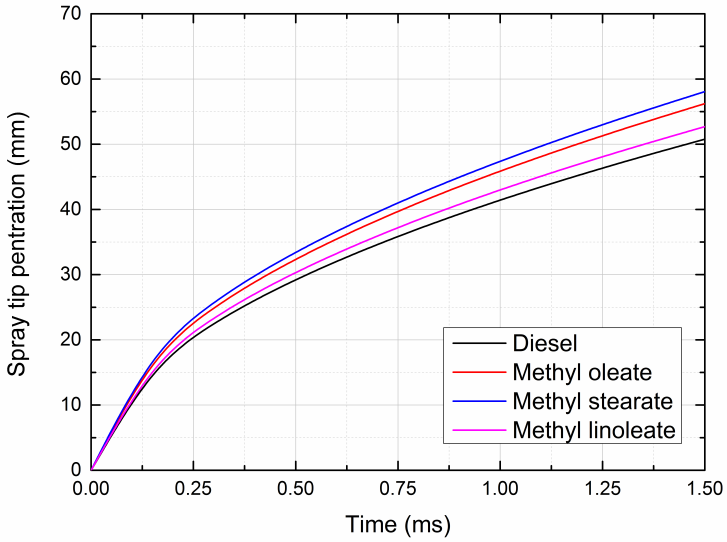

Figure 5.24: Spray tip penetration of diesel and methyl esters at injection pressure of 100MPa under ambient pressure of 6MPa and temperature of 300K

to diesel and other methyl esters may be due to two reasons: (a) higher spray momentum due to high discharge coefficient (see Fig.5.23a) [159] of the methyl stearate and/or (b) poor atomization leading to large droplets attributed by the low injection velocity (as shown in Fig.5.23 b) and lesser turbulence and cavitation at the exit of the nozzle (see Fig.5.22) due to its high viscous nature. The longer penetration length may have significant effect on the peak heat release rate during premixed combustion, ignition delay and early NO_x formation under normal engine operating conditions, as longer penetration helps in better air utilization and mixing due to fresh charge entrainment into spray plume further downstream. However long penetration may also lead to spray impingement on combustion chamber walls, which eventually leads to reduced combustion efficiency and increased unburned hydrocarbon formation [15].

Fig.5.25 shows the overall Sauter Mean Diameter (SMD) obtained from the simulation at 1.5ms after start of injection for different injection pressures under ambient pressure of 6MPa and temperature of 300K. The overall SMD also shows the same trend as that of spray tip penetration with methyl stearate having large droplets and diesel having small droplet size. It is very likely that large droplet size

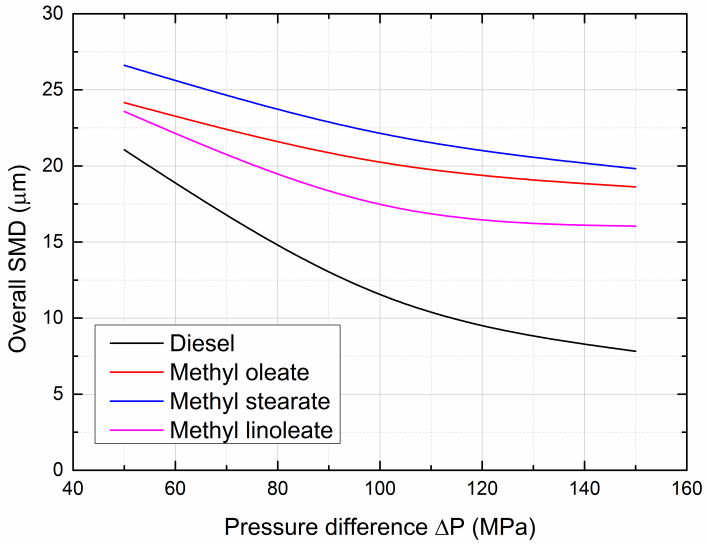

Figure 5.25: Overall SMD of diesel and methyl esters at different injection pressures under ambient pressure of 6MPa and temperature of 300K

may also be the reason for the long penetration lengths predicted for the methyl esters, as large droplets possess large momentum due to its size compared to diesel fuel resulting in long penetration lengths. According to Faeth and coworkers [247, 248], the limits of the breakup regimes in the atomization process are affected by the sufficiently large values of liquid viscosity. The effect of viscosity on breakup and atomization is well captured by the non-dimensional number called Ohnesorge number.

Therefore, to get greater insight into the atomization behavior of methyl esters, the numerical results are presented in the form non-dimensional numbers like Ohnesorge number and Weber number. Fig.5.26 shows the plot between Ohnesorge number and Weber number for various fuels under different injection pressure and ambient pressure of 6MPa at temperature of 300K. The Weber number and the Ohnesorge number are calculated from the overall droplet SMD and average velocity of the droplet at 1.5ms after start of injection. From Fig.5.26, it is clear that the diesel fuel is characterized by high Weber number and low Ohnesorge number. The methyl esters are generally characterized by lower Weber number and higher Ohnesorge number than diesel. The difference in Ohnesorge number

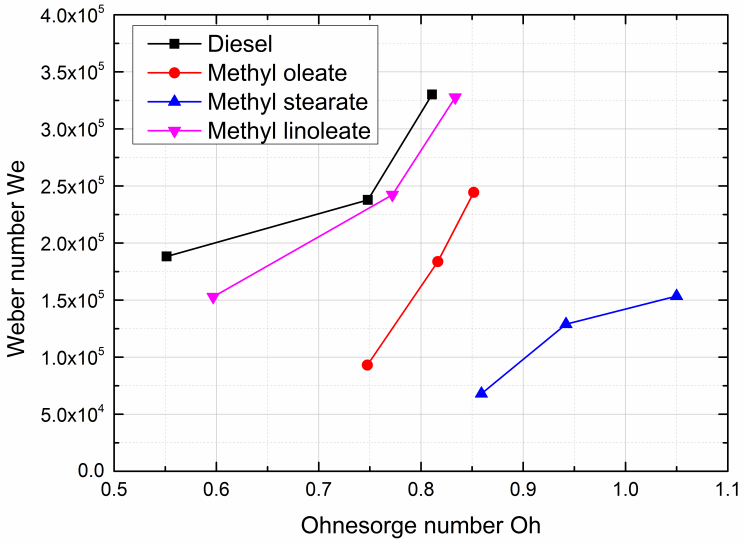

Figure 5.26: Ohnesorge number vs. Weber number for different fuels

is due to high viscosity of the methyl esters compared to diesel fuel. According Faeth et al. [247] all the fuels fall above Weber number of 80, shows that they all undergo shear breakup mechanism. However, the fuel with low Weber numbers indicates that the breakup takes place at a slow rate and also leads to low evaporation rate. From this point of view, biodiesel containing high composition of methyl oleate and stearate undergoes slow breakup of droplets, which indicate that they have poor atomization compared to biodiesel having methyl linoleate as its major component. This slow rate of breakup may affect the combustion process in engine operation, and may lead to increased local NO_x concentrations because of high inherent oxygen molecules present in methyl esters.

Fig.5.27 shows the liquid length of different fuels under ambient temperature of 1000K at different injection pressures and ambient pressure of 6MPa. The simulations were performed under inert atmosphere of nitrogen to avoid combustion. The liquid length shown in the figure is the value taken at 1.5ms after start of injection. The liquid length for all the fuel increases with the increase of injection pressure as the spray gains more momentum with increasing injection velocity. At high temperature, the liquid length obtained from the simulation shows a differ-

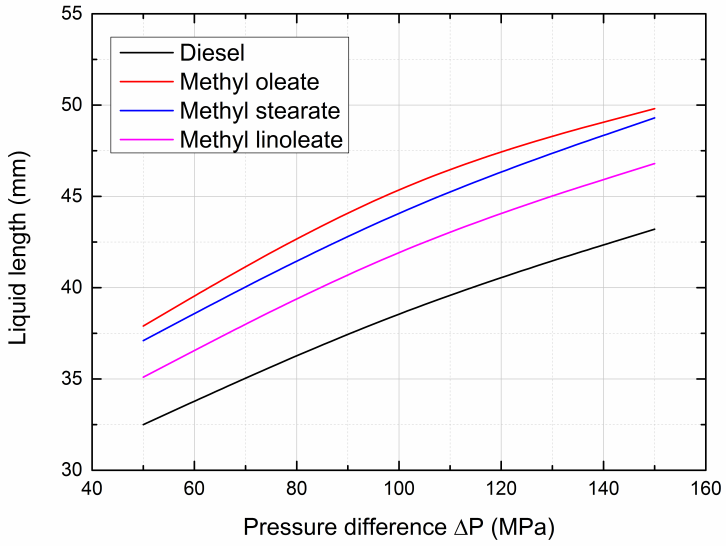

Figure 5.27: Liquid length for various fuels at different injection pressures under ambient pressure of 6MPa and temperature of 1000K

ent trend from the spray tip penetration measured at low temperature. At low temperature methyl stearate has longer spray tip penetration followed by methyl oleate, methyl linoleate and diesel in the order of decreasing viscosity. However at high temperature, the methyl oleate has longer liquid length followed by methyl stearate, methyl linoleate and diesel, this may be due to the combined effect of viscosity and latent heat of vaporization of different fuels. As methyl oleate has the highest latent heat of vaporization (Fig.5.21a), it requires more heat energy to vaporize and hence has longer liquid length at all injection pressures. However, methyl linoleate has higher latent heat of vaporization than methyl stearate, its low viscosity has improved its atomization and hence evaporation rate is improved resulting in shorter liquid length. From Fig.5.26, the high value of Ohnesorge number and Weber number of methyl linoleate also confirms that it undergoes better atomization than methyl stearate, which should be the reason for its shorter liquid lengths than methyl stearate. From these results, it is clear that biodiesel with major composition of methyl oleate has long liquid lengths at high temperatures because of its combined effect of viscosity and latent heat of vaporization, followed by biodiesel with major composition of methyl stearate and linoleate.

5.5.3.4 Spray characteristics of biodiesel fuels

Fig.5.28 shows the comparison between the experimental and simulation spray tip penetration of soy methyl ester (SME) biodiesel. The SME contains 54.67% methyl linoleate, 24.22% methyl stearate, 10.83% methyl palmitate, 6.78% methyl linolenate and 4.31% methyl stearate by mass [235]. The experimental values were obtained from Park et al. [246]. The simulation results were obtained for thermo-physical properties of SME, calculated based on mixture composition method, and major components in SME - methyl linoleate and methyl oleate. From the figure, it is clear that the spray tip penetration predicted using thermo-physical properties calculated by mixture composition method matches very well with the experimental results followed by methyl linoleate and methyl oleate. As the major composition is methyl linoleate the prediction of spray characteristics with its properties are on par with the mixture composition method. However, for methyl oleate, since its percentage by mass is only half of that of methyl linoleate, it deviates more from experimental results. So from this result, it can be observed that the properties of major composition of biodiesel can be used to predict the spray characteristics as close with properties calculated from mixture composition method. For good combustion simulation, it is always advisable to use the properties of biodiesel determined using the mixture composition method. Nevertheless, for fundamental understanding of any new or novel biodiesel spray characteristics, the properties of its major composition can be used with relative accuracy.

Fig.5.29 a and b shows the comparison between the experimental and simulation results in terms of spray tip penetration, fuel volume and equivalence ratio for B20 and B100 fuels respectively for injection pressure of 100MPa and ambient pressure of 3MPa. The experimental results are obtained in-house for waste cooking oil biodiesel (WCO) and its blend as reported in Chapter 3. The spray tip penetration and fuel volume are plotted against time whereas; the equivalence ratio is plotted against spray tip penetration. From the figure, it is clear that simulation results are found in agreement with the experimental results. The

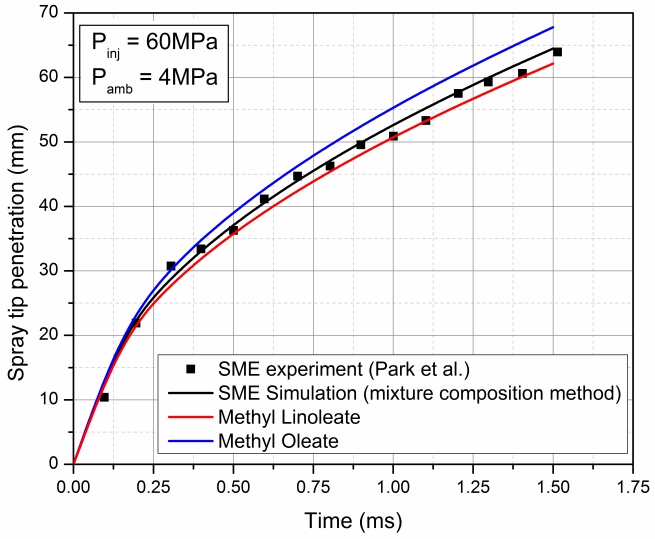

Figure 5.28: Comparison between simulation results of different fuel properties with experimental result

equivalence ratio was obtained directly from the simulation results and compared with the empirical results obtained from the experiment and also found in good agreement with each other. This shows the turbulence and cavitation developed inside the injector nozzle holes have significant effect on the spray development process.

5.6 Summary

A new hybrid spray model was developed by incorporating cavitation induced spray sub model into KHRT spray model. The internal flow simulation in the orifice of injector shows that the cavitation bubbles are swept out of the nozzle outlet. This showed that cavitation plays a significant role in primary spray breakup. Hence the cavitation induced spray sub model was incorporated into the KIVA4 CFD code along with the KHRT model. The newly developed spray model was extensively validated with the experimental results of constant volume combustion chamber obtained from the literature and also with the experimental results of combustion characteristics obtained from internal combustion engine by

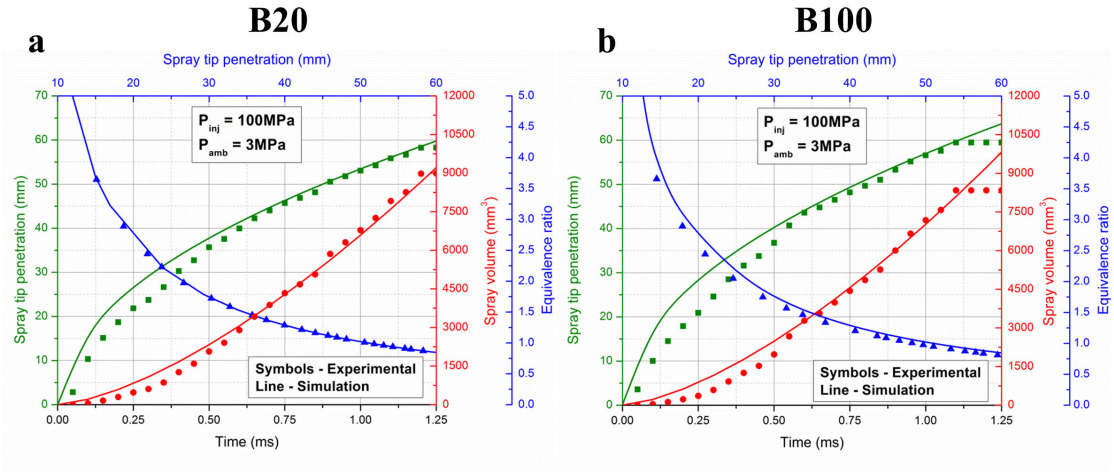

Figure 5.29: Comparison between in house experimental and simulation results for waste cooking oil biodiesel

the authors. The new hybrid spray model accurately captures the spray characteristics and obeys very well with both the constant volume combustion chamber experimental results of Sandia National laboratory and in house.

From numerical results on methyl esters the following observations are made:

- Methyl stearate tends to inhibit cavitation followed by methyl oleate and methyl linoleate under different injection pressure and ambient pressures due to their higher viscosity compared to diesel. This shows that biodiesel with high composition of methyl stearate is subjected to lesser cavitation in injector nozzles.

- The mass flow rate of methyl esters is higher compared to that of diesel because of the lower cavitation of the esters, which eventually leads to a high discharge coefficient than that for diesel. Injection velocity of methyl esters is lower than that of diesel because of the high viscous loss in the flow of methyl esters.

- From spray simulation it is found that methyl esters have higher spray tip penetration than diesel because of their high viscosity and bigger droplet diameter. In particular, methyl stearate has the highest penetration and largest droplet diameter followed by methyl oleate and methyl linoleate.

- Two non-dimensional numbers, Ohnesorge number and Weber number signify that viscosity of the fuel is the most dominant property in determining the spray atomization process. It is also observed that the methyl linoleate may atomize at par with diesel, but for methyl oleate and methyl stearate, the atomization is poorer.

- At high ambient temperature, it is observed that the liquid length of spray depends on both the viscosity and latent heat of vaporization of the fuels. Methyl oleate with highest Latent heat of vaporization has the longest liquid length followed by methyl stearate and methyl linoleate.

From the numerical simulations done with methyl esters, it seems biodiesel with high percentage composition of methyl linoleate may be favorable in terms better spray atomization than methyl oleate and methyl stearate. Biodiesel with high percentage composition of methyl stearate has poor atomization at low ambient temperature and methyl oleate at high ambient temperature.

The new spray model has been proved to be capable of predicting spray characteristics accurately. Therefore, it is appropriate to use this new hybrid spray model in simulating the engine combustion process. In the next chapter, 3D modeling of combustion process in engine with the new model is presented.

Table 5.4: Thermo-physical properties

Thermo-physical property	Prediction method	Empirical relation
Latent heat of vaporization	Pitzer accentric factor correlation [249]	$\frac{\Delta H_v}{RT_c} = 7.08\left(1-T_r\right)^{0.354} + 10.95\omega\left(1-T_r\right)^{0.456}$ where ΔH_v is the latent heat of vaporization in $^{\mathrm{J}}/_{\mathrm{mol}}$, R is the universal gas constant in $^{\mathrm{J}}/_{\mathrm{molK}}$, $T_r = \frac{T}{T_c}$ is the reduced temperature, T is the temperature in K, T_c is the critical temperature in K
Vapor pressure	Lee-Kesler method [249]	$\ln P_{vpr} = f^{(0)}\left(T_r\right) + \omega f^{(1)}\left(T_r\right)$ $f^{(0)} = 5.92714 - \frac{6.09648}{T_r} - 1.28862\ln T_r + 0.169347T_r^6$ $f^{(1)} = 15.2518 - \frac{15.6875}{T_r} - 13.472\ln T_r + 0.43577T_r^6$ where $P_{vpr} = \frac{P}{P_c}$ is the reduced vapor pressure, P_c is the critical pressure in bar, $\omega = \frac{\alpha}{\beta}$ is the accentric factor $\alpha = -\ln P_c - 5.97214 + 6.0948\theta^{-1} + 1.28862\ln\theta - 0.169347\theta^6$ $\beta = 15.2518 - 15.6875\theta^{-1} - 13.4721\ln\theta + 0.43577\theta^6$, $\theta = \frac{T_b}{T_c}$
Viscosity	Letsou and Stiel method [249]	$\eta_{SL}\xi = \left(\eta_L\xi\right)^{(0)} + \omega\left(\eta_L\xi\right)^{(1)}$ $\left(\eta_L\xi\right)^{(0)} = 10^{-3}\left(2.648 - 3.725T_r + 1.309T_r^2\right)$ $\left(\eta_L\xi\right)^{(1)} = 10^{-3}\left(7.425 - 13.39T_r + 5.933T_r^2\right)$ $\xi = 0.176\left(\frac{T_c}{M^3P_c^4}\right)^{\frac{1}{6}}$ where, η_{SL} is the viscosity in cP

		M is the molecular weight in $^{g}/_{mol}$
Surface Tension	Corresponding states correlation [249]	$\frac{\alpha}{P_c^{\frac{2}{3}} T_c^{\frac{1}{3}}} = (0.132\alpha_c - 0.279)(1 - T_r)^{\frac{11}{9}}$ $\alpha_c = 0.9076 \left[1 + \frac{T_{br} \ln\left(\frac{P_c}{1.01325}\right)}{1 - T_{br}}\right]$ where, σ is the surface tension in $^{dyne}/_{cm}$ α_c is the Riedel parameter
Thermal Conductivity	Latini et al. method [249]	$\lambda_L = \frac{A(1-T_r)^{0.38}}{T_r^{\frac{1}{6}}}$, $A = \frac{A^* T_b^{\alpha}}{M^{\beta} T_c^{\gamma}}$ where, $\lambda_L$is the thermal conductivity in $^{W}/_{mK}$, $A^* = 0.0415$, $\alpha = 1.2$, $\beta = 1.0$, $\gamma = 0.167$ for esters
Density	Modified Rackett equation [249]	$\rho_s = \rho_{ref} * Z_{RA}^{\phi}$, $Z_{RA} = 0.29056 - 0.08775\omega$ $\phi = (1 - T_r)^{\frac{2}{7}} - \left(1 - T_r^R\right)^{\frac{2}{7}}$ where, ρ_s is the density in $^{g}/_{cm^3}$, ρ_{ref} is the known density at reference temperature T_R in $^{g}/_{cm^3}$ ω is the accentric factor

6

Effect of injection strategies on engine performance and emissions[1]

6.1 Experimental investigation

Compression ignition (CI) engines play a significant role as a power source in most industries, to generate electricity, and to power most transportation commodities from boats to trucks. They are typically chosen for such applications because of their fuel efficiency and longer service life compared to spark ignited (SI) gasoline

[1]Excerpts of this chapter, in part, is a reprint of previous publication titled "*Optimization of biodiesel fueled engine to meet emission standards through varying nozzle opening pressure and static injection timing*", Applied Energy 130, 450-457, 2014. DOI: 10.1016/j.apenergy.2014.02.033. and "*Numerical investigation on the effects of injection rate shaping on combustion and emission characteristics of biodiesel fueled CI engine*", (Submitted for a special issue in Applied Energy)

engines. Furthermore, the stationary diesel engines (genset engines) are gaining popularity and increasing in numbers among developing countries due to power crisis albeit leading to the twin crisis of fossil fuel depletion and environmental degradation due to exhaust emissions. Despite its numerous advantages, CI engines also possess some disadvantages. According to Health Effect Institute (HEI) [11], the exhaust emissions from engines have detrimental effects on the health. In order to tackle the emission issues, various norms were imposed on genset engines across the world. For example, one such norm implemented in India to reduce emissions from genset engines is shown in Table 6.1. The genset engines should be tested over the 5 mode ISO 8178 D2 cycle for homologation type approval to ensure it meets required emission norms [13].

Table 6.1: Emission standards for diesel engines for gensets

Engine Power	Date	CO	HC	NO_x	PM	Smoke [a]
		g/kWh				m^{-1}
P≤19kW	Jul 2005	3.5	1.3	9.2	0.3	0.7
19kW<P≤50kW	Jul 2004	3.5	1.3	9.2	0.3	0.7
50kW<P≤176kW	Jan 2004	3.5	1.3	9.2	0.3	0.7
176kW<P≤800kW	Nov 2004	3.5	1.3	9.2	0.3	0.7

[a] Smoke opacity should be measured at full load

In order to reduce the dependency on depleting fossil fuels researchers are studying the use of various biodiesel and blend fuels with existing engines with or without any modifications to the engines [237, 250, 251, 252, 253, 55]. Mahua methyl ester (Madhuca Indica) [250], a biodiesel which is produced by trans esterification process from non-edible oil, is one of the promising candidates identified from such researches with an estimated annual production potential of 181 thousand metric tons in India [254]. Furthermore, its combustion and emission characteristics are well studied. In 2007, Raheman and Ghadge [255] reported that by increasing the proportion of biodiesel in its blends with diesel, the brake specific

fuel consumption (BSFC) was increased and brake thermal efficiency (BTE) was decreased. Interestingly, they have also reported that at 100% load conditions, the BTE of B20 blend (25%) was higher than diesel (24%) and at other loads it was at par with diesel fuel. The smoke level and carbon monoxide (CO) in exhaust emissions were reduced, whereas oxides of nitrogen (NO_x) increased with increase in percentage of mahua biodiesel in the blends. Later in 2009, Godiganur et al. [256] also reported very similar results with their study on mahua methyl ester as fuel with different engine specification. Overall literature results [255, 256] suggest that mahua biodiesel could be safely blended with diesel up to 20% without significantly affecting the engine performance and emissions. In general any biodiesel used with engine without any modification gives higher NO_x emission because of oxygen present within the biodiesel molecules [236]. Therefore, alteration of fuel injection parameters like injection pressure and injection timing can remedy this issue, as they have a stronger effect on NO_x emissions for direct injection engines [15, 257, 232]. Kannan and Anand [57] have studied the effect of injection pressure and injection timing on waste cooking oil and found that the combined effect of higher injection pressure of 280 bar and an advanced injection timing of 25.5 $^\circ$ bTDC significantly improves BTE, in-cylinder pressure and heat release rate while reducing nitric oxide (NO) and smoke emission. Similarly, Puhan et al. [53] studied the effect of injection pressure on high linolenic linseed oil methyl ester at an optimized pressure of 240 bar and observed the engine to operate at a thermal efficiency similar to that of diesel, but with reduced emissions of CO, unburned hydrocarbon and smoke. However, they also observed an increase in the NO_x when compared to diesel. The combustion analysis showed that the ignition delay is shorter at higher injection pressures compared to diesel. Pandian et al. [55] investigated the effects of injection pressure, injection timing and nozzle tip protrusion on the performance and emission of DI engine fueled by pongamia bio-diesel. The optimization was done based on the statistical tool known as design of experiments using the response surface methodology (RSM).

The optimal injection timing, injection pressure and nozzle tip protrusion were found to be 21° bTDC, 225 bar, 2.5 mm respectively for lower emissions of NO_x, CO, Hydrocarbon (HC) and smoke opacity and higher brake thermal efficiency. In a most recent study, Sayin et al. [258] studied the effect of injection pressure on canola oil methyl ester – diesel blends and found that increased injection pressure gave better results for BSFC and BTE compared to the original 20MPa and decreased injection pressures. Therefore from the literature, it was very clear that by implementing fuel injection strategies could reduce emissions and improve performance, although none of them showed whether it could meet the existing emission norms.

In this study, varying nozzle opening pressure (NOP) and injection timing were applied to meet the genset emission norms with biodiesel blend. 20% mahua biodiesel was used to meet current genset emission norms implemented in India. The tests were done in compliance with ISO 8178 D2 cycle to ensure the engine meet the stringent emission norms. As per ISO 8178 D2 cycle, 10%, 25%, 50%, 75% and 100% load conditions at 1500 rpm were tested with both diesel and 20% biodiesel. The optimization was carried out for B20 by varying nozzle opening pressure (225, 250 and 275 bar) and varying injection timing (19, 21, 23, 25, 27 ° bTDC). The parameters like BSFC, BTE, exhaust gas temperature (EGT), in-cylinder pressure and heat release rate were measured in order to evaluate the performance and combustion characteristics and NO_x, HC, CO and smoke emissions were measured at various nozzle opening pressures and injection timing.

6.1.1 Experimental setup

The experimental set up consists of a Kirloskar TV1 stationary diesel engine with a water cooled eddy current dynamometer as shown in Fig.6.1. The engine specifications are given in Table 6.2. Kirloskar TV1 stationary diesel engine is chosen for this study, since single cylinder diesel engines with mechanical fuel injection systems are more suitable for biodiesel blend fuels to operate in long run. Also

stationary diesel engines or gensets used in marine and agricultural applications are operated at a particular speed and loading conditions for a long time. This engine used in the study is a common type of engine used in agricultural applications throughout the country, as India is predominantly an agricultural country; the engines of this kind are used in high numbers by farmers for both small scale power generation and irrigation purposes. The fuel flow rate was measured on volume basis using a burette and a stop watch. AVL 619 indimeter along with Indwin software were used to measure the in-cylinder pressure, heat release rate, pressure rise rate and variations in cycle. Measurement of combustion chamber pressure was obtained from an AVL transducer with the sensitivity of 16:11 pC/bar. Non-dispersive infrared analyzer (NDIR-AVL-444 Digas) was used to measure exhaust emissions like NO_x, HC, CO_2, CO and O_2. To ensure that the exhaust gas is free of moisture content and particulates before entering the analyzer, the exhaust gas was passed through moisture separator (cold trap) and filter element. The exhaust gases NO_x and HC were measures in parts per million (ppm) of hexane equivalents while and CO, CO_2 and O_2 emissions were measured in terms of volume percentage. The accuracy and the measuring range of the analyzer are given in Table 6.3. The exhaust gas temperature was measured using a K-type thermocouple which was coupled with a digital display. Smoke level was measured using a standard AVL437C smoke meter. The diesel and mahua methyl ester meeting the standards (EN14214 and ASTM 6751-02) as shown in Table 6.4 were used in this study. B20 was prepared by mixing 20% by volume of mahua methyl ester with diesel.

6.1.1.1 ISO 8178 D2 Cycle

ISO 8178 is an international standard used for emission certification and/or type approval in many countries worldwide, especially in India. Therefore, the D2 cycle (Fig.6.2) of ISO 8178 (also called 5 mode test cycle) is used as standard for testing in this study.

The weighting factors for the five modes are used to calculate the composite

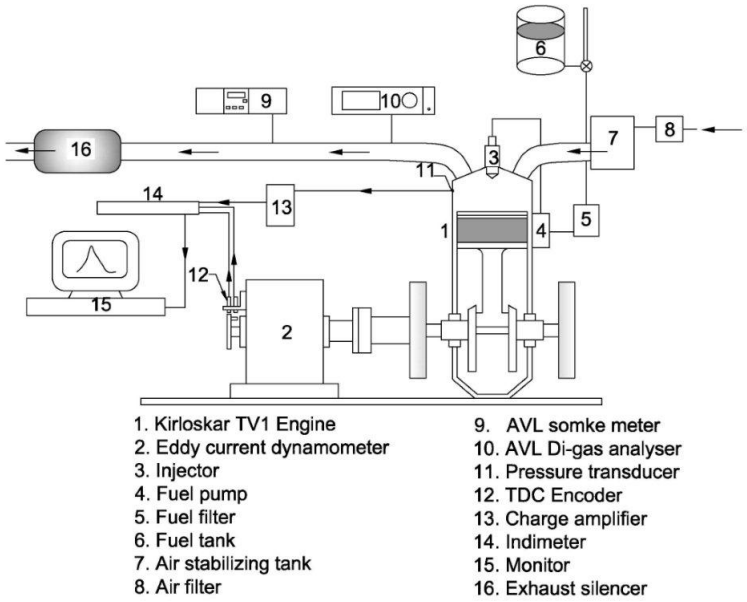

Figure 6.1: Schematic of engine setup

Table 6.2: Engine specification

Type	Kirloskar TV1
No. of cylinders	one
Bore	87.5 mm
Stroke	110 mm
Compression ratio	17.5:1
Rated power	5.2kW at 1500 rpm
Dynamometer	Eddy current
Type of injection	Mechanical pump-nozzle injection
No. of nozzle holes	3
Lubricating oil	SAE40

Table 6.3: Accuracy and measuring range of AVL-444 digas analyzer

Measured quantity	Measuring range	Resolution	Accuracy
CO	0∼10 vol%	0.01 vol%	$<$ 0.6 vol% $\pm$0.03 vol
CO_2	0∼20 vol%	0.1 vol%	$<$ 10 vol% $\pm$0.5 vol
HC	0∼20000 ppm	$\leq$2000:1 ppm	$<$ 200 ppm $\pm$10 ppm
O_2	0∼22 vol%	0.01 vol%	$<$ 2 vol% $\pm$0.1 vol
NO_x	0∼5000 ppm	1 ppm	$<$ 500 ppm $\pm$50 ppm

emissions. To normalize the composite emissions values to a unit power basis, the composite emissions values are divided by a weighted power value according to

Table 6.4: Fuel properties of diesel and biodiesel blend used

Fuel properties	Diesel	B20	Standards	
			ASTM 6751-02	EN 14214
Density at 15 ° C (kg/m^3)	822	856	-	860-900
Viscosity at 40 ° C (m^2/s)	$2.6 * 10^{-6}$	$2.88 * 10^{-6}$	$1.9 - 6.0 * 10^{-6}$	$3.5 - 5.0 * 10^{-6}$
Calorific value (MJ/kg)	42.7	41.7	-	-
Acid value ($mgKOH/g$)	-	0.36	<0.8	<0.5
Flash point ($^\circ C$)	74	96	>130	>120
Pour Point ($^\circ C$)	-23	-3	-	-
Water content (%)	1.6	0.03	<0.03	<0.05
Ash content (%)	0.90	0.01	<0.02	<0.02
Carbon residue (%)	3.70	1.07	-	<0.3

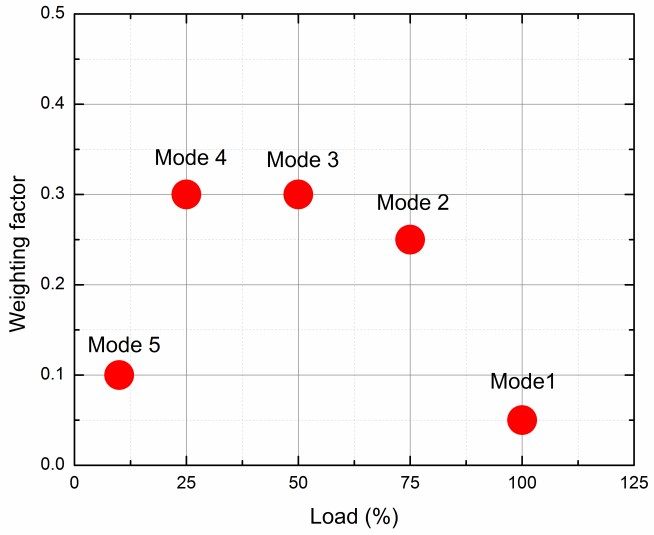

Figure 6.2: ISO 8178 D2 cycle

the following formula [259]

$$E_{comp} = \frac{\sum_{i=1}^{n} (WF_i * E_i)}{\sum_{i=1}^{n} (WF_i * P_i)} \tag{6.1}$$

where, E_{comp} is weighted composite emissions (g/kWh), WF_i is weighting factor for mode i, E_i is emissions for mode i,(g/h), P_i is power for mode i (kWh) and n is number of modes. Applying the emission weighting factors to the measured

emissions in each mode, with a subsequent normalizing to a weighted power basis, produces the composite emissions values.

6.1.1.2 Calculation method

The composite emission E_{comp} is calculated using the Eq. 6.1. The emissions measured are in parts per million (ppm), hence it should be converted into (g/h), so that it can be conveniently used in Eq.6.1. For conversion purposes, the following formula were used

$$E_{NO_x}\,(g/h) = 0.001587 * E_{NO_x}\,(ppm) * K_{NO_x} * \dot{m}_e \tag{6.2}$$

$$E_{CO}\,(g/h) = 0.000966 * E_{CO}\,(ppm) * \dot{m}_e \tag{6.3}$$

$$E_{HC}\,(g/h) = 0.000479 * E_{HC}\,(ppm) * \dot{m}_e \tag{6.4}$$

whereK_{NO_x} is the NO_x correction factor and $\dot{m}_e$ is the exhaust mass flow rate (kg/h).

By principle of conservation of mass, the mass flow rate of exhaust gas is given as

$$\dot{m}_e = \dot{m}_a + \dot{m}_f \tag{6.5}$$

where $\dot{m}_a$ is the mass flow rate of intake air (kg/h) and $\dot{m}_f$ is the mass flow rate of fuel (kg/h).

The impact of ambient temperature and humidity on NO_x emissions is important to make comparisons of the NO_x emissions from engines tested at different locations and/or with variations in the ambient conditions. In order to allow day-to-day and location-to-location comparisons various correction factors have been developed. The goal for these correction factors is to standardize the NO_x emis-

sions to reference conditions. For generators, the NO_x correction factor developed by Fritz and Dodge [260] was suggested by EPA [261]. The NO_x correction factor is given by the following equation

$$K_{NO_x} = \frac{1}{K_H K_T} \tag{6.6}$$

where,

$$K_H = \frac{C_1 + C_2 e^{(-0.0143)(10.714)}}{C_1 + C_2 e^{(-0.0143)(1000H)}} \tag{6.7}$$

$$K_T = \frac{1}{1 - 0.017\,(T_{30} - T_A)} \tag{6.8}$$

where $C_1 = -8.7 + 164.5e^{-0.0218(A/F)}$, $C_2 = 130.7 + 3941e^{-0.0248(A/F)}$, H is the specific humidity on a dry basis of the intake air (g/kg) , A/F is the mass of air intake to mass of fuel supplied, T_{30} is the temperature measured at intake manifold when operated at $30\,^\circ C$ ambient temperature, T_A is the temperature measured at intake manifold during normal operation of engine ($^\circ C$).

6.1.1.3 Uncertainty analysis

The uncertainty analysis is vital to ascertain the confidence in the experimental results. By using the Propagation of uncertainty principle suggested by Holman [262], the total uncertainty in the experiment due to uncertainty in measurement of various parameters like total fuel consumption (TFC), brake power (BP), brake specific fuel consumption (BSFC), brake thermal efficiency (BTE), carbon monoxide (CO), hydrocarbon (HC), smoke, oxides of nitrogen (NO_X), exhaust gas temperature (EGT), and Combustion pressure (CP) were calculated as follows

Total experimental uncertainty = [(uncertainty of TFC)^2 + (uncertainty of BP)^2 + (uncertainty of BSFC)^2 + (uncertainty of BTE)^2 + (uncertainty of CO)^2 + (uncertainty of HC)^2 + (uncertainty of smoke)^2 + (uncertainty of NO_X)^2 + (uncertainty of EGT)^2 + (uncertainty of CP)^2]$^{1/2}$

$= [(1)^2 + (0.2)^2 + (1)^2 + (1)^2 + (0.2)^2 + (0.1)^2 + (1)^2 + (0.2)^2 + (0.15)^2 + (1)^2]^{1/2}$

$= 2.26\%$

6.1.2 Experimental method

6.1.2.1 Nozzle opening pressure (NOP)

In order to study the effect of nozzle opening pressure on engine performance, combustion and emission characteristics, the injection timing was kept constant at manufacturer's default value of 23 ° bTDC. Three nozzle opening pressures (225, 250 and 275 bar) were studied and the results were compared with diesel at nozzle opening pressure of 225 bar. The NOP was adjusted by increasing or decreasing the preload of the spring inside the injector. The preload was adjusted by adding or removing shims. The process was continued till the required NOP was obtained.

6.1.2.2 Static injection timing

The effect of injection timing (19, 21, 23, 25, 27 ° bTDC) was studied by keeping the nozzle opening pressure to a default value of 225 bar. In mechanical fuel injection systems, the start of injection is difficult to control as it depends on fuel transport in the pump, high pressure pipes and the injector. However, the start of injection is closely related to the start of pump delivery, which can be set easily to any desired value. The timing was varied by adjusting the shim thickness at the connection point between the pump and the engine. Increasing the shim thickness retards the start of pump delivery and by reducing shim thickness; advance in start of pump delivery was achieved.

6.1.3 Results and Discussion

6.1.3.1 Effect of nozzle opening pressure

The effect of NOP on combustion parameters like in-cylinder pressure and heat release rate at 100% load are shown in Fig.6.3. It is clear from the in-cylinder pressure curves that the maximum pressure achieved is more or less equal for all nozzle opening pressures compared to diesel. Meanwhile, an increase in NOP tends to retard the dynamic injection timing. It is clear from Fig.6.3 that the heat release rate of B20 at 225 bar NOP is advanced compared to diesel and for 250 bar it is advanced to diesel but retarded compared to 225 bar, and at 275 bar NOP, the HRR is in par with the diesel. The advanced start of combustion for B20 compared to diesel at same NOP is because of higher bulk modulus of B20. The advance in injection timing due to the higher bulk modulus of biodiesel blend fuels was reported by various researchers in literature [263, 94]. The increase in NOP of B20 fuel retards the fuel injection as the time taken for the fuel to transport from the fuel injection pump to the injector and build the required NOP increases with increasing NOP. Thereby increase in NOP to 275 bar compensates the advanced injection timing due to higher bulk modulus of biodiesel blend and its HRR is in par with the diesel fuel.

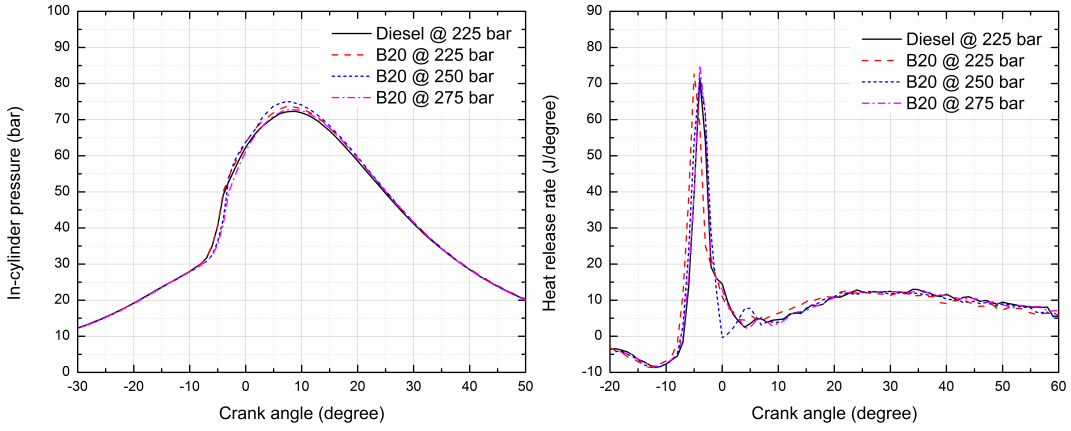

Figure 6.3: In-cylinder pressure and heat release rate at varying NOP

Performance parameters such as BTE and BSFC are shown in Fig.6.4. It can be observed from the figure that BTE for B20 under various NOP is higher than that of diesel due to the presence of oxygen in B20 which improves the combustion process [104]. Furthermore, as the NOP increases from 225 bar to 250 bar, BTE is increased due to improved fuel atomization at high fuel injection pressure. However, when the NOP was further increased to 275 bar, there is no further improvement in the BTE, which is due to combined effect of retarded injection timing and the improved fuel atomization. As a result of enhanced combustion, the BSFC for B20 is lesser than diesel at all loads.

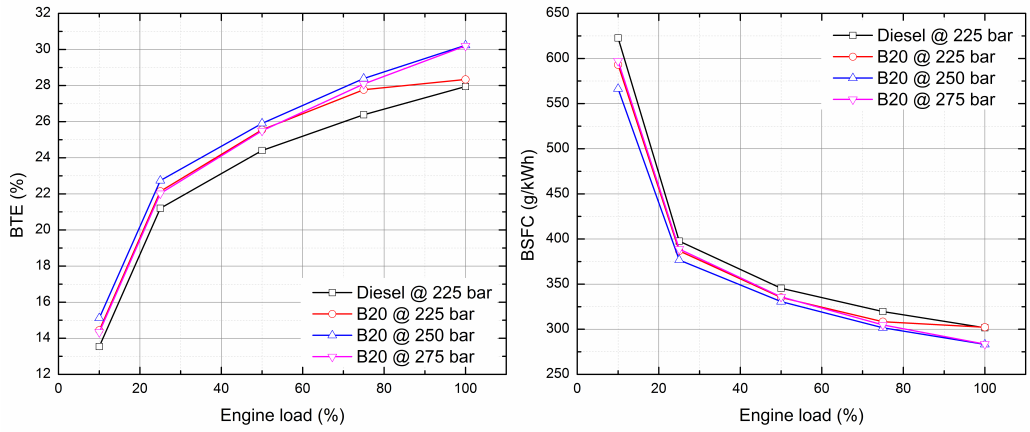

Figure 6.4: BTE and BSFC at varying engine loads for different NOP

The composite emissions of NO_x, HC and CO at different NOP are shown in Fig.6.5. They are calculated based on the Eq.6.1 for ISO 8178 D2 cycle followed throughout the experiments. The emissions are compared with the Indian emission norms for genset as shown in Table 6.1 for power $\leq$ 19 kW as the maximum power output of the engine used is 5.2kW at 1500 rpm.

The composite emission of corrected NO_x shows a decreasing trend as the NOP increases, this is because of the fact that by increasing the NOP, the start of combustion retards. When the NOP is set to 275 bar, the composite emission of corrected NO_x was calculated to be 8.67 g/kWh which is less than the legislative norms for NO_x, i.e., 9.3 g/kWh. The composite HC emission is very low for

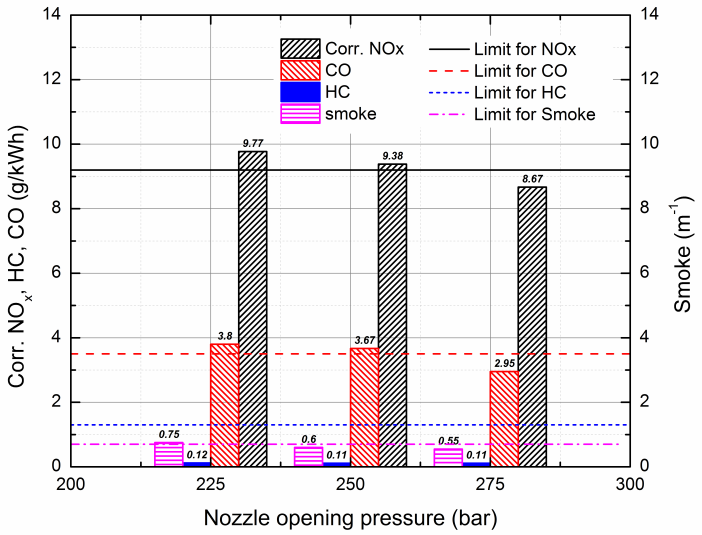

Figure 6.5: Composite emissions at varying NOP

all NOP conditions and there is a slight drop with the increase of NOP. This may be due to presence of oxygen within the biodiesel which tends to reduce the HC formation and a higher NOP means a better atomization. The value of composite HC observed at 275 bar NOP is 0.11 g/kWh which is very much lower than the legislative norm value of 1.3 g/kWh. The composite CO emission shows a decreasing trend with increasing NOP due to improved atomization. The minimum composite CO of 2.95 g/kWh is observed at 275 bar NOP which is lower than the legislative norm value of 3.5 g/kWh.

The variation of smoke emission is also shown in Fig.6.5 for different NOP. The smoke shown is for full load condition as per regulatory norms. The smoke measured in Hartridge smoke unit (HSU) was converted to K coefficient of light absorption (m^{-1}) for comparison with the emission regulations [264]. Smoke emissions are typically caused by an inadequate supply of air for combustion during times of engine acceleration, or by low combustion temperatures. However for the B20 blend, the biodiesel offers sufficient oxygen for burning. The aromatics which are known to contribute soot formation is reduced by the inherent oxygen molecule in the biodiesel and helps to promote complete combustion by delivering

oxygen to the prolepsis zone of the burning fuel [265]. Also an increase in NOP results in smaller fuel particles introduced into the combustion chamber, which also leads to enhanced fuel air mixing and aides in smoke reduction. It is evident from the Figure that at 275 bar NOP the smoke emission is lesser at full load condition and also within regulatory norms. Similar results were also reported by other researchers with different biodiesel and its blends [57, 55].

By comparing both emissions and performance of B20 with various NOP, it was found that by changing only the nozzle opening pressure from 225 to 275 bar, we could meet the genset emission norms without significant effect on performance with B20 blend of mahua biodiesel. By increasing NOP to 275 bar, the NO_x, CO, HC and smoke emissions achieved are lesser by 5.7%, 15.7%, 91.5%, 21.4% compared to the emission limits respectively along with an improvement in BSFC by 6% compared to diesel.

6.1.3.2 Effect of static injection timing

The effect of injection timing on in-cylinder pressure and heat release rate are shown in Fig.6.6. With the advance of fuel injection timing, the peak pressure increases and appears earlier due to the fact that more fuel is burnt before TDC. The maximum in-cylinder pressure is achieved at 27 ° bTDC injection timing.

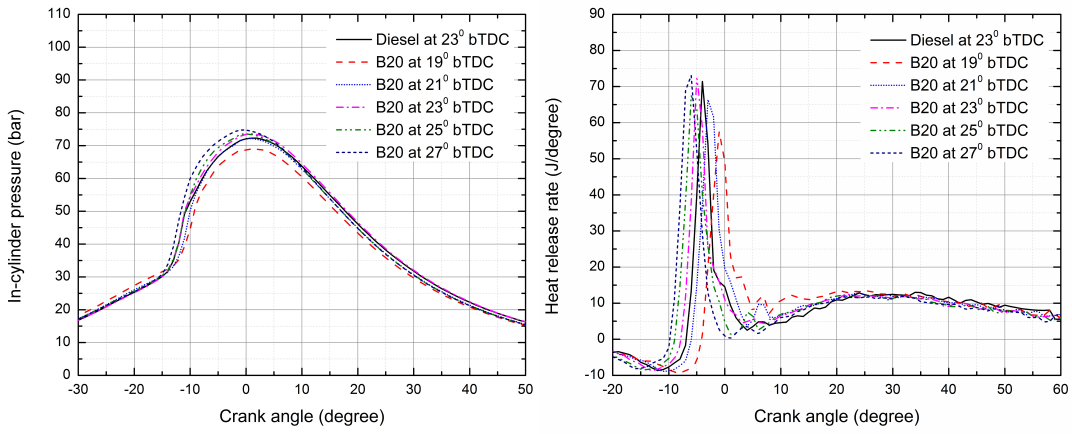

Figure 6.6: In-cylinder pressure and heat release rate at varying NOP

The heat release rate also shows the same trend as in-cylinder pressure, i.e., with the advance of fuel injection timing, the start of combustion takes place earlier, and the peak heat release rate increases. This is because more fuel is burnt during premixed combustion phase due to relatively longer ignition delay as a result of lower temperature inside the combustion chamber during injection.

The performance parameters – BTE and BSFC are shown in Fig.6.7 for different static injection timing compared to diesel. The least BSFC compared was observed when the injection timing was 25 ° bTDC which again increases as injection timing is further advanced to 27 ° bTDC. When retarding the injection timing to 21 ° and 19 ° bTDC, the BSFC is found deteriorated compared to original injection timing of 23 ° bTDC but still comparable with the diesel fuel at 23 ° bTDC. By advancing the injection timing to 27 ° bTDC, the peak pressure rise is achieved before the piston reaches TDC, but this causes reduction in engine power output. To maintain the same power output for comparison purposes fuel quantity was further increased. Therefore, fuel consumption per output power increased when the injection timing is advanced to 27 ° bTDC. However, retarding injection timing leads to late combustion. Then the pressure rise occurs when the cylinder volume was expanding, which results in reduced effective pressure to do work leading to higher fuel consumption for the same power output [266]. The BTE is also higher for all loads at injection timing of 25 ° bTDC and gets poorer when further advanced. But by retarding the timing there is no significant degradation of BTE.

The composite emissions at different static injection timing for B20 are compared to the regulatory norms and shown in Fig.6.8. It is clear that the composite corrected NO_x decreases with retarding injection timing. When injection timing is advanced, higher temperatures are attained inside the combustion chamber because more fuel-air mixture is burnt in premixed combustion phase due to increased ignition delay. On the hand, retarded injection timing results in reduced NO_x emissions. Similar results were obtained by other researchers with different

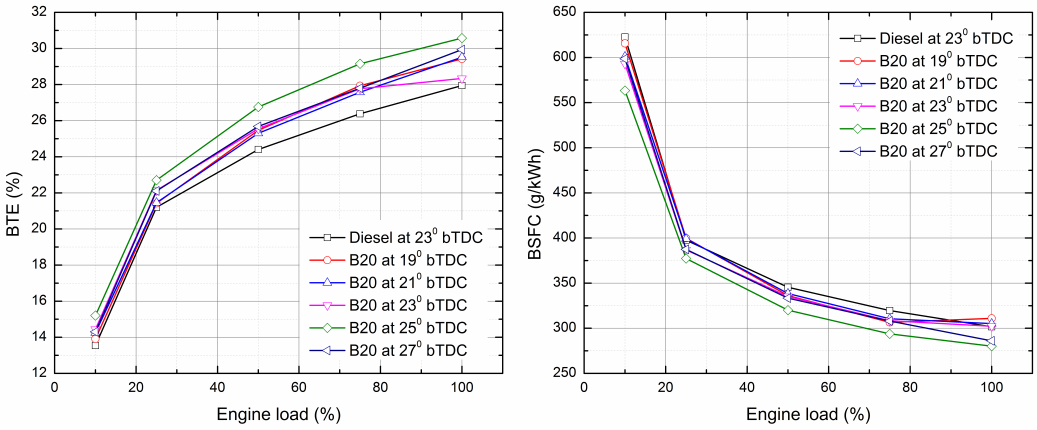

Figure 6.7: BTE and BSFC at varying engine loads for different static injection timing

fuels [267, 102]. However, interestingly, when the composite corrected NO_x emissions were compared with regulatory norms, it is found that either 19 ° or 21 ° bTDC injection timing meets the standards.

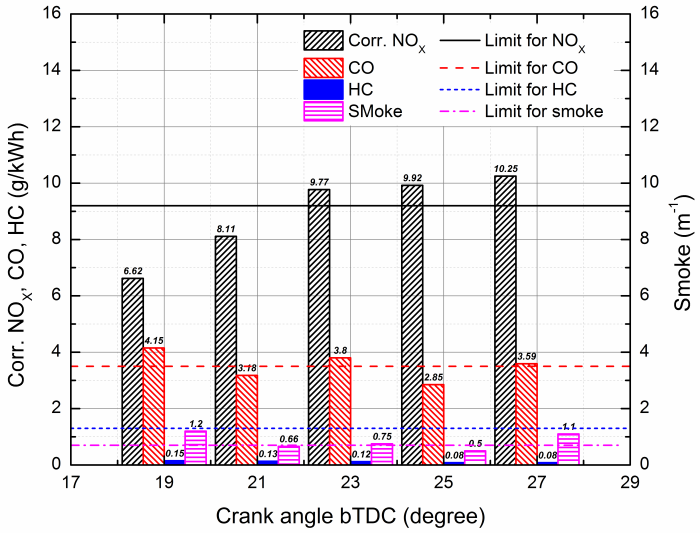

Figure 6.8: Composite emissions at different static injection timing

Fig.6.9, shows the trade-off between NO_x emissions with BSFC at 100% engine load. The NO_x-BSFC trade-off shows that there is no significant deterioration in BSFC compared with the reduction in NO_x emissions by retarding the injection timing. The BSFC is increased by 1% and 2.9% compared to NO_x reduction of

11.8% and 28.0% at the injection timings 21 ° and 19 ° bTDC, respectively.

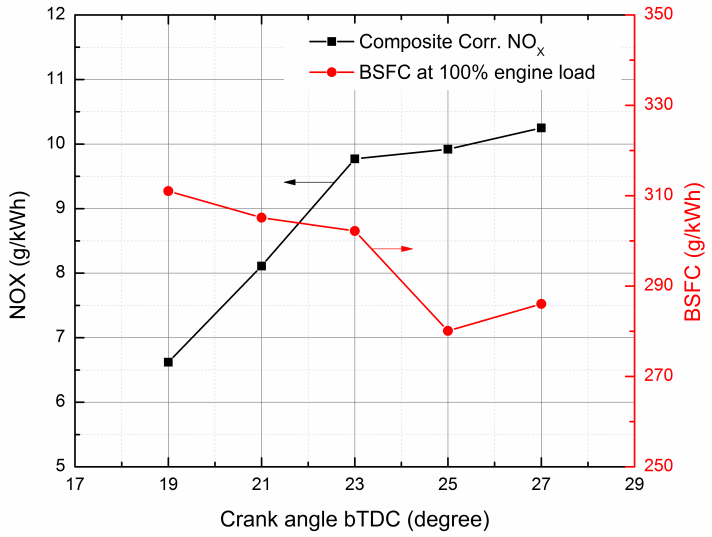

Figure 6.9: Corrected NO_x emissions - BSFC trade-off at different static injection timing

The composite HC emissions are not significantly affected by injection timing. This is because the diesel engine is always operating at low fuel/air equivalence ratio. Here it should be noted that, for HC emissions, all the injection timings meet the regulatory norms.

There is no explicit law observed on the CO emissions with the variation of fuel injection time. Generally, the composite CO emission shows the least value at the fuel injection timing of 25 ° bTDC corresponding to the optimized combustion. When the composite CO emissions are compared with regulatory norms, 21 ° and 25 ° bTDC injection timing is favorable to meet the standards.

The smoke emissions at 100% engine load are apparently lower at the fuel injection timing of 21-25 ° bTDC than that at 19 ° and 27 ° bTDC. The primary constituent of smoke is agglomerated carbon particles (soot) formed in regions of the combustion mixtures that are oxygen deficient. When fuel is injected too early, i.e., at 27 ° bTDC, the formation of high temperature zone accelerates the decomposition of fuel. During this premixed combustion phase poly aromatic hydrocarbons are formed which are precursors of soot. Aromatic hydrocarbons have

a greater tendency to form soot in burning which increases Soluble Organic Fraction (SOF) emissions. Also as explained earlier in order to obtain same power output fuel quantity was increased at 27 ° bTDC. Since the fuel quantity is increased, the injection process would be longer leading to longer combustion process also resulting in higher soluble organic fraction (SOF). Some literature also shows increase in SOF when biodiesel is used [268, 269, 270]. This increase in SOF eventually resulted in higher smoke emissions. When the injection timing is too late, for example, 19 ° bTDC produces more smoke emissions. This trend can be explained by the longer injection duration as a consequence of low LHV, and lesser time for combustion [271]. The smoke emissions at 21 °, 23 °, and 25 ° bTDC are generally low, can meet the emission regulation.

Overall, the injection timing of 21 ° bTDC, meets all the regulatory emission norms of genset diesel engines with a performance comparable to that of diesel. Furthermore, by retarding the injection timing to 21 ° bTDC, the NO_x, CO, HC and smoke emissions achieved are lesser by 11.8%, 11.1%, 90% and 5.7% respectively in comparison to emission limits, accompanied by marginal increase of 1.15% in BSFC compared to diesel at 23 ° bTDC injection timing.

6.2 Numerical investigation

6.2.1 Governing Equations

Simulations were conducted using integrated KIVA4 and CHEMKIN CFD codes. KIVA4 code solves the governing equations of conservation of mass, momentum and energy as shown in equations by using finite volume scheme.

The conservation of mass is given as

$$\frac{\partial \rho_m}{\partial t} + \nabla \bullet (\rho_m \overrightarrow{u}) = \nabla \bullet \left[\rho D \nabla \left(\frac{\rho_m}{\rho} \right) \right] + \dot{\rho_m^c} + \dot{\rho^s} \delta_{m1} \tag{6.9}$$

where, ρ_m is the mass density of species m, ρ is the total mass density, $\overrightarrow{u}$ is

the fluid velocity vector, $\dot{\rho}^s$ and $\dot{\rho_m^c}$ are the chemical source term and spray source term respectively originated by chemical reactions and evaporation of liquid fuel to gas, δ is the Dirac delta function and D is the diffusion coefficient and is given by Fick's law as

$$D = \frac{\mu}{\rho Sc} \tag{6.10}$$

where, μ is the turbulent viscosity and Sc is the Schmidt number which is input constant.

Since mass is conserved in chemical reactions, by summing Eq.6.11 over all species, we can obtain the total fluid density equation as follows

$$\frac{\partial \rho}{\partial t} + \nabla \bullet (\rho \vec{u}) = \dot{\rho}^s \tag{6.11}$$

$$\dot{\rho}^s = -\int f \rho_d 4\pi r^2 R d\vec{v} dr dT_d dy d\dot{y} \tag{6.12}$$

The conservation of momentum is given as

$$\frac{\partial (\rho \vec{u})}{\partial t} + \nabla \bullet (\rho \vec{u} \vec{u}) = -\frac{1}{a^2} \nabla p - A_0 \nabla \left(\frac{2}{3} \rho k \right) + \nabla \bullet \sigma + F^s \vec{+} \rho \vec{g} \tag{6.13}$$

where, p is the fluid pressure, a is a dimensionless quantity used in conjunction with the Pressure Gradient Scaling (PGS) method for low M flows, the quantity A_0 is zero in laminar calculations and unity when turbulence model is used, k is the turbulent kinetic energy, $\vec{F^s}$ is the rate of momentum gain per unit volume due to the spray, $\vec{g}$ is the droplet acceleration due to gravitational force which is assumed constant and σ is the viscous stress tensor given as

$$\sigma = \mu \left[\nabla \vec{u} + (\nabla \vec{u})^T \right] + \lambda \nabla \bullet \vec{u} N \tag{6.14}$$

where, μ and λ are the coefficients of viscosity, superscript T denotes the transpose and N is the unit dyadic.

The conservation of energy is given as

$$\frac{\partial (pI)}{\partial t} + \nabla \bullet (\rho \vec{u} I) = -p\nabla \bullet \vec{u} + (1 - A_0)\, \sigma : \nabla \vec{u} - \nabla \bullet \vec{J} + A_0 \rho \varepsilon + Q^c + \dot{Q}^s \quad (6.15)$$

where, I is the specific internal energy exclusive of chemical energy, ε is the dissipation rate, and $\vec{J}$ is the heat flux vector and is the sum of contributions due to heat conduction and enthalpy diffusion given by

$$\vec{J} = -K\nabla T - \rho D \sum_m h_m \nabla \left(\frac{\rho_m}{\rho} \right) \quad (6.16)$$

where, K is the thermal conductivity, T is the fluid temperature and h_m is the specific enthalpy of species m. $\dot{Q}^c$ is the source term due to chemical heat release, $\dot{Q}^s$ is the source term due to spray interactions which is given as follows

$$Q^s = -\int f\rho_d \left(4\pi r^2 R \left[I\left(T_d\right) + \frac{1}{2}\left(\vec{v} - \vec{u}\right)^2 \right]^{\cdot} + \frac{4}{3}\pi r^2 \left[c_1 T_d + \dot{F} \bullet \left(\dot{\vec{v}} - \vec{u} - \dot{\vec{u}} \right) \right] \right) d\vec{v} dr dT_d dy d\dot{y} \quad (6.17)$$

The turbulence model is used to solve the two additional transport equations for the turbulent kinetic energy and its dissipation rate as follows

$$\frac{\partial \rho k}{\partial t} + \nabla \bullet (\rho \vec{u} k) = -\frac{2}{3}\rho k \nabla \bullet \vec{u} + \sigma : \nabla \bullet \left[\left(\frac{\mu}{P_{r_k}} \right) \nabla k \right] - \rho\varepsilon + \dot{W}^s \quad (6.18)$$

$$\frac{\partial \rho \varepsilon}{\partial t} + \nabla \bullet (\rho \vec{u} \varepsilon) = -\left(\frac{2}{3} C_{\varepsilon_1} - C_{\varepsilon_3} + \frac{2}{3} C_\mu C_\eta \frac{k}{\varepsilon} \nabla \bullet \vec{u} \right) \rho\varepsilon \nabla \bullet \vec{u} + \nabla \bullet \left[\left(\frac{\mu}{P_{r_\varepsilon}} \right) \nabla \varepsilon \right] + \frac{\varepsilon}{k} \left[\left(C_{\varepsilon_1} - C_\eta \right) \sigma : \nabla \vec{u} - C_{\varepsilon_2} \rho\varepsilon + C_s \dot{W}^s \right] \quad (6.19)$$

where, the quantities $C_{\varepsilon_1} = 1.42$,$C_{\varepsilon_2} = 1.68$,C_{ε_3} ,C_η ,$P_{r_k} = 1.39$ and $P_{r_\varepsilon} = 1.39$ are empirical constants whose values are determined from experiments. The value of C_s taken as 1.5 as suggested based on the postulate of length scale conservation in spray/ turbulence interactions and $\dot{W}^s$ is the source term which arise due to interaction with the spray and is given as

$$\dot{W}^s = -\left(\frac{2}{3}C_{\varepsilon_1} - C_{\varepsilon_3}\right)\rho\varepsilon\nabla \bullet \vec{u} \tag{6.20}$$

$$C_{\varepsilon_3} = 0.41333 + (-1)^{\delta}\, 0.06899 C_\eta \eta \quad \begin{cases} \delta = 1 \quad if \quad \nabla \bullet \vec{u} < 0 \\ \delta = 0 \quad if \quad \nabla \bullet \vec{u} > 0 \end{cases} \tag{6.21}$$

$$C_\eta = \frac{\eta\left(1 - \frac{\eta}{\eta_0}\right)}{1 + \beta\eta^3} \tag{6.22}$$

where, $\beta = 0.012$ and $\eta_0 = 4.38$

$$\eta = S\frac{k}{\varepsilon} \tag{6.23}$$

$$S = (2S_{ij}S_{ij})^{\frac{1}{2}} \tag{6.24}$$

$$S_{ij} = \frac{1}{2}\left(\frac{\partial u_i}{\partial x_j} + \frac{\partial u_j}{\partial x_i}\right) \tag{6.25}$$

For the spray break-up process, the newly developed hybrid spray model was used. In addition to this models, the standard collision model, coalescence model multi-component fuel evaporation model of KIVA4 are used.

6.2.2 KIVA-CHEMKIN coupling

KIVA4 and CHEMKIN II codes are coupled to solve the detailed chemical reaction mechanisms. At each time step, the KIVA code gives the species concentrations and their thermodynamic properties calculated at each cell of the computational domain to the CHEMKIN code. In return the CHEMKIN code gives back the newly calculated species values to the KIVA code after solving the reactions. Fig.6.10 explains the mechanism of KIVA-CHEMKIN integration.

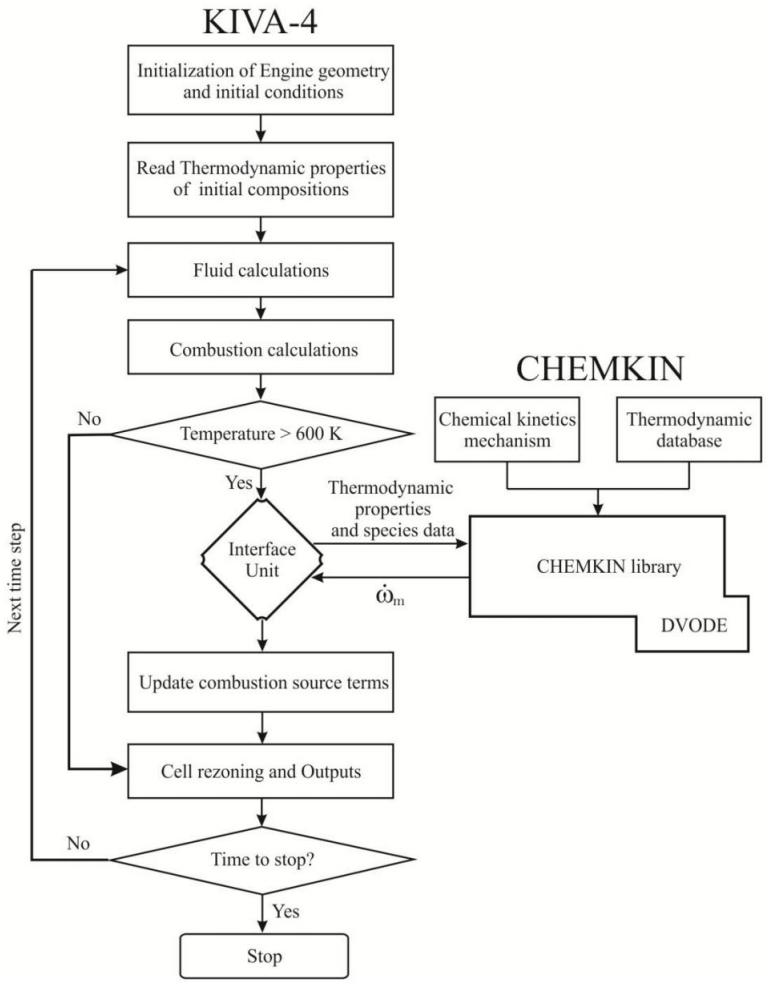

Figure 6.10: Flow chart of integrated KIVA-CHEMKIN code

The Diesel oil surrogate (DOS) fuel detailed chemical reaction model was used to model diesel fuel [272]. This mechanism contains 305 reactions involving 70 different species (see Appendix C). In this model, the $C_{14}H_{28}$was assumed to decompose into n-heptane C_7H_{16} and toluene C_7H_8 by the following reaction

$$1.5C_{14}H_{28} + 0.5O_2 \Rightarrow 2C_7H_{16} + C_7H_8 + H_2O \tag{6.26}$$

For the biodiesel reaction, a multi chemistry mechanism developed at ERC [273] using methyl decanoate (MD) and methyl-9-decenoate (MD9D) and n-heptane was assumed in this study. This mechanism involves 69 species and 204 reactions (see Appendix D). For pure biodiesel, a fuel mixture of 25% MD, 25% MD9D and 50% n-heptane in mole was used. In order to better model the fuel spray atomization, and evaporation, the detailed thermo-physical properties were calculated based on the methods reported in Chapter 5. It was found that the properties of major composition of biodiesel can be used to predict the spray characteristics and evaporation of biodiesel fuel with relative accuracy. In this case, the biodiesel derived from waste cooking oil consists of methyl palmitate (47.15%) and methyl oleate (36.41%) as its major compositions. Therefore, the detailed thermo-physical properties of methyl palmitate ($C_{17}H_{34}O_2$) and methyl oleate ($C_{19}H_{36}O_2$) were assigned to saturated methyl ester (MD) and unsaturated methyl ester (MD9D) respectively.

6.2.3 Mesh generation

For the CFD simulations, the combustion chamber of 2KD-FTV engine was modeled and meshed using Ansys ICEM CFD software. Based on the bowl geometry and number of injector holes, a 60 ° sector mesh as shown in Fig.6.11 was generated by taking advantage of symmetric periodic and boundary conditions to reduce the computational cost. The mesh consists of 3540 elements including the piston crevice region, when the piston is at top dead center. The fuel spray region was meshed using fine polar mesh in order to capture the spray break-up process in detail.

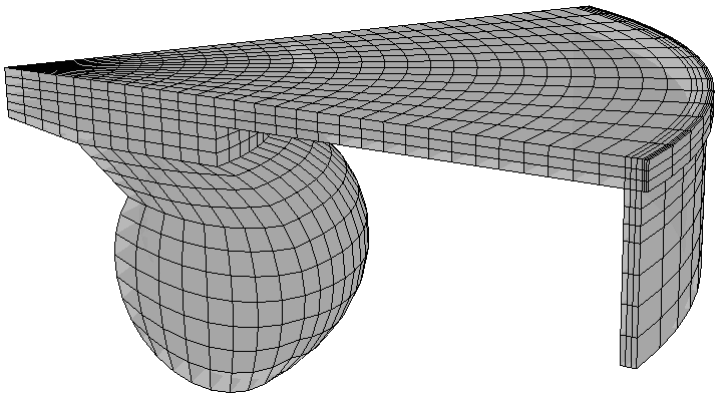

Figure 6.11: Grid used for engine simulations

6.2.4 Validation

For numerical validations, the experiments were conducted on a four cylinder, turbocharged, inline engine with common rail fuel injection system as shown in Fig.6.12. The engine was connected to an AVL water cooled passive eddy current dynamometer (AVL DP 160). The dynamometer is capable of providing maximum braking power of 160kW and a maximum torque of 400Nm at an accuracy of ±0.3%. The in-cylinder pressure was measured using water cooled AVL pressure transducer (AVL GH13P), which can measure pressure up to 250bar with a resolution of 1 ° CA. The pressure transducer was installed in the first cylinder. The fuel consumption rate was measured with AVL 733S1.8 fuel balance with an accuracy of ±1%. The air flow rate was measured using AVL Sensyflow air flow meter with a resolution of 100ms. The engine specifications are given in Table 6.5.

Table 6.5: Specifications of the engine in NUS

Engine Type	Direct injection, four stroke, four cylinder inline, turbocharged engine
Bore and Stroke	92 x 93.8 mm
Swept volume	2494cc
Connecting rod length	158.5 mm
Compression ratio	18.5:1
Rated power	75 kW at 3600 rpm
Rated torque	200Nm
Fuel injection system	Common rail injection system
No of orifices	6 Holes
Orifice diameter	175±3μm

In order to validate the numerical results, engine combustion characteristics

Figure 6.12: Engine setup in NUS

like experimental in-cylinder pressure data and heat release rate were used. Two different speeds (3600 and 2400 rpm) and two different loading conditions (100% and 50% load) were used to validate the numerical results for diesel fuel. Fig.6.13 shows the comparison of in-cylinder pressure and heat release rate between experimental and simulation results for diesel fuel. In order to validate the reaction mechanism and different models used for biodiesel simulations, the experimental and simulation results were compared (see Fig.6.14) in terms of in-cylinder pressure and heat release rate (HRR) at engine speed of 2400 rpm and 50% loading condition. The heat release rate for both experiment and simulation results were calculated based on the formula [15]

$$\frac{dQ}{dt} = \frac{\gamma}{\gamma - 1} P \frac{dV}{d\theta} + \frac{1}{\gamma - 1} V \frac{dP}{d\theta} \tag{6.27}$$

where, $\frac{dQ}{dt}$ is the heat release rate per crank angle, θ is crank angle, P is the in-cylinder pressure, V is the cylinder volume and γ is the ratio of specific heats. The value of γ is taken as 1.35 for compression stroke and 1.3 for expansion stroke.

As we know, the performance of diesel engine is determined by the combustion process. To better understand the combustion characteristics, the apparent heat release rates were also compared for all cases. Quantitative information on combustion phenomenon can be achieved from the in-cylinder pressure data obtained from engine operating cycle. The heat release rate is used to identify the ignition

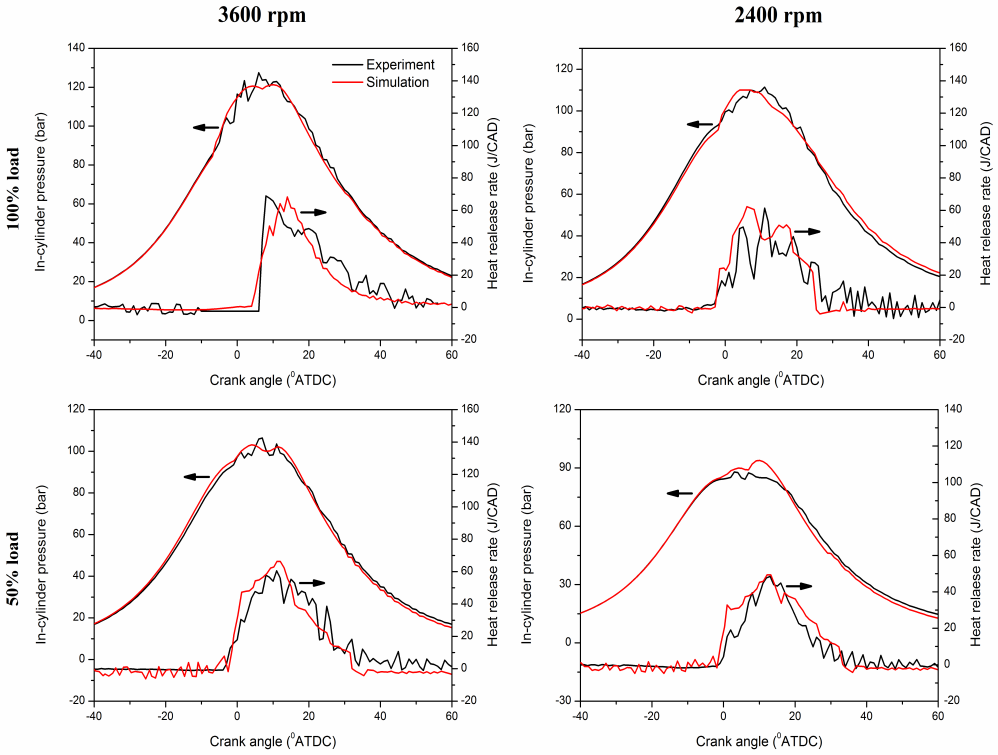

Figure 6.13: Comparison of simulation and experimental combustion parameters for diesel fuel

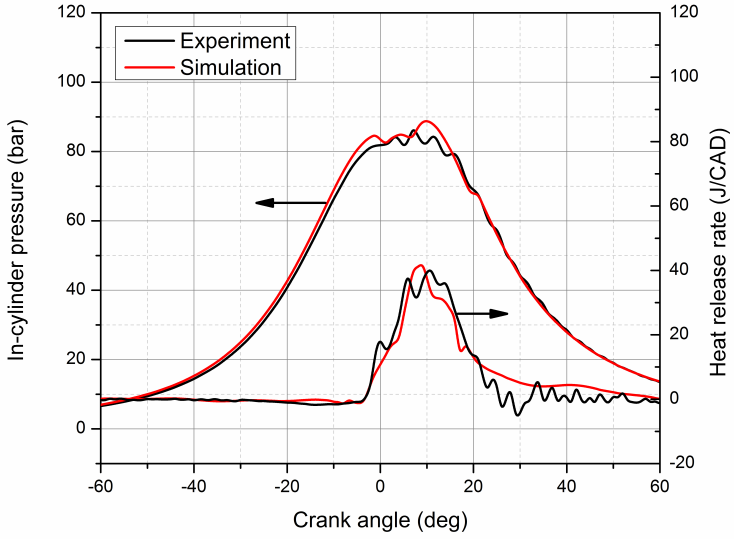

Figure 6.14: Comparison of simulation and experimental combustion parameters for biodiesel fuel

delay and combustion duration. As seen from Figs.6.13 and 6.14, the predicted in-cylinder pressure and ignition delay time are consistent with the experimental

results of both diesel and biodiesel fuels. This is because the new spray model predicts the vapor penetration and liquid length accurately, which implies the air fuel mixing, ignition and combustion process are also predicted accurately. This indicates that the new hybrid spray model developed and the reaction mechanism of both diesel and biodiesel fuels captures the detail of the combustion process in the engine very well.

6.2.5 Results and discussion

6.2.5.1 Effect of boot length on combustion and emissions

In these simulations, boot pressure was kept constant at 50% of original injection pressure and the boot length was varied in terms of 25, 50 and 75% of total injection duration and named as short, medium and long boot lengths respectively. The SOI and duration of injection were maintained the same as original injection rate, therefore to inject same quantity, the injection pressure just after boot length were increased. The injection velocity profile needed for the engine simulations was obtained from the internal nozzle flow simulations in prior for different injection pressure profiles as shown in Fig.6.15.

From Fig.6.15, it can be seen from the cumulative injected mass, during the boot length period, all profiles possess same injection rate as both injection pressure and velocity are same during this period of injection. During main injection duration, the injection rate is high for long boot length followed by medium and short boot lengths. This is due to higher injection pressure associated with long boot length profile to compensate the total fuel injection. The injection velocity profiles follow the injection pressure profiles, since velocity is directly proportional to the pressure difference across the injector nozzle holes.

Figs.6.16a and b show the combustion and emission comparison of different boot lengths. It was found that for different boot lengths, the in-cylinder pressure and HRR decreases compared to original injection rate, because of less fuel being injected during initial stage of injection, which reduces accumulated fuel and

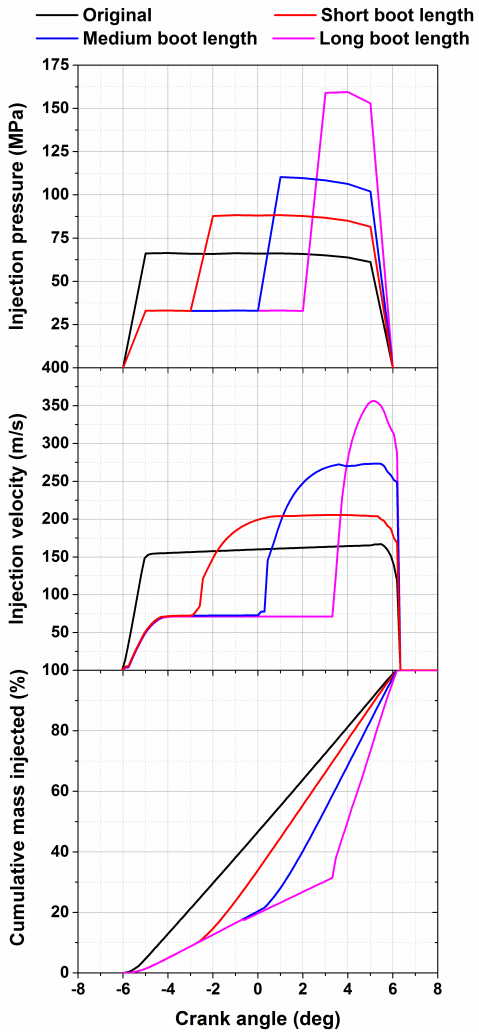

Figure 6.15: Injection pressure, velocity and cumulative injected mass for boot length profiles

premixed combustion. This may be due to different levels of vaporization of fuel droplets. The smaller droplets vaporize faster and are involved in the combustion process earlier than the larger droplets. The droplet size is directly governed by the injection velocity. Hence, during early injection period, the peak heat release rate for original injection rate profile is higher compared to different boot lengths as the velocity of the original profile is high and eventually results in more but smaller droplets. During the controlled combustion phase, the heat release rate for long boot length is higher compared to other profiles. This is clearly due to the higher injection rate and this leads to fine atomization of fuel droplets resulting in enhanced vaporization and combustion [274, 275].

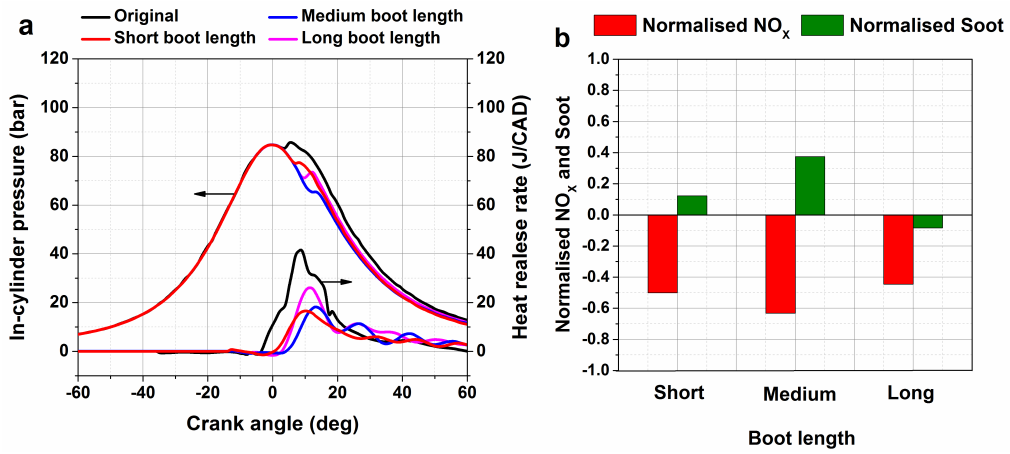

Figure 6.16: a) Combustion and b) emission characteristics of different boot length profiles

From Fig.6.16b, it can be found that NO_x emissions were predominantly decreased with different boot lengths for the same reason. However the NO_x emissions for long and short are slightly higher than medium boot length, because during the long boot length, in order to maintain fuel quantity; higher injection pressure was used immediately after the boot length. This higher injection pressure leads to higher injection velocity (see Fig.6.15), which may result in better fuel-air mixing due to smaller droplet formations and eventually increased NO_x emissions. For short boot length, advanced high injection pressure increases the injection rate during the premixed combustion phase compared to long and medium boot length profiles which would have brought forth a slight increase in NO_x emissions. Generally, as NO_x emissions decrease, soot emissions increase, however, for long boot length, the soot emissions were decreased, which may be due to increased injection pressure leading to smaller droplets as explained earlier which undergoes higher oxidation rate because of high temperature and oxygen content available from the fuel.

Figs.6.17, 6.18, 6.19 and 6.20 show contours of in-cylinder temperature, NO, CO and soot emissions respectively for different boot length profiles at 12 $^\circ$ and 20 $^\circ$ aTDC. It can be seen that, NO emissions are lower for medium boot length compared to other profiles. This is due to the lower in-cylinder temperature, which is evident from the temperature contours. However, for medium boot length, both

CO and soot emissions are higher compared to short and long boot lengths. The temperature contour at 20 ° aTDC for long boot length shows high temperature distribution which ascertains the increase in heat release rate during controlled combustion phase due to enhanced fuel vaporization which helped in CO and soot oxidation. From the results, it can be observed that NO_x emission is low for medium boot length but it comes at the expense of high CO and soot emissions. If NO_x-soot trade-off is considered then the optimum would be long boot length injection rate shape.

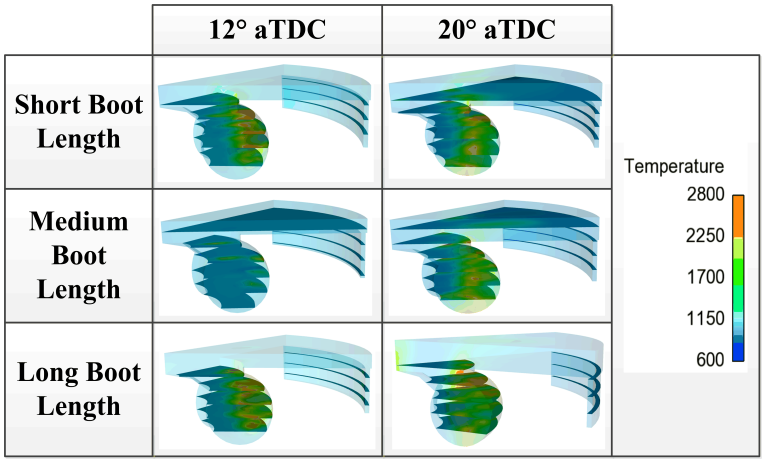

Figure 6.17: Contours of in-cylinder temperature for different boot length profiles

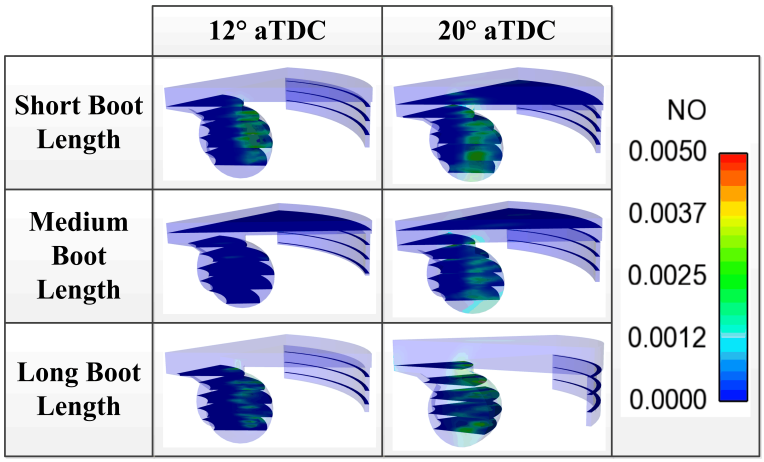

Figure 6.18: Contours of NO emissions for different boot length profiles

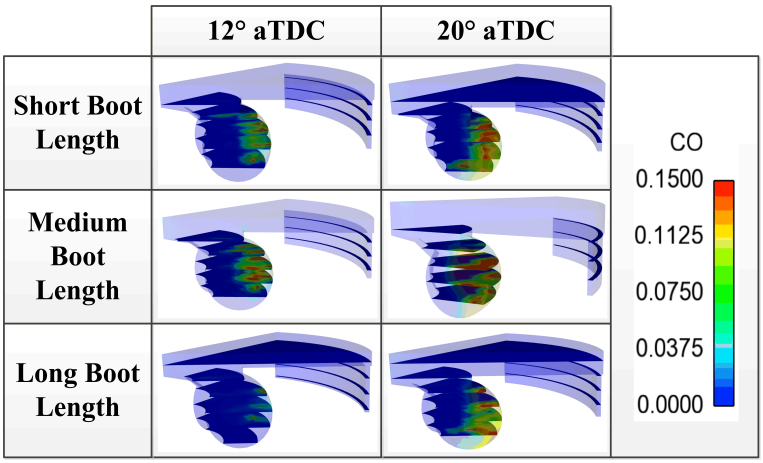

Figure 6.19: Contours of CO emissions for different boot length profiles

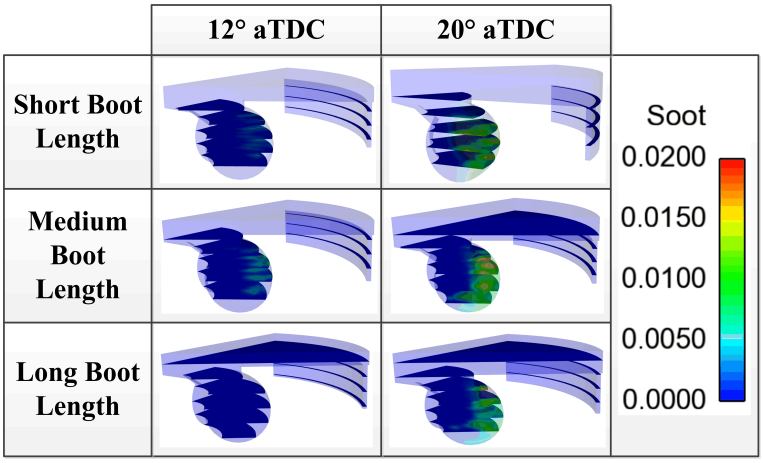

Figure 6.20: Contours of soot emissions for different boot length profiles

6.2.5.2 Effect of boot pressure on combustion and emissions

To study the effect of boot pressure on combustion and emissions, boot length was maintained as 50% of total injection duration. The boot pressure was varied in terms of 25, 50 and 75% of original injection pressure as low, medium and high boot pressure respectively. Similar to boot length simulations, the injection pressure after boot pressure was increased in order to maintain fuel injection quantity as shown in Fig.6.15. It should be noted that medium boot pressure profile is the same as medium boot length profile, but for convenience, the name medium boot pressure is used in further discussion. The injection velocity for different boot pressure profiles are also obtained through internal nozzle simulations as done earlier for boot length profiles.

Fig.6.21 shows the injection pressure, injection velocities and cumulative injected mass for different boot pressure profiles. It can be observed that during boot length, the injection rate of low boot pressure profile is low whereas after boot length its injection rate is increased in order to maintain total fuel quantity. Similarly, high boot pressure has highest injection rate among other profiles during boot length and lowest injection rate after boot length until end of injection.

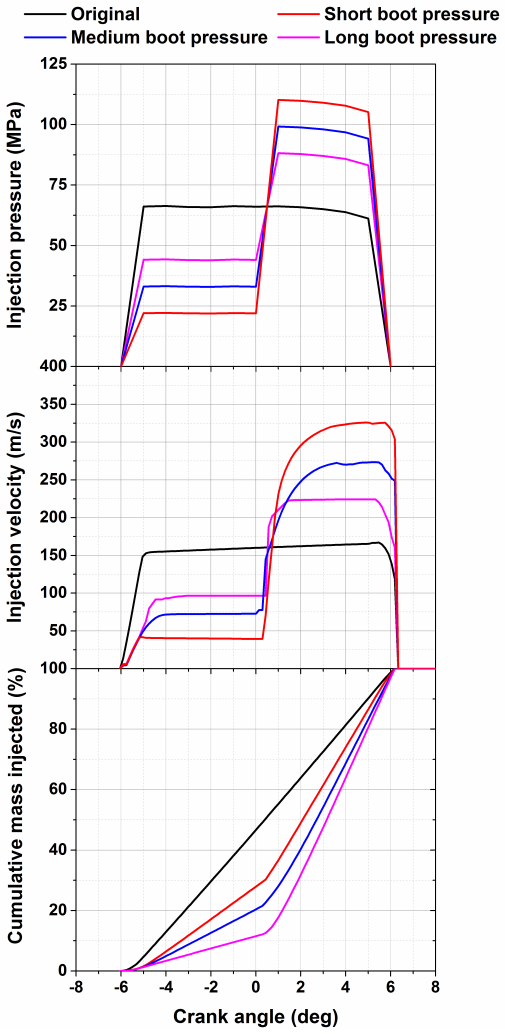

Figure 6.21: Injection pressure, velocity and cumulative injected mass for boot pressure profiles

Figs.6.22a and b show combustion and emission characteristics of different boot pressure profiles. Interestingly, it can be observed that unlike different boot length profiles, not every boot pressure profile produces lower in-cylinder pressure. In fact low boot pressure profile gives heat release rate on par with original injection rate.

This is due to high injection velocity immediately after boot length which produces smaller droplets that eventually involve in enhanced combustion to produce same level of heat release rate but with slight retardation. However, high boot pressure and medium boot pressure, present low in-cylinder pressure and heat release rate compared to both original and low boot pressure rate profiles. This is due to the higher velocity during boot length period compared to low boot pressure but less fuel injected than original injection rate profile. Also it can be noted from heat release rate, that the start of combustion occurs in the order of high boot pressure followed by low and medium boot pressure which evidently supports the different level of atomization which governs the combustion process. It is interesting to note that the start of combustion for low boot pressure is slightly advanced than medium boot pressure. This may be due to the injection pressure immediately after boot length duration has more pronounced effect on combustion than during boot length for medium boot pressure profile.

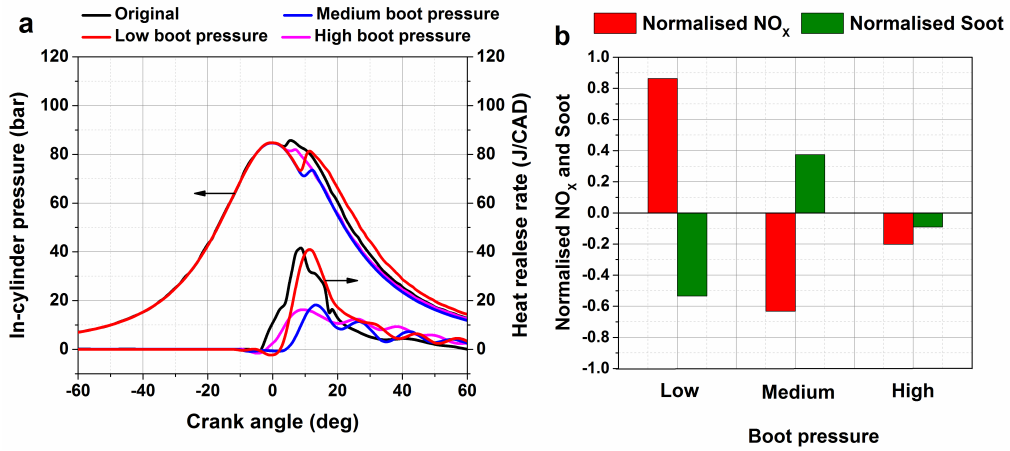

Figure 6.22: a) Combustion and b) emission characteristics of different boot pressure profiles

From Fig.6.22 b, it was found that both medium and high boot pressure gave less NO_x emission compared to original injection rate and low boot pressure profile. This is because of less fuel injected during initial injection period. However, the decrease in NO_x emission is relatively lower for high boot pressure profile due to higher injection velocity which may lead to slightly better air-fuel mixing and enhances the NO_x formation. NO_x emission of low boot pressure is higher than

original and other boot pressure profiles due to high amount of fuel injected with high injection pressure immediately after boot length period causing better air-fuel mixing and enhanced combustion leading to high temperature favoring high NO_x emissions. This is also evident from the high HRR from Fig.6.22a. Soot emissions are lower for both low and high boot pressures. Low soot emissions are observed with both low and high boot pressures. Low soot emission associated with low boot pressure is due to better fuel atomization and fuel-air mixing immediately after the boot length. On the other hand, for high boot pressure, the high heat release rate during controlled combustion phase compared to other profiles has favored soot oxidation.

Figs.6.23, 6.24, 6.25 and 6.26 show contours of in-cylinder temperature and NO, CO and soot emissions respectively for different boot pressure profiles at 12 ° and 20 ° aTDC. From temperature contours it is evident that the low boot pressure profile produces high in-cylinder temperature and eventually results in high NO_x emissions as shown in NO_x contours. For high boot pressure, it can be observed that both soot and NO_x emissions are comparatively lesser than low boot pressure. Therefore, for NO_x-soot trade-off, high boot pressure would be better boot pressure profile.

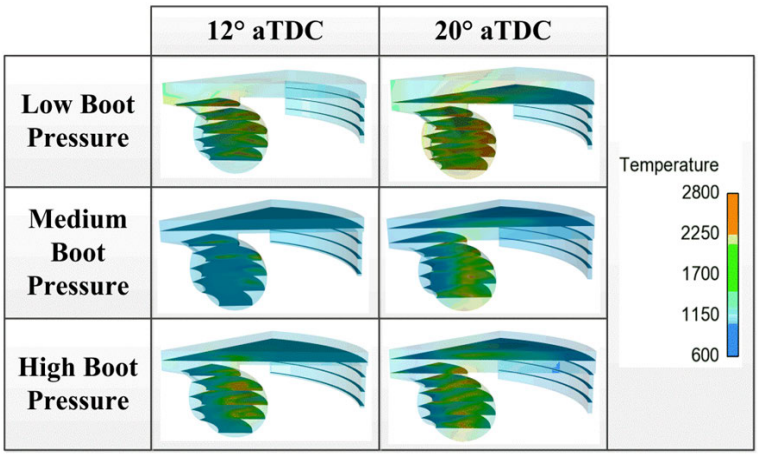

Figure 6.23: Contours of in-cylinder temperature for different boot pressure profiles

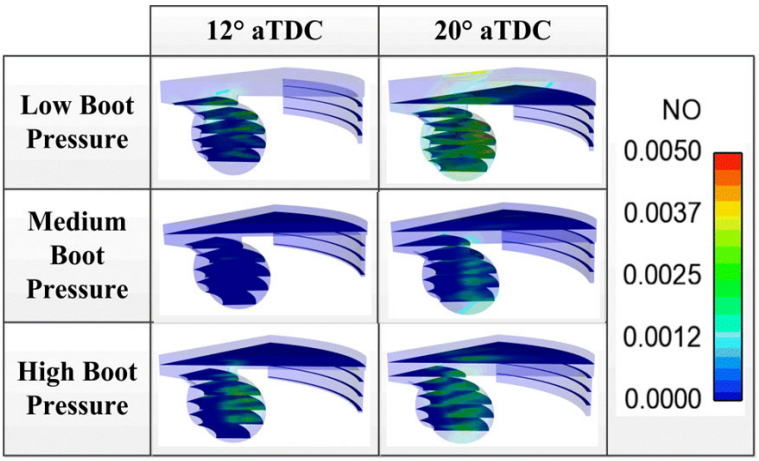

Figure 6.24: Contours of NO emissions for different boot pressure profiles

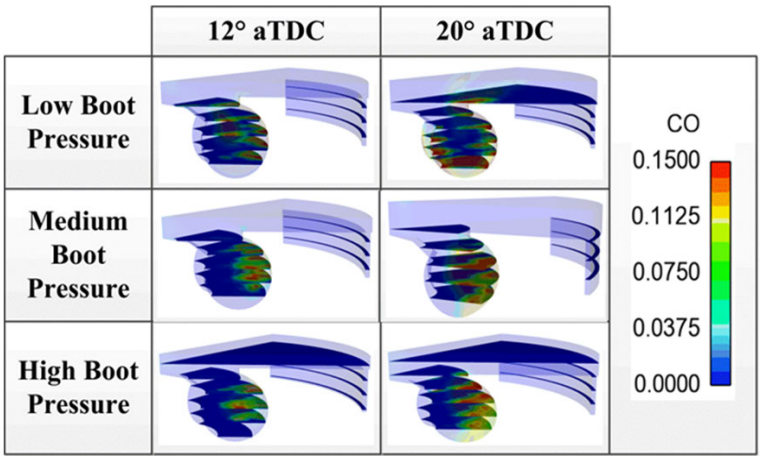

Figure 6.25: Contours of CO emissions for different boot pressure profiles

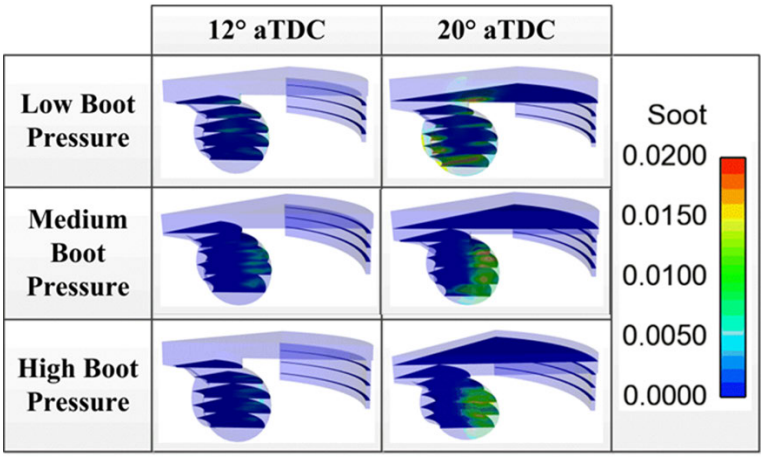

Figure 6.26: Contours of soot emissions for different boot pressure profiles

6.3 Summary

In this study, B20 blend of mahua methyl ester was tested for its usability in genset engines. The single cylinder diesel engine was tested with B20 mahua methyl ester

under ISO 8178 D2 cycle to meet genset emission standards prevailing in India. By varying injection parameters like nozzle opening pressure and injection timing, the emissions were measured to check whether it meets regulatory norms. From the study the following conclusions were drawn

- B20 biodiesel can be used in genset engines without any deterioration to performance compared to diesel except for high NO_x emissions at manufacturer default nozzle opening pressure of 225 bar and injection timing of 23 $^\circ$ bTDC.

- By increasing nozzle opening pressure to 275 bar, B20 blend meets all the regulatory emission norms by good margin and with improved performance parameters like BTE and BSFC.

- By retarding static injection timing to 21 $^\circ$ bTDC, B20 blend meets emission norms again with good margin without significant effect on performance parameters.

As a concluding remark, B20 blend of mahua methyl ester can be used with genset engines either by increasing its NOP to 275 bar or by retarding its static injection timing to 21 $^\circ$ bTDC from manufacturers' defaults to meet CPCB emission standards for genset engines prevailing in India without significantly affecting the performance compared to diesel fuel.

The effect of injection rate shaping on performance and emission characteristics of biodiesel fueled diesel engine has been investigated using KIVA4 CFD code. Different boot profiles have been studied by varying boot pressure and boot lengths. From KIVA-4 simulation results, it was found that NO_x emissions were reduced for all boot length profiles and medium and high boot pressure profiles due to less fuel injected and lower injection velocity during initial period of injection. However, it was found that NO_x-soot trade-off could be achieved only with long boot length, and high boot pressure injection rate profiles compared to original injection rate for biodiesel. From this study, it can be concluded that,

at medium load and medium engine speed, boot shaped injection profiles can be effectively used to obtain NO_x-soot trade-off for biodiesel powered diesel engines.

7

Conclusions and future recommendations

7.1 Conclusions and contributions

7.1.1 Fundamental study on spray characteristics

As one of the major objectives of this thesis is to study the spray characteristics and fuel-air mixing in detail, an experimental setup has been designed and commissioned in NUS. The setup was used to capture the spray development process using high speed camera under the ambient pressure condition prevalent inside the combustion chamber during the injection process. From the experimental results, it was ascertained that different fuels exhibited different atomization behavior predominantly affected by its thermo-physical properties. Pure bio diesel (B100) showed poor atomization characteristics when compared to diesel fuel due to its

high viscosity. However, the bio diesel blend (B20) with diesel showed very similar spray properties with diesel fuel which also ascertains the comparable engine performance and emission characteristics attributed when using B20 blend in diesel engines. The experimental momentum flux and momentum co efficient data prove the presence of cavitation inside the injector nozzle holes and these data were later used in validation of cavitation model.

7.1.2 Internal nozzle flow modeling

The internal nozzle flow characteristics and cavitation phenomenon have been studied extensively using Fluent CFD package. The Schnerr-Sauer two phase model was used in modeling the cavitation inside the injector nozzle holes. The model was then well validated against the experimental results from literature and with the momentum flux results obtained in-house. The model showed good agreement with the experimental results. Then a comprehensive parametric study has been conducted to establish the effect of different factors like pressure difference, density, viscosity and different geometries. The results from the simulation also showed that cavitation and turbulence generated inside the nozzle hole has predominant effect on the primary atomization. Then this model was further used in simulating the cavitation inception for different fuels like diesel, biodiesel and blend fuels. As visualization inside the nozzle under very high injection pressure is not practically viable, the modeling helped in attaining better understanding on the vapor phase and turbulence generated inside the injector nozzles and further using these results to study the primary breakup of the fuel spray in a new hybrid spray model developed.

7.1.3 Spray modeling

A new hybrid spray model was developed by combining cavitation induced spray sub model to classical KHRT spray model to capture the physical phenomenon involved in the spray development process with high accuracy. This model used

the results of local distribution of flow field variables like vapor fraction, average turbulent kinetic energy and area coefficient from injector nozzle hole simulations. This new hybrid spray model was then extensively validated against experimental results from Sandia National laboratory and in-house experiments for different fuels. The model has been proved capable of predicting the spray development process and its quantitative characteristics of different fuels. It was also found that the spray characteristics of biodiesel in general were affected by the thermo-physical properties of its major constituent methyl ester. Biodiesel with high percentage composition of methyl stearate showed poor atomization at low ambient temperature and biodiesel with major composition of methyl oleate showed poor atomization characteristics at high ambient temperature. The new model has proved its mettle in predicting spray characteristics at par with various experimental results. Therefore it has great potential application in engine modeling to simulate performance and emission characteristics accurately.

7.1.4 Engine experiments

To study the effect of injection parameters such as injection timing and injection pressure, a single cylinder agricultural genset engine was used. The engine was tested under ISO 8178 D2 cycle recommended for testing genset engines. The engine was fueled with Mahua biodiesel blend (B20) with diesel. Then the obtained emission results for different injection timing and injection pressures were compared with emission limits (CPCB-I) set by Central Pollution Control Board of India. It was found that by changing injection timing and injection pressure, the emissions from the engine fueled with biodiesel blend can be kept within the limits. It was also found that better trade-off between NOx and fuel consumption could be achieved in addition to better NOx-soot trade-off by adjusting the injection parameters. Thus, in line with the objective of this thesis it was shown that by varying the injection parameters both NOx and soot emissions could be reduced without significant effect on fuel consumption.

7.1.5 Engine modeling

The 3D CFD modeling of engine performance and emission characteristics fueled by pure biodiesel fuel was done using KIVA4 CFD code. The new hybrid model developed was implemented into the KIVA4 package to accurately model the spray characteristics and fuel-air mixing process. From the literature, it was found that the injection rate shaping has a potential to obtain NOx-soot trade-off, however, this injection strategy was less explored by researchers in spite of its capabilities. Therefore, in this study, this strategy was explored in detail to obtain better engine out emissions. At first, the injection rate shape was modeled in Fluent CFD package by varying boot pressure and boot length to obtain necessary input data for engine simulations such as injection velocity, area coefficient, vapor fraction at nozzle exit and average turbulent kinetic energy. Then the engine simulations were performed by varying boot length and boot pressures. It was found that better NOx-soot trade-off could be achieved with long boot length and high boot pressure profiles compared to standard square shaped injection profile, and both NOx and soot emissions could be reduced simultaneously by changing injection rate shapes.

7.2 Recommendations for future work

7.2.1 Spray experiments

In this study, the spray research was confined to macroscopic characteristics like spray tip penetration, angle, and volume due to experimental limitations. However, experimental data on droplet size and droplet size distribution are very important to improve the accuracy of the spray model further. Therefore, one of the research directions arisen from this work is to study microscopic characteristics through advanced laser diagnostic equipment like PDPA (Phase Doppler Particle Analyzer) and PLIF (Planar Laser Induced Fluorescence) to obtain qual-

itative data on liquid and vapor phases. The experimental data from these devices can be used to further refine the spray model in predicting non-evaporative and evaporative sprays.

7.2.2 Spray simulations

In this work, the simulation of cavitation inside the injector nozzle holes was carried out in Fluent CFD package and spray simulation was carried out with KIVA4 CFD package. This is because, Fluent is a general purpose CFD package which is very good for flow related problems and KIVA4 is a special CFD package to simulate internal combustion engines and to reap the benefit of these two platforms the simulation in this work was done in two stages. However, it would be better if both simulations could be done in coupled way using a single CFD package. That single CFD package should be capable of simulating flow field problems and engine simulations. There are few software capable of doing this kind of coupled simulations like AVL FIRE, STAR-CD and recently Converge CFD is also joining the league, however, these software are commercial packages and provide limited user interventions or modifications to the models if required. Therefore, the potential CFD package that can be used for coupled simulation should be capable of simulating general flow problems along with internal combustion simulations and should also be open source where the user can modify the models to suit his/her application. One such CFD package is OpenFOAM which has proved its mettle in simulating both cavitation [276] and internal combustion engines [277]. Therefore, further development of the unified modeling can be focused on OpenFOAM platform.

7.2.3 Engine experiments

The control system currently available with the multi-cylinder engine in NUS is closed ECU (Electronic Control Unit) which restricts changing any injection parameter like injection pressure, timing, rate shapes and employing multiple in-

jections. This shortcoming of the engine can be overcome when custom designed control module is implemented to existing engine. If the user friendly control unit is implemented then further research can be focused on combustion phasing using different injection strategies to aim at improving engine efficiency and reduce emissions.

7.2.4 Engine modeling

The engine modeling also depends on reaction mechanism for particular fuel under investigation to obtain more accurate combustion and emission characteristics. Although the skeletal mechanism used in this study is currently a very good mechanism available in the literature, there are still some uncertainties in prediction of soot due to the lack of experimental results and details of the soot formation mechanism. Therefore, another research direction could be the development of a detailed soot model for better prediction of soot emissions.

References

[1] European vehicle market statistics: Pocketbook 2012, 2012.

[2] J. E. Dec, A conceptual model of di diesel combustion based on laser-sheet imaging, SAE Technical Paper, 1997.

[3] N. L. Mills, H. Törnqvist, M. C. Gonzalez, E. Vink, S. D. Robinson, S. Söderberg, N. A. Boon, K. Donaldson, T. Sandström, A. Blomberg, et al., Ischemic and thrombotic effects of dilute diesel-exhaust inhalation in men with coronary heart disease, New England Journal of Medicine 357 (2007) 1075–1082.

[4] M. Riedl, D. Diaz-Sanchez, Biology of diesel exhaust effects on respiratory function, Journal of Allergy and Clinical Immunology 115 (2005) 221–228.

[5] A. Sydbom, A. Blomberg, S. Parnia, N. Stenfors, T. Sandström, S. Dahlen, Health effects of diesel exhaust emissions, European Respiratory Journal 17 (2001) 733–746.

[6] T. Suzuki, I. C. Engine, N. A. Otto, H. Engine, S. Carnot, E. Life, E. Compartments, R. Royce, D.-B. D. Engine, The romance of engines, Training 2010 (1997) 03–15.

[7] C. Pope, M. Thun, M. Namboodiri, D. Dockery, J. Evans, F. Speizer, C. Heath, et al., Particulate air pollution as a predictor of mortality in a prospective study of us adults., American journal of respiratory and critical care medicine 151 (1995) 669–674.

[8] K. Katsouyanni, J. Schwartz, C. Spix, G. Touloumi, D. Zmirou, A. Zanobetti, B. Wojtyniak, J. Vonk, A. Tobias, A. Ponka, et al., Short term effects of air pollution on health: a european approach using epidemiologic time series data: the aphea protocol., Journal of epidemiology and community health 50 (1996) S12–S18.

[9] N. Li, S. Kim, M. Wang, J. Froines, C. Sioutas, A. Nel, Use of a stratified oxidative stress model to study the biological effects of ambient concentrated and diesel exhaust particulate matter, Inhalation toxicology 14 (2002) 459–486.

[10] N. Li, M. Hao, R. Phalen, W. Hinds, A. Nel, et al., Particulate air pollutants and asthma. a paradigm for the role of oxidative stress in pm-induced adverse health effects., Clinical immunology (Orlando, Fla.) 109 (2003) 250.

[11] J. Zhang, J. McCreanor, P. Cullinan, K. Chung, P. Ohman-Strickland, I. Han, L. Jarup, M. Nieuwenhuijsen, Health effects of real-world exposure to diesel exhaust in persons with asthma., Research report (Health Effects Institute) (2009) 5.

[12] M. Attfield, P. Schleiff, J. Lubin, A. Blair, P. Stewart, R. Vermeulen, J. Coble, D. Silverman, The diesel exhaust in miners study: a cohort mortality study with emphasis on lung cancer, Journal of the National Cancer Institute 104 (2012) 869–883.

[13] Emission standards, european union, cars and light trucks, `https://www.dieselnet.com/standards/`, 2014. Online; accessed 10 September 2014.

[14] The Eurpean Parliament and the Council of the European Union, Regulation (EC) No 715/2007 of the european parliament and of the council, Official Journal of the Eurpopean Union (2007).

[15] J. Heywood, Internal combustion engine fundamentals (1988).

[16] D. A. Langer, N. Petek, Maximizing the effectiveness of water-blended fuel in reducing emissions by varying injection timing or using after-treatment device (2001).

[17] G. Abd-Alla, Using exhaust gas recirculation in internal combustion engines: a review, Energy Conversion and Management 43 (2002) 1027–1042.

[18] A. Maiboom, X. Tauzia, J. Hetet, Influence of egr unequal distribution from cylinder to cylinder on nox–pm trade-off of a hsdi automotive diesel engine, Applied Thermal Engineering 29 (2009) 2043–2050.

[19] X. Tauzia, A. Maiboom, S. Shah, Experimental study of inlet manifold water injection on combustion and emissions of an automotive direct injection diesel engine, Energy 35 (2010) 3628–3639.

[20] M. Ishida, S. Yamamoto, H. Ueki, D. Sakaguchi, Remarkable improvement of nox-pm trade-off in a diesel engine by means of bioethanol and egr, Energy 35 (2010) 4572–4581.

[21] D. Agarwal, S. Singh, A. Agarwal, Effect of exhaust gas recirculation (egr) on performance, emissions, deposits and durability of a constant speed compression ignition engine, Applied Energy 88 (2011) 2900–2907.

[22] T. Johnson, et al., Diesel emission control in review, SAE Transactions 110 (2001) 128–144.

[23] T. Johnson, Diesel particulate filter technology, SAE International, 2007.

[24] T. Johnson, Diesel emission control in review, SAE Int. J. Fuels Lubr 1 (2008) 68–81.

[25] T. Johnson, Review of diesel emissions and control, International Journal of Engine Research 10 (2009) 275–285.

[26] T. Johnson, Diesel emissions in review, SAE International Journal of Engines 4 (2011) 143–157.

[27] T. Morimune, H. Yamaguchi, Y. Yasukawa, Study of catalytic reduction of nox in exhaust gas from a diesel engine, Experimental thermal and fluid science 18 (1998) 220–230.

[28] G. Fulks, G. Fisher, K. Rahmoeller, M. Wu, E. DHerde, J. Tan, A review of solid materials as alternative ammonia sources for lean nox reduction with scr, SAE Technical Paper (2009) 01–0907.

[29] M. Stanciulescu, J. Charland, J. Kelly, Effect of primary amine hydrocarbon chain length for the selective catalytic reduction of nox from diesel engine exhaust, Fuel 89 (2010) 2292–2298.

[30] W. Cartellieri, W. Kriegler, F. Schweinzer, Strategies to meet worldwide heavy-duty diesel emission standards, Proceedings of the Institution of Mechanical Engineers, Part D: Journal of Automobile Engineering 206 (1992) 161–171.

[31] U. Adler, Diesel fuel injection, Robert Bosch GmBH, 1994.

[32] B. Pundir, Engine emissions: Pollutant formation and advances in control technology, Alpha Science International Limited, 2007.

[33] B. Mahr, Future and potential of diesel injection systems, in: THIESEL 2002 Conference on Thermo-and Fluid-Dynamic Processes in Diesel Engines, pp. 5–17.

[34] J. Wloka, C. Potsch, G. Watchmeister, Injection spray visualization for 3000 bar diesel injection, in: ILASS-Europe.

[35] J. Wloka, S. Pflaum, G. Wachtmeister, Potential and challenges of a 3000 bar common-rail injection system considering engine behavior and emission level, SAE International Journal of Engines 3 (2010) 801–813.

[36] D. Siebers, Liquid-phase fuel penetration in diesel sprays, SAE (1998).

[37] J. D. Naber, D. L. Siebers, Effects of gas density and vaporization on penetration and dispersion of diesel sprays, Technical Report, SAE technical paper, 1996.

[38] P. Jianfeng, Y. Wenming, C. Siawkiang, L. Detao, X. Hong, Z. Jingang, T. Aikun, Spray and combustion visualization of biodiesel in a direct injection diesel engine., Thermal Science 17 (2013).

[39] J. Dent, A basis for the comparison of various experimental methods for studying spray penetration, Society of Automotive Engineers, 1971.

[40] H. Hiroyasu, T. Kadota, M. Arai, Supplementary comments: fuel spray characterization in diesel engines, Combustion modeling in reciprocating engines (1980) 369–408.

[41] Y. Icingur, D. Altiparmak, Effect of fuel cetane number and injection pressure on a di diesel engine performance and emissions, Energy conversion and management 44 (2003) 389–397.

[42] I. Celikten, An experimental investigation of the effect of the injection pressure on engine performance and exhaust emission in indirect injection diesel engines, Applied Thermal Engineering 23 (2003) 2051–2060.

[43] B. Moser, A. Williams, M. Haas, R. McCormick, Exhaust emissions and fuel properties of partially hydrogenated soybean oil methyl esters blended with ultralow sulfur diesel fuel, Fuel and Processing Technology 90 (2009) 1122–1128.

[44] E. Buyukkaya, Effect of soybean methyl ester on diesel engine performance and emissions, International journal of Vehicle Design 54 (2010) 111–122.

[45] H. An, W. Yang, S. Chou, K. Chua, Combustion and emissions characteristics of diesel engine fueled by biodiesel at partial load conditions, Applied Energy 99 (2012) 363–371.

[46] R. Vallinayagam, S. Vedharaj, W. Yang, P. Lee, K. Chua, S. Chou, Combustion performance and emission characteristics study of pine oil in a diesel engine, Energy 57 (2013) 344–351.

[47] W. Yang, H. An, S. Chou, S. Vedharaji, R. Vallinagam, M. Balaji, F. Mohammad, K. Chua, Emulsion fuel with novel nano-organic additives for diesel engine application, Fuel 104 (2013) 726–731.

[48] M. Gumus, C. Sayin, M. Canakci, The impact of fuel injection pressure on the exhaust emissions of a direct injection diesel engine fueled with biodiesel–diesel fuel blends, Fuel (2011).

[49] C. Sayin, M. Gumus, Impact of compression ratio and injection parameters on the performance and emissions of a di diesel engine fueled with biodiesel-blended diesel fuel, Applied Thermal Engineering 31 (2011) 3182–3188.

[50] M. Canakci, C. Sayin, A. Ozsezen, A. Turkcan, Effect of injection pressure on the combustion, performance, and emission characteristics of a diesel engine fueled with methanol-blended diesel fuel, Energy & Fuels 23 (2009) 2908–2920.

[51] K. Purushothaman, G. Nagarajan, Effect of injection pressure on heat release rate and emissions in ci engine using orange skin powder diesel solution, Energy Conversion and Management 50 (2009) 962–969.

[52] K. Purushothaman, G. Nagarajan, Studies on a ci engine using orange skin powder diesel solution with different fuel nozzle opening pressure, Thermal Science 13 (2009) 103–112.

[53] S. Puhan, R. Jegan, K. Balasubbramanian, G. Nagarajan, Effect of injection pressure on performance, emission and combustion characteristics of high linolenic linseed oil methyl ester in a di diesel engine, Renewable Energy 34 (2009) 1227–1233.

[54] S. Jindal, B. Nandwana, N. Rathore, V. Vashistha, Experimental investigation of the effect of compression ratio and injection pressure in a direct injection diesel engine running on jatropha methyl ester, Applied Thermal Engineering 30 (2010) 442–448.

[55] M. Pandian, S. Sivapirakasam, M. Udayakumar, Investigation on the effect of injection system parameters on performance and emission characteristics of a twin cylinder compression ignition direct injection engine fuelled with pongamia biodiesel–diesel blend using response surface methodology, Applied Energy 88 (2011) 2663–2676.

[56] K. Belagur, R. Chitimini, Effect of injector opening pressures on the performance, emission and combustion characteristics of di diesel engine running on honne oil and diesel fuel blend, Thermal Science 14 (2010) 1051–1061.

[57] G. Kannan, R. Anand, Effect of injection pressure and injection timing on di diesel engine fuelled with biodiesel from waste cooking oil, Biomass and Bioenergy (2012).

[58] C. Hung, J. Martin, J. Koo, Injection Pressure Effects Upon Droplet Behavior in Transient Diesel Sprays, Technical Report, DTIC Document, 1997.

[59] D. Pierpont, R. Reitz, Effects of injection pressure and nozzle geometry on di diesel emissions and performance, SAE paper 950604 (1995).

[60] T. Su, C. Chang, R. Reitz, P. Farrell, A. Pierpont, T. Tow, Effects of injection pressure and nozzle geometry on spray smd and di emissions, SAE paper 952360 (1995).

[61] L. Dodge, S. Simescu, G. Neely, M. Maymar, D. Dickey, C. Savonen, Effect of small holes and high injection pressures on diesel engine combustion, SAE paper (2002) 01–0494.

[62] L. Pickett, D. Siebers, Soot in diesel fuel jets: effects of ambient temperature, ambient density, and injection pressure, Combustion and Flame 138 (2004) 114–135.

[63] X. Wang, Z. Huang, W. Zhang, O. Kuti, K. Nishida, Effects of ultra-high injection pressure and micro-hole nozzle on flame structure and soot formation of impinging diesel spray, Applied Energy 88 (2011) 1620–1628.

[64] J. Desantes, V. Bermudez, J. Garcia, E. Fuentes, Effects of current engine strategies on the exhaust aerosol particle size distribution from a heavy-duty diesel engine, Journal of aerosol science 36 (2005) 1251–1276.

[65] D. Kittelson, Engines and nanoparticles: a review, Journal of Aerosol Science 29 (1998) 575–588.

[66] J. Pagan, Study of particle size distributions emitted by a diesel engine, SAE Technical Paper (1999) 1141.

[67] T. Lahde, T. Ronkko, M. Happonen, C. Soderstrom, A. Virtanen, A. Solla, M. Kyto, D. Rothe, J. Keskinen, Effect of fuel injection pressure on a heavy-duty diesel engine nonvolatile particle emission, Environmental science & technology 45 (2011) 2504–2509.

[68] P. Herzog, The ideal rate of injection for swirl supported diesel engines, in: IMECHE Seminar on Diesel Fuel Injection Systems, London, pp. 10–1.

[69] M. Connolly, D. Richeson, N. Hamparian, Fuel injection with pulse rate shaping cam, 1995. US Patent 5,425,341.

[70] J. Regueiro, Method of fuel injection rate control, 1993. US Patent 5,261,366.

[71] M. Ganser, Common rail injector with injection rate control, SAE Tech. paper 981927 (1998).

[72] T. Nishimura, Effects of fuel injection rate on combustion and emission in a di diesel engine (1998).

[73] Y. Tarr, Injection rate shaping nozzle assembly for a fuel injector, 1999. US Patent 5,860,597.

[74] F. Camplin, M. Flinn, J. Graves, L. Zuo, Fuel injection rate shaping apparatus for a unit fuel injector, 1996. US Patent 5,566,660.

[75] F. Camplin, Rate shaping control valve for fuel injection nozzle, 1996. US Patent 5,505,384.

[76] F. Camplin, M. Flinn, L. Zuo, Fuel injection rate shaping apparatus for a unit injector, 1997. US Patent 5,632,444.

[77] B. Yen, L. Peters, J. Perr, A. Ghuman, D. Ashwill, Injection rate shaping nozzle assembly for a fuel injector, 1997. US Patent 5,647,536.

[78] L. Zuo, Injection rate shaping control ported barrel for a fuel injection system, 1995. US Patent 5,423,484.

[79] C. Liu, B. Yen, L. Peters, J. Perr, R. Durrett, D. Case, D. Ashwill, C. Sorg, J. Lane, M. Cavanagh, et al., Fuel injection rate shaping control system, 1997. US Patent 5,619,969.

[80] C. Liu, A. Ghuman, B. Yen, L. Peters, E. Smith, Hydraulically actuated fuel injector with injection rate shaping pressure intensifier, 1999. US Patent 5,894,992.

[81] S. Chockley, Hydraulically-actuated fuel injector with rate shaping spool control valve, 2000. US Patent 6,053,421.

[82] P. English, Stepped rate shaping fuel injector, 1999. US Patent 5,868,317.

[83] E. Graves, Two-stage plunger for rate shaping in a fuel injector, 1998. US Patent 5,709,341.

[84] L. Peters, J. Perr, A. Ghuman, B. Yen, C. Buchanan, R. Samuel, K. Vogt, J. Carroll III, J. Denton, D. Schisler, et al., Injection rate shaping nozzle assembly for a fuel injector, 1998. US Patent 5,765,755.

[85] S. Kohketsu, K. Tanabe, K. Mori, Flexibly controlled injection rate shape with next generation common rail system for heavy duty di diesel engines, SAE paper (2000) 01–0705.

[86] K. Tanabe, S. Kohketsu, K. Mori, K. Kawai, Innovative injection rate control with next generation common rail fuel injection system, in: FISITA World Automotive Congress, Seoul, paper F2000A055, volume 286.

[87] J. Hwang, H. Kal, M. Kim, J. Park, L. Shenghua, A. Martychenko, J. Chae, Effect of fuel injection rate on pollutant emissions in di diesel engine, SAE paper (1999) 01–0195.

[88] J. Benajes, R. Payri, S. Molina, V. Soare, Investigation of the influence of injection rate shaping on the spray characteristics in a diesel common rail system equipped with a piston amplifier, Journal of fluids engineering 127 (2005) 1102–1110.

[89] N. Beck, S. Chen, Injection Rate Shaping and High Speed Combustion Analysis: New Tools for Diesel Engine Combustion Development, Society of Automotive Engineers, 1990.

[90] J. Desantes, J. Benajes, S. Molina, C. Gonzalez, The modification of the fuel injection rate in heavy-duty diesel engines. part 1: Effects on engine performance and emissions, Applied thermal engineering 24 (2004) 2701–2714.

[91] J. Desantes, J. Benajes, S. Molina, C. Gonzalez, The modification of the fuel injection rate in heavy-duty diesel engines: Part 2: Effects on combustion, Applied thermal engineering 24 (2004) 2715–2726.

[92] M. Ghaffarpour, R. Baranescu, NOx Reduction Using Injection Rate Shaping and Intercooling in Diesel Engines, Society of Automotive Engineers, 1996.

[93] M. Ghaffarpour, M. Azarfam, A. Noorpoor, Emission reduction in diesel engines using new fuel injection system, JSME International Journal Series B 49 (2006) 1298–1306.

[94] M. Tat, J. Van Gerpen, Measurement of biodiesel speed of sound and its impact on injection timing, National Renewable Energy Laboratory, NREL/SR-510-31462 (2003).

[95] M. Tat, J. Van Gerpen, Speed of sound and isentropic bulk modulus of alkyl monoesters at elevated temperatures and pressures, Journal of the American Oil Chemists' Society 80 (2003) 1249–1256.

[96] J. Sybist, A. Boehman, Behavior of a diesel injection system with biodiesel fuel, SAE technical paper 1039 (2003).

[97] B. Kegl, A. Hribernik, Experimental analysis of injection characteristics using biodiesel fuel, Energy & fuels 20 (2006) 2239–2248.

[98] F. Caresana, Impact of biodiesel bulk modulus on injection pressure and injection timing. the effect of residual pressure, Fuel 90 (2011) 477–485.

[99] J. Suryawanshi, N. Deshpande, Effect of injection timing retard on emissions and performance of a pongamia oil methyl ester fuelled ci engine, SAE Technical Paper 1 (2005) 3677.

[100] O. Nwafor, G. Rice, A. Ogbonna, Effect of advanced injection timing on the performance of rapeseed oil in diesel engines, Renewable Energy 21 (2000) 433–444.

[101] J. Narayana Reddy, A. Ramesh, Parametric studies for improving the performance of a jatropha oil-fuelled compression ignition engine, Renewable Energy 31 (2006) 1994–2016.

[102] T. Ganapathy, R. Gakkhar, K. Murugesan, Influence of injection timing on performance, combustion and emission characteristics of jatropha biodiesel engine, Applied energy 88 (2011) 4376–4386.

[103] A. Yahya, S. Marley, Performance and exhaust emissions of a compression ignition engine operating on ester fuels at increased injection pressure and advanced timing, Biomass and Bioenergy 6 (1994) 297–319.

[104] H. Raheman, S. Ghadge, Performance of diesel engine with biodiesel at varying compression ratio and ignition timing, Fuel 87 (2008) 2659–2666.

[105] A. Monyem, J. Gerpen, M. Canakci, et al., The effect of timing and oxidation on emissions from biodiesel-fueled engines., Transactions of the ASAE 44 (2001) 35–42.

[106] M. Gumus, C. Sayin, M. Canakci, Effect of fuel injection timing on the injection, combustion, and performance characteristics of a direct-injection (di) diesel engine fueled with canola oil methyl ester- diesel fuel blends, Energy & Fuels 24 (2010) 3199–3213.

[107] M. Mani, G. Nagarajan, Influence of injection timing on performance, emission and combustion characteristics of a di diesel engine running on waste plastic oil, Energy 34 (2009) 1617–1623.

[108] V. Hariram, G. Mohan Kumar, The effect of injection timing on combustion, performance and emission parameters with aome blends as a fuel for compression ignition engine, European Journal of Scientific Research 79 (2012) 653–665.

[109] G. Abd Alla, H. Soliman, O. Badr, M. Abd Rabbo, Effect of injection timing on the performance of a dual fuel engine, Energy conversion and Management 43 (2002) 269–277.

[110] N. Noguchi, H. Terao, C. Sakata, Performance improvement by control of flow rates and diesel injection timing on dual-fuel engine with ethanol, Bioresource technology 56 (1996) 35–39.

[111] C. Sayin, K. Uslu, M. Canakci, Influence of injection timing on the exhaust emissions of a dual-fuel ci engine, Renewable Energy 33 (2008) 1314–1323.

[112] C. Sayin, M. Canakci, Effects of injection timing on the engine performance and exhaust emissions of a dual-fuel diesel engine, Energy conversion and management 50 (2009) 203–213.

[113] B. Kegl, Experimental investigation of optimal timing of the diesel engine injection pump using biodiesel fuel, Energy & Fuels 20 (2006) 1460–1470.

[114] K. Zeng, Z. Huang, B. Liu, L. Liu, D. Jiang, Y. Ren, J. Wang, Combustion characteristics of a direct-injection natural gas engine under various fuel injection timings, Applied thermal engineering 26 (2006) 806–813.

[115] Z. Huang, S. Shiga, T. Ueda, H. Nakamura, T. Ishima, T. Obokata, M. Tsue, M. Kono, Effect of fuel injection timing relative to ignition timing on the natural-gas direct-injection combustion, Journal of engineering for gas turbines and power 125 (2003) 783.

[116] S. Mohammed, M. Baharom, A. Aziz, et al., The effects of fuel-injection timing at medium injection pressure on the engine characteristics and emissions of a cng-di engine fueled by a small amount of hydrogen in cng, International Journal of Hydrogen Energy 36 (2011) 11997–12006.

[117] S. Jaichandar, P. Tamilporai, Low heat rejection engines–an overview, SAE paper (2003) 01–0405.

[118] R. Kamo, N. Mavinahally, L. Kamo, W. Bryzik, E. Schwartz, Injection characteristics that improve performance of ceramic-coated diesel engines, SAE paper (1999) 01–0972.

[119] A. Parlak, H. Yasar, C. Hacsimoglu, A. Kolip, The effects of injection timing on nox emissions of a low heat rejection indirect diesel injection engine, Applied thermal engineering 25 (2005) 3042–3052.

[120] E. Buyukkaya, T. Engin, M. Cerit, Effects of thermal barrier coating on gas emissions and performance of a lhr engine with different injection timings and valve adjustments, Energy conversion and management 47 (2006) 1298–1310.

[121] E. Buyukkaya, M. Cerit, Experimental study of nox emissions and injection timing of a low heat rejection diesel engine, International journal of thermal sciences 47 (2008) 1096–1106.

[122] M. Badami, F. Mallamo, F. Millo, E. Rossi, Influence of multiple injection strategies on emissions, combustion noise and bsfc of a di common rail diesel engine, SAE paper (2002) 01–0503.

[123] D. Montgomery, R. Reitz, Six-mode cycle evaluation of the effect of egr and multiple injections on particulate and nox emissions from a di diesel engine, SAE paper 960316 (1996).

[124] S. Shundoh, M. Komori, K. Tsujimura, S. Kobayashi, Nox reduction from diesel combustion using pilot injection with high pressure fuel injection, SAE Special Publications (1992) 25–36.

[125] J. Benajes, S. Molina, R. Novella, K. DeRudder, Influence of injection conditions and exhaust gas recirculation in a high-speed direct-injection diesel engine operating with a late split injection, Proceedings of the Institution of Mechanical Engineers, Part D: Journal of Automobile Engineering 222 (2008) 629–641.

[126] M. Durnholz, H. Endres, P. Frisse, Preinjection a measure to optimize the emission behavior of di-diesel engine, SAE paper 940674 (1994).

[127] D. Pierpont, D. Montgomery, R. Reitz, Reducing particulate and nox using multiple injections and egr in a di diesel, SAE paper 950217 (1995).

[128] T. Tow, D. Pierpont, R. Reitz, Reducing particulate and nox emissions by using multiple injections in a heavy duty di diesel engine, SAE paper 940897 (1994).

[129] S. Chen, Simultaneous reduction of nox and particulate emissions by using multiple injections in a small diesel engine, SAE paper (2000) 01–3084.

[130] Y. Hotta, M. Inayoshi, K. Nakakita, K. Fujiwara, I. Sakata, Achieving lower exhaust emissions and better performance in an hsdi diesel engine with multiple injection, SAE Paper (2005) 01–0928.

[131] C. Choi, R. Reitz, An experimental study on the effects of oxygenated fuel blends and multiple injection strategies on di diesel engine emissions, Fuel 78 (1999) 1303–1317.

[132] T. Fang, C. Lee, Bio-diesel effects on combustion processes in an hsdi diesel engine using advanced injection strategies, Proceedings of the Combustion Institute 32 (2009) 2785–2792.

[133] K. Verbiezen, A. Donkerbroek, R. Klein-Douwel, A. Van Vliet, P. Frijters, X. Seykens, R. Baert, W. Meerts, N. Dam, J. Ter Meulen, Diesel combustion: In-cylinder no concentrations in relation to injection timing, Combustion and Flame 151 (2007) 333–346.

[134] T. Fang, Y.-C. Lin, T. M. Foong, C.-f. Lee, Biodiesel combustion in an optical hsdi diesel engine under low load premixed combustion conditions, Fuel 88 (2009) 2154–2162.

[135] M. R. Herfatmanesh, P. Lu, M. A. Attar, H. Zhao, Experimental investigation into the effects of two-stage injection on fuel injection quantity, combustion and emissions in a high-speed optical common rail diesel engine, Fuel 109 (2013) 137–147.

[136] S. Merola, C. Tornatore, S. Iannuzzi, L. Marchitto, G. Valentino, Combustion process investigation in a high speed diesel engine fuelled with n-butanol diesel blend by conventional methods and optical diagnostics, Renewable Energy 64 (2014) 225–237.

[137] J. Rife, J. B. Heywood, Photographic and performance studies of diesel combustion with a rapid compression machine, Technical Report, SAE Technical Paper, 1974.

[138] H. Kobayashi, T. Kamimoto, S. Matsuoka, A photographic and thermodynamic study of diesel combustion in a rapid compression machine, Technical Report, SAE Technical Paper, 1981.

[139] D. L. Siebers, Liquid-phase fuel penetration in diesel sprays (1998).

[140] E. Delacourt, B. Desmet, B. Besson, Characterisation of very high pressure diesel sprays using digital imaging techniques, Fuel 84 (2005) 859–867.

[141] A. K. Agarwal, V. H. Chaudhury, Spray characteristics of biodiesel blends in a high pressure constant volume spray chamber, Experimental Thermal and Fluid Science 42 (2012) 212–218.

[142] X. Wang, Z. Huang, O. A. Kuti, W. Zhang, K. Nishida, Experimental and analytical study on biodiesel and diesel spray characteristics under ultra-high injection pressure, International Journal of Heat and Fluid Flow 31 (2010) 659–666.

[143] S. Soid, Z. Zainal, Spray and combustion characterization for internal combustion engines using optical measuring techniques–a review, Energy 36 (2011) 724–741.

[144] J. Shao, Y. Yan, G. Greeves, S. Smith, Quantitative characterization of diesel sprays using digital imaging techniques, Measurement Science and Technology 14 (2003) 1110.

[145] Y. Gao, J. Deng, C. Li, F. Dang, Z. Liao, Z. Wu, L. Li, Experimental study of the spray characteristics of biodiesel based on inedible oil, Biotechnology Advances 27 (2009) 616–624.

[146] S. H. Park, H. J. Kim, C. S. Lee, Macroscopic spray characteristics and breakup performance of dimethyl ether (dme) fuel at high fuel temperatures and ambient conditions, Fuel 89 (2010) 3001–3011.

[147] Y. Yi, Gb 150.3-2011 pressure vessels - part 3: Design changes key points 29 (2003) 14–25.

[148] K. B. Doyle, M. A. Kahan, M. Westborough, Design strength of optical glass, in: Proceedings of SPIE, volume 5176, pp. 14–25.

[149] J. Zecher, F. Dadkhah, Ansys workbench tutorial with multimedia cd release 12 (2009).

[150] V. Macián, V. Bermúdez, R. Payri, J. Gimeno, New technique for determination of internal geometry of a diesel nozzle with the use of silicone methodology, Experimental techniques 27 (2003) 39–43.

[151] N. Otsu, A threshold selection method from gray-level histograms, Automatica 11 (1975) 23–27.

[152] J. Canny, A computational approach to edge detection, Pattern Analysis and Machine Intelligence, IEEE Transactions on (1986) 679–698.

[153] R. Payri, J. Garcia, F. Salvador, J. Gimeno, Using spray momentum flux measurements to understand the influence of diesel nozzle geometry on spray characteristics, Fuel 84 (2005) 551–561.

[154] C. Rakopoulos, D. Rakopoulos, E. Giakoumis, D. Kyritsis, Validation and sensitivity analysis of a two zone diesel engine model for combustion and emissions prediction, Energy conversion and management 45 (2004) 1471–1495.

[155] R. Payri, S. Ruiz, F. Salvador, J. Gimeno, On the dependence of spray momentum flux in spray penetration: Momentum flux packets penetration model, Journal of mechanical science and technology 21 (2007) 1100–1111.

[156] E. Von Berg, W. Edelbauer, A. Alajbegovic, R. Tatschl, M. Volmajer, B. Kegl, L. C. Ganippa, Coupled simulations of nozzle flow, primary fuel jet breakup, and spray formation, Journal of engineering for gas turbines and power 127 (2005) 897–908.

[157] F. Payri, V. Bermudez, R. Payri, F. Salvador, The influence of cavitation on the internal flow and the spray characteristics in diesel injection nozzles, Fuel 83 (2004) 419–431.

[158] J.-M. Shi, M. S. Arafin, Cfd investigation of fuel property effect on cavitating flow in generic nozzle geometries, ILASS-Europe 2010 (2010).

[159] J.-G. Nerva, C. L. Genzale, S. Kook, J. M. García-Oliver, L. M. Pickett, Fundamental spray and combustion measurements of soy methyl-ester biodiesel, International Journal of Engine Research 14 (2013) 373–390.

[160] K. Muralidharan, D. Vasudevan, Performance, emission and combustion characteristics of a variable compression ratio engine using methyl esters of waste cooking oil and diesel blends, Applied energy 88 (2011) 3959–3968.

[161] M. Lapuerta, J. Rodríguez-Fernández, J. R. Agudelo, Diesel particulate emissions from used cooking oil biodiesel, Bioresource Technology 99 (2008) 731–740.

[162] Y.-C. Lin, K.-H. Hsu, C.-B. Chen, Experimental investigation of the performance and emissions of a heavy-duty diesel engine fueled with waste cooking oil biodiesel/ultra-low sulfur diesel blends, Energy 36 (2011) 241–248.

[163] C. Arcoumanis, M. Gavaises, B. French, Effect of fuel injection process on the structure of diesel sprays, SAE Paper (1997).

[164] G. Stiesch, Modeling engine spray and combustion processes, Springer, 2003.

[165] N. Takenaka, T. Kadowaki, Y. Kawabata, I. Lim, C. Sim, Visualization of cavitation phenomena in a diesel engine fuel injection nozzle by neutron radiography, Nuclear Instruments and Methods in Physics Research, Section A 1-3 (2005) 129–133.

[166] T. Innamura, H. Saito, T. Onodera, H. Sakamoto, A. Kumakawa, Cavitating flow in rectangular nozzle with orifice, in: ILASS, pp. 273–280.

[167] Z. He, W. Zhong, Q. Wang, Z. Jiang, Y. Fu, An investigation of transient nature of the cavitating flow in injector nozzles, Applied Thermal Engineering (2013).

[168] R. Payri, F. Salvador, J. Gimeno, O. Venegas, Study of cavitation phenomenon using different fuels in a transparent nozzle by hydraulic characterization and visualization, Experimental Thermal and Fluid Science (2012).

[169] C. Soteriou, R. Andrews, M. Smith, Direct injection diesel sprays and the effect of cavitation and hydraulic flip, SAE 15 (1995) 116–126.

[170] C. Soteriou, M. Smith, R. Andrews, Diesel injection: laser light sheet illumination of the development of cavitation in orifices, in: IMECHE conference transactions, pp. 137–158.

[171] W. Bergwerk, Flow pattern in diesel nozzle spray holes, Proceedings of the Institution of Mechanical Engineers 173 (1959) 655–660.

[172] H. Chaves, M. Knapp, A. Kubitzek, F. Obermier, T. Schneider, Experimental study of cavitation in the nozzle hole of diesel injectors using transparent nozzles, SAE (1995).

[173] C. Arcoumanis, H. Flora, M. Gavaises, N. Kampanis, R. Horrocks, Investigation of cavitation in a vertical multi-hole injector, SAE transactions 108 (1999) 661–678.

[174] C. Arcoumanis, M. Badami, H. Flora, M. Gavaises, Cavitation in real-size, multi-hole diesel injector nozzles, SAE transactions 109 (2000) 1485–1500.

[175] C. Badock, R. Wirth, A. Fath, A. Leipertz, Investigation of cavitation in real size diesel injection nozzles, International Journal of Heat and Fluid Flow 20 (1999).

[176] J. Desantes, R. P. F. Salvador, J. D. L. Morena, Influence of cavitation on spray break-up and spray behavior at stationary conditions, Fuel (2010).

[177] F. Payri, V. Bermudez, R. R. F. Salvador, The influence of cavitation on the internal flow and the spray characteristics in diesel injection nozzles, Fuel 83 (2004).

[178] H. K. Suh, C. S. Lee, Effect of cavitation in nozzle orifice on the diesel fuel atomization characteristics, International journal of heat and fluid flow 29 (2008) 1001–1009.

[179] M. De Giorgi, A. Ficarella, M. Tarantino, Evaluating cavitation regimes in an internal orifice at different temperatures using frequency analysis and visualization, International Journal of Heat and Fluid Flow (2012).

[180] L. Ganippa, G. Bark, S. Andersson, J. Chomiak, Comparison of cavitation phenomena in transparent scale-up single hole diesel nozzle, in: CAV.

[181] H. Hiroyasu, M. Arai, M. Shimizu, Break-up length of liquid jet and internal flow in a nozzle, in: ICLASS, pp. 177–184.

[182] W. Nurick, Orifice cavitation and its effect on spray mixing, Journal of Fluid Engineering 98 (1976) 681–687.

[183] R. Payri, F. Salvador, J. Gimeno, J. De la Morena, Study of cavitation phenomena based on a technique for visualizing bubbles in a liquid pressurized chamber, International Journal of Heat and Fluid Flow 30 (2009) 768–777.

[184] N. Tamaki, M. Shimizu, H. Hiroyasu, Enhancement of the atomization of a liquid jet by cavitation in a nozzle hole, Atomization and Sprays 11 (2001) 125–137.

[185] E. Winklhofer, E. kull, E. Kelz, A. Morozov, Comprehensive hydraulic and flow field documentation in model throttle experiments under cavitation conditions, in: ILASS, pp. 574–579.

[186] X. Margot, S. Hoyas, A. Gil, S. Patouna, Numerical modelling of cavitation: validation and parametric studies, Engineering Applications of Computational Fluid Mechanics 6 (2012) 15–24.

[187] A. Andriotis, M. Gavaises, C. Arcoumanis, Vortex flow and cavitation in diesel injector nozzles, Journal of Fluid Mechanics 610 (2008) 195–215.

[188] G. Schnerr, J. Sauer, Physical and numerical modeling of unsteady cavitation dynamics, in: Fourth International Conference on Multiphase Flow.

[189] W. Yuan, J. Sauer, G. Schnerr, Modeling and computation of unsteady cavitation flows in injection nozzles, Mec. Ind. 2 (2001) 383–394.

[190] Fluent, Ansys Fluent 12.0 - Theory Guide, Ansys. Inc., 2009.

[191] M. Li, A. Mulemane, M.-C. Lai, R. Poola, Simulating diesel injectors based on different cavitation modeling approaches, ASME.

[192] S. Som, A. Ramirez, S. Aggarwal, E. El-Hannouny, D. Longman, et al., Investigation of nozzle flow and cavitation characteristics in a diesel injector., J. Eng. Gas Turbines Power 132 (2010).

[193] P. O'Rourke, A. Amsden, The TAB method for numerical calculation of spray droplet breakup, Technical Report, Los Alamos National Lab., NM (USA), 1987.

[194] F. Peng, H. Weller, N. Nordin, Modelling injector flow including cavitation effects for diesel application, in: 5th Joint ASME / JSME Fluids Engineering Conference, volume 2, pp. 465–474.

[195] M. Battistoni, C. N. Grimaldi, Numerical analysis of injector flow and spray characteristics from diesel injectors using fossil and biodiesel fuels, Applied Energy 97 (2012) 656–666.

[196] M. Battistoni, C. Grimaldi, Analysis of transient cavitating flows in diesel injectors usingdiesel and biodiesel fuels, SAE - Int J fuels Lubricants (2010).

[197] W. Yuan, A. Hansen, Q. Zhang, Vapor pressure and normal boiling point predictions of pure methyl esters and biodiesel fuels, Fuel 84 (2005) 943–950.

[198] W. Yuan, A. Hansen, Q. Zhang, Predicting the temperature dependent viscosity of biodiesel fuels, Fuel 88 (2009) 1120–1126.

[199] C. Allen, K. Watts, R. Ackmanb, Predicting the surface tension of biodiesel fuels from their fatty acid composition, J Am Oil Chem Soc 76 (1999) 317–323.

[200] A. Wierzba, Deformation and breakup of liquid drops in a gas stream at nearly critical weber numbers, Experiments in Fluids 9 (1990) 59–64.

[201] G. Taylor, The shape and acceleration of a drop in a high speed air stream, The scientific papers of GI Taylor 3 (1963) 457–464.

[202] F. Tanner, Liquid jet atomization and droplet breakup modeling of non-evaporating diesel fuel sprays, SAE technical paper 970050 (1997) 127–140.

[203] F. Tanner, Development and validation of a cascade atomization and drop breakup model for high-velocity dense sprays, Atomization and Sprays 14 (2004) 211–242.

[204] R. D. Reitz, Modeling atomization process in high-pressure vaporizing sprays, Atomization and spray technology (1987).

[205] R. Reitz, Atomization and other breakup regimes of a liquid jet (1978).

[206] R. Reitz, F. Bracco, Mechanism of atomization of a liquid jet, Physics of Fluids 25 (1982) 1730–1742.

[207] R. Reitz, Spray technology short course, Pittsburgh, PA, May 7 (1996).

[208] M. Patterson, R. Reitz, Modeling the effects of fuel spray characteristics on diesel engine combustion and emission, SAE paper 980131 (1998).

[209] T. Su, M. Patterson, R. Reitz, P. Farrell, Experimental and numerical studies of high pressure multiple injection sprays, SAE paper 960861 (1996).

[210] J. Xin, L. Ricart, R. Reitz, Computer modeling of diesel spray atomization and combustion, Combustion Science and Technology 137 (1998) 171–194.

[211] P. Senecal, K. Richards, E. Pomraning, T. Yang, M. Dai, R. McDavid, M. Patterson, S. Hou, T. Sethaji, A new parallel cut-cell cartesian cfd code for rapid grid generation applied to in-cylinder diesel engine simulations, SAE paper (2007) 01.

[212] D. Joseph, J. Belanger, G. Beavers, Breakup of a liquid drop suddenly exposed to a high-speed airstream, International Journal of Multiphase Flow 25 (1999) 1263–1303.

[213] G. Bianchi, P. Pelloni, Modeling the diesel fuel spray break-up by using a hybrid model, SAE paper (1999) 01–0226.

[214] C. Arcoumanis, M. Gavaises, Linking nozzle flow with spray characteristics in a diesel fuel injection system, Atomization and Sprays 8 (1998) 307–347.

[215] L. Bayvel, Liquid atomization, volume 1040, CRC, 1993.

[216] S. Som, S. Aggarwal, Effects of primary breakup modeling on spray and combustion characteristics of compression ignition engines, Combustion and Flame 157 (2010) 1179–1193.

[217] F. Bracco, Modeling of engine sprays, Technical Report, Princeton Univ., NJ (USA). Dept. of Mechanical and Aerospace Engineering, 1985.

[218] R. D. Reitz, Modeling atomization processes in high-pressure vaporizing sprays, Atomisation Spray Technology 3 (1987) 309–337.

[219] J. C. Beale, R. D. Reitz, Modeling spray atomization with the kelvin-helmholtz/rayleigh-taylor hybrid model, Atomization and sprays 9 (1999).

[220] C. Rakopoulos, K. Antonopoulos, D. Rakopoulos, Multi-zone modeling of diesel engine fuel spray development with vegetable oil, bio-diesel or diesel fuels, Energy Conversion and Management 47 (2006) 1550–1573.

[221] Z. Zhao, M. Xie, Numerical simulation about interaction between pressure swirl spray and hot porous medium, Energy Conversion and Management 49 (2008) 1047–1055.

[222] H. Watanabe, Y. Suwa, Y. Matsushita, Y. Morozumi, H. Aoki, S. Tanno, T. Miura, Spray combustion simulation including soot and no formation, Energy conversion and management 48 (2007) 2077–2089.

[223] S. A. Basha, K. Raja Gopal, In-cylinder fluid flow, turbulence and spray models-a review, Renewable and Sustainable Energy Reviews 13 (2009) 1620–1627.

[224] S. Wei, F. Wang, X. Leng, X. Liu, K. Ji, Numerical analysis on the effect of swirl ratios on swirl chamber combustion system of di diesel engines, Energy Conversion and Management 75 (2013) 184–190.

[225] K. Huh, A. Gosman, A phenomenological model of diesel spray atomization, in: Proceedings of the international conference on multiphase flows, pp. 24–27.

[226] G. Bianchi, P. Pelloni, F. Corcione, L. Allocca, F. Luppino, Modeling atomization of high-pressure diesel sprays, Journal of engineering for gas turbines and power 123 (2001) 419–427.

[227] A. Amsden, P. O'Rourke, T. Butler, 'kiva-3: A kiva program with bock-structured mesh for complex geometries,'. los alamos national labs, la-12503-ms (1993).

[228] A. A. Amsden, Kiva-3: A kiva program with block-structured mesh for complex geometries (1993).

[229] F. P. Kärrholm, H. Weller, N. Nordin, Modelling injector flow including cavitation effects for diesel applications, ASME.

[230] Y. Sharma, B. Singh, Development of biodiesel-current scenario, Renewable and Sustainable Energy Reviews 13 (2009) 1646–1651.

[231] V. B. Borugadda, V. V. Goud, Biodiesel production from renewable feedstocks - status and opportunities, Renewable and Sustainable Energy Reviews 16 (2012) 4763–4784.

[232] B. Mohan, W. a. C. Yang, Fuel injection strategies for performance improvement and emissions reduction in compression ignition engines-a review, Renewable and Sustainable Energy Reviews 28 (2013) 664–676.

[233] V. I. Golovitchev, J. Yang, Construction of combustion models for rapeseed methyl ester bio-diesel fuel for internal combustion engine applications, Biotechnology advances 27 (2009) 641–655.

[234] Y. Ra, R. D. Reitz, J. McFarlane, C. S. Daw, Effects of fuel physical properties on diesel engine combustion using diesel and bio-diesel fuels, Technical Report, SAE Technical Paper, 2008.

[235] W. Yuan, A. Hansen, Q. Zhang, et al., Predicting the physical properties of biodiesel for combustion modeling, Transactions of the ASAE 46 (2003) 1487–1493.

[236] S. Hoekman, C. Robbins, Review of the effects of biodiesel on nox emissions, Fuel Processing Technology 96 (2012) 237–249.

[237] S. Singh, D. Singh, Biodiesel production through the use of different sources and characterization of oils and their esters as the substitute of diesel: A review, Renewable and Sustainable Energy Reviews 14 (2010) 200–216.

[238] S. Choi, Y. Oh, The spray characteristics of unrefined biodiesel, Renewable Energy 42 (2012) 136–139.

[239] O. A. Kuti, J. Zhu, K. Nishida, X. Wang, Z. Huang, Characterization of spray and combustion processes of biodiesel fuel injected by diesel engine common rail system, Fuel 104 (2013) 838–846.

[240] Y. Lee, K. Y. Huh, Numerical study on spray and combustion characteristics of diesel and soy-based biodiesel in a ci engine, Fuel 113 (2013) 537–545.

[241] H. M. Ismail, H. K. Ng, X. Cheng, S. Gan, T. Lucchini, G. DErrico, Development of thermophysical and transport properties for the cfd simulations of in-cylinder biodiesel spray combustion, Energy and Fuels 26 (2012) 4857–4870.

[242] S. Som, D. Longman, A. Ramírez, S. Aggarwal, A comparison of injector flow and spray characteristics of biodiesel with petrodiesel, Fuel 89 (2010) 4014–4024.

[243] H. An, W. Yang, A. Maghbouli, S. Chou, K. Chua, Detailed physical properties prediction of pure methyl esters for biodiesel combustion modeling, Applied energy 102 (2013) 647–656.

[244] Y. Ra, R. D. Reitz, A vaporization model for discrete multi-component fuel sprays, International Journal of Multiphase Flow 35 (2009) 101–117.

[245] W. Zhong, Z. He, Q. Wang, Z. Jiang, Y. Fu, Investigation of the cavitating flow in injector nozzles for diesel and biodiesel, in: 7th International Symposium on multiphase flow, heat mass transfer and energy conversion, volume 1547, AIP Publishing, pp. 40–46.

[246] S. H. Park, H. J. Kim, H. K. Suh, C. S. Lee, A study on the fuel injection and atomization characteristics of soybean oil methyl ester (sme), International Journal of Heat and Fluid Flow 30 (2009) 108–116.

[247] G. Faeth, L.-P. Hsiang, P.-K. Wu, Structure and breakup properties of sprays, International Journal of Multiphase Flow 21 (1995) 99–127.

[248] L.-P. Hsiang, G. M. Faeth, Drop properties after secondary breakup, International Journal of Multiphase Flow 19 (1993) 721–735.

[249] B. E. Poling, J. M. Prausnitz, O. John Paul, R. C. Reid, The properties of gases and liquids, volume 5, McGraw-Hill New York, 2001.

[250] S. No, Inedible vegetable oils and their derivatives for alternative diesel fuels in ci engines: A review, Renewable and Sustainable Energy Reviews 15 (2011) 131–149.

[251] D. Bora, D. Baruah, Assessment of tree seed oil biodiesel: A comparative review based on biodiesel of a locally available tree seed, Renewable and Sustainable Energy Reviews 16 (2012) 1616–1629.

[252] A. K. Agarwal, Biofuels (alcohols and biodiesel) applications as fuels for internal combustion engines, Progress in energy and combustion science 33 (2007) 233–271.

[253] M. M. Roy, W. Wang, J. Bujold, Biodiesel production and comparison of emissions of a di diesel engine fueled by biodiesel–diesel and canola oil–diesel blends at high idling operations, Applied Energy 106 (2013) 198–208.

[254] S. Ghadge, H. Raheman, Process optimization for biodiesel production from mahua (madhuca indica) oil using response surface methodology, Bioresource Technology 97 (2006) 379–384.

[255] H. Raheman, S. Ghadge, Performance of compression ignition engine with mahua (madhuca indica) biodiesel, Fuel 86 (2007) 2568–2573.

[256] S. Godiganur, C. Suryanarayana Murthy, R. Reddy, 6bta 5.9 g2-1 cummins engine performance and emission tests using methyl ester mahua (madhuca indica) oil/diesel blends, Renewable Energy 34 (2009) 2172–2177.

[257] B. Kegl, S. Pehan, Influence of biodiesel on injection, fuel spray, and engine characteristics, Thermal Science 12 (2008) 171–182.

[258] C. Sayin, M. Gumus, M. Canakci, Effect of fuel injection pressure on the injection, combustion and performance characteristics of a di diesel engine fueled with canola oil methyl esters-diesel fuel blends, Biomass and Bioenergy (2012).

[259] Environmental technology verification report - mobile source emission control device, 2006.

[260] S. Fritz, L. Dodge, Correction procedure for humidity effects on nox emissions from locomotive engines, Southwest Research Institute (1997).

[261] L. Dodge, T. Callahan, T. Ryan, Humidity and temperature correction factors for nox emissions from diesel engines, Southwest Research Institute (2003).

[262] J. Holman, Experimental techniques for engineers, Tata McGraw Hill, New Delhi (2004).

[263] J. P. Szybist, A. L. Boehman, J. D. Taylor, R. L. McCormick, Evaluation of formulation strategies to eliminate the biodiesel no_x effect, Fuel Processing Technology 86 (2005) 1109–1126.

[264] Worldwide emissions standards - heavy duty and off-road vehicles, 2011.

[265] B. Venkanna, C. Reddy, S. Wadawadagi, Performance, emission and combustion characteristics of direct injection diesel engine running on rice bran oil/diesel fuel blend, International journal of chemical and biomolecular engineering 14 (2009) 15.

[266] S. Bari, C. Yu, T. Lim, Effect of fuel injection timing with waste cooking oil as a fuel in a direct injection diesel engine, Proceedings of the Institution of Mechanical Engineers, Part D: Journal of Automobile Engineering 218 (2004) 93–104.

[267] C. Sayin, M. Ilhan, M. Canakci, M. Gumus, Effect of injection timing on the exhaust emissions of a diesel engine using diesel–methanol blends, Renewable Energy 34 (2009) 1261–1269.

[268] K. Yehliu, A. L. Boehman, O. Armas, Emissions from different alternative diesel fuels operating with single and split fuel injection, Fuel 89 (2010) 423–437.

[269] M. Lapuerta, O. Armas, R. Ballesteros, J. Fernandez, Diesel emissions from biofuels derived from spanish potential vegetable oils, Fuel 84 (2005) 773–780.

[270] M. S. Graboski, R. L. McCormick, Combustion of fat and vegetable oil derived fuels in diesel engines, Progress in energy and combustion science 24 (1998) 125–164.

[271] O. Armas, K. Yehliu, A. L. Boehman, Effect of alternative fuels on exhaust emissions during diesel engine operation with matched combustion phasing, Fuel 89 (2010) 438–456.

[272] M. Bergman, V. I. Golovitchev, Application of transient temperature vs. equivalence ratio emission maps to engine simulations, Technical Report, SAE Technical Paper, 2007.

[273] J. Brakora, R. Reitz, A comprehensive combustion model for biodiesel-fueled engine simulations, Technical Report, SAE Technical Paper, 2013.

[274] H. Juneja, Y. Ra, R. D. Reitz, Optimization of injection rate shape using active control of fuel injection, Technical Report, SAE Technical Paper, 2004.

[275] V. Luckhchoura, Modeling of injection-rate shaping in diesel engine combustion, Ph.D. thesis, Universitätsbibliothek, 2010.

[276] A. Sou, B. Biçer, A. Tomiyama, Numerical simulation of incipient cavitation flow in a nozzle of fuel injector, Computers and Fluids 103 (2014) 42–48.

[277] G. D'Errico, T. Lucchini, G. Montenegro, M. Zanardi, Development of openfoam application for internal combustion engine simulation (2007).

A

Drawing of high pressure chamber

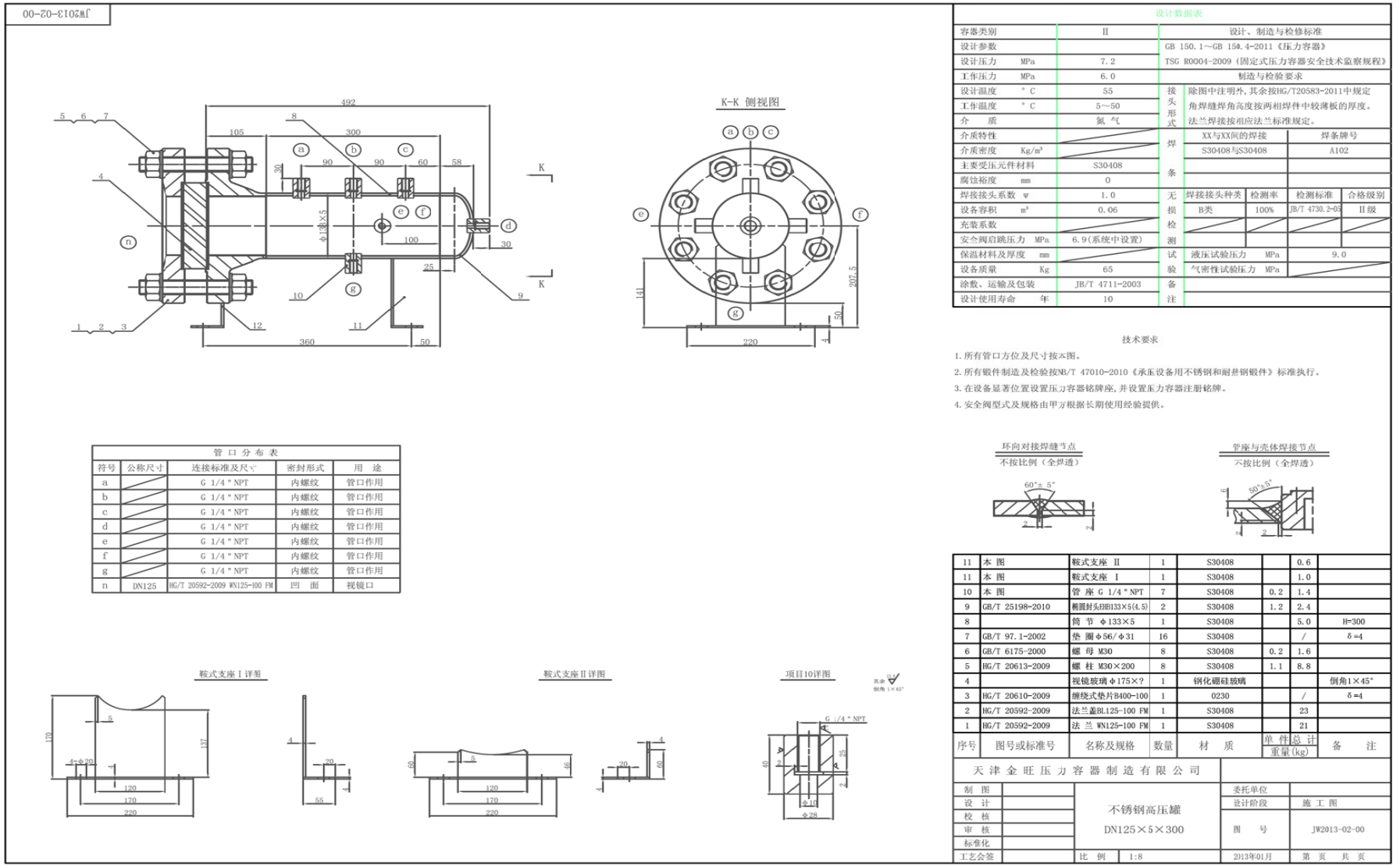

Figure A.1: Detailed drawing of high pressure chamber

CERTIFICATE OF TEST

Serial No.
2013-0170

REPORT OF EXAMINATION OF
Receiver

Safe Working Pressure
6000.0 kN/sq.m.

NAME OF OWNER : **National University of Singapore**
Department of Mechanical Engineering
LOCATION : **Energy Conversion Lab**
E2-B-02
: **9 Engineering Drive 1**
: **Singapore 117576**
:

WORKPLACE NO.
NUS

NEXT INSPECTION DATE
17/03/2015

PARTICULARS OF VESSEL

BRAND NAME	: ACEFUND	YEAR MANUFACTURED	: 2013
COUNTRY OF MFG	: CHINA	DATE REGISTERED	: 18/03/2013
REGISTRATION NO	: NA	MOBILITY	: Stationary
TYPE OF VESSEL	: Receiver	HEATING SURFACE	: NA
POSITION	: Horizontal	TEST PRESSURE	: 9500.0 kN/sq.m
VOLUME	: 6 litres	HEAT SOURCE	: NA
MDMT	: NA	DESIGN CODE	:

DESCRIPTION

TANK / VESSEL

	SHAPE	SIDE PRESSURE ACTS ON	THICKNESS	MATERIAL
HEAD 1	: Flat	Others	40.0 mm	
HEAD 2	: Ellipsoidal	Concave	5.7 mm	
SHELL	:		5.7 mm	
DIA1/WIDTH	: 133 mm		DIA2/WIDTH :	
HEIGHT/LENGTH	: 405 mm			

PRESSURE TEST DAT : 13/03/2013 THICKNESS TEST DATE : 13/03/2013

DESCRIPTION OF TEST PERFORMED	TEST DATES
Visual Examination	18/03/2013
Running Test	18/03/2013

OBSERVATIONS : Horizontal tank of 6 litres

CONDITIONS : New

Subject to the reservation above, I thoroughly examined the pressure vessel described (so far as its construction permits), including its fittings, attachment and appliances and that the above is a true report of my examination.

EDRIC LEONG SUARN KIE
AUTHORISED EXAMINER
18/03/2013

Figure A.2: PE certificate

B

Drawings of force sensor fixture

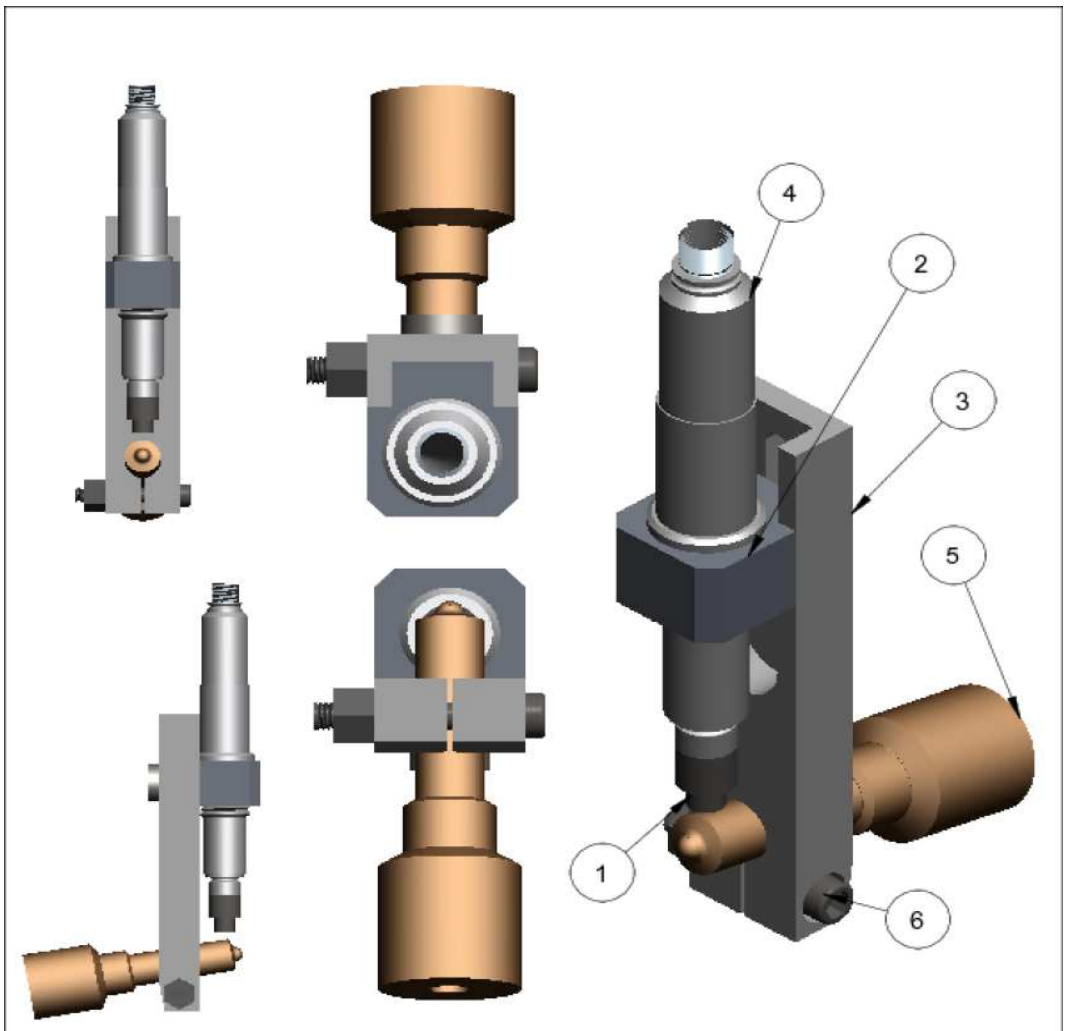

FORCE SENSOR ASSEMBLY

Drawn by :
BALAJI MOHAN
National University Of Singapore

Bill Of Materials

S.No	Components
1	Sensor Cap
2	Sensor Nut
3	Support
4	Sensor
5	Injector Nozzle
6	Allen Screw

Figure B.1: Assembly view of force sensor with fixture

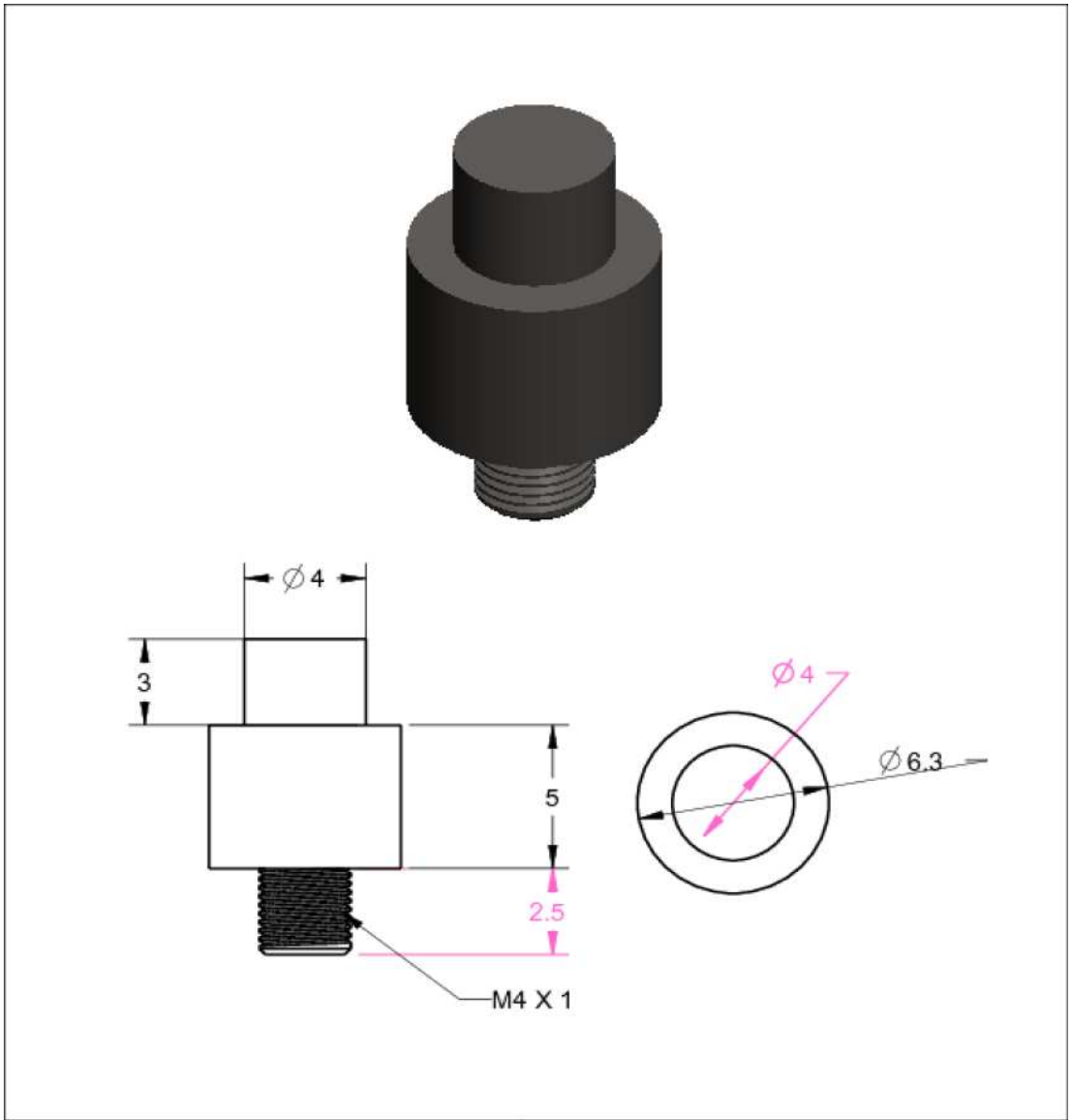

SENSOR CAP	Material : Aluminium	
	Drawing No. : 1	
	Projection : First Angle	
	Unit : mm	Scale - 1:1
	Tolerances :	
Drawn by : BALAJI MOHAN National University Of Singapore	Linear Dimensions : + /- 0.2	Angular Dimensions : +/- 60'

Figure B.2: Sensor cap

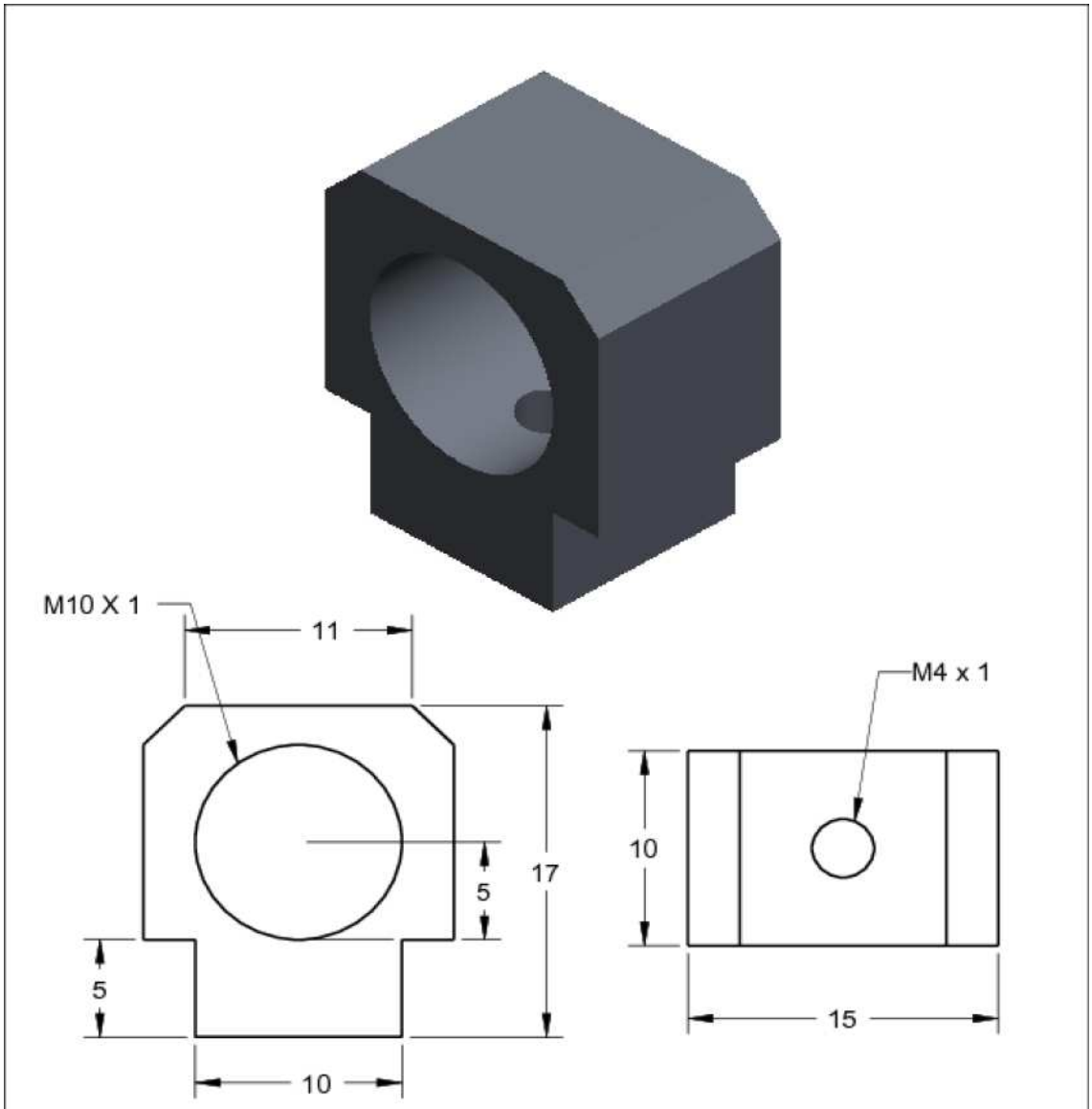

SENSOR NUT	Material : Aluminium	
	Drawing No. : 2	
	Projection : First Angle	
	Unit : mm	Scale - 1:1
	Tolerances :	
Drawn by : BALAJI MOHAN National University Of Singapore	Linear Dimensions : + /- 0.5	Angular Dimensions : +/- 60'

Figure B.3: Sensor nut

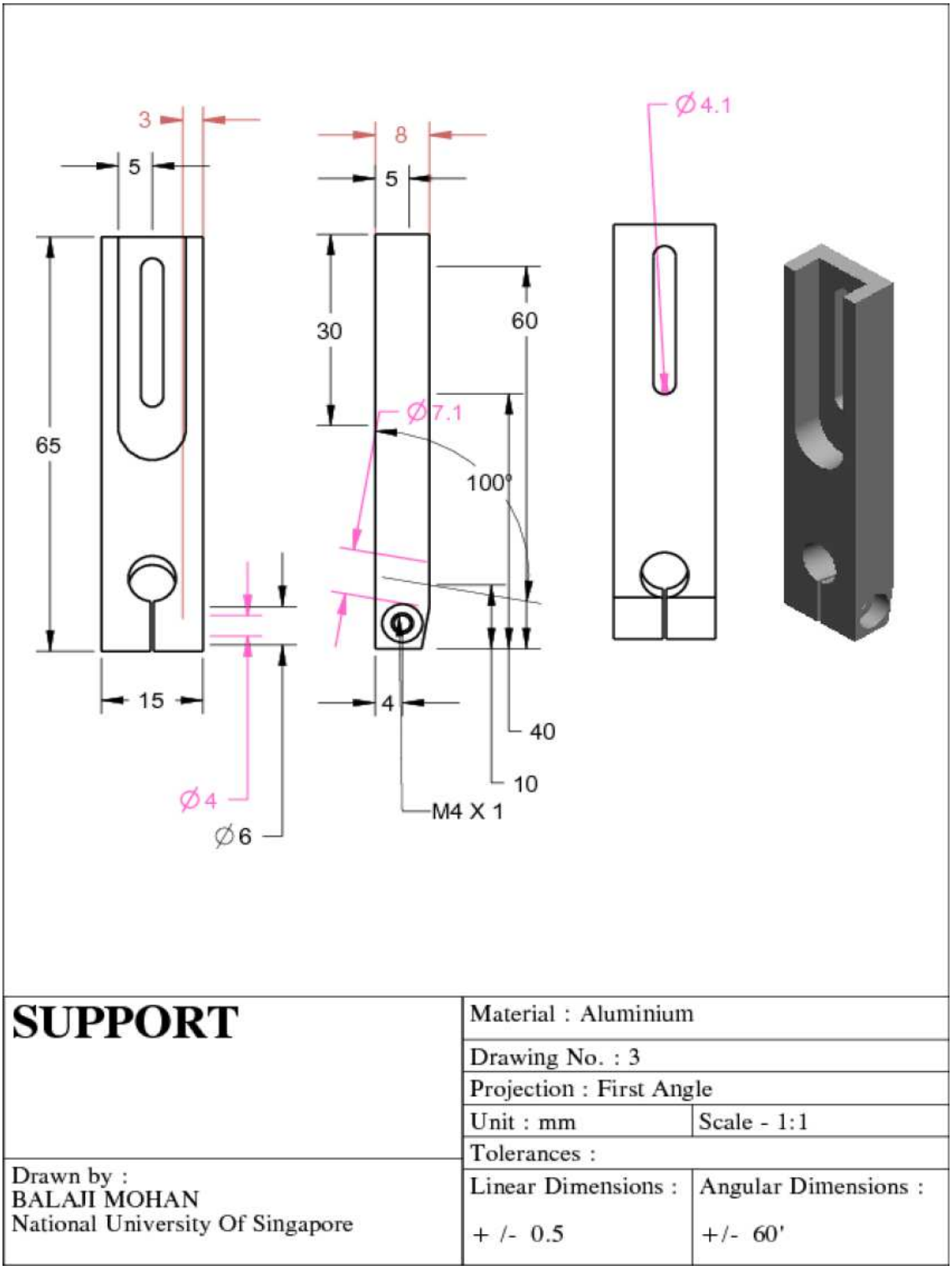

SUPPORT	Material : Aluminium	
	Drawing No. : 3	
	Projection : First Angle	
	Unit : mm	Scale - 1:1
	Tolerances :	
Drawn by : BALAJI MOHAN National University Of Singapore	Linear Dimensions : + /- 0.5	Angular Dimensions : +/- 60'

Figure B.4: Sensor support

C

Diesel reaction mechanism

```
ELEMENTS
 C H O N
END
SPECIE
C14H28 O2 N2 CO2 H2O H H2 O N OH CO NO HO2 H2O2 CH2O C2H2 C(S) CH4
CH3 CH3O CH2 HCO C7H15-1 C7H15-2 C7H15O2 C7H14O4H C7H14O2H C7KET21
C6H12 C5H11CHO C5H11CO C5H11 C4H9 C4H C3H7 C3H6 C3H5 C3H4 C3H3 C3H2
C2H HCCO C2H3 C2H4 C2H5 C2H6 C4H2 C4H3 C4H5 A1- A1 A1C2H- A1C2H
A1C2H2 A1C2H)2 A2-1 A2 A2R5- A2R5 CH2CO C6H5CO C6H5CHO C6H5 C7H8
C7H16 C7H8O C7H7 C6H5O CH3CHO CH3O2 CH2CHO N2O NO2 C7KET12 C5H5
C6H6 C6H5OH
END
REACTIONS
 5C14H28 + O2 = 3C7H8 + 7C7H16 + 2H2O     1.000E+37   0.0   10500.0
 4C7H16 + 23O2 = 28HCO + 18H2O            5.000E+11   0.0   27500.0
 A2R5 = 12C(S) + 4H2                      2.000E+03   0.0       0.0
 C4H2 = 4C(S) + H2                        1.000E+04   0.0       0.0
 C7H14O2H + O2 = C7H14O4H                 4.600E+11   0.0       0.0
  DUPLICATE
 C7H14O4H = C7KET12 + OH                  1.000E+13   0.0   26400.0
 C7H14O4H = C7KET21 + OH                  2.965E+13   0.0   26700.0
  DUPLICATE
 C7KET12 = C5H11CHO + HCO + OH            1.050E+16   0.0  4.160E+4
 C7KET21 = C5H11CO + CH2O + OH            1.500E+16   0.0  4.420E+4
  DUPLICATE
 C7H16 + C7H7 = C7H15-1 + C7H8            5.000E+12   0.0       0.0
 C7H16 + C7H7 = C7H15-2 + C7H8            5.000E+12   0.0       0.0
 C7H16 + C6H5  = A1 + C7H15-1             1.000E+12   0.0       0.0
 C7H16 + C6H5 = A1 + C7H15-2              5.000E+11   0.0       0.0
 C7H16 + O2 = C7H15-1 + HO2               1.500E+13   0.0   48810.0
 C7H16 + O2 = C7H15-2 + HO2               3.000E+14   0.0   47380.0
 C7H16 + H = C7H15-1 + H2                 5.600E+07   2.0    7667.0
 C7H16 + H  = C7H15-2 + H2                4.380E+07   2.0    4750.0
 C7H16 + OH = C7H15-1 + H2O               8.610E+09   1.1    1815.0
 C7H16 + OH = C7H15-2 + H2O               6.800E+09   1.3     690.5
 C7H16 + HO2 = C7H15-1 + H2O2             8.000E+12   0.0   19300.0
 C7H16 + HO2 = C7H15-2 + H2O2             1.000E+13   0.0   16950.0
 C7H16 = C4H9 + C3H7                      3.400E+16   0.0   80710.0
 C7H16 = C5H11 + C2H5                     3.400E+16   0.0   80710.0
 C7H15-1 + O2 = C7H15O2                   2.000E+12   0.0       0.0
 C7H15-2 + O2 = C7H15O2                   2.500E+12   0.0       0.0
 C7H15O2 = C7H14O2H                       5.000E+12   0.0   20380.0     ! 11
 C7H14O2H + O2 = C7H14O4H                 2.000E+11   0.0       0.0
  DUPLICATE
```

```
 C7H14O4H = C7KET21 + OH                 1.000E+11   0.0  2.385E+4    ! 2.965E+13   0.0
26700.0
  DUPLICATE
 C7KET21 = C5H11CO + CH2O + OH           1.500E+16   0.0  4.240E+4
  DUPLICATE
 C5H11CHO + O2 = C5H11CO + HO2           2.000E+13   0.5  4.220E+4
 C5H11CHO + OH = C5H11CO + H2O           1.000E+13   0.0  0.000E+0
 C5H11CHO + H = C5H11CO + H2             4.000E+13   0.0  4.200E+3
 C5H11CHO + O = C5H11CO + OH             5.000E+12   0.0  1.790E+3
 C5H11CHO + HO2 = C5H11CO + H2O2         2.800E+12   0.0  1.360E+4
 C5H11CHO + CH3 = C5H11CO + CH4          1.700E+12   0.0  8.440E+3
 C5H11CO = C5H11 + CO                    1.000E+11   0.0  9.600E+3
 C5H11 = C2H5 + C3H6                     3.200E+13   0.0   28300.0
 C7H15-1 = C2H4 + C5H11                  2.500E+13   0.0   28810.0
 C7H15-2 = CH3 + C6H12                   3.000E+13   0.0   29800.0
 C6H12 = C3H7 + C3H5                     1.000E+16   0.0   68000.0
 C6H12 = C3H6 + C3H6                     1.000E+16   0.0   68000.0
 C6H12 + OH = C5H11 + CH2O               1.000E+11   0.0  -4.00E+3
 C6H12 + O = C5H11 + HCO                 1.000E+11   0.0  -1.05E+3
 C7H15-2 = C4H9 + C3H6                   1.500E+13   0.0   28600.0
 C7H15-1 = C7H15-2                       2.000E+11   0.0   18050.0
 C4H9 = C3H6 + CH3                       7.360E+17  -1.40  30230.0      !7.367E+17  -1.40
3.023E+04
 C4H9 = C2H5 + C2H4                      2.500E+13   0.0   28810.0
 C3H7 = C2H4 + CH3                       9.600E+13   0.0   30950.0
 C3H7 = C3H6 + H                         1.250E+14   0.0   36900.0
 C3H7 + CH3 = C2H5 + C2H5                1.900E+13  -0.3       0.0
 C3H7 + O2 = C3H6 + HO2                  1.000E+12   0.0    4980.0
 C3H7 + H = CH3 + C2H5                   4.060E+06   2.19    890.0
 C3H6 = C2H3 + CH3                       6.250E+15   0.0   85500.0
 C3H6 + H = C3H5 + H2                    5.000E+12   0.0    1500.0
 C3H6 + CH3 = C3H5 + CH4                 9.000E+12   0.0    8480.0
 C3H6 + O2 = C3H5 + HO2                  4.000E+12   0.0   39900.0
 C3H5 + HO2 = C2H3 + CH2O + OH           1.000E+12   0.0       0.0
 C3H5 + H = C3H4 + H2                    1.000E+13   0.0       0.0
 C3H5 + O2 = CH3 + CH2O + CO             4.000E+12   0.0       0.0
 C3H4 + OH = C2H3 + CH2O                 1.000E+12   0.0       0.0
 C3H4 + OH = C2H4 + HCO                  1.000E+12   0.0       0.0
 C3H4 + O2 = C3H3 + HO2                  4.000E+13   0.0   39160.0
 CH3O + CO = CH3 + CO2                   1.570E+14   0.00  11800.0
 CH3O + H = CH2O + H2                    2.000E+13   0.00      0.0
 CH3O + H = CH3 + OH                     1.000E+14   0.00      0.0
 CH3O + OH = CH2O + H2O                  5.000E+12   0.00      0.0
 CH3O + O = CH2O + OH                    1.000E+13   0.00      0.0
```

```
CH3O + O2 = CH2O + HO2                  4.280E-13   7.60  -3530.0
CH3O = CH2O + H                         3.000E+12   0.00  27420.0
C3H3 + C3H3 = A1                        2.000E+12   0.0       0.0
C4H5 + C2H3 = A1 + H2                   1.840E+13   0.0    7070.0
C7H8 + H = A1 + CH3                     1.200E+12   0.0    5148.0
C7H8 + C6H5 = C7H7 + A1                 2.103E+12   0.0    4400.0
C6H5CHO + H = A1 + HCO                  1.200E+13   0.0    5148.0
C6H5CHO + C6H5 = C6H5CO + A1            7.010E+11   0.0    4400.0
C6H5CO + HO2 = C6H5 + CO2 + OH          2.000E+13   0.0       0.0
C6H5CO + O2 = C6H5O + CO2               3.000E+11   0.0    2870.0
A1 + O2 = C6H5 + HO2                    6.300E+13   0.0   60000.0
A1 + OH = C6H5 + H2O                    1.600E+08   1.42   1450.0
C6H5 + CH2O = A1 + HCO                  1.750E+10   0.0       0.0
A1 + O = C6H5 + OH                      2.000E+13   0.0   14704.0
C6H5 + H = A1                           2.200E+14   0.0       0.0
CO + OH = CO2 + H                       3.510E+07   1.30     70.0
CO + O2 = CO2 + O                       4.600E+13   0.0   41000.0
CO + HO2 = CO2 + OH                     1.500E+14   0.0   23650.0
CO + O + M = CO2 + M                    6.170E+14   0.0    3000.0 ! 10 4.170E+14
H + O2 = O + OH                         1.915E+14   0.0   16440.0
 REV /5.481E+11 0.39 -2.93E+02 /
O + H2 = OH + H                         5.080E+04   2.67   6292.0
 REV /2.667E+04 2.65 4880.0 /
OH + H2 = H + H2O                       2.160E+08   1.51   3430.0
 REV / 2.298E+09 1.40 1.832E+04 /
O + H2O = OH + OH                       2.970E+06   2.02  13400.0
 REV / 1.465E+05 2.11 -2904.0 /
H2 + M = H + H + M                      4.577E+19  -1.40 1.044E+5
 REV / 1.146E+20 -1.68 8.20E+02 /
 H2 /2.5/ H2O /12.0/
O2 + M = O + O + M                      4.515E+17  -0.64 1.189E+5
 REV / 6.165E+15 -0.5 0.0 /
 H2 /2.5/ H2O /12.0/
OH + M = O + H + M                      9.880E+17  -0.74 1.021E+5
 REV / 4.714E+18 -1.0 0.0 /
 H2 /2.5/ H2O /12.0/
H2O + M = H + OH + M                    1.912E+23  -1.83 1.185E+5
 REV /4.500E+22 -2.0 0.0 /
 H2 /0.73/ H2O /12.0/
H + O2(+M) = HO2(+M)                    1.475E+12   0.60      0.0
 LOW / 3.4820E+16 -4.11E-01 -1.115E+03 /
 TROE / 0.5 1.0E-30 1.0E+30 1.0E+100 /
 H2 /1.3/ H2O /14.0/
HO2 + H = H2 + O2                       1.660E+13   0.00    823.0
```

```
 REV / 3.164E+12 0.35 5.551E+04 /
HO2 + H = OH + OH                       7.079E+13   0.00    295.0
 REV / 2.027E+10 0.72 3.684E+04 /
HO2 + O = OH + O2                       3.250E+13   0.00      0.0
 REV / 3.252E+12 0.33 5.328E+04 /
HO2 + OH = H2O + O2                     2.890E+13   0.00   -497.0
 REV / 5.861E+13 0.24 6.908E+04 /
H2O2 + O2 = HO2 + HO2                   4.634E+16  -0.35  50670.0
 REV / 4.20E+14 0.0 11980.0 /
 DUPLICATE
H2O2 + O2 = HO2 + HO2                   1.434E+13  -0.35  37060.0
 REV / 1.30E+11 0.0 -1629.0 /
 DUPLICATE
H2O2(+M) = OH + OH(+M)                  2.951E+14   0.00  48430.0
 LOW / 1.202E+17  0.0 45500.0 /
 TROE / 0.5 1.0E-30 1.0E+30 1.0E+100 /
 H2 /2.5/ H2O /12.0/
H2O2 + H = H2O + OH                     2.410E+13   0.00   3970.0
 REV / 1.269E+08 1.31 71410.0 /
H2O2 + H = H2 + HO2                     6.025E+13   0.0    7950.0
 REV / 1.041E+11 0.70 2.395E+04 /
H2O2 + O = OH + HO2                     9.550E+06   2.00   3970.0
 REV / 8660.0 2.68 1.856E+04 /
H2O2 + OH = H2O + HO2                   1.000E+12   0.0       0.0
 REV / 1.838E+10 0.59 3.089E+04 /
 DUPLICATE
H2O2 + OH = H2O + HO2                   5.800E+14   0.0    9557.0
 REV / 1.066E+13 0.59 4.045E+04 /
 DUPLICATE
CH2O + O2 = HCO + HO2                   1.000E+14   0.00  39000.0      ! 6.2
CH2O + HO2 = HCO + H2O2                 3.000E+12   0.00   8000.0
CH2O + CH3 = HCO + CH4                  5.540E+03   2.81  5.86E+3
CH2O + M = HCO + H + M                  3.300E+16   0.00  8.10E+4
HCO + HCO = CH2O + CO                   3.010E+13   0.00      0.0
HCO + HCO = CO + CO + H2                3.010E+13   0.00      0.0     !  12
HCO + OH = H2O + CO                     3.000E+13   0.00      0.0
HCO + H = H2 + CO                       1.190E+13   0.30      0.0
HCO + O = OH + CO                       3.000E+13   0.00      0.0
HCO + O = H + CO2                       3.000E+13   0.00      0.0
HCO + O2 = HO2 + CO                     3.300E+13  -0.40      0.0
HCO + M = H + CO + M                    1.870E+17  -1.00  17000.0
HCO + HO2 = CO2 + OH + H                3.000E+13   0.00      0.0
CH4 + O2 = CH3 + HO2                    7.900E+13   0.00  56000.0
CH4 + H = CH3 + H2                      6.600E+08   1.60  10840.0
```

```
CH4 + OH = CH3 + H2O                    1.600E+06   2.10   2460.0
CH4 + O = CH3 + OH                      1.020E+09   1.50   8604.0
CH4 + HO2 = CH3 + H2O2                  1.000E+13   0.00  18700.0
CH4 + CH2 = CH3 + CH3                   4.000E+12   0.00   -570.0
CH3 + HCO = CH4 + CO                    1.200E+14   0.00      0.0
CH3 + HCO = CH2O + CH2                  3.000E+13   0.00      0.0
CH3 + H = CH4                           1.900E+36  -7.00   9050.0
CH3 + H = CH2 + H2                      9.000E+13   0.00  15100.0
CH3 + CH3O = CH4 + CH2O                 4.300E+14   0.00      0.0
CH3 + CH3 = C2H6                        2.120E+16  -0.97    620.0
CH3 + CH3(+M) = C2H6(+M)                8.770E+16  -1.18    654.0 ! 16  6.77
    LOW  /  1.400E+41   -7.030   2762.00/
    TROE/   .6190  73.20  1180.00  9999.00 /
    H2/2.0/ H2O/6.0/ CH4/2.0/ CO/1.50/ CO2/2.0/ C2H6/3.0/
CH3 + CH3 = C2H5 + H                    4.990E+12   0.10  10600.0
CH3 + O = CH2O + H                      8.000E+13   0.00      0.0
CH3 + OH = CH2 + H2O                    7.500E+06   2.00   5000.0
CH3 + OH = CH2O + H2                    4.000E+12   0.00      0.0
CH3 + CH2 = C2H4 + H                    3.000E+13   0.00   -570.0
CH3 + HO2 = CH3O + OH                   5.000E+13   0.00      0.0
CH3 + O2 = CH3O + O                     4.670E+13   0.00  30000.0
CH3 + O2 = CH2O + OH                    2.310E+12   0.00  20310.0
CH3 + C2H4 = CH4 + C2H3                 6.620E+00   3.70   9482.0
CH3 + CH3 = C2H4 + H2                   1.000E+15   0.00  31000.0
CH2 + OH = CH2O + H                     2.500E+13   0.00      0.0
CH2 + O2 = HCO + OH                     4.300E+10   0.00   -500.0
CH2 + O2 = CO2 + H2                     6.900E+11   0.00    500.0
CH2 + O2 = CO + H2O                     2.000E+10   0.00  -1000.0
CH2 + O2 = CH2O + O                     5.000E+13   0.00   9000.0
CH2 + O2 = CO2 + H + H                  1.600E+12   0.00   1000.0
CH2 + O2 = CO + OH + H                  8.600E+10   0.00   -500.0
CH2 + CH2 = C2H2 + H2                   1.200E+13   0.0     800.0
CH2 + CH2 = C2H2 + H + H                1.200E+14   0.0     800.0
CH2 + CO2 = CH2O + CO                   1.000E+11   0.00   1000.0
C2H4 + H = C2H3 + H2                    1.100E+14   0.00   8500.0
C2H4 + O = CH3 + HCO                    1.600E+09   1.20    746.0
C2H4 + O = CH2O + CH2                   3.000E+04   1.88    180.0
C2H4 + O = C2H3 + OH                    1.510E+07   1.91   3790.0
C2H4 + OH = CH2O + CH3                  6.000E+13   0.0     960.0       ! 13
C2H4 + HO2 = C2H3 + H2O2                7.100E+11   0.0   17110.0
C2H4 + OH = C2H3 + H2O                  6.020E+13   0.00   5955.0       ! 6.02  5955
C2H4 + M = C2H2 + H2 + M                1.500E+15   0.00  55800.0
C2H4 + M = C2H3 + H + M                 2.600E+17   0.0   96570.0
C2H4 + H = C2H5                         2.600E+43  -9.25  52580.0
```

```
 C2H6 + O2 = C2H5 + HO2                  1.000E+13   0.00  48960.0
 C2H5 + O2 = C2H4 + HO2                  2.000E+10   0.0   -2200.0
 C2H4 + O2 = C2H3 + HO2                  4.200E+14   0.00  57590.0      ! 14
 C2H4 + C2H4 = C2H5 + C2H3               5.000E+14   0.0   64700.0       ! 14
 C2H5 + HO2  = C2H4 + H2O2               3.000E+11   0.00      0.0
 C2H2 + O2 = HCO + HCO                   4.000E+12   0.00  28000.0
 C2H2 + O = CH2 + CO                     1.020E+07   2.00   1900.0
 C2H2 + H + M = C2H3 + M                 5.540E+12   0.00   2410.0
 C2H3 + H = C2H2 + H2                    4.000E+13   0.00      0.0
 C2H3 + O2 = CH2O + HCO                  4.000E+12   0.00   -250.0
 C2H3 + O2 = C2H2 + HO2                  1.337E+06   1.61   -384.0      ! 1.000E+12   0.0
10000.0
 C2H3 + OH = C2H2 + H2O                  5.000E+12   0.00      0.0
 C2H3 + CH2 = C2H2 + CH3                 3.000E+13   0.00      0.0
 C2H3 + HCO = C2H4 + CO                  6.034E+13   0.0       0.0
 C2H3 + C2H3 = C2H2 + C2H4               1.450E+13   0.0       0.0
 C2H3 + O = C2H2 + OH                    1.000E+13   0.0       0.0
 C2H2 + CH2 = C3H3 + H                   1.200E+13   0.0    6620.0
 C3H3 + OH = C3H2 + H2O                  1.000E+13   0.0       0.0
 C3H3 + O = CH2O + C2H                   1.000E+13   0.0       0.0
 C2H3 = C2H2 + H                         4.600E+40  -8.80  46200.0
 C2H2 = C2H + H                          2.373E+32  -5.28 130688.0
 C2H + O2 = HCO + CO                     5.000E+13   0.00   1500.0
 C2H + H2 = H + C2H2                     4.900E+05   2.50    560.0
 C2H2 + O = C2H + OH                     4.600E+19  -1.41  28950.0
 C2H2 + OH = C2H + H2O                   3.370E+07   2.00  14000.0
 C2H2 + OH = CH2CO + H                   2.180E-04   4.50  -1000.0
 C2H2 + OH = CH3 + CO                    4.830E-04   4.00  -2000.0
 C2H2 + C2H = C4H2 + H                   9.600E+13   0.0       0.0
 C4H  + H2 = H + C4H2                    4.900E+05   2.5     560.0
 C4H2 + OH = C4H + H2O                   3.370E+07   2.0   14000.0
 C4H2 + C2H = C4H + C2H2                 2.000E+13   0.0       0.0
 C4H2 + O = C3H2 + CO                    2.700E+13   0.0    1720.0
 C3H2 + O = C2H2 + CO                    5.800E+13   0.0       0.0
 C3H2 + OH = HCO + C2H2                  5.800E+13   0.0       0.0
 C3H2 + CH2 = C4H3 + H                   3.000E+13   0.0       0.0
 C3H3 + C3H3 = C6H5 + H                  2.000E+12   0.0       0.0
 C3H2 + HCCO = C4H3 + CO                 1.000E+13   0.0       0.0
 CH2CO + H = HCCO + H2                   5.000E+13   0.00   8000.0
 CH2CO + H = CH3  + CO                   1.130E+13   0.00   3428.0
 CH2CO + O = HCCO + OH                   1.000E+13   0.00   8000.0
 C2H2 + C2H2 = C4H2 + H2                 1.000E+17   0.00  81000.0
 C2H2 + C2H = C4H3                       4.500E+37  -7.68   7100.0
 C2H3 + C2H2 = C4H5                      8.100E+37  -8.09  13400.0
```

```
C2H2 + O = HCCO + H                    1.020E+07   2.0    1900.0
C4H5 + O2 = C2H4 + CO + HCO            4.160E+10   0.00   2500.0
C4H3 + M = C4H2 + H + M                1.000E+14   0.0   30000.0
C4H3 + H = C2H2 + C2H2                 6.300E+25  -3.34  10014.0
C4H3 + H = C4H2 + H2                   1.500E+13   0.00      0.0
C4H3 + OH = C4H2 + H2O                 5.000E+12   0.00      0.0
C2H  + OH = H + HCCO                   2.000E+13   0.0       0.0
C4H3 + C2H2 = C6H5                     2.800E+03   2.9    1400.0
C6H6 + H = A1 + H                      3.700E+20  -2.35   6800.0
C4H3 + C2H2 = A1-                      1.900E+63 -15.25  30600.0
C4H5 + C2H2 = A1 + H                   1.600E+18  -1.88   7400.0
C6H5 = A1-                             3.500E+46 -10.44  33600.0
C6H5 + C2H = A1C2H                     2.540E+17  -1.489  1541.0
A1 + H = A1- + H2                      2.590E+14   0.0   16000.0
A1 + OH = A1- + H2O                    1.060E+08   1.42   1450.0
A1- + H = A1                           1.000E+14   0.00      0.0
C4H3 + C4H2 = A1C2H-                   1.900E+63 -15.25  30600.0
A1 + C2H = A1C2H + H                   5.000E+13   0.0       0.0
A1- + C2H2 = A1C2H2                    7.900E+29  -5.15  13700.0
A1- + C2H2 = A1C2H + H                 2.500E+29  -4.43  26400.0
A1C2H + H = A1C2H2                     1.600E+32  -5.72  11090.0
A1C2H + H = A1C2H- + H2                2.500E+14   0.0   16000.0
A1C2H + OH = A1C2H- + H2O              1.600E+08   1.42   1450.0
A1C2H- + H + M = A1C2H + M             1.000E+14   0.00      0.0
A1- + C2H3= A1C2H2 + H                 9.400E+00   4.14  23234.0
A1- + C4H2 = A2-1                      5.100E+48 -10.53  28000.0
A1C2H2 + H = A1C2H + H2                1.500E+13   0.0       0.0
A1C2H2 + OH = A1C2H + H2O              2.500E+12   0.0       0.0
A1C2H- + C2H2 = A2-1                   5.100E+48 -10.53  28000.0
A1C2H- + C2H2 = A1C2H)2 + H            2.100E+10   0.85  13700.0
A1C2H)2 + H = A2-1                     1.500E+51 -10.77  25500.0
A1C2H + C2H = A1C2H)2 + H              5.000E+13   0.0       0.0
A1C2H2 + C2H2 = A2 + H                 1.600E+18  -1.88   7400.0
A2 + H = A2-1 + H2                     2.500E+14   0.0   16000.0
A2 + OH = A2-1 + H2O                   1.600E+08   1.42   1450.0
A2-1 + O2 = A1C2H + HCO + CO           2.100E+12   0.0    7470.0
A2-1 + C2H2 = A2R5 + H                 1.100E+07   1.71   3900.0
A2R5 + O = A2-1 + HCCO                 2.200E+13   0.0    4530.0
A2R5- + O2 = A2-1 + CO + CO            2.100E+12   0.0    7470.0
A2R5 + H = A2R5- + H2                  2.500E+14   0.0   16000.0
A2R5 + OH = A2R5- + H2O                1.600E+08   1.42   1450.0
A2R5- + H = A2R5                       1.000E+14   0.00      0.0
HCCO + O2 = OH + CO + CO               1.600E+12   0.0     854.0
HCCO + CH2 = C2H3 + CO                 3.000E+13   0.0       0.0
```

```
C2H  + C2H = C4H2                       1.800E+13   0.0       0.0
C3H4 + O = HCCO + CH3                   6.300E+12   0.0    2010.0
HCCO + HCCO = C2H2 + CO + CO            1.000E+13   0.0       0.0
CH2O + O = HCO + OH                     3.800E+13   0.00   3540.0
CH2O + H = HCO + H2                     2.300E+10   1.05   3270.0
CH2O + OH = HCO + H2O                   1.430E+10   1.20   -447.0   ! 2.34
C2H5 + O = CH3CHO + H                   1.090E+14   0.0       0.0
 DUPLICATE
C2H5 + O = CH2O + CH3                   4.240E+13   0.0       0.0
C2H5 + O = C2H4 + OH                    3.460E+13   0.0       0.0
CH2CO + O = HCO + HCO                   1.050E+13   0.00   2400.0
CH2CO + OH = HCCO + H2O                 1.500E+13   0.00   2000.0
CH2CO + OH = HCO + CH2O                 2.040E+12   0.0       0.0
CH2CO + OH = CH3 + CO2                  3.100E+13   0.0       0.0
CH2CO + M = CH2 + CO + M                3.000E+16   0.00  6.00E+4
C2H3 + O = CH2CO + H                    3.000E+13   0.00      0.0
C3H3 + O2 = CH2CO + HCO                 3.000E+10   0.00   2878.0
C3H4 + O = CH2CO + CH2                  2.000E+07   1.8    1000.0
C4H3 + O2 = HCCO + CH2CO                1.000E+12   0.0       0.0
C6H5 + O2 = CH2CO + HCCO + C2H2         7.800E+16  -1.76      0.0
A1C2H + OH = A1- + CH2CO                2.180E-04   4.5   -1000.0
A1C2H)2 + OH = A1C2H- + CH2CO           2.180E-04   4.5   -1000.0
A2 + OH = A1C2H + CH2CO + H             1.300E+13   0.0   10600.0
A2 + O = CH2CO + A1C2H                  2.200E+13   0.0    4530.0
A2R5 + OH = A2-1 + CH2CO                1.300E+13   0.0   10600.0
C4H5 + C3H4 = C7H8 + H                  2.000E+11   0.0    3600.0
C7H7 + H = C7H8                         1.200E+14   0.0       0.0
C7H8 = C6H5 + CH3                       1.400E+16   0.0   99800.0
C7H8 + O2 = C7H7 + HO2                  3.000E+14   0.0   42400.0
C7H8 + OH = C7H7 + H2O                  1.780E+13   0.0    2583.0
C7H8 + O = C7H7 + OH                    1.000E+08   1.5    8000.0
C7H8 + H = C7H7 + H2                    1.500E+14   0.0    8235.0
C7H8 + CH3 = C7H7 + CH4                 3.160E+11   0.0    9500.0
C7H8 + C2H3 = C7H7 + C2H4               3.980E+12   0.0    8000.0
C7H7 + O = C6H5CHO + H                  5.000E+13   0.0       0.0
C7H7 + O = C6H5 + CH2O                  8.000E+13   0.0       0.0
C7H7 + O2 = C6H5O + CH2O                6.300E+13  -1.07  10840.0
C7H7 + HO2 = C6H5CHO + H    + OH        6.000E+13   0.0       0.0
C7H7 + HO2  = C6H5 + CH2O + OH          6.000E+12   0.0       0.0
C7H7 + OH = C7H8O                       5.000E+13   0.0       0.0
C7H7 + C6H5OH = C7H8 + C6H5O            1.050E+11   0.0    9500.0
C7H8O + OH = C6H5CHO + H2O + H          8.430E+12   0.0    2583.0
C7H8O + O2 = C6H5CHO + H + HO2          2.000E+14   0.0   41400.0
C7H8O + H = C6H5OH + CH3                1.200E+13   0.0    5148.0
```

```
C7H8O + H = C7H8 + OH                    2.210E+13   0.0    7910.0
C7H8O + C7H7 = C6H5CHO + C7H8 + H        2.110E+11   0.0    9500.0
C6H5CHO + O2 = C6H5CO  + HO2             1.020E+13   0.0   38950.0
C6H5CHO + OH = C6H5CO + H2O              1.710E+09   1.18   -447.0
C6H5CHO + H = C6H5CO + H2                5.000E+13   0.0    4928.0
C6H5CHO + O = C6H5CO + OH                9.040E+12   0.0    3080.0
C6H5CO = C6H5 + CO                       3.980E+14   0.0   29400.0
C6H5 + CH3 = C7H7 + H                    5.700E-02   5.0   15700.0
C6H5 + HO2 = C6H5O + OH                  5.000E+13   0.0    1000.0
C6H5 + O2 = C6H5O + O                    2.600E+13   0.0    6120.0
C6H5O = C5H5 + CO                        2.510E+11   0.0   43900.0
C6H5 + OH = C6H5O + H                    5.000E+13   0.0       0.0
C6H5O + O = C5H5 + CO2                   1.000E+13   0.0       0.0
C6H5OH  + H = C6H5O + H2                 1.150E+14   0.0   12400.0
C6H5OH  + O = C6H5O + OH                 2.810E+13   0.0    7352.0
C6H5OH  + HO2 = C6H5O + H2O2             3.000E+13   0.0   15000.0
C6H5OH  + C2H3 = C2H4 + C6H5O            6.000E+12   0.0       0.0
C6H5OH  + OH = H2O + C6H5O               1.390E+08   1.43   -962.0
C(S) + O2 = O + CO                       3.000E+11   0.00  26800.0 ! 12
C(S) + H2O = CO + H2                     3.000E+11   0.00  42800.0 ! 12
C(S) + OH = CO + H                       3.000E+12   0.00  32600.0 ! 7.E+12
C(S) + OH + OH = CO2 + H2                3.000E+12   0.00  32600.0 ! 7.E+12
C(S) + OH + O  = CO2 + H                 3.000E+12   0.00  32600.0
C(S) + NO2 = CO + NO                     1.000E+12   0.00  18800.0
C3H7 + HO2 = CH3CHO + CH3 + OH           2.410E+13   0.0       0.0
C3H7 + O = CH3CHO + CH3                  4.820E+13   0.0       0.0
C2H4 + HO2 = CH3CHO + OH                 6.030E+09   0.0    7949.0
C2H5 + O = CH3CHO + H                    6.620E+13   0.0       0.0
 DUPLICATE
C2H3 + OH = CH3CHO                       3.010E+13   0.0       0.0
CH3CHO = CH3 + HCO                       7.000E+15   0.0   81674.0
CH3CHO + O2 = HO2 + CH3 + CO             3.010E+13   0.0   39150.0
C2H3 + O2 = CH2CHO + O                   3.500E+14  -0.61   5260.0
C2H4 + O = CH2CHO + H                    1.210E+06   2.08      0.0
O + CH2CHO = H + CH2 + CO2               1.500E+13   0.00      0.0
O2 + CH2CHO = OH + CO + CH2O             2.000E+13   0.00   4200.0
O2 + CH2CHO = OH + HCO + HCO             2.350E+10   0.00      0.0
H + CH2CHO = CH3 + HCO                   2.200E+13   0.00      0.0
H + CH2CHO = CH2CO + H2                  1.100E+13   0.00      0.0
CH3 + O2 = CH3O2                         9.020E+58 -15.0   17204.0
CH3O2 + CH3 = CH3O + CH3O                2.410E+13   0.0       0.0
CH3O2 + O = CH3O + O2                    3.610E+13   0.0       0.0
CH3O2 + H = CH3O + OH                    9.640E+13   0.0       0.0
C2H4 + CH3O2 = CH3CHO + CH3O             7.000E+13   0.0   14500.0
```

```
 OH + CH2CHO = H2O + CH2CO                1.200E+13   0.00      0.0
 N + NO = N2 + O                          3.500E+14   0.0     330.0
 N + O2 = NO + O                          9.000E+09   1.0    6500.0
 N + OH = NO + H                          7.333E+13   0.0    1120.0
 N + CO2 = NO + CO                        1.900E+11   0.0    3400.0
 N2O + O = N2 + O2                        1.400E+12   0.0   10810.0
 N2O + O = NO + NO                        2.900E+13   0.0   23150.0
 N2O + H = N2 + OH                        4.400E+14   0.0   18880.0
 N2O + OH = N2 + HO2                      2.000E+12   0.0   21060.0
 N2O + NO = N2 + NO2                      2.750E+14   0.0   50000.0
 NO2 + N = NO + NO                        1.000E+12   0.0       0.0
 NO + HO2 = NO2 + OH                      2.110E+12   0.0    -480.0
 NO + O + M = NO2 + M                     1.060E+20  -1.41      0.0
     H2/2.0/ H2O/6.0/ CH4/2.0/ CO/1.5/ CO2/2.0/ C2H6/3.0/
 NO2 + O = NO + O2                        3.900E+12   0.0    -240.0
 NO2 + H = NO + OH                        1.320E+14   0.0     360.0
 NO + CH3O2 = NO2 + CH3O                  2.530E+12   0.0    -358.0
 NO2 + CH3 = NO + CH3O                    1.500E+13   0.0       0.0
 N2O + M = N2 + O + M                     1.300E+11   0.0   59620.0
END
```

D

Biodiesel reaction mechanism

```
ELEMENTS
H  O   C  N
END
SPECIES
MD MD9D NC7H16 O2 N2 CO2 H2O H H2 O N  OH CO NO HO2 H2O2 CH3O
CH2O HCO CH3 CH4 C2H2 C2H3 C2H4 C2H5 C3H4 C3H5 C3H6 C3H7
C7H15-2 C7H15O2 C5H11CO C4H9 CH2CHO CH2CO  MS6D N2O
NO2 A2R5 C(S)  C4H2 C7H14O2H C7H15-1 C6H5 A1 C5H11 C3H3
C2H C4H3 HCCO A1- A1C2H A1C2H- A2-1 A1C2H)2 A2 A2R5-
CH3O2 CH3O2H C6H2 C7H14O2HO2 CH3CHO C6H12 C7H15O C7H15O2H
C7KET21 A1C2H2 CH2 C2H6 CH3OH CH3CO C4H8-1  C5H10-1
  C2H4O2H  C2H4O1-2  C4H6  MD2J MD3J MD10J
MS7J C5H11-1 MO7D   MP2D MD2D C7H15-4 C5H9-14 MD9D8J MD9D3J
MD3O2 C7H14OOH2-4  C7H15-3 C5H10OOH1-3  MD3OOH5J C5H10O1-3
MD3OOH5O2 C7H14OOH2-4O2 MDKET23 MDKET23O MS7OXO MO8OXO MD69D
MD69D2J  MD9D3O2 MD9D8O2  MD8DXO2  MD9D8O  MD9D6OOH8J
MD8DXOOH7J MD9D8OOH MD9D6OOH8O2  MD8DXOOH7O2 MD9DKET23
END
REACTIONS
CH2O+CH3O<=>CH3OH+HCO 6.620E+11 0.00 2294.0
REV/ 8.393E+10 0.07 17710.0 /
CH4+CH3O<=>CH3+CH3OH 6.119E+02 2.87 8248.0
REV/ 1.440E+01 3.10 6935.0 /
CH3O+HO2<=>CH2O+H2O2 3.010E+11 0.00 0.0
REV/ 1.074E+12 -0.03 65270.0 /
CH3OH(+M)<=>CH3+OH(+M) 1.900E+16 0.00 91730.0
LOW / 2.9500E+44 -7.3500E+00 9.5460E+04 /
TROE / 4.1400E-01 2.7900E+02 5.4590E+03 1.0000+100 /
CH3OH+H<=>CH3O+H2 3.600E+12 0.00 6095.0
REV/ 1.676E+11 0.21 5868.0 /
CH3OH+OH<=>CH3O+H2O 5.130E+05 2.13 2450.0
REV/ 2.541E+05 2.24 17120.0 /
CH3OH+CH2O<=>CH3O+CH3O 7.981E+12 0.45 81490.0
REV/ 6.030E+13 0.00 0.0 /
CH3O2+CH3O2<=>CH2O+CH3OH+O2 3.110E+14 -1.61 -1051.0
CH3O2+OH<=>CH3OH+O2 6.000E+13 0.00 0.0
REV/ 1.536E+13 0.43 59160.0 /
C2H5+H(+M)<=>C2H6(+M) 5.210E+17 -0.99 1580.0
LOW / 1.9900E+41 -7.0800E+00 6.6850E+03 /
TROE / 8.4200E-01 1.2500E+02 2.2190E+03 6.8820E+03 /
H2/2/
 H2O/6/
 CO/1.5/
 CO2/2/
 CH4/2/
 C2H6/3/
```

```
C2H6+HO2<=>C2H5+H2O2 3.460E+01 3.61 16920.0
REV/ 1.849E+00 3.60 3151.0 /
H2+CH3O2<=>H+CH3O2H 1.500E+14 0.00 26030.0
REV/ 1.689E+18 -1.14 8434.0 /
C2H4O2H<=>C2H5+O2 1.814E+45 -11.50 14600.0
REV/ 7.523E+42 -10.88 -18160.0 /
C2H5+O2<=>C2H4O1-2+OH 1.626E+11 -0.31 6150.0
REV/ 3.633E+13 -0.63 39840.0 /
C2H5+O2<=>CH3CHO+OH 8.265E+02 2.41 5285.0
REV/ 2.247E+03 2.30 65970.0 /
C2H4O2H<=>C2H4O1-2+OH 8.848E+30 -6.08 2.066E+04
REV/ 8.199E+30 -5.78 3.793E+04 /
C2H4O2H<=>C2H4+HO2 3.980E+34 -7.25 2.325E+04
REV/ 1.922E+32 -6.59 2.021E+04 /
C2H4O1-2<=>CH3+HCO 3.630E+13 0.00 5.720E+04
REV/ 1.006E+04 1.55 -2.750E+03 /
C2H4O1-2<=>CH3CHO 7.407E+12 0.00 5.380E+04
REV/ 9.013E+10 0.21 8.080E+04 /
CH3CHO+H<=>CH3CO+H2 1.110E+13 0.00 3.110E+03
REV/ 7.674E+09 0.63 1.706E+04 /
CH3CHO+O<=>CH3CO+OH 5.940E+12 0.00 1.868E+03
REV/ 2.156E+09 0.61 1.441E+04 /
CH3CHO+OH<=>CH3CO+H2O 2.000E+06 1.80 1.300E+03
REV/ 1.471E+04 2.33 3.014E+04 /
CH3CHO+O2<=>CH3CO+HO2 3.010E+13 0.00 3.915E+04
REV/ 1.092E+11 0.28 -1.588E+03 /
CH3CHO+CH3<=>CH3CO+CH4 1.760E+03 2.79 4.950E+03
REV/ 1.111E+03 2.98 2.044E+04 /
CH3CHO+HO2<=>CH3CO+H2O2 3.010E+12 0.00 1.192E+04
REV/ 1.205E+12 -0.06 9.877E+03 /
CH3O2+CH3CHO<=>CH3O2H+CH3CO 3.010E+12 0.00 1.192E+04
REV/ 2.344E+13 -0.51 8.282E+03 /
CH3CHO+OH<=>CH2CHO+H2O 1.720E+05 2.40 8.150E+02
REV/ 1.336E+05 2.51 2.495E+04 /
CH3CO(+M)<=>CH3+CO(+M) 3.000E+12 0.00 1.672E+04
LOW / 1.2000E+15 0.0000E+00 1.2518E+04 /
CH3CO+H<=>CH2CO+H2 2.000E+13 0.00 0.000E+00
REV/ 3.841E+15 -0.55 6.073E+04 /
CH3CO+O<=>CH2CO+OH 2.000E+13 0.00 0.000E+00
REV/ 2.016E+15 -0.57 5.932E+04 /
CH3CO+CH3<=>CH2CO+CH4 5.000E+13 0.00 0.000E+00
REV/ 8.766E+18 -0.99 6.227E+04 /
C2H4+CH3O<=>C2H3+CH3OH 1.200E+11 0.00 6.750E+03
REV/ 8.138E+08 0.29 -7.830E+02 /
C2H4+HO2<=>C2H4O1-2+OH 2.230E+12 0.00 1.719E+04
REV/ 4.280E+14 -0.36 3.750E+04 /
```

```
C3H6<=>C3H5+H 2.010E+61 -13.26 1.185E+05
REV/ 1.024E+61 -13.52 3.084E+04 /
DUPLICATE
C3H6<=>C3H5+H 5.620E+71 -16.58 1.393E+05
REV/ 4.255E+68 -16.16 3.031E+04 /
DUPLICATE
C3H6+O<=>C2H5+HCO 1.580E+07 1.76 -1.216E+03
REV/ 9.272E+01 2.72 2.312E+04 /
C3H6+O<=>C3H5+OH 5.240E+11 0.70 5.884E+03
REV/ 5.593E+10 0.70 2.038E+04 /
DUPLICATE
C3H6+O<=>C3H5+OH 6.030E+10 0.70 7.632E+03
REV/ 9.569E+06 1.37 8.060E+02 /
DUPLICATE
C3H6+OH<=>C3H5+H2O 3.120E+06 2.00 -2.980E+02
REV/ 6.750E+06 1.91 3.050E+04 /
DUPLICATE
C3H6+OH<=>C3H5+H2O 1.110E+06 2.00 1.451E+03
REV/ 3.571E+03 2.59 1.093E+04 /
DUPLICATE
C3H6+HO2<=>C3H5+H2O2 9.640E+03 2.60 1.391E+04
REV/ 1.135E+06 1.92 1.382E+04 /
C3H6+H<=>C3H5+H2 1.730E+05 2.50 2.492E+03
REV/ 3.518E+04 2.52 1.840E+04 /
DUPLICATE
C3H6+H<=>C3H5+H2 4.050E+05 2.50 9.794E+03
REV/ 1.224E+02 3.19 4.380E+03 /
DUPLICATE
C3H6+H<=>C2H4+CH3 1.449E+34 -5.81 1.850E+04
REV/ 4.572E+28 -4.54 2.716E+04 /
C3H6+O2<=>C3H5+HO2 4.000E+12 0.00 3.990E+04
REV/ 4.267E+12 -0.33 1.117E+03 /
DUPLICATE
C3H6+O2<=>C3H5+HO2 1.400E+12 0.00 6.070E+04
REV/ 2.220E+09 0.34 5.990E+02 /
DUPLICATE
C3H6+CH3<=>C3H5+CH4 2.210E+00 3.50 5.675E+03
REV/ 4.102E+02 3.07 2.312E+04 /
DUPLICATE
C3H6+CH3<=>C3H5+CH4 8.400E-01 3.50 1.166E+04
REV/ 2.318E-01 3.75 7.782E+03 /
DUPLICATE
C3H5<=>C2H2+CH3 2.397E+48 -9.90 8.208E+04
REV/ 2.610E+46 -9.82 3.695E+04 /
DUPLICATE
C3H5<=>C3H4+H 3.066E+13 0.21 6.128E+04
```

```
REV/ 2.400E+11 0.69 3.007E+03 /
DUPLICATE
C3H5+H<=>C3H4+H2 1.810E+13 0.00 0.000E+00
REV/ 5.657E+10 0.76 4.529E+04 /
DUPLICATE
C3H4+C3H6<=>C3H5+C3H5 8.391E+17 -1.29 3.369E+04
REV/ 1.000E+12 0.00 0.000E+00 /
C3H5+O2<=>C3H4+HO2 2.180E+21 -2.85 3.076E+04
REV/ 3.575E+19 -2.44 2.136E+04 /
DUPLICATE
C3H5<=>C2H2+CH3 2.163E+40 -8.31 4.511E+04
REV/ 1.610E+40 -8.58 2.033E+04 /
DUPLICATE
C3H5<=>C3H4+H 3.508E+14 -0.44 4.089E+04
REV/ 8.500E+12 0.00 2.000E+03 /
DUPLICATE
C3H5+O2<=>C3H4+HO2 1.890E+30 -5.59 1.554E+04
REV/ 2.085E+31 -5.86 2.746E+04 /
DUPLICATE
C3H5+O2<=>CH2O+CH3CO 3.710E+25 -3.96 7.043E+03
REV/ 1.872E+27 -4.43 1.012E+05 /
C3H4+OH<=>CH2CO+CH3 3.120E+12 0.00 -3.970E+02
REV/ 1.806E+17 -1.38 3.607E+04 /
C3H4+O<=>C2H4+CO 7.800E+12 0.00 1.600E+03
REV/ 4.814E+08 1.24 1.210E+05 /
C3H4+O<=>C2H2+CH2O 3.000E-03 4.61 -4.243E+03
REV/ 2.320E+02 3.23 8.119E+04 /
C2H2+CH3<=>C3H4+H 6.740E+19 -2.08 3.159E+04
REV/ 4.400E+25 -3.34 2.264E+04 /
C4H9<=>C4H8-1+H 2.867E+12 0.25 3.540E+04
REV/ 2.500E+11 0.51 2.620E+03 /
C4H8-1<=>C3H5+CH3 1.500E+19 -1.00 7.340E+04
REV/ 1.350E+13 0.00 0.000E+00 /
C4H8-1<=>C2H3+C2H5 1.000E+19 -1.00 9.677E+04
REV/ 9.000E+12 0.00 0.000E+00 /
C4H6<=>C2H3+C2H3 4.027E+19 -1.00 9.815E+04
REV/ 1.260E+13 0.00 0.000E+00 /
C4H6+OH<=>C2H5+CH2CO 1.000E+12 0.00 0.000E+00
REV/ 3.730E+12 0.00 3.002E+04 /
C4H6+OH<=>CH2O+C3H5 1.000E+12 0.00 0.000E+00
REV/ 3.501E+06 0.00 7.106E+04 /
C4H6+OH<=>C2H3+CH3CHO 1.000E+12 0.00 0.000E+00
REV/ 5.437E+11 0.00 1.855E+04 /
C4H6+O<=>C2H4+CH2CO 1.000E+12 0.00 0.000E+00
REV/ 6.377E+11 0.00 9.434E+04 /
C4H6+O<=>CH2O+C3H4 1.000E+12 0.00 0.000E+00
```

```
REV/ 1.075E+12 0.00 7.905E+04 /
C2H3+C2H4<=>C4H6+H 5.000E+11 0.00 7.300E+03
REV/ 1.000E+13 0.00 4.700E+03 /
MD+H=MD2J+H2     3.620E+06   2.540   06756.0
MD+HO2=MD2J+H2O2    7.220E+03   2.550   10530.0
MD+OH=MD2J+H2O     1.146E+11   0.510   00063.0
MD+O2=MD2J+HO2     4.080E+13   0.000   41350.0
MD+O=MD2J+OH     3.936E+05   2.400   01150.0
MD+CH3=MD2J+CH4     2.720E+00   3.650   07154.0
MD+CH3O=MD2J+CH3OH    3.800E+10   0.000   02800.0
MD+CH3O2=MD2J+CH3O2H    7.220E+03   2.550   10530.0
MD+H=MD3J+H2     9.100E+06   2.400   04471.0   !1.3E+06
MD+HO2=MD3J+H2O2    4.116E+05   2.500   14860.0 !5.88E+04
MD+OH=MD3J+H2O     1.046E+10   1.610  -00035.0  !3.269E+08 4.67E+07
MD+O=MD3J+OH     4.162E+06   2.440   02846.0 !5.946E+05
MD+CH3=MD3J+CH4     5.880E+05   2.130   07574.0 !8.4E+04
MD+CH3O=MD3J+CH3OH    7.700E+11   0.000   05000.0 !1.1E+11
MD+CH3O2=MD3J+CH3O2H    4.116E+05   2.500   14860.0 !5.88E+04
MD+H=MD10J+H2     9.400E+04   2.750   06280.0
MD+HO2=MD10J+H2O2    4.050E+04   2.500   16690.0
MD+OH=MD10J+H2O     5.270E+09   0.970   01590.0
MD+O=MD10J+OH     1.046E+06   2.420   04766.0
MD+CH3=MD10J+CH4    4.520E-01   3.650   07154.0
MD+CH3O2=MD10J+CH3O2H    4.050E+04   2.500   16690.0
MD9D+H=MD10J     2.500E+11   0.510   02620.0
MS7J+C3H6=MD3J     2.200E+03   2.480   06130.0 !8.8E+03
MD9D+H=MD3J     4.240E+11   0.510   01230.0
MO7D+C2H5=MD3J     8.800E+03   2.480   06130.0
C3H7+MS6D=MD3J     8.800E+03   2.480   06130.0
MD2D+H=MD3J     1.000E+13   0.000   02900.0
C7H15-1+MP2D=MD2J    1.000E+11   0.000   07600.0
MS6D+H=MS7J     2.500E+11   0.510   02620.0
C2H4+C5H11-1=C7H15-1    8.800E+03   2.480   06130.0
C3H7+C2H4=C5H11-1    8.800E+03   2.480   06130.0
C5H10-1+H=C5H11-1    2.500E+11   0.510   02620.0
C3H7+C4H8-1=C7H15-3    8.800E+03   2.480   06130.0
CH3+C6H12=C7H15-3    8.800E+03   2.480   06130.0
C2H5+C5H10-1=C7H15-4    1.760E+04   2.480   06130.0
CH2CO+C4H9=C5H11CO    1.000E+11   0.000   07600.0
C5H11-1+CO=C5H11CO    1.510E+11   0.000   04810.0
C5H11-1+O2=C5H10-1+HO2    1.600E+12   0.000   05000.0
MD2J+O2=MD2D+HO2    1.600E+12   0.000   05000.0
MD3J+O2=MD2D+HO2    1.600E+12   0.000   05000.0
MD3J+O2=MD9D+HO2    1.600E+12   0.000   05000.0
MD10J+O2=MD9D+HO2    1.600E+12   0.000   05000.0
MS7J+O2=MS6D+HO2    1.600E+12   0.000   05000.0
```

```
C7H15-1=C7H15-3     3.800E+10   0.670   36600.0
 DUPLICATE
C7H15-1=C7H15-4     7.850E+11  -0.120   20600.0
C7H15-1=C7H15-3     1.830E+02   2.550   10960.0
 DUPLICATE
C7H15-3=C7H15-4     3.560E+10   0.880   39100.0
MD10J=MD3J     3.560E+10   0.880   37300.0
DUPLICATE
MD10J=MD3J     3.800E+10   0.670   36600.0
DUPLICATE
MD10J=MD3J     7.850E+11  -0.120   20600.0
DUPLICATE
MD10J=MD3J     1.830E+02   2.550   10960.0
DUPLICATE
C5H10-1+H=C5H9-14+H2    3.376E+05   2.360   00207.0
DUPLICATE
C5H10-1+H=C5H9-14+H2    1.300E+06   2.400   04471.0
DUPLICATE
C5H10-1+HO2=C5H9-14+H2O2   4.820E+03   2.550   10530.0
DUPLICATE
C5H10-1+HO2=C5H9-14+H2O2   5.880E+04   2.500   14860.0
DUPLICATE
C5H10-1+OH=C5H9-14+H2O    2.764E+04   2.640  -01919.0
DUPLICATE
C5H10-1+OH=C5H9-14+H2O    4.670E+07   1.610  -00035.0
DUPLICATE
C5H10-1+O2=C5H9-14+HO2    2.200E+12   0.000   37220.0
DUPLICATE
C5H10-1+O2=C5H9-14+HO2    4.000E+13   0.000   50160.0
DUPLICATE
C5H10-1+O=C5H9-14+OH    6.600E+05   2.430   01210.0
DUPLICATE
C5H10-1+O=C5H9-14+OH    5.946E+05   2.440   02846.0
DUPLICATE
C5H10-1+CH3=C5H9-14+CH4    3.690E+00   3.310   04002.0
DUPLICATE
C5H10-1+CH3=C5H9-14+CH4    8.400E+04   2.130   07574.0
DUPLICATE
C5H10-1+CH3O=C5H9-14+CH3OH   4.000E+01   2.900   08609.0
DUPLICATE
C5H10-1+CH3O=C5H9-14+CH3OH   1.100E+11   0.000   05000.0
DUPLICATE
C5H10-1+CH3O2=C5H9-14+CH3O2H   4.820E+03   2.550   10530.0
DUPLICATE
C5H10-1+CH3O2=C5H9-14+CH3O2H   5.880E+04   2.500   14860.0
DUPLICATE
```

```
C5H10-1+C2H3=C5H9-14+C2H4   2.211E+00   3.500   04690.0
DUPLICATE
C5H10-1+C2H3=C5H9-14+C2H4   4.000E+11   0.000   16800.0
DUPLICATE
C5H10-1+C2H5=C5H9-14+C2H6   1.000E+11   0.000   09800.0
DUPLICATE
C5H10-1+C2H5=C5H9-14+C2H6   5.000E+10   0.000   10400.0
DUPLICATE
CH3+C4H6=C5H9-14     3.580E+04   2.480   06130.0
C2H3+C3H6=C5H9-14     2.000E+11   0.000   02007.0
MD9D3J=MD9D8J     3.670E+12  -0.600   07100.0
C3H5+C3H7=C6H12    2.500E+16   0.000   71000.0
DUPLICATE
C3H5+C2H5=C5H10-1    2.500E+16   0.000   71000.0
C5H9-14+H=C5H10-1    1.000E+14   0.000   00000.0
C6H12=C3H6+C3H6    3.980E+12   0.000   57630.0
C5H10-1=C3H6+C2H4    3.980E+12   0.000   57630.0
MD9D=C3H6+MS6D     3.980E+12   0.000   57630.0
C7H15-2+O2=C7H15O2    7.540E+12   0.000   00000.0
DUPLICATE
C7H15-3+O2=C7H15O2    7.540E+12   0.000   00000.0
C7H15-4+O2=C7H15O2    7.540E+12   0.000   00000.0
C5H11-1+O2=C5H10OOH1-3    4.520E+12   0.000   00000.0
MD10J+O2=MD3O2     4.520E+12   0.000   00000.0
MD3J+O2=MD3O2     5.278E+13   0.000   00000.0 !7.54E+12
MD2J+O2=MD3O2     7.540E+12   0.000   00000.0
C7H15O2=C7H14OOH2-4    5.000E+10   0.000   20850.0   !2.5E+10
MD3O2=MD3OOH5J     2.084E+10   0.000   20850.0 !1.75E+11 2.5E+10
C5H10OOH1-3=C5H10O1-3+OH   7.500E+10   0.000   15250.0
C5H10OOH1-3=C4H8-1+CH2O+OH   8.283E+13  -0.170   30090.0
C7H14OOH2-4=C5H10-1+CH3CHO+OH   5.364E+17  -1.400   26750.0
MD3OOH5J=MO7D+CH3CHO+OH    5.364E+17  -1.400   26750.0
MD3OOH5J+O2=MD3OOH5O2    5.278E+13   0.000   00000.0 !7.54E+12
C7H14OOH2-4+O2=C7H14OOH2-4O2   1.508E+13   0.000   00000.0 !7.54E+12
MD3OOH5O2=MDKET23+OH    8.750E+10   0.000   17850.0 !1.25E+10
MDKET23=MDKET23O+OH    2.100E+16   0.000  41600.0  !1.05E+16
CH3CO+MO8OXO=MDKET23O    3.330E+10   0.000   06397.0
CH2CHO+MO8OXO=MDKET23O    3.330E+10   0.000   06397.0
MD9D=MS7J+C3H5     1.953E+14 0.000 71000.0    !2.50E+16
MD9D+H=MD9D3J+H2     6.500E+06   2.400   04471.0   !1.3E+06
MD9D+HO2=MD9D3J+H2O2    2.940E+05   2.500   14860.0 !5.88E+04
MD9D+OH=MD9D3J+H2O    2.335E+08   1.610  -00035.0 !2.335E+08 4.67E+07
MD9D+O=MD9D3J+OH     2.973E+06   2.440   02846.0  !5.946E+05
MD9D+CH3=MD9D3J+CH4    4.200E+05   2.130   07574.0  !8.4E+04
MD9D+CH3O=MD9D3J+CH3OH    5.500E+11   0.000   05000.0 !1.1E+11
MD9D+CH3O2=MD9D3J+CH3O2H   2.940E+05   2.500   14860.0  !5.88E+04
```

```
MD9D+H=MD9D8J+H2      3.376E+05   2.360   00207.0
MD9D+HO2=MD9D8J+H2O2    4.820E+03   2.550   10530.0
MD9D+OH=MD9D8J+H2O    2.764E+04   2.640  -01919.0
MD9D+O2=MD9D8J+HO2    2.200E+12   0.000   37220.0
MD9D+O=MD9D8J+OH      6.600E+05   2.430   01210.0
MD9D+CH3=MD9D8J+CH4    3.690E+00   3.310   04002.0
MD9D+CH3O2=MD9D8J+CH3O2H   4.820E+03   2.550   10530.0
MD9D3J=C3H5+MS6D    3.310E+13   0.000   21460.0
C2H3+MO7D=MD9D3J      2.000E+11   0.000   02007.0
H+MD69D=MD9D3J     7.500E+11   0.510   02620.0 !2.5E+11
MD9D3J+O2=MD69D+HO2    4.800E+12 0.000 05000.0 !1.6E+12
MD69D+H=MD69D2J+H2    3.620E+06   2.540   06756.0
MD69D+HO2=MD69D2J+H2O2    7.220E+03   2.550   10530.0
MD69D+OH=MD69D2J+H2O    1.146E+11   0.510   00063.0
MD69D+O2=MD69D2J+HO2    4.080E+13   0.000   41350.0
MD69D+O=MD69D2J+OH    3.936E+05   2.400   01150.0
MD69D+CH3=MD69D2J+CH4    2.720E+00   3.650   07154.0
MD69D+CH3O=MD69D2J+CH3OH   3.800E+10   0.000   02800.0
MD69D+CH3O2=MD69D2J+CH3O2H   7.220E+03   2.550   10530.0
MD69D=C2H2+MO7D     2.520E+13   0.000   59020.0
MD9D3J+O2=MD9D3O2     2.262E+13   0.000   00000.0  !7.54E+12
MD9D8J+O2=MD9D8O2     7.540E+12   0.000   00000.0
MD9D8J+O2=MD8DXO2     4.520E+12   0.000   00000.0
MD9D8O2=MO8OXO+CH2CHO    1.700E+09   1.000   26228.4
MD9D8J+MD9D8O2=MD9D8O+MD9D8O   7.000E+12   0.000  -01000.0
MD9D3O2=MD9D6OOH8J    1.250E+10   0.000   16350.0
DUPLICATE
MD9D3O2=MD9D6OOH8J    1.000E+11   0.000   22350.0
DUPLICATE
MD8DXO2=MD8DXOOH7J    1.563E+09   0.000   13550.0
MD9D8O2+HO2=MD9D8OOH+O2    7.000E+12   0.000   01710.0
MD9D8O2+H2O2=MD9D8OOH+HO2   2.410E+12   0.000   09940.0
MD9D8O2+MD9D8O2=MD9D8O+MD9D8O+O2  1.400E+16  -1.610   01860.0
MD9D8OOH=MD9D8O+OH    1.050E+16   0.000   41600.0
C2H3+MO8OXO=MD9D8O    3.330E+10   0.000   06397.0
MD69D+HO2=MD9D6OOH8J    1.000E+11   0.000   11750.0
MD9D6OOH8J+O2=MD9D6OOH8O2   7.540E+12   0.000   00000.0
MD8DXOOH7J+O2=MD8DXOOH7O2   7.540E+12   0.000   00000.0
MD9D6OOH8O2=MD9DKET23+OH   1.250E+10   0.000   17850.0
MD8DXOOH7O2=MD9DKET23+OH   1.563E+09   0.000   13550.0
MD9DKET23=OH+MS7OXO+C2H2+HCO   1.050E+16   0.000   41600.0
NC7H16+H=C7H15-3+H2      2.600E+06   2.400   4.471E+03
            REV/ 3.928E+03   2.740   1.126E+04 /
NC7H16+H=C7H15-4+H2      1.300E+06   2.400   4.471E+03
            REV/ 3.913E+03   2.740   1.126E+04 /
NC7H16+O=C7H15-1+OH      1.930E+05   2.680   3.716E+03
```

```
            REV/ 4.025E+03   2.630   5.893E+03 /
NC7H16+O=C7H15-2+OH      9.540E+04   2.710   2.106E+03
            REV/ 6.330E+01   3.050   6.798E+03 /
NC7H16+O=C7H15-3+OH      9.540E+04   2.710   2.106E+03
            REV/ 6.330E+01   3.050   6.798E+03 /
NC7H16+O=C7H15-4+OH      4.770E+04   2.710   2.106E+03
            REV/ 6.306E+01   3.050   6.798E+03 /
NC7H16+OH=C7H15-3+H2O      9.400E+07   1.610  -3.500E+01
            REV/ 6.148E+05   1.950   2.191E+04 /
NC7H16+OH=C7H15-4+H2O      4.700E+07   1.610  -3.500E+01
            REV/ 6.125E+05   1.950   2.191E+04 /
NC7H16+HO2=C7H15-3+H2O2     1.120E+13   0.000   1.769E+04
            REV/ 4.348E+11   0.010   8.165E+03 /
NC7H16+HO2=C7H15-4+H2O2     5.600E+12   0.000   1.769E+04
            REV/ 4.332E+11   0.010   8.165E+03 /
NC7H16+CH3=C7H15-1+CH4     9.040E-01   3.650   7.154E+03
            REV/ 1.121E+00   3.600   1.191E+04 /
NC7H16+CH3=C7H15-2+CH4     5.410E+04   2.260   7.287E+03
            REV/ 2.135E+03   2.600   1.455E+04 /
NC7H16+CH3=C7H15-3+CH4     5.410E+04   2.260   7.287E+03
            REV/ 2.135E+03   2.600   1.455E+04 /
NC7H16+CH3=C7H15-4+CH4     2.705E+04   2.260   7.287E+03
            REV/ 2.127E+03   2.600   1.455E+04 /
NC7H16+O2=C7H15-3+HO2      4.000E+13   0.000   5.015E+04
            REV/ 1.098E+09   0.670  -5.410E+02 /
NC7H16+O2=C7H15-4+HO2     2.000E+13   0.000   5.015E+04
            REV/ 1.094E+09   0.670  -5.410E+02 /
NC7H16+CH3O=C7H15-1+CH3OH     3.160E+11   0.000   7.000E+03
            REV/ 1.200E+10   0.000   9.200E+03 /
NC7H16+CH3O=C7H15-2+CH3OH     2.190E+11   0.000   5.000E+03
            REV/ 8.900E+09   0.000   7.200E+03 /
NC7H16+CH3O=C7H15-3+CH3OH     2.190E+11   0.000   5.000E+03
            REV/ 8.900E+09   0.000   7.200E+03 /
NC7H16+CH3O=C7H15-4+CH3OH     1.095E+11   0.000   5.000E+03
            REV/ 8.900E+09   0.000   7.200E+03 /
NC7H16+CH3O2=C7H15-1+CH3O2H     1.210E+13   0.000   2.043E+04
            REV/ 3.600E+12   0.000   9.800E+03 /
NC7H16+CH3O2=C7H15-2+CH3O2H     8.064E+12   0.000   1.770E+04
            REV/ 2.376E+11   0.000   3.700E+03 /
NC7H16+CH3O2=C7H15-3+CH3O2H     8.064E+12   0.000   1.770E+04
            REV/ 2.376E+11   0.000   3.700E+03 /
NC7H16+CH3O2=C7H15-4+CH3O2H     4.032E+12   0.000   1.770E+04
            REV/ 2.376E+11   0.000   3.700E+03 /
 A2R5                    =>12C(S)  + 4H2               2.000E+10   0.0    0.0
 C6H2                    => 6C(S)  + H2                2.000E+10   0.0    0.0
 NC7H16 + O2            = C7H15-1 + HO2               2.500E+13   0.00   48810.0
```

```
NC7H16 + O2           = C7H15-2 + HO2            2.000E+14   0.00   47380.0
NC7H16 + H            = C7H15-1 + H2             5.600E+07   2.00    7667.0
NC7H16 + H            = C7H15-2 + H2             4.380E+07   2.00    4750.0
NC7H16 + OH           = C7H15-1 + H2O            8.610E+09   1.10    1815.0
NC7H16 + OH           = C7H15-2 + H2O            6.000E+09   1.30     690.0
NC7H16 + HO2          = C7H15-1 + H2O2           1.120E+13   0.00   19300.0
NC7H16 + HO2          = C7H15-2 + H2O2           3.300E+13   0.00   16950.0
C7H15-2               = CH3 + C6H12               2.508E+13   0.29   29290.
C7H15-1               = C2H4 + C5H11              2.500E+13   0.00   28810.
C7H15-2               = C3H6 + C4H9               2.200E+13   0.00   28100.
NC7H16 + C7H15O2       = C7H15-1 + C7H15O2H       2.420E+14   0.00   20430.0
NC7H16 + C7H15O2       = C7H15-2 + C7H15O2H       8.064E+13   0.00   17700.0
C7H15O2 + HO2         = C7H15O2H + O2           1.750E+09   0.00   -3275.0
C7H15O2 + H2O2        = C7H15O2H + HO2          2.400E+12   0.00   10000.0
C7H15O2H              = C7H15O + OH             6.000E+18   0.00   42500.0
C7H15O                = CH2O + C6H12 + H        4.683E+17  -1.34   20260.0
C7H15-1 + O2          = C7H15O2                 2.000E+12   0.00       0.0
C7H15-2 + O2          = C7H15O2                 2.000E+12   0.00       0.0
DUPLICATE
C7H15O2               = C7H14O2H                6.000E+11   0.00   20380.0
C7H14O2H + O2         = C7H14O2HO2              4.600E+11   0.00       0.0
C7H14O2HO2            = C7KET21 + OH            1.485E+13   0.00   24900.0
C7KET21               = C5H11CO + CH2O + OH     1.500E+16   0.00   43000.0
C5H11CO               = C5H11 + CO              1.000E+11   0.00    9600.0
C5H11                 = C2H4 + C3H7             5.200E+13   0.00   28300.0
C6H12                 = C3H7 + C3H5             1.200E+16   0.00   68000.0
DUPLICATE
C4H9                  = C2H5 + C2H4             2.500E+13   0.00   28810.0
C3H7                  = C2H4 + CH3              9.600E+13   0.00   30950.0
C3H7                  = C3H6 + H                1.250E+14   0.00   36900.0
C3H7 + O2             = C3H6 + HO2              1.000E+12   0.00    4980.0
C3H7 + H              = C2H5 + CH3              4.060E+06   2.19     890.0
C3H7 + HO2            => C2H5 + CH2O + OH       2.410E+13   0.00       0.0
C3H7 + CH3            = C2H5 + C2H5             1.927E+13  -0.32       0.0
C3H6                  = C2H3 + CH3              3.150E+15   0.00   85500.0
C3H6 + H              = C3H5 + H2               5.000E+12   0.00    1500.0
DUPLICATE
C3H6 + CH3            = C3H5 + CH4              9.000E+12   0.00    8480.0
DUPLICATE
C3H6 + O2             = C3H5 + HO2              4.000E+12   0.00   39900.0
DUPLICATE
C3H6 + O              = CH2CO + CH3 + H         2.500E+07   1.76      76.0
C3H5                  = C3H4 + H                4.000E+13   0.00   69760.0
DUPLICATE
C3H5 + H              = C3H4 + H2               1.000E+13   0.00       0.0
DUPLICATE
```

```
C3H5 + O2           = C3H4 + HO2              6.000E+11   0.00   10000.0
DUPLICATE
C3H4 + OH           = C2H3 + CH2O             1.000E+12   0.00       0.0
C3H4 + OH           = C2H4 + HCO              1.000E+12   0.00       0.0
C3H4 + O2           = C3H3 + HO2              4.000E+13   0.00   39160.0
H + O2              = O + OH                  1.920E+14   0.00   16439.0
O + H2              = OH + H                  5.080E+04   2.67    6290.0
OH + H2             = H2O + H                 2.160E+08   1.51    3430.0
O + H2O             = OH + OH                 2.970E+06   2.02   13400.0
O + OH + M          = HO2 + M                 1.000E+16   0.00       0.0
   H2/2.00/
O2/6.0/
H2O/6.00/
CH4/2.00/
CO/1.50/
CO2/3.50/
C2H6/3.00/
H + O2 + M          = HO2 + M                 3.600E+17  -0.72       0.0
   H2/2.00/
O2/6.0/
H2O/6.00/
CH4/2.00/
CO/1.50/
CO2/3.50/
C2H6/3.00/
OH + HO2            = H2O + O2                7.500E+12   0.00       0.0
H + H + M           = H2 + M                  1.000E+18  -1.00       0.0
   H2/0./
H2O/0./
CO2/0./
H + H + H2O         = H2 + H2O                6.000E+19  -1.25       0.0
H + OH + M          = H2O + M                 1.600E+22  -2.00       0.0
H + O + M           = OH + M                  6.200E+16  -0.60       0.0
HO2 + H             = H2 + O2                 1.250E+13   0.00       0.0
HO2 + H             = OH + OH                 1.700E+14   0.00     875.0
HO2 + O             = O2 + OH                 1.400E+13   0.00    1073.0
HO2 + HO2           = H2O2 + O2               1.000E+12   0.00       0.0
H2O2 + H            = HO2 + H2                1.600E+12   0.00    3800.0
H2O2 + H            = H2O + OH                1.000E+13   0.00    3590.0
H2O2 + OH           = H2O + HO2               1.000E+13   0.00    1800.0
H2O2 + O            = OH + HO2                4.000E+13   0.00    5900.0
H2O2 + M            = OH + OH + M             4.300E+16   0.00   45500.0
   H2/2.00/
O2/6.0/
H2O/6.00/
CH4/2.00/
```

```
CO/1.50/
CO2/3.50/
C2H6/3.00/
CO + O + M            = CO2 + M                    6.170E+14   0.00    3000.0
   H2/2.00/
O2/6.0/
H2O/6.00/
CH4/2.00/
CO/1.50/
CO2/3.50/
C2H6/3.00/
CO + OH               = CO2 + H                    3.510E+07   1.30    -758.0
CO + O2               = CO2 + O                    1.600E+13   0.00   41000.0
CO + HO2              = CO2 + OH                   5.800E+13   0.00   22930.0
CH2 + O               = HCO + H                    8.000E+13   0.00       0.0
CH2 + OH              = CH2O + H                   2.500E+13   0.00       0.0
CH2 + O2              = CO2 + H2                   6.900E+11   0.00     500.0
CH2 + O2              = CH2O + O                   5.000E+13   0.00    9000.0
CH2 + O2              = CO2 + H + H                1.600E+12   0.00    1000.0
CH2 + CH2             = C2H2 + H + H               1.200E+14   0.00     800.0
CH3 + HO2             = CH3O + OH                  2.500E+13   0.00       0.0
CH3 + O2              = CH3O + O                   4.670E+13   0.00   30000.0
CH3 + O2              = CH2O + OH                  3.800E+11   0.00    9000.0
CH3 + O2              = CH3O2                      3.020E+59 -15.00   17204.0
CH3 + O               = CH2O + H                   8.000E+13   0.00       0.0
CH3 + OH              = CH2 + H2O                  7.500E+06   2.00    5000.0
CH3 + OH              = CH2O + H2                  4.000E+12   0.00       0.0
CH3 + HCO             = CH4 + CO                   1.200E+14   0.00       0.0
CH3 + H               = CH4                        1.900E+36  -7.00    9050.0
CH3 + H               = CH2 + H2                   9.000E+13   0.00   15100.0
CH3 + CH3O            = CH4 + CH2O                 4.300E+14   0.00       0.0
CH3 + CH3 (+M)        = C2H6 (+M)                  2.120E+16  -0.97     620.0
     LOW  /  1.770E+50   -9.670   6220.00/
     TROE/  0.5325  151.00  1038.00  4970.00 /
   H2/2.0/
H2O/6.0/
CH4/2.0/
CO/1.5/
CO2/2.0/
C2H6/3.0/
CH3 + CH3             = C2H5 + H                   4.990E+12   0.10   10600.0
CH3 + HCO             = CH2O + CH2                 3.000E+13   0.00       0.0
CH3 + CH3             = C2H4 + H2                  1.000E+15   0.00   31000.0
CH3 + CH2             = C2H4 + H                   3.000E+13   0.00    -570.0
CH3 + M               = CH2 + H + M                1.000E+16   0.00   90600.0
CH4 + O2              = CH3 + HO2                  7.900E+13   0.00   56000.0
```

```
CH4 + H              = CH3 + H2              6.600E+08   1.60   10840.0
CH4 + OH             = CH3 + H2O             1.600E+06   2.10    2460.0
CH4 + O              = CH3 + OH              1.020E+09   1.50    8604.0
CH4 + HO2            = CH3 + H2O2            1.000E+13   0.00   18700.0
CH4 + CH2            = CH3 + CH3             4.000E+12   0.00    -570.0
HCO + OH             = H2O + CO              1.000E+14   0.00       0.0
HCO + H              = H2 + CO               1.190E+13   0.30       0.0
HCO + O              = OH + CO               3.000E+13   0.00       0.0
HCO + O              = H + CO2               3.000E+13   0.00       0.0
HCO + O2             = HO2 + CO              6.600E+13  -0.30       0.0
HCO + M              = H + CO + M            9.350E+16  -1.00   17000.0
HCO + HO2            = CO2 + OH + H          3.000E+13   0.00       0.0
CH2O + O2            = HCO + HO2             6.200E+13   0.00   39000.0
CH2O + O             = HCO + OH              1.800E+13   0.00    3080.0
CH2O + H             = HCO + H2              2.190E+08   1.80    3000.0
CH2O + OH            = HCO + H2O             2.430E+10   1.20    -447.0
CH2O + HO2           = HCO + H2O2            3.000E+12   0.00    8000.0
CH2O + M             = CO + H2 + M           6.250E+15   0.00   69540.0
CH2O + M             = HCO + H + M           4.000E+23  -1.66   91120.0
CH2O + CH3           = CH4 + HCO             5.500E+03   2.80    6000.0
CH2CO + H            = CH3 + CO              1.100E+13   0.00    3400.0
CH2CO + O            = HCO + HCO             1.000E+13   0.00    2400.0
CH2CO + M            = CH2 + CO + M          2.000E+16   0.00   60000.0
CH2CO + O            = HCCO + OH             5.000E+13   0.00    8000.0
CH2CO + OH           = HCCO + H2O            1.000E+13   0.00    2000.0
CH2CO + H            = HCCO + H2             7.500E+13   0.00    8000.0
CH2CHO               = CH2CO + H             3.094E+15  -0.26   50820.0
CH2CHO + O2          = CH2O + CO + OH        2.000E+13   0.00    4200.0
CH2CHO + O           = CH2CO + OH            1.000E+13   0.00       0.0
CH2CHO + OH          = CH2CO + H2O           5.000E+12   0.00       0.0
CH3O + CO            = CH3 + CO2             1.570E+14   0.00   11800.0
CH3O + M             = CH2O + H + M          1.000E+14   0.00   25000.0
CH3O + H             = CH2O + H2             2.000E+13   0.00       0.0
CH3O + OH            = CH2O + H2O            1.000E+13   0.00       0.0
CH3O + O             = CH2O + OH             1.000E+13   0.00       0.0
CH3O + O2            = CH2O + HO2            1.200E+11   0.00    2600.0
CH3O + H             = CH3 + OH              1.000E+14   0.00       0.0
CH3O2 + HO2          = CH3O2H + O2           4.630E+11   0.00   -2583.0
CH3O2 + CH4          = CH3O2H + CH3          1.810E+11   0.00   18480.0
CH3O2 + CH3          = CH3O + CH3O           2.410E+13   0.00       0.0
CH3O2 + O            = CH3O + O2             3.610E+13   0.00       0.0
CH3O2 + CH2O         = CH3O2H + HCO          1.000E+12   0.00   11665.0
CH3O2 + CH3O2        = CH3O + CH3O + O2      2.800E+11   0.00    -780.0
CH3O2 + H2O2         = CH3O2H + HO2          2.400E+12   0.00   10000.0
CH3O2 + C2H4         = C2H3 + CH3O2H         7.100E+11   0.00   17110.0
CH3O2H                = CH3O + OH            3.000E+16   0.00   42920.0
```

```
CH3O2H + OH            = CH3O2 + H2O              1.000E+13   0.00    -258.0
CH3O2H + O             = CH3O2 + OH               2.000E+13   0.00    4750.0
C2H + O2              = HCCO + O                  3.000E+13   0.00       0.0
C2H + O2              = HCO + CO                  5.000E+13   0.00    1500.0
C2H + H2              = C2H2 + H                  4.900E+05   2.50     560.0
C2H + OH              = HCCO + H                  2.000E+13   0.00       0.0
C2H2 + O2             = HCO + HCO                 4.000E+12   0.00   28000.0
C2H2 + O              = CH2 + CO                  1.020E+07   2.00    1900.0
C2H2 + O              = HCCO + H                  1.350E+07   2.00    1900.0
C2H2 + O              = C2H + OH                  4.600E+19  -1.41   28950.0
C2H2 + OH             = C2H + H2O                 3.370E+07   2.00   14000.0
C2H2 + C2H            = C4H2 + H                  9.600E+13   0.00       0.0
C2H2 + HCCO           = C3H3 + CO                 1.000E+11   0.00    3000.0
C2H2 + C2H            = C4H3                    4.500E+37  -7.68    7100.0
C2H2 + OH             = CH2CO + H                 3.200E+11   0.00     200.0
C2H2 + M              = C2H + H + M               4.300E+16   0.00  108000.0
C2H2 + O2             = HCCO + OH                 1.300E+09   1.60   30100.0
C2H2 + O2             = C2H + HO2                 1.200E+13   0.00   34520.0
C2H2 + CH3            = CH4 + C2H                 1.800E+11   0.00   17270.0
C2H2 + C2H2           = C4H2 + H2                 1.000E+14   0.00   52200.0
C2H2 + CH2            = H + C3H3                  1.200E+13   0.00    6620.0
C2H3 + H              = C2H2 + H2                 4.000E+13   0.00       0.0
C2H3 + O2             = CH2O + HCO                4.000E+12   0.00    -250.0
C2H3 + OH             = C2H2 + H2O                3.000E+13   0.00       0.0
C2H3 + O              = C2H2 + OH                 1.000E+13   0.00       0.0
C2H3                  = C2H2 + H                  4.600E+40  -8.80   46200.0
C2H3 + O2             = CH2CHO + O                1.240E+14  -0.12    1696.0
C2H3 + O2             = C2H2 + HO2                1.000E+12   0.00       0.0
C2H3 + CH3            = CH4 + C2H2                1.000E+13   0.00       0.0
C2H4 + H              = C2H3 + H2                 1.100E+14   0.00    8500.0
C2H4 + O              = CH3 + HCO                 1.600E+09   1.20     746.0
C2H4 + O              = CH2O + CH2                3.000E+04   1.88     180.0
C2H4 + O              = CH2CHO + H                3.200E+10   0.63    1370.0
C2H4 + O              = C2H3 + OH                 1.510E+07   1.91    3790.0
C2H4 + OH             = CH2O + CH3                6.000E+13   0.00     960.0
C2H4 + HO2            = C2H3 + H2O2               7.100E+11   0.00   17110.0
C2H4 + OH             = C2H3 + H2O                9.020E+13   0.00    5955.0
C2H4 + M              = C2H2 + H2 + M             1.500E+15   0.00   55800.0
C2H4 + M              = C2H3 + H + M              2.600E+17   0.00   96570.0
C2H4 + CH3            = C2H3 + CH4                6.620E+00   3.70    9482.0
C2H4 + CH3 (+ M)      = C3H7 (+ M)                2.550E+06   1.60    5700.0
      LOW/ 3.00E+63  -14.6  18170./
      TROE/ .1894  277.0  8748.0  7891.0 /
   H2/2.00/
H2O/6.00/
CH4/2.00/
```

```
CO/1.50/
CO2/2.00/
C2H6/3.00/
C2H5 + O2            = C2H4 + HO2                4.000E+10   0.00   -2200.0
C2H5 + HO2           = C2H4 + H2O2               3.000E+11   0.00       0.0
C2H5 + CH3           = CH4 + C2H4                2.000E+13  -0.50       0.0
C2H6 + O2            = C2H5 + HO2                1.000E+13   0.00   48960.0
C2H6 + CH3           = C2H5 + CH4                5.500E-07   6.00    6300.0
C2H6 + H             = C2H5 + H2                 5.400E+02   3.50    5210.0
C2H6 + O             = C2H5 + OH                 3.000E+07   2.00    5115.0
C2H6 + OH            = C2H5 + H2O                8.700E+09   1.05    1810.0
HCCO + H             = CH2 + CO                  1.500E+14   0.00       0.0
HCCO + OH            = CO + CO + H2              1.000E+14   0.00       0.0
HCCO + O             = H + CO + CO               1.000E+14   0.00       0.0
HCCO + O2            = OH + CO + CO              3.200E+12   0.00     854.0
HCCO + CH2           = C2H3 + CO                 3.000E+13   0.00       0.0
HCCO + CH3           = C2H4 + CO                 5.000E+13   0.00       0.0
C3H3 + O             = CH2O + C2H                2.000E+13   0.00       0.0
C3H3 + C3H3          = C6H5 + H                2.000E+12   0.00       0.0
C3H3 + C3H3          = A1                        2.000E+10   0.00       0.0
C4H2 + H             = C4H3                    1.100E+42  -8.72   15300.0
C4H2 + C2H           = C6H2 + H                  1.00E+14    0.00       0.0
C4H3 + H           = C2H2 + C2H2               6.300E+25  -3.34   10014.0
C4H3 + H           = C4H2 + H2                 1.500E+13   0.00       0.0
C4H3 + OH          = C4H2 + H2O                5.000E+12   0.00       0.0
C4H3 + M           = C4H2 + H + M              3.160E+15   0.00   45000.0
C4H3 + C2H2        = A1-                       1.900E+63 -15.25   30600.0
C4H3 + C2H2        = C6H5                    3.800E+21  -3.17    6400.0
C4H3 + C4H2        = A1C2H-                    1.900E+63 -15.25   30600.0
C6H5                 = A1-                     3.500E+46 -10.44   33600.0
A1 + H               = A1- + H2                  2.590E+14   0.00   16000.0
A1 + OH              = A1- + H2O                 1.060E+08   1.42    1450.0
A1 + C2H             = A1C2H + H                 5.000E+13   0.00       0.0
A1- + H              = A1                        1.000E+14   0.00       0.0
A1- + C2H2           = A1C2H2                  7.900E+29  -5.15   13700.0
A1- + C2H2           = A1C2H + H                 2.500E+29  -4.43   26400.0
A1- + C2H3           = A1C2H2 + H              9.400E+00   4.14   23234.0
A1C2H + H            = A1C2H2                  1.600E+32  -5.72   11090.0
A1C2H + H            = A1C2H- + H2               2.500E+14   0.00   16000.0
A1C2H + OH           = A1C2H- + H2O              1.600E+08   1.42    1450.0
A1C2H2 + H           = A1C2H + H2              1.500E+13   0.00       0.0
A1C2H2 + OH          = A1C2H + H2O             2.500E+12   0.00       0.0
A1C2H- + C2H2        = A2-1                      5.100E+48 -10.53   28000.0
A1C2H- + C2H2        = A1C2H)2 + H               2.100E+10   0.85   13700.0
A1C2H)2 + H          = A2-1                      1.500E+51 -10.77   25500.0
A1C2H + C2H          = A1C2H)2 + H               5.000E+13   0.00       0.0
```

```
A1C2H2 + C2H2         = A2 + H                    1.600E+18  -1.88    7400.0
A2 + H                = A2-1 + H2                   2.500E+14   0.00   16000.0
A2 + OH               = A2-1 + H2O                  1.600E+08   1.42    1450.0
A2-1 + O2             = A1C2H + HCO + CO            2.100E+12   0.00    7470.0
A2-1 + C2H2           = A2R5 + H                    1.100E+07   1.71    3900.0
A2R5 + OH             = A2R5- + H2O                 1.600E+08   1.42    1450.0
A2R5 + H              = A2R5- + H2                  2.500E+14   0.00   16000.0
A2R5- + O2            => A2-1 + CO + CO             2.100E+12   0.00    7470.0
A2R5- + H (+ M)       = A2R5 (+ M)                  1.000E+14   0.00       0.0
      LOW/ 6.6E+75  -16.30  7000.  /
      TROE / 1.0 0.1 584.9  6113.  /
      H2/2.0/
H2O/6.0/
CH4/2.0/
CO/1.5/
CO2/2.0/
C2H6/3.0/
N + NO                = N2 + O                      2.700E+13   0.00     355.0
N + O2                = NO + O                      9.000E+09   1.00    6500.0
N + OH                = NO + H                      3.360E+13   0.00     385.0
N2O + O               = N2 + O2                     1.400E+12   0.00   10810.0
N2O + O               = NO + NO                     2.900E+13   0.00   23150.0
N2O + H               = N2 + OH                     3.870E+14   0.00   18880.0
N2O + OH              = N2 + HO2                    2.000E+12   0.00   21060.0
N2O (+M)              = N2 + O (+M)                 7.910E+10   0.00   56020.0
    LOW  /  6.370E+14   0.00  56640.0 /
    H2/2.00/
H2O/6.00/
CH4/2.00/
O2/0.4/
N2/0.4/
CO/1.50/
CO2/2.00/
C2H6/3.00/
HO2 + NO              = NO2 + OH                    2.110E+12   0.00    -480.0
NO + O + M            = NO2 + M                     1.060E+20  -1.41       0.0
    H2/2.00/
H2O/6.00/
CH4/2.00/
O2/0.4/
N2/0.4/
CO/1.50/
CO2/2.00/
C2H6/3.00/
NO2 + O               = NO + O2                     3.900E+12   0.00    -240.0
NO2 + H               = NO + OH                     1.320E+14   0.00     360.0
```

```
 CO + N2O              = CO2 + N2                  5.010E+13   0.00   44000.0
 CO + NO2              = CO2 + NO                  9.030E+13   0.00   33800.0
C2H5+O=CH3CHO+H                                 1.09E+14    0.0        0.0
   DUPLICATE
C3H7+HO2=CH3CHO+CH3+OH                          2.41E+13    0.0        0.0
C2H4+HO2=CH3CHO+OH                              6.03E+09    0.0     7949.0
C2H5+O=CH3CHO+H                                 6.62E+13    0.0        0.0
  DUPLICATE
C2H3+OH=CH3CHO                                  3.01E+13    0.0        0.0
CH3CHO=CH3+HCO                                  7.00E+15    0.0    81674.0
C2H4+CH3O2=CH3CHO+CH3O                          7.00E+13    0.0    14500.0
C(S) + O2 = O + CO                           3.000E+11   0.00  26800.0
 C(S) + H2O = CO + H2                         3.000E+11   0.00  42800.0
 C(S) + OH = CO + H                           3.000E+12   0.00  32600.0
END
```